Damage Mechanics of Cementitious Materials and Structures

Damage Mechanics Of Cementitious Materials and Structures

Edited by
Gilles Pijaudier-Cabot
Frédéric Dufour

iSTE

WILEY

First published 2012 in Great Britain and the United States by ISTE Ltd and John Wiley & Sons, Inc.

ISTE Ltd
27-37 St George's Road
London SW19 4EU
UK

www.iste.co.uk

John Wiley & Sons, Inc.
111 River Street
Hoboken, NJ 07030
USA

www.wiley.com

Library of Congress Cataloging-in-Publication Data

Damage mechanics of cementitious materials / edited by Gilles Pijaudier-Cabot, Frederic Dufour.
p. cm.
Includes bibliographical references and index.
ISBN 978-1-84821-340-1
1. Concrete--Deterioration. 2. Fracture mechanics. I. Pijaudier-Cabot, Gilles. II. Dufour, Frederic.
TA440.D285 2012
620.1'36--dc23
2011044636

British Library Cataloguing-in-Publication Data
A CIP record for this book is available from the British Library
ISBN: 978-1-84821-340-1

Printed and bound in Great Britain by CPI Group (UK) Ltd., Croydon, Surrey CR0 4YY

FSC
www.fsc.org
MIX
Paper from
responsible sources
FSC® C013604

Table of Contents

Preface

This book is prepared in honor of the retirement of Prof. Jacky Mazars, following a workshop held in Schladming (Austria) in March 2010 under the auspices of Oxand SA with whom Jacky has been closely related recently.

Mazars graduated in 1972 from Ecole Normale Supérieure de l'Enseignement Technique in Cachan. He obtained what was at that time the highest degree at the university, the *thèse de Doctorat d'Etat*, from the University of Pierre and Marie Curie – Paris in 1984.

His association with Ecole Normale Supérieure de l'Enseignement Technique, which later on became Ecole Normale Supérieure (ENS) de Cachan, has played a pivotal role in his scientific career and also had a major impact on the scientific community in civil engineering. It was at the beginning of his career that continuum damage mechanics took off in France under the impulse of Prof. Jean Lemaitre. Mazars took on his share of this job, applying the principles of continuum damage modeling to concrete. His pioneering doctoral thesis is the angular block on which many scientists in civil engineering built their career and research activities.

During the 1980s, Mazars directed the research group at the Laboratoire de Mécanique et Technologie in Cachan.

He has been at the origin of research in Civil Engineering in Cachan and his group, with others in Paris and in Lyon, took the leadership in computational mechanics of concrete structures in France. At that time, research in civil engineering emerged with the help of CNRS within the GRECO Géomatériaux, and Cachan became a major contributor to this collaborative network. It was also in Cachan that the workshop on Damage and Strain Localization was held in 1988, co-chaired by Zdeněk Bažant and Jacky Mazars. Strain and damage localization was a very hot topic at that time and this workshop contributed a lot to the international recognition of the French school on this subject.

The involvement of Mazars at ENS de Cachan has not been limited to research. After being promoted to full professor in 1989, he took on the chairmanship of the Civil Engineering department in 1990 and created the Master's in Civil Engineering at Cachan. Very soon this Master's program became a reference, due not only to the quality of the research and teaching environment, but also to the close links that Jacky contributed to create and enrich with major French-speaking universities: Laval and Sherbrooke in Québec, Liège in Belgium, and Ecole Polytechnique Fédérale in Lausanne. This Master's program and the specificity of ENS, a school entirely devoted to the formation of professors and researchers, created the best conditions for a number of cooperation programs leading to joint PhDs and to international research programs (European programs, Nato sponsorship, France-Berkeley funds, etc.). In 1995, Mazars became the Deputy Director of ENS Cachan. This time it was ENS "at large" that benefited from his energy and his involvement toward a solid and equilibrated development of research and academic programs. For sure, Jacky did not withhold his time and effort for the benefits of all the faculty staff and students in Cachan.

During the 1990s, after a strong cooperation with EDF related to thermo-hygro-mechanical-coupled effects in concrete dams, Jacky's interests in research shifted from durability problems to earthquake engineering; he promoted very important research programs on the new shaking table at CEA Saclay (CASSBA, CAMUS, etc.) and in the framework of JRC Ispra networks. He also became the vice-president of the French Association of Earthquake Engineering (AFPS).

The year 2000 was a turning point in Jacky's career. He moved to Grenoble at the Institut National Polytechnique and geared his research activities toward risk assessment and vulnerability of structures. He created the federation of laboratories "VOR" (vulnerability of structures against risks) and started an association with the "Ministry of Defense – DGA" dealing with the dynamic response of concrete structures. This partnership brought the Giga testing machine in Grenoble, a unique piece of equipment from which very original research results have been obtained and many others are expected. Mazars became the Director of the Laboratoire "Sols, Solides, Structures and Risques (3S-R)" in 2003. He left this position when he became Professor Emeritus at the end of 2009.

Mazars has contributed with key results in constitutive modeling of structural concrete, dynamic, and seismic response of concrete structures, durability and experiments under very high confinement pressures. He belongs to the group of leading experts in these fields in France and in the international community. He has directed many national and international projects and is on the advisory committee of several scientific journals. He has supervised 32 PhD candidates and written over 40 peer-reviewed papers. Jacky's motivation for research and teaching (he is still a *Professeur associé* at Sherbrooke University) has always been close to industrial and practical issues. This is an outstanding quality, not a simple idea but a spirit put to practice. He is recognized as an expert by EDF for nuclear infrastructures and this is also what has been behind his involvement with Oxand over the past years, just to “put the ideas at work”.

Our first idea was to conceive the workshop in Shladming as a friendly gathering aimed at honoring Mazars’s achievements. After the workshop, however, and in view of the quality and the wide scope of the various talks from the invited speakers, we thought that we should grasp the opportunity of assembling a volume dedicated to the recent advances in the spectrum covered by Jacky’s involvement in research. The keyword in this involvement is certainly damage mechanics applied to cementitious materials and more importantly to civil engineering structures. This is exactly the road map of this volume, starting with considerations at the molecular level in the first two chapters and ending with applied case studies on industrial or full-scale structures. In between, fracture and damage of concrete is certainly the link. Modern issues dealing with size/scale effects, deterministic and probabilistic failure models, advanced constitutive modeling, and computational schemes are addressed, providing henceforth a “panorama” of outstanding recent achievements in the modeling of concrete and concrete structures.

Gilles PIJAUDIER-CABOT
Université de Pau et des Pays de l’Adour, France

Frédéric DUFOUR
Institut National Polytechnique de Grenoble, France

Chapter 1

Bottom-Up: From Atoms to Concrete Structures

1.1. Introduction

More concrete is produced than any other synthetic material on Earth. The current worldwide cement production stands at 2.3 billion tons, enough to produce more than 20 billion tons or one cubic meter of concrete per capita per year. There is no other material that can replace concrete in the foreseeable future to meet the legitimate needs of our society's housing, shelter, infrastructure, and so on. But concrete faces an uncertain future, due to a non-negligible ecological footprint that amounts to 5%–10% of the worldwide CO_2 production. It now appears that mechanics can be the discipline that enables the development of a sustainable green concrete future.

We adopt here the perspective originating from Galileo's Strength of Materials Theory that weight, and thus, CO_2 emission, increases with the volume of the produced

---

Chapter written by Franz-Josef ULM and Roland J-M PELLENQ.

material, while strength of structural members increases with the cross-section. Hence, as one increases the strength of a material by a factor of x, the other reduces the environmental footprint by $1/x$ for pure compressive members such as columns and perfect arches and shells, $x^{-2/3}$ for beams in bending and $x^{-1/2}$ for slabs. Similarly, if one adopted a Linear Elastic Fracture model, an increase of the fracture toughness $K_{Ic} = y\, K_{Ic0}$ would entail a reduction of the environmental footprint by $1/y$ for columns and $y^{-4/5}$ for (notched) beams in bending or in torsion. All this hints towards a critical role of mechanics, and in particular, strength of materials, fracture, and damage mechanics of concrete, in redesigning concrete materials and structures for the coming of age of global warming. In contrast to the classical top-down empirical approaches, we have chosen a bottom-up approach that starts at the electron and atomic scale to nanoengineer the fundamental building block of concrete, to assess the properties by nanoindentation, and to upscale strength, fracture, and stiffness properties from nanoscales to macroscales of day-to-day concrete engineering applications. The key to all this is the mechanics at the interface of physics and engineering. This chapter reviews some recent developments of this bottom-up approach.

1.2. A realistic molecular model for calcium-silicate-hydrates

The first step in setting up a bottom-up approach is to address the fundamental unit of concrete material behavior at electron and atomic scale. But, despite decades of studies of calcium-silicate-hydrate (C-S-H), the structurally complex binder phase of concrete and the interplay between chemical composition and density remain essentially unexplored. Together these characteristics of C-S-H define and modulate the physical and mechanical properties of this “liquid stone” gel phase.

1.2.1. *Background*

Much of our knowledge of C-S-H has been obtained from structural comparisons with crystalline C-S-H, based on HFW Taylor's postulate that real C-S-H was a structurally imperfect layered hybrid of two natural mineral analogs: tobermorite of 14-Å interlayer spacing and jennite. While this suggestion is plausible in morphological terms, this model is incompatible with two basic characteristics of real C-S-H, specifically the calcium-to-silicon ratio (C/S) and the density. Recently, small-angle neutron scattering measurements have fixed the C/S ratio at 1.7 and the density at 2.6 g/cm^3 [ALL 07], values that cannot be obtained clearly from either tobermorite (C/S = 0.83, 2.18 g/cm^3) or jennite (C/S = 1.5, 2.27 g/cm^3); see for instance [SHA 09]. From the standpoint of constructing a molecular model of C-S-H, this means that these crystalline minerals are not strict structural analogs. This brought about the development of a realistic molecular C-S-H, based on a bottom-up atomistic simulation approach that considers only the chemical specificity of the system as the overriding constraint [PEL 09]. By allowing for short silica chains distributed as monomers, dimers, and pentamers, this C-S-H archetype of a molecular description of interacting CaO, SiO_2, and H_2O units provides not only realistic values of the C/S ratio and the density computed by grand canonical Monte Carlo simulation of water adsorption at 300 K. The model, displayed in Figure 1.1, with a chemical composition of $(CaO)_{1.65}(SiO_2)(H_2O)_{1.75}$, also predicts other essential structural features and fundamental physical properties amenable to experimental validation. This model suggests that the C-S-H gel structure includes both glass-like short-range order and crystalline features of the mineral tobermorite.

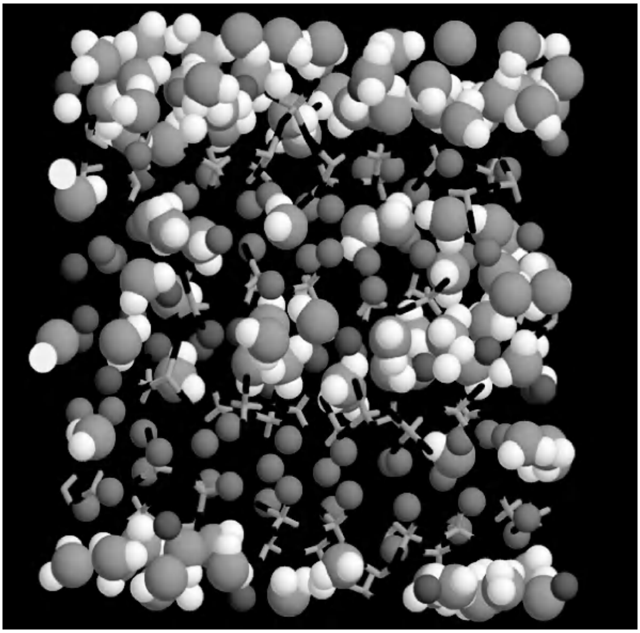

Figure 1.1. *Computational molecular model of C-S-H: the large gray and white spheres are oxygen and hydrogen atoms of water molecules, respectively; the small gray spheres are calcium ions; medium and dark gray sticks are silicon and oxygen atoms in silica tetrahedra (adapted from [PEL 09])*

C_{ij}(GPa)	1	2	3	4	5	6
1	93.5	45.4	26.1	0.6	–0.1	3.46
2		94.9	30.0	–4.6	1.8	–3.0
3			68.5	–4.3	–2.7	–0.6
4				19.2	0.3	1.82
5					16.1	–0.4
6						31.2

Table 1.1. *Elastic tensor of C-S-H determined from molecular dynamic simulations (Voigt notation) (from [PEL 09])*

1.2.2. *Molecular properties of C-S-H*

One of the great advantages of having a realistic molecular model of C-S-H is that it is possible to probe the structure mechanically. The first quantity of interest is the elasticity content of the molecular structure, which is given in Table 1.1 in the form of components of the elasticity tensor. As we may expect from a glassy-layered hybrid, the elasticity exhibits a high degree of anisotropy. For further applications, it will be useful to consider the random polycrystal properties, in the form of the Voigt–Reuss–Hill approximation classically used in mineralogy. As shown by Povolo and Bolmaro [POV 87], both the Voigt and Reuss models are built using the invariance of the trace of the 9 × 9 matrix representing the stiffness and compliance tensors, respectively. This leads to the observation (made by Hill) that the Voigt and Reuss averages only use 9 of the 21 independent elastic constants. Denoted by $I_1 = C_{iijj}$ and $I_1{}^* = C_{ijij}$ the traces (or linear invariants) of tensors C_{iikl} and C_{ijjl}, respectively, the Voigt average is obtained from a comparison of those traces with their corresponding isotropic expressions, leading to:

$$K^{Voigt} = \frac{1}{9} I_1; \quad G^{Voigt} = \frac{1}{30}(3I_1^* - I_1) \qquad [1.1]$$

Applying a similar procedure to the compliance tensor $S_{ijkl} = C_{ijkl}^{-1}$, the Reuss average is obtained:

$$K^{\text{Reuss}} = \frac{1}{J_1}; \quad G^{\text{Reuss}} = \frac{15}{6J_1^* - 2J_1} \qquad [1.2]$$

where $J_1 = S_{iijj}$ and $J_1{}^* = S_{ijij}$ are the corresponding traces of the compliance tensors S_{iikl} and S_{ijjl}, respectively. The Reuss–Voigt–Hill polycrystal properties are obtained as the arithmetic mean of Reuss and Voigt bounds, which yields for C-S-H:

$$K^{C-S-H} = 49\,\text{GPa}; \qquad G^{C-S-H} = 23\,\text{GPa} \qquad [1.3]$$

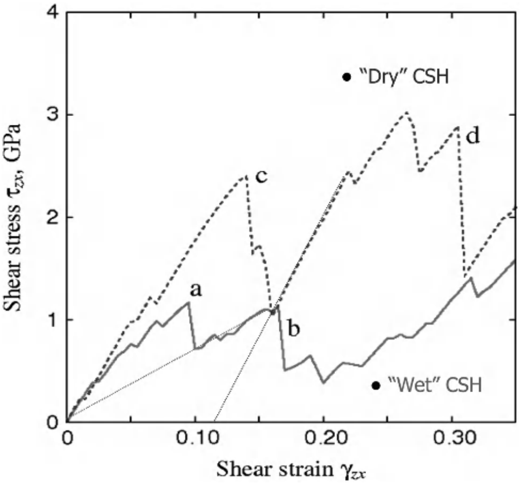

Figure 1.2. *Relationship between the shear stress and the shear strain for the C-S-H model with (solid line) and without (dashed line) water molecules (results obtained by A. Kushima and S. Yip; adapted from [PEL 09])*

A second useful insight the molecular model can provide is about the strength behavior, by simulating for instance the stress–strain behavior of the C-S-H model in affine shear deformation (strain controlled) after first relaxing the computational cell using MD at 300 K, under constant NVT ensemble conditions. A series of shear strains in increments of 0.005 is imposed; after each increment the atomic configuration is relaxed and the shear stress determined from the virial expression. Figure 1.2 displays the shear stress–strain response of the C-S-H model. Two configurations are herein considered: the "wet" model, in which water is present particularly in the interlayer space, and the "dry" model, in which all water molecules have been removed. The stress–strain response shows that the presence of water in the interlayer space leads to a localization of deformation into a narrow band defined by a wet interlayer, akin to a fracturing or damage process. By contrast, the "dry" model shows a plastic deformation behavior, with irreversible (plastic) deformation upon unloading.

This shows that there are some strength reserves at a molecular scale of C-S-H that could enhance strength and (ductile) deformation behavior of C-S-H.

1.2.3. *From molecular properties to C-S-H microtexture*

The molecular model of C-S-H has been validated against several experimentally accessible properties, including density, extended X-ray absorption fine structure (EXAFS) spectroscopy signals measuring short-range order around Ca atoms, longer range correlations revealed in X-ray diffraction intensity, vibrational density of states measured by infrared spectroscopy, and nanoindentation measurements of elasticity and strength properties (for details, see [PEL 09]). Here, we restrict ourselves to the comparison with nanoindentation experiments. Nanoindentation measurements of C-S-H do not probe the particle properties, but rather the C-S-H gel properties. From a straightforward dimensional analysis, the link between particle properties and microstructure is provided by [ULM 07]:

$$\begin{aligned} H &= \frac{P}{A_c} = h_s \times \Pi_H(\mu, \eta, \eta_0) \\ M &= c\frac{\left(dP/dh\right)_{h_{\max}}}{\sqrt{A_c}} = m_s \times \Pi_M(\nu, \eta, \eta_0) \end{aligned} \qquad [1.4]$$

where H is the hardness, and M is the indentation modulus that is accessible from the applied force P, the indentation depth h, and the projected contact area A_c. In return, h_s and m_s are the particle hardness and plane stress modulus, respectively, with the latter being defined for an isotropic material by:

$$m_s = 4G\frac{3K+G}{3K+4G} = 65\,\text{GPa} \qquad [1.5]$$

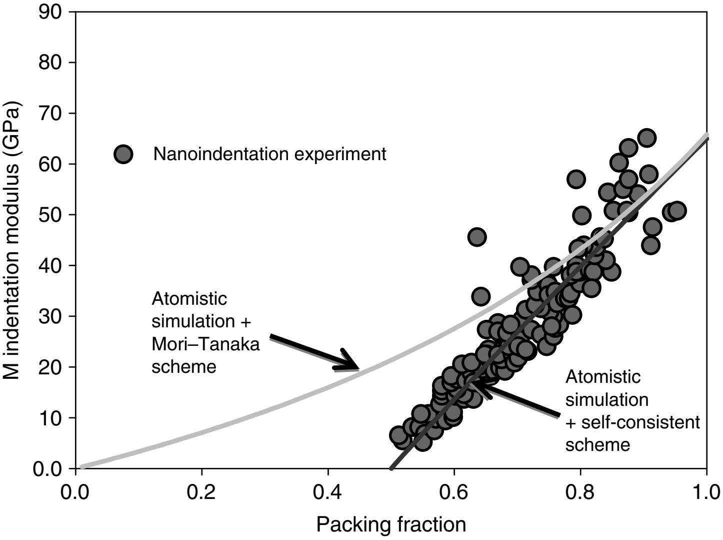

Figure 1.3. *Nanoindentation data (from [VAN 09]) compared with two micromechanics models. The input for the model is the elastic C-S-H properties (indentation modulus = 65 GPa, Poisson's ratio = 0.3) (adapted from [PEL 09])*

where we used the values for K and G in equation [1.3] determined from MD simulations. Furthermore, functions $\prod_H$ and $\prod_M$ in equation [1.4] are dimensionless functions of the friction coefficient μ, the Poisson's ratio ν, and the packing density η. Linear and nonlinear microporomechanics [DOR 06] provide a convenient way to determine these functions analytically [CON 07, CAR 08]. Moreover, combining the elastic properties determined from the C-S-H model with these micromechanics models with no adjustable parameters, we can probe the texture and the extent of anisotropic structures within cement paste at micrometer length scales of randomly oriented C-S-H particles. Figure 1.3 compares the prediction of two micromechanics models along with nanoindentation results; one model is a porous bicontinuous matrix approach captured by the so-called

Mori–Tanaka scheme, and the other model is a granular approach captured by the self-consistent scheme. From this comparison, we first observe that the granular approach better describes the experimental data over the entire domain of C-S-H particle packing fractions. Second, both the approaches give acceptable predictions at larger packing fractions. That is, at the microtexture scale, Mori–Tanaka and self-consistent micromechanics approaches, parameterized only with nanoscale-derived elasticity constants, indicate that cement paste can be conceptualized as a cohesive granular material rather than a porous bicontinuous matrix.

1.3. Probing C-S-H microtexture by nanoindentation

With the molecular properties of C-S-H in hand, it becomes possible to assess the microstructure of cement-based materials at micrometer scale, and ultimately to make the link between microstructure and meso- and macroscale properties. The keys herein are the dimensionless scaling relations $\prod_H$ and $\prod_M$ in equation [1.4].

1.3.1. *Does particle shape matter?*

The determination of functions $\prod_H$ and $\prod_M$ requires the choice of particle morphology. For perfectly disordered materials, the key quantity to be considered is the percolation threshold, that is the critical packing density below which the composite material has neither strength nor stiffness. This percolation threshold depends on the particle shape for randomly oriented particulate materials [SAN 07]; but less so whenever some privileged orientation is present [ORT 10]. Clearly, as seen in transmission electron microscopy images of C-S-H, the elementary particle has an aspect ratio.

Anyway, as far as the mechanics response is concerned, it turns out that particle shape does not matter as soon as the packing density of the porous material is greater than 60%. This is obviously the case of cement-based materials (as their industrial success is due to their strength performance), and also of most other natural composite materials, such as bone and compacted clays (shale). We can thus conclude that the effect of particle shape is negligible as far as the mechanical performance is concerned [ULM 08] (see Figure 1.4). The negligible effect of the particle shape on the homogenized mechanical properties largely simplifies the micromechanical analysis. It thus suffices to consider spherical particles and a distinct disordered morphology of the solid phase similar to a polycrystal, characterized by a solid percolation threshold of $\eta_0 = 0.5$. These relations can be found, for the indentation modulus, in [CON 07] and, for the indentation hardness, in [CAR 08].

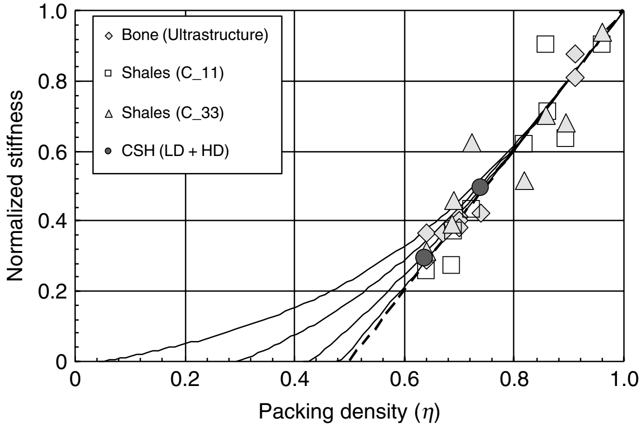

Figure 1.4. *Normalized stiffness vs. packing density scaling relations. The percolation threshold of 0.5 corresponds to a perfectly disordered material composed of spherical particles, while lower percolation thresholds are representative of disordered materials with particle shape (here ellipsoids) (adapted from [ULM 08])*

1.3.2. *Implementation for back analysis of packing density distributions*

Consider then a series of N indentation tests on a heterogeneous material. What is measured in these tests are N times (M, H) values at each indentation point representative of a composite response. Assuming that the solid phase is the same, i.e. C-S-H with now well-defined elasticity properties, and that all of what changes between indentation points is the packing density, there are two unknown particles (h_s and μ) and N packing densities. Hence, for $N >> 2$, the system is highly determined-over, which makes it possible to assess microstructure and particle properties [ULM 07]. We can then proceed with a statistical analysis of the packing density distributions, as shown in Figure 1.5.

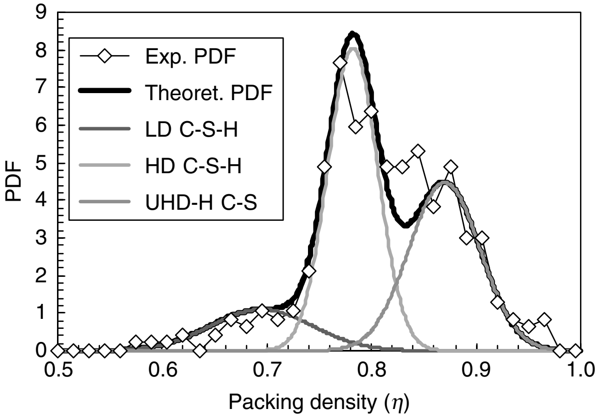

Figure 1.5. *Probability density plot (PDF) of packing density distribution determined from 400 nanoindentation tests on a w/c = 0.3 cement paste, together with a phase deconvolution obtained by fitting Gaussian distributions to the experimental PDF (adapted from [VAN 09])*

The interesting feature which emerges from this analysis is the presence of different C-S-H gel phases in the microstructure, namely low-density (LD) phase and high-density (HD) phase, as originally proposed by Jennings *et al.* (for a recent review, see [JEN 07]), with mean packing densities close to two limit packing densities of spherical objects, that is the 64% packing density of the random close-packed limit for the LD phase and the 74% of the ordered face-centered cubic (fcc) or hexagonal close-packed (hcp) packing for the HD phase. In addition, a third ultra-high-density (UHD) phase appears in the packing fraction distribution, particularly for cement pastes with low water-to-cement (w/c) ratios [VAN 10]. Indeed, a comprehensive nanoindentation analysis of cement pastes prepared at different w/c ratio shows that LD dominates cement-based materials prepared at high w/c mass ratios; HD and UHD control the microstructure of low w/c ratio materials (Figure 1.6). This shows that nanoindentation combined with micromechanics-based indentation analysis provides a means to probe the microstructure of the C-S-H gel at micrometer scale of cement-based materials.

1.3.3. *Functionalized properties: nanogranular origin of concrete creep*

It is now possible to make the link between microstructure and mechanical performance. Besides elasticity and strength, a main concern for concrete is creep. Concrete creep occurs at a rate that deteriorates the durability and truncates the lifespan of concrete structures. One challenge in establishing this link between creep properties and microstructure is that creep of C-S-H needs to be experimentally measured at the scale of the microstructure of the C-S-H gel. We consider here nanoindentation creep tests, in addition to nanoindentation tests of stiffness and elasticity that allow the determination of the packing density distribution. The difference between the two types of test is in a holding phase: following a fast loading (5 s), in nanoindentation creep tests a constant load is applied for some 180 s, in contrast to microstructure tests in which the dwelling time is 5 s.

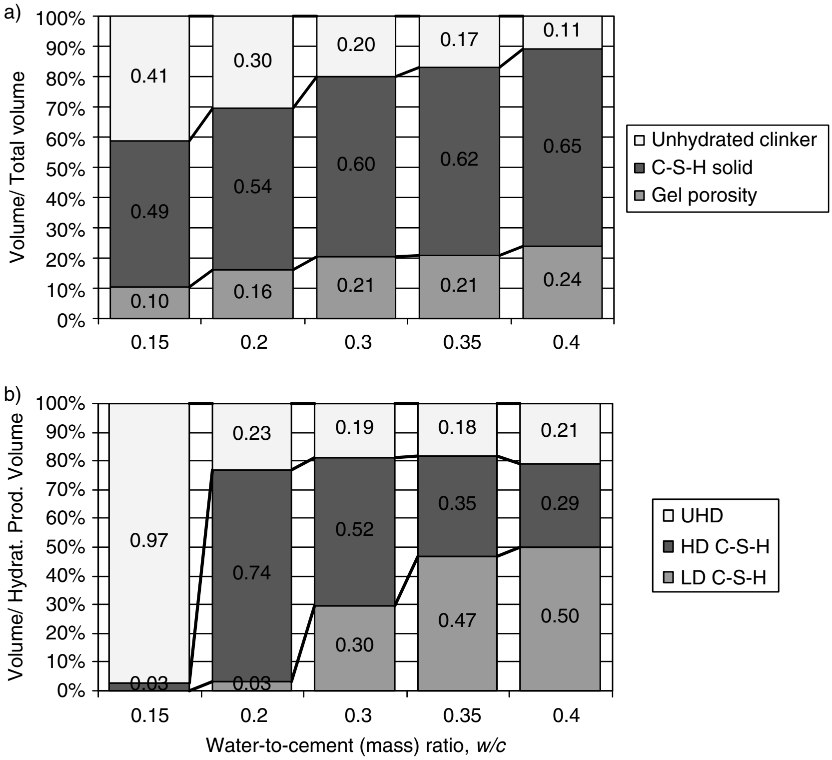

Figure 1.6. *Volume fraction distributions in the microstructure: (a) volume fractions of the cement paste composite; (b) volume fractions of the hydration phases (adapted from [VAN 10])*

During the 180 s dwelling time, the change in indentation depth $\Delta h(t) = h(t) - h_0$ is recorded as a function of time. In all tests on C-S-H phases, after correcting for thermal drift effects of the indenter equipment, a least-square fitting of $\Delta h(t) = h(t) - h_0$ demonstrates an indentation creep compliance of the C-S-H phases that is logarithmic with regard to time (Figure 1.7). The indentation creep compliance rate is determined as [VAN 06, VAN 09]:

$$\dot{L} = 2a_U\dot{h} / P_{\max} = 1/(Ct) \qquad [1.6]$$

where $a_U = \sqrt{A_c/\pi}$ is the contact radius at the end of the dwelling phase, while C, which has the same dimension as that of an elastic modulus, is justly termed contact creep modulus [VAN 09]. This creep modulus C depends on the packing density, as shown in Figure 1.8. It is in the order of C_{LD}=120.4±22.6 GPa, C_{HD}=183.6±30.5 GPa, and C_{UHD}=318.6±32.2 GPa. The value for C_{LD}=120.4±22.6 GPa comes remarkably close to macroscopic values of the long-term creep of normal strength concrete, while the value for C_{UHD}=318.6±32.2 GPa is not far off from the long-term creep values of high-strength concrete – with one major difference: a nanoindentation creep test takes 3 minutes, a long-term macroscopic creep test requires several years of force deformation control under highly controlled environmental conditions [ACK 01].

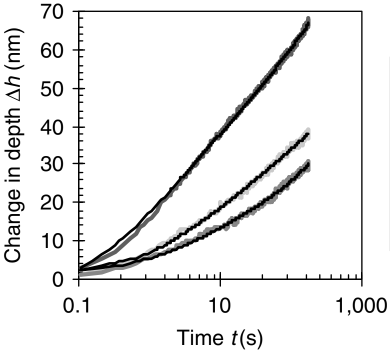

Figure 1.7. *During the 180 s dwelling time, the change in indentation depth is recorded as a function of time and is fitted with a logarithmic function (for details, see [VAN 09])*

This observation opens new perspectives for creep assessment of concrete materials and structures: by probing micrometer-sized volumes of materials. Nanoindentation creep experiments provide quantitative results in a six orders of magnitude shorter time and on samples six orders of magnitude smaller in size than classical macroscopic creep tests. This “length–time equivalence” (large time scales can be accessed by looking at small length scales) may turn out invaluable for the implementation of sustainable concrete materials whose durability will meet the increasing worldwide demand of construction materials for housing, schools, hospitals, energy and transportation infrastructure, and so on.

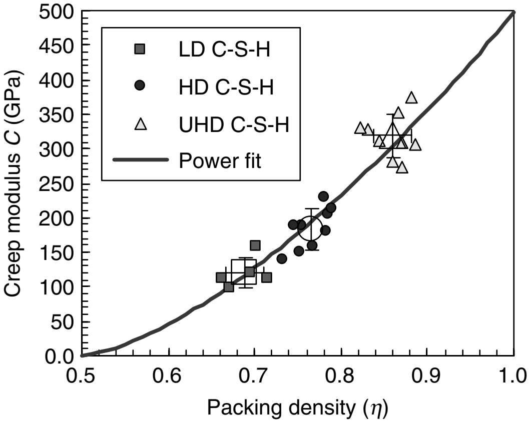

Figure 1.8. *Creep modulus – packing density relation (adapted from [VAN 09])*

1.4. Conclusions

The premise of the bottom-up approach is to identify new degrees of freedoms for concrete material and structural design, from electrons and atoms to structures. While still in its infancy, the first results obtained with this bottom-up approach reveal some interesting perspectives for enhancing the sustainability of this omnipresent material. With a focus on strength enhancement, we note:

– On the atomic scale, strength enhancement may be achieved by fine-tuning the chemistry of cement-based materials. Classical cement-based materials exhibit a calcium-to-silicon ratio (C/S) of 1.7, which determines mechanical properties of the molecular structure. A change in chemistry is expected to enhance those properties.

– At the scale of the microtexture, a denser packing of elementary C-S-H particles has the premise to enhance both the strength behavior and the durability performance, for instance, in terms of concrete creep.

– From the micro to the macro of concrete structures, continuum micromechanics provide a powerful framework to translate progress in materials science into day-to-day engineering applications.

As engineers move into the fundamentals of the physics of materials and physicists move into engineering applications, the boundary between physics and engineering is finally blurred. It is on this basis that we expect that progress on the concrete front will translate into societal benefits. In this way, we believe that computational and experimental mechanics of concrete will be redefined.

1.5. Bibliography

[ACK 01] ACKER P, ULM F.-J., "Creep and shrinkage of concrete: physical origins and practical measurements", *Nuclear Engineering and Design*, vol. 203, nos. 2–3, pp. 143–158, 2001.

[ALL 07] ALLEN A.J., THOMAS J.J., JENNINGS H.M., "Composition and density of nanoscale calcium-silicate-hydrate in cement", *Nature Materials*, vol. 6, no. 4, pp. 311–316, 2007.

[CAR 08] CARIOU S., ULM F.J., DORMIEUX L., "Hardness-packing density scaling relations for cohesive-frictional porous materials", *Journal of the Mechanics and Physics of Solids*, vol. 56, no. 8, pp. 924–952, 2008.

[CON 07] CONSTANTINIDES G., ULM F.J., "The nanogranular nature of C-S-H", *Journal of the Mechanics and Physics of Solids*, vol. 55, no. 1, pp. 64–90, 2007.

[DOR 06] DORMIEUX L., KONDO D., ULM F.J., *Microporomechanics*, J. Wiley & Sons, Chichester, UK, 2006.

[JEN 07] JENNINGS H.M., THOMAS J.J., GEVRENOV J.S., CONSTANTINIDES G., ULM F.J., "A multi-technique investigation of the nanoporosity of cement paste", *Cement and Concrete Research*, vol. 37, no. 3, pp. 329–336, 2007.

[ORT 10] ORTEGA J.-A., ULM F.J., ABOUSLEIMAN Y., "The effect of particle shape and grain-scale properties of shale: a micromechanics approach", *International Journal of Numerical and Analytical Methods in Geomechanics*, vol. 34, no. 11, pp. 1124–1156, 2010.

[PEL 09] PELLENQ R.J.-M., KUSHIMA A., SHAHSAVARI R., VAN VLIET K.J., BUEHLER, M.J., YIP S., ULM F.J., "A realistic molecular model of cement hydrates", *Proceedings of the National Academy of Sciences*, USA, vol. 106, no. 38, pp. 16102–16107, 2009.

[POV 87] POVOLO F., BOLMARO R.E., "Average elastic-constants and tensor invariants", *Physica Status Solidi (a)*, vol. 99, no. 2, pp. 423–436, 1987.

[SAN 07] SANAHUJA J., DORMIEUX L., CHANVILLARD G., "Modelling elasticity of a hydrating cement paste", *Cement and Concrete Research*, vol. 37, pp. 1427–1439, 2007.

[SHA 09] SHAHSAVARI R., BUEHLER M.J., PELLENQ R.J.-M., ULM F.J., "First-principles study of elastic constants and interlayer interactions of complex hydrated oxides: case study of tobermorite and jennite", *Journal of American Ceramic Society*, vol. 92, no. 10, pp. 2323–2330, 2009.

[ULM 07] ULM F.J., VANDAMME M., BOBKO C., ORTEGA J.A., TAI K., ORTIZ C., "Statistical indentation techniques for hydrated nanocomposites: concrete, bone, and shale", *Journal of American Ceramic Society*, vol. 90, no. 9, pp. 2677–2692, 2007.

[ULM 08] ULM F.J., JENNINGS H.M., "Does C-S-H particle shape matter?" *Cement and Concrete Research*, vol. 38, nos. 8–9, pp. 1126–1129, 2008.

[VAN 06] VANDAMME M., ULM F.J., "Viscoelastic solutions for conical indentation", *International Journal of Solids and Structures*, vol. 43, no. 10, pp. 3142–3165, 2006.

[VAN 09] VANDAMME M., ULM F.J., "Nanogranular origin of concrete creep", *Proceedings of the National Academy of Sciences*, vol. 106, no. 26, pp. 10552–10557, 2009.

[VAN 10] VANDAMME M., ULM F.J., FONOLLOSA P., "Nanogranular packing of C-S-H at substochiometric conditions", *Cement and Concrete Research*, vol. 40, no. 1, pp. 14–26, 2010.

Chapter 2

Poromechanics of Saturated Isotropic Nanoporous Materials

Poromechanics offers a consistent theoretical framework for describing the mechanical response of porous solids. When dealing with fully saturated nanoporous materials, which exhibit pores of the nanometer size, additional effects due to adsorption and confinement of the fluid molecules in the smallest pores must be accounted for. From the mechanical point of view, these phenomena result in volumetric deformations of the porous solid, the so-called "swelling" phenomenon, and in a change of the apparent permeability. The present work investigates how poromechanics may be refined in order to capture adsorption and molecular-packing-induced effects in nanoporous solids. The revisited formulation introduces an effective pore pressure, defined as a thermodynamic variable at the representative volume element scale (mesoscale), which is related to the mechanical

---

Chapter written by Romain VERMOREL, Gilles PIJAUDIER-CABOT, Christelle MIQUEU and Bruno MENDIBOURE.

work of the fluid at the pore scale (nanoscale). Accounting for the thermodynamic equilibrium of the system, this effective pore pressure is obtained as a function of the bulk fluid pressure, the temperature, and the total and excess adsorbed masses of fluid. We derive the analytical swelling strains due to sorption and molecular packing. A good understanding in the comparison with experimental data dealing with the swelling of coal due to methane and carbon dioxide sorption is observed, as a preliminary stage toward modeling partially saturated solids and applications to cement paste.

2.1. Introduction

Poromechanics offers a consistent theoretical framework for describing the mechanical response of fully saturated or partially saturated porous solids. The theory is based on the superposition of the solid and liquid phases. In the case of fully saturated porous solids, it is assumed that the fluid–solid interaction is restricted to the influence of the pressure on the inner surface of the porous material. In partially saturated porous solids, additional forces, i.e. capillary forces are introduced. Many authors have used this modern theoretical framework, which is thoroughly described, e.g. in [COU 04], [COU 10].

We are going to specifically focus on “nanoporous” materials, e.g. solids with pores down to the nanometer size ($\leq 2\,\mathrm{nm}$). Hardened cement paste or tight rocks are among those materials, which can be used in construction, or may be encountered in the production of gas from very tight reservoirs or coal seams. Aside from the classical fluid–solid interaction observed in macroporous materials, there are additional effects that should be considered in such materials: (i) adsorption is important because the inner surface of the pores is very large and surface forces cannot be neglected anymore; (ii) in very small pores, the molecules of fluid are confined. Interaction between molecules of fluid is modified; it cannot develop in the same way as it would if the fluid were placed in a large container. This effect, denoted as molecular packing, includes fluid–fluid and fluid–solid interactions.

From the macroscopic mechanical point of view, these phenomena result into volumetric deformations of the porous solid. Swelling is commonly observed during sorption–desorption of several gases such as carbon dioxide or methane in charcoal, see, e.g. the paper by Levine [LEV 96] although seminal experimental works of Meehan [MEE 27] or Bangham and Fakhroury [BAN 28] date back to the 1920s. In the more complex context of unsaturated cement pastes, the variation of disjoining pressure due to the variation of relative humidity is one of the most probable mechanism's for desiccation-induced shrinkage [BEL 05]. Disjoining pressures follow a similar scheme as adsorption effects, except that a gas/fluid interface is involved in addition to the solid/fluid interface. Hence, shrinkage upon desiccation can be regarded as a volumetric deformation upon desorption.

In this chapter, we are going to investigate how the poromechanical theory may be refined to take account of adsorption and molecular packing in nanopores. In order to provide the reader with an illustration of these effects, we start with molecular simulations of a slit pore containing a simple fluid. We examine the variation of pore pressure with the bulk fluid pressure to which it is connected and with the pore width. Then, in view of the complexity of the local – atomistic – effects at this scale, we turn toward averaged, macroscopic considerations. The formulation which is thoroughly described in [VER] introduces an effective pore pressure as a thermodynamical variable defined at the representative elementary volume (REV) scale. Accounting for the thermodynamic equilibrium of the system composed of the nanoporous skeleton, the interstitial and external bulk reference fluid, the relation between the effective pore pressure and quantities measurable in experiments such as the temperature, the bulk fluid pressure, and the total and excess adsorbed mass of fluid is obtained. The swelling of a porous material, saturated with a simple fluid, is obtained as a function of adsorption and mechanical parameters. Finally, the case of fluid transport in such a nanoporous material is considered. A Darcy-type relation is derived, in which an effective intrinsic permeability appears. This permeability is a function of the bulk fluid pressure, and it decreases as the bulk pressure increases.

In the illustrations, we will focus on activated carbon and coal saturated with a simple gas, which are materials rather remote to cement paste. These examples should be understood as a first step toward a formulation applicable to cement paste which is partially saturated. Only physisorption is considered and electrical effects are neglected, which aids in simplification. Also, the porous material is fully saturated, and preferential sorption is thus not considered (which is another complexity of the problem). Yet, the foregoing discussion provides some insight on the pertinence of the approach and sets the scene for more complex applications, those involved in the understanding of the time-dependent response of cement-based materials.

2.2. Results from molecular simulations

We consider a slit pore of width H, as shown in Figure 2.1a. Monte Carlo simulations are performed in the grand canonical ensemble. The fluid–fluid interactions are described with a 12-6 Lennard-Jones potential and the solid–fluid interaction by the integrated 10-4-3 potential. Numerous studies, based on molecular simulations [MEN, PIJ, KNO 10] and discrete Fourier transform (DFT) methods [YAN 10], focus on modeling the spatial variations of the fluid properties, namely the fluid density, viscosity, and pore pressure, at the scale of a single nanopore. We will focus on the normal pressure inside the pore only. The pore pressure P is the component perpendicular to the surface of the pore. In confined fluids, the pressure is not a scalar, and the tangent and normal pressures to the surface of the pore are different. The normal pressure P is computed with the Viriel estimate, as described by Varnik *et al.* [VAR 00].

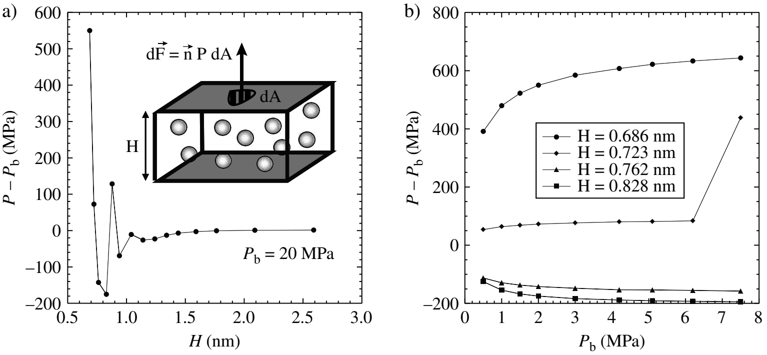

Figure 2.1. *(a) Component of the pore pressure perpendicular to the pore wall vs. the pore size, for a bulk pressure equal to 2 MPa (methane into graphitic slit pores at 353 K). Inserted figure: Model of graphite parallel slit pore used in GCMC simulations. (b) Component of the pore pressure perpendicular to the pore wall vs. bulk pressure, for different pore sizes (methane into graphitic slit pores at 353 K). Dots represent the molecular simulations results; solid lines are guides for the eyes*

In the present calculations, the solid phase is graphite and the fluid phase is methane at 353 K. For a bulk pressure equal to 2 MPa, the evolution of the pore pressure with the pore width is plotted in Figure 2.1a. Oscillations corresponding to the structuration of the fluid into layers are observed. This structuration effect results from the confinement of the fluid molecules between the two infinitely rigid pore walls. Note the range of variation of the pore pressure, with very high values for small pore sizes. Figure 2.1b shows the pore pressure versus the bulk pressure for several pore sizes. This is clearly a nonlinear relation which is very much dependent on the pore size H.

In summary, the grand canonical molecular computations (GCMC) indicate that adsorption and confinement of the fluid molecules in the nanopores result in pressure differentials between the interstitial fluid and the external bulk solution. From the mechanical point of view, these adsorption-induced pressure differentials are likely to provoke volumetric deformations of the nanoporous material. The difficulty is that the pore pressure strongly depends on the geometry of the pores and on the pore size distribution. The smallest pores contribute the most to high pressures, only the fluid is not ordered in the pore. Therefore, it is rather difficult to provide an overall picture of the mechanical effect of fluid confinement, upscaling results from molecular simulations directly. In the following sections, we are going to show how the poromechanical theory may be refined in order to take into account these singular effects in a global way, based on some energy equivalence.

2.3. Poromechanical model

In this section, we present the poromechanical model for saturated isotropic nanoporous solids. After introducing the general nomenclature and definitions, we define the effective pore pressure. Then, we derive the expressions for the dissipations following the theory of the thermodynamics of porous continua proposed by Coussy [COU 04]. Referring to the principle of thermodynamical equilibrium, we derive an equation which relates the state variables of the interstitial fluid to those of the bulk external fluid.

2.3.1. *Nomenclature and definitions*

The porous medium is an open thermodynamic system, which consists of the superposition of a porous solid phase, the skeleton, and an interstitial fluid phase that can exchange fluid mass with the external reference bulk solution. Hence, the use of a subscript s or f refers to a variable related to the skeleton or to the interstitial fluid, respectively. Moreover, the subscript b is used when referring to the bulk solution. For instance, a quantity χ, related to the phase π will be written χ_π, with $\pi = f$, s, and b for the interstitial fluid, the skeleton, and the bulk fluid, respectively.

Poromechanics describes the behavior of a porous medium at the mesoscale of the REV at which the different variables are defined. Though, when dealing with nanoporous solids, in which the thermodynamical state of the intersititial fluid depends locally on the pore size and geometry, quantities defined at the nanoscale of the pores are involved as well. Quantities related to the pore nanoscale are superscripted with the letter n. We emphasize that the pore scale variables appearing in this work stand for the mean quantities calculated over the volume of a pore of a specific size and geometry. For example, the pore scale fluid density ρ_f^n, which depends on the pore size and geometry, stands for the mean fluid density calculated over the volume of the pore.

The porosity is defined as the ratio of the volume of the connected pores to that of the total volume of the porous solid. In other words, the occluded pores are not accounted for in the definition of the porosity. In the context of nanoporous materials, the proportion of occluded porosity might depend on the nature of the saturating fluid, as only pores larger than the fluid molecules size are accessible. We note ϕ and φ to be the Lagrangian and Eulerian porosity, respectively, and we write:

$$\phi = \frac{1}{\Omega_0} \int_{\Omega_0} d\Omega_0 \, \phi^p \qquad [2.1]$$

$$\varphi = \frac{1}{\Omega^e} \int_{\Omega^e} d\Omega^e \, \varphi^p \qquad [2.2]$$

where Ω_0 and Ω^e stand for the Lagrangian and the Eulerian REV. ϕ^p and φ^p are, respectively, the partial Lagrangian and Eulerian porosity, i.e. the porosity related to all the pores of a specific size and geometry in the REV. Relations [2.1] and [2.2] exemplify how mesoscale extensive quantities are obtained from summation of their nanoscale counterparts over the REV.

2.3.2. *Effective pore pressure*

Classical poromechanics account for the stress related to the skeleton and the stress related to the fluid separately. In a saturated porous solid, in which no confinement effects occur, the stress partition in the Eulerian frame is expressed as

$$\begin{aligned} \underline{\underline{\Sigma}}^e &= (1-\varphi)\underline{\underline{\Sigma}}_s^e + \varphi\underline{\underline{\Sigma}}_f^e \\ &= (1-\varphi)\underline{\underline{\Sigma}}_s^e - \varphi P_b \underline{\underline{\mathbb{1}}} \end{aligned} \qquad [2.3]$$

where $\underline{\underline{\Sigma}}^e$ is the global stress tensor related to the porous continuum in the Eulerian frame, $\underline{\underline{\Sigma}}_s^e$ and $\underline{\underline{\Sigma}}_f^e$ are the skeleton and fluid stress tensors in the Eulerian frame, respectively, and P_b is the bulk fluid pressure. Thus, the intrinsic averaged stress within the fluid is addressed through the spherical tensor $-P_b\underline{\underline{\mathbb{1}}}$. This comes down to considering that the fluid applies an isotropic pressure on the pores walls, which is equal to the bulk pressure.

At the scale of the nanopores, molecular simulations clearly show that the fluid stress tensor is anisotropic and depends locally on the size and the geometrical shape of the pores. With the exception of some synthetic materials [GOG 03], nanoporous solids such as coal or cement paste usually exhibit a continuous pore size distribution, with distributed pore geometries and spatial orientations. The calculation of effective poromechanical properties based on micro–macro upscaling methods is an open problem. Existing methods are often restricted to the description of model nanoporous materials (e.g. in [PEN 09]). Nevertheless, numerous experimental studies demonstrate that the sorption-induced strains in nanoporous solids are isotropic as long as the material structure is isotropic [LEV 96, DAY 08a, OTT 08]. Thus, in the case of isotropic saturated nanoporous materials, at the scale of the REV we can consider that the interstitial fluid acts as an effective fluid exerting an isotropic pore pressure P_f on the pores walls. Let us point out that the effective pore pressure may be different from the bulk fluid pressure P_b. As a result, in the nanoporous material, the stress partition is given by

$$\begin{aligned}\underline{\underline{\Sigma}}^e &= (1-\varphi)\underline{\underline{\Sigma}}^e_s + \varphi\underline{\underline{\Sigma}}^e_f \\ &= (1-\varphi)\underline{\underline{\Sigma}}^e_s - \varphi P_f \underline{\underline{\mathbb{1}}}.\end{aligned} \qquad [2.4]$$

In the limit of small strains, the stress partition in the Lagrangian frame is given by [COU 10]

$$\underline{\underline{\Sigma}} = (1-\phi)\underline{\underline{\Sigma}}_s - \phi P_f \underline{\underline{\mathbb{1}}}. \qquad [2.5]$$

Following a reasoning based on the conservation of the internal energy of the interstitial fluid, the effective pore pressure can be expressed in terms of the nanoscale variables of the fluid. Because it is an extensive quantity, the Lagrangian Gibbs energy G_f of the interstitial fluid (defined per unit REV volume) may be obtained by summation over the porous space:

$$G_f = \frac{1}{\Omega_0}\int_{\Omega_0} d\Omega_0\, \phi^p \rho_f^n g_f^n \qquad [2.6]$$

where g_f^n is the specific Gibbs energy (energy per unit mass) of the interstitial fluid at the pores scale. Using the thermodynamic identity at the pores scale, the specific Gibbs energy may be written in terms of the specific Helmholtz energy ψ_f^n and specific fluid mechanical work w_f^n:

$$g_f^n = \psi_f^n + w_f^n. \qquad [2.7]$$

Consecutively, substituting [2.7] into [2.6], we obtain

$$G_f = \frac{1}{\Omega_0} \int_{\Omega_0} d\Omega_0 \, \left(\phi^p \rho_f^n \psi_f^n + \phi^p \rho_f^n w_f^n \right)$$
$$= \Psi_f + \frac{1}{\Omega_0} \int_{\Omega_0} d\Omega_0 \, \phi^p \rho_f^n w_f^n. \qquad [2.8]$$

In addition, the Gibbs energy may be expressed using the thermodynamic identity at the REV scale as follows:

$$G_f = \Psi_f + \phi P_f \qquad [2.9]$$

in which ϕP_f stands for the interstitial fluid mechanical work at the REV scale. By identification of equations [2.8] and [2.9], we find

$$P_f = \frac{1}{\phi \Omega_0} \int_{\Omega_0} d\Omega_0 \, \phi^p \rho_f^n w_f^n. \qquad [2.10]$$

Equation [2.10] relates the effective pore pressure to the fluid mechanical work at the pore scale. Moreover, [2.10] ensures that the interstitial fluid mechanical work, expressed in terms of the REV-scale variables, equals the actual fluid mechanical work calculated from the nanoscale.

2.3.3. *Thermodynamical equilibrium condition*

The poromechanical theory distinguishes three sources of dissipation: the skeleton dissipation, the fluid dissipation, and the thermal dissipation. The skeleton dissipation Φ_s is expressed in the Lagrangian frame as [COU 04]

$$\Phi_s = \underline{\underline{\Sigma}} : \frac{d\underline{\underline{\Delta}}}{dt} - g_f \vec{\nabla}.\vec{M} - S\frac{dT}{dt} - \frac{d\Psi}{dt} \geq 0 \qquad [2.11]$$

where $\underline{\underline{\Delta}}$ is the Lagrangian strain tensor, $\vec{M}$ is the Lagrangian relative flow vector of fluid mass, T is the temperature, and S and Ψ are the global entropy and the global Helmholtz free energy of the porous medium {skeleton; interstitial fluid} in the Lagrangian frame, respectively. This expression of the skeleton dissipation is identical to the expression encountered in standard poromechanics. Nevertheless, in the case of the nanoporous continuum, the difference with standard poromechanics lies in the expression of the specific Gibbs energy that involves the effective pore pressure instead of the bulk fluid pressure:

$$g_f = \psi_f + \frac{\phi P_f}{m_f} \tag{2.12}$$

Let us consider now a nanoporous solid immersed in an adiabatic and infinitely rigid container filled with a mass m of fluid. In such conditions, the system {skeleton; interstitial fluid; bulk fluid} is an isolated thermodynamic system. In the limit of reversible transformations, the skeleton dissipation of the open thermodynamic system {skeleton; interstitial fluid} vanishes, and we can write

$$\frac{d\Psi}{dt} = \underline{\Sigma} : \frac{d\underline{\underline{\Delta}}}{dt} - g_f \vec{\nabla}.\vec{M} - S\frac{dT}{dt}. \tag{2.13}$$

The conservation of the interstitial fluid mass is expressed as

$$\frac{dm_f}{dt} + \vec{\nabla}.\vec{M} = 0. \tag{2.14}$$

By identifying the specific Gibbs energy g_f to the chemical potential μ_f of the interstitial fluid, and using [2.14], we can write the total differential of the Helmholtz free energy of the system {skeleton; interstitial fluid}:

$$d\Psi = \underline{\Sigma} : d\underline{\Delta} + \mu_f dm_f - SdT. \tag{2.15}$$

The differential of the Helmholtz free energy of the bulk fluid is written as

$$d\Psi_b = -P_b d\phi_b + \mu_b dm_b - S_b dT \tag{2.16}$$

in which ϕ_b is the ratio of the volume occupied by the bulk fluid (i.e. the volume of the container minus the volume of the porous solid) to the volume of the container. In addition, μ_b, m_b, and S_b are the chemical potential, the mass, and the entropy of the bulk fluid, respectively. The conservation of the total fluid mass $m_t = m_f + m_b$ in the isolated system implies $dm_f = -dm_b$. Therefore, [2.16] may be rearranged as

$$d\Psi_b = -P_b d\phi_b - \mu_b dm_f - S_b dT. \qquad [2.17]$$

The isolated system {skeleton; interstitial fluid; bulk fluid} reaches thermodynamical equilibrium when the global Helmholtz free energy of the system, $\Psi_t = \Psi + \Psi_b$ is minimal. Using relations [2.15] and [2.17], we can express the thermodynamical equilibrium condition that must be satisfied by the fluid phase as the equality of the chemical potential of the interstitial fluid and bulk fluid:

$$\mu_f = \mu_b. \qquad [2.18]$$

In addition, the chemical potential μ_f of the interstitial fluid at the REV scale may be obtained by summation of the nanoscale chemical potential μ_f^n over the porous space:

$$\mu_f = \frac{1}{m_f} \int_{\Omega_0} d\Omega_0 \, \phi^p \rho_f^n \mu_f^n. \qquad [2.19]$$

The thermodynamical equilibrium condition [2.18] is then satisfied if $\mu_f^n = \mu_b$. When the system is at equilibrium, the bulk solution is in chemical equilibrium with the interstitial fluid in each pore. Interestingly, the poromechanical model yields the same equilibrium condition as the one used in most molecular simulations dealing with pore scale modeling. Indeed, to address the thermodynamical state of fluids at equilibrium, grand canonical Monte Carlo simulation methods assume the equality of the chemical potential throughout the fluid phase [FRE 02]. Furthermore, molecular dynamic studies on fluid sorption in porous media, which do not impose any *a priori* equilibrium condition, yield results in fair agreement with GCMC methods [SAR 01]. As a consequence, the equality of the chemical potentials throughout the fluid phase stands as a consistent thermodynamical equilibrium condition.

2.3.4. *Constitutive equation of the effective pore pressure*

Accounting for the equation of conservation of the fluid mass [2.14], a rearranged expression for the skeleton dissipation can be obtained:

$$\Phi_s = \underline{\Sigma} : \frac{d\underline{\Delta}}{dt} + g_f \frac{dm_f}{dt} - S\frac{dT}{dt} - \frac{d\Psi}{dt} \geq 0. \qquad [2.20]$$

We may also write

$$S = S_s + m_f s_f \qquad [2.21]$$

$$\Psi = \Psi_s + m_f \psi_f. \qquad [2.22]$$

In the limit of reversible transformations (no dissipation), by substituting [2.12], [2.21], and [2.22] into [2.20], we obtain

$$d\Psi_s = \underline{\Sigma} : d\underline{\Delta} + P_f d\phi - S_s dT. \qquad [2.23]$$

This is the general expression of the differential of the Helmholtz free energy of the skeleton.

Now, let ϕ^* be the corrected porosity defined as

$$\phi^* = \frac{1}{\Omega_0} \int_{\Omega_0} d\Omega_0 \, \frac{\rho_f^n}{\rho_b} \phi^p. \qquad [2.24]$$

Thus, we have $m_f = \rho_b \phi^*$, and by substituting into [2.12], we obtain a rearranged expression of the thermodynamic identity:

$$g_f = \psi_f + \frac{\phi P_f}{\rho_b \phi^*}. \qquad [2.25]$$

By considering the specific Gibbs energy equal to the chemical potential, $g_f = \mu_f$, and if we account for the thermodynamical equilibrium condition [2.18], then we can rewrite the specific Helmholtz free energy of the fluid as follows:

$$\psi_f = \psi_b + \psi_{\text{int}} \tag{2.26}$$

in which ψ_{int} is a specific interaction energy related to the effects of adsorption and molecular packing of fluid molecules in the nanopores, defined as

$$\psi_{\text{int}} = \frac{P_b}{\rho_b} - \frac{P_f}{\rho_b}\left(\frac{\phi}{\phi^*}\right). \tag{2.27}$$

In the same fashion, we can decompose the specific entropy of the interstitial fluid as

$$s_f = s_b + s_{\text{int}} \tag{2.28}$$

in which s_{int} is the interaction entropy due to the effects of adsorption and confinement of fluid molecules in the nanopores. This quantity and the interaction free energy will be discussed in section 2.5.

In the limit of reversible transformations, by substituting [2.21], [2.22], and [2.26]–[2.28] into [2.20], we obtain

$$d\Psi_s = \underline{\underline{\Sigma}} : d\underline{\underline{\Delta}} - \phi^* dP_b + d(\phi P_f) - (S_s + \rho_b \phi^* s_{\text{int}})dT \tag{2.29}$$

This is the expression of the Helmholtz free energy of the skeleton in the restricted case of thermodynamical equilibrium of the fluid phase. Upon comparing [2.29] and [2.23], we find the constitutive equation of the effective pore pressure and interaction entropy in its incremental form

$$\phi dP_f - \phi^* dP_b - \rho_b \phi^* s_{\text{int}} dT = 0. \tag{2.30}$$

Relation [2.30] relates the quantities resulting from adsorption and confinement of the fluid molecules, i.e.

$(P_f\,;\,s_{\text{int}})$, to measurable quantities $(P_b\,;\,T\,;\,\phi\,;\,\phi^*)$. In the limit of isothermal transformations, the incremental constitutive equation reduces to

$$dP_f = \left(\frac{\phi^*}{\phi}\right) dP_b. \qquad [2.31]$$

The ratio ϕ^*/ϕ is greater than unity if the mass of interstitial fluid is greater than the mass of bulk fluid occupying the same volume. In other terms, the ratio ϕ^*/ϕ quantifies the degree of confinement of the interstitial fluid. Consecutively, the more the interstitial fluid is confined, the higher the effective pore pressure.

2.3.5. *Effect on the volumetric strain*

In reversible and isothermal conditions, the differential of the Helmholtz free energy of the nanoporous skeleton is given by

$$d\Psi_s = \underline{\Sigma} : d\underline{\Delta} + P_f d\phi. \qquad [2.32]$$

Classically, in the limit of a reversible response, the constitutive equations are given by

$$\Sigma_{ij} = \frac{\partial \Psi_s}{\partial \Delta_{ij}} = \left\{(K + b^2N)\epsilon - bN\phi\right\}\delta_{ij} + 2Ge_{ij} \qquad [2.33]$$

$$P_f = \frac{\partial \Psi_s}{\partial \phi} = -bN\epsilon + N\phi \qquad [2.34]$$

where $\Delta_{ij} = e_{ij} + (\epsilon/3)\,\delta_{ij}$, K is the apparent modulus of incompressibility, G is the shear modulus, and b and N are the Biot coefficient and modulus, respectively.

Consider now that the nanoporous solid is placed in a container filled with a fluid at bulk pressure P_b. As a result, the stress tensor $\underline{\Sigma}$ reduces to the hydrostatic bulk pressure acting on the skeleton:

$$\underline{\Sigma} = -P_b \underline{\mathbb{1}}. \qquad [2.35]$$

Moreover, the Biot coefficient is related to the apparent modulus of incompressibility K and to the modulus of the material composing the skeleton matrix K_s:

$$b = 1 - \frac{K}{K_s}. \qquad [2.36]$$

From the above relations and from the constitutive equation of the effective pore pressure (see equation [2.31]), equations [2.33] and [2.34], in their incremental form, yield the volumetric deformation increment, denoted as $d\epsilon$, as a function of the increment of bulk pressure:

$$d\epsilon = \left\{ \left(1 - \frac{K}{K_s}\right) \frac{\phi^*}{\phi} - 1 \right\} \frac{dP_b}{K}. \qquad [2.37]$$

The swelling strain ϵ is obtained by summation of $d\epsilon$ between P_{b0} and P_b:

$$\epsilon - \epsilon_0 = \int_{P_{b0}}^{P_b} \frac{dP_b}{K} \left\{ \left(1 - \frac{K}{K_s}\right) \frac{\phi^*}{\phi} - 1 \right\} \qquad [2.38]$$

2.3.6. *Effect on the permeability*

In order to arrive at the equivalent of Darcy's law for nanoporous materials, let us consider the fluid dissipation. In the Eulerian frame, it is given by [COU 04]

$$\Phi_f^e = \left\{ -\vec{\nabla}^e (g_f)_T + (\vec{f} - \vec{\gamma}_f) \right\} . \vec{w} \geq 0 \qquad [2.39]$$

where $\vec{\nabla}^e (g_f)_T$ is the Eulerian gradient of specific Gibbs energy of the fluid at constant temperature, $\vec{f}$ and $\vec{\gamma}_f$ are the body force density and fluid acceleration, respectively, and $\vec{w}$ is the Eulerian relative flow vector of fluid mass. Let $\nu = \varphi(\vec{V}_f - \vec{V}_s)$ be the filtration vector in the Eulerian frame. The relative flow vector of fluid mass is related to the filtration vector as

$$\vec{w} = \frac{m_f^e}{\varphi}\vec{\nu}. \qquad [2.40]$$

By definition, the Eulerian fluid mass m_f^e and the Eulerian porosity φ are related to their Lagrangian counterparts as

$$m_f^e d\Omega^e = m_f d\Omega_0 \qquad [2.41]$$

$$\varphi d\Omega^e = \phi d\Omega_0. \qquad [2.42]$$

Using the above definitions and noting that $m_f = \rho_b \phi^*$, we write the flow vector of mass in terms of the porosity ratio as follows:

$$\vec{w} = \rho_b \left(\frac{\phi^*}{\phi}\right) \vec{\nu}. \qquad [2.43]$$

In addition, the differential of the specific free energy is given by

$$dg_f = \left(\frac{\phi}{\rho_b \phi^*}\right) dP_f - s_f dT. \qquad [2.44]$$

By substituting [2.43] and [2.44] into [2.39], we obtain a rearranged expression of the fluid dissipation:

$$\Phi_f^e = \left\{-\vec{\nabla}^e(P_f) + \rho_b \left(\frac{\phi^*}{\phi}\right)(\vec{f} - \vec{\gamma}_f)\right\}.\vec{\nu}. \qquad [2.45]$$

Darcy's law defines a linear relation between the filtration $\vec{\nu}$ and the force that drives the filtration. According to equation [2.45], Darcy's law reads

$$\vec{\nu} = \kappa \left\{ -\vec{\nabla}^{e}(P_f) + \rho_b \left(\frac{\phi^*}{\phi} \right) (\vec{f} - \vec{\gamma}_f) \right\} \qquad [2.46]$$

where κ is the permeability of the nanoporous material.

Let us consider a bulk pressure gradient driving a flow through a nanoporous membrane, which separates two bulk solutions. In the permanent regime, on each side of the membrane, we assume that the interstitial fluid located at the borders of the nanoporous material is in thermodynamical equilibrium with the neighboring bulk solution. Consecutively, by using equation [2.30], we relate the bulk pressure differential to the effective pore pressure differential as follows:

$$d(P_f)_T = \left(\frac{\phi^*}{\phi} \right) d(P_b)_T \qquad [2.47]$$

Substituting [2.47] in the Darcy's law leads to the following expression:

$$\vec{\nu} = \kappa_f \left\{ -\vec{\nabla}^{e}(P_b) + \rho_b(\vec{f} - \vec{\gamma}_f) \right\} \qquad [2.48]$$

in which κ_f is the effective permeability of the nanoporous material, defined as

$$\kappa_f = \left(\frac{\phi^*}{\phi} \right) \kappa. \qquad [2.49]$$

Therefore, the effective permeability, as it accounts for fluid confinement effects, is greater than the actual permeability κ if the porosity ratio is greater than unity. In other words, at a given bulk pressure gradient, the more the interstitial fluid is confined, the greater the flux of fluid mass and the greater the effective permeability.

2.4. Adsorption-induced swelling and permeability change in nanoporous materials

Let us show first how the effective pore pressure, the effective permeability, and the swelling strain may be deduced from adsorption measurements. As shown in Figure 2.2, the Gibbs adsorption isotherm stands for a measurement of the number n_{ex} of adsorbate moles that exceeds the number of fluid molecules at bulk conditions. Let n_{t} be the total number of moles of interstitial fluid (see Figure 2.2). Then, the ratio of porosities may be expressed as

$$\frac{\phi^*}{\phi} = (1 - n_{\mathrm{ex}}/n_{\mathrm{t}})^{-1} \qquad [2.50]$$

so that the effective pore pressure and effective permeability is given by

$$P_f - P_{f0} = \int_{P_{b0}}^{P_b} dP_b (1 - n_{\mathrm{ex}}/n_{\mathrm{t}})^{-1} \qquad [2.51]$$

$$\kappa_f = (1 - n_{\mathrm{ex}}/n_{\mathrm{t}})^{-1} \, \kappa \qquad [2.52]$$

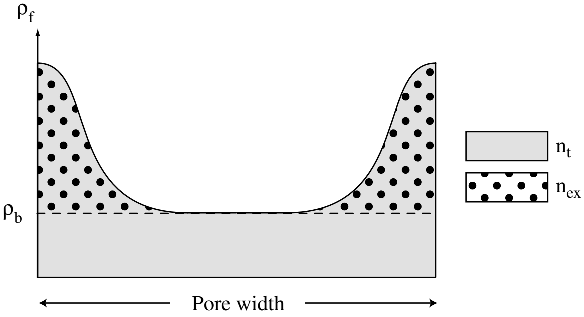

Figure 2.2. *Sketch of the fluid density profile in a nanopore. The gray-colored area stands for the total number of interstitial fluid n_t present in the pore. The dotted area stands for the excess quantity of interstitial fluid which corresponds to the excess number of moles n_{ex} of the Gibbs adsorption isotherm*

Equations [2.51] and [2.52] show that, at constant bulk pressure, the effective pore pressure and effective permeability increase with the ratio $n_{\mathrm{ex}}/n_{\mathrm{t}}$. In the limit of weak adsorption and weak confinement effects, $n_{\mathrm{t}} \gg n_{\mathrm{ex}}$ as the interstitial fluid is in the same thermodynamical sate as that of the bulk fluid. In such conditions, equations [2.51] and [2.52] indicate that the effective pore pressure and effective permeability equal the bulk fluid pressure and the actual permeability, respectively.

Substituting [2.50] into [2.38] yields the expression of the volumetric strain as a function of n_{t} and n_{ex}:

$$\epsilon - \epsilon_0 = \int_{P_{b0}}^{P_b} \frac{dP_b}{K} \left\{ \left(1 - \frac{K}{K_s}\right) (1 - n_{\mathrm{ex}}/n_{\mathrm{t}})^{-1} - 1 \right\}. \quad [2.53]$$

As a result, knowledge of the nanoporous material poroelastic properties K and K_s, and measurement of the sorbed fluid quantities n_{ex} and n_{t} are necessary in order to compute the adsorption-induced volumetric strain. Most experimental studies of gas sorption on porous materials focus on the measurement of the Gibbs adsorption isotherm [ROU 99]. Experimental adsorption studies do not usually provide the total number of moles of interstitial fluid contained in the porous adsorbent during sorption. The total number of interstitial fluid moles can still be estimated assuming that the porous material undergoes small strains on sorption, which is consistent with most experimental studies found in the literature. Under the approximation of small strains, the porosity of the material can be considered as constant, and thus, we have

$$n_{\mathrm{t}} \simeq n_{\mathrm{ex}} + \frac{\rho_b V_\phi}{M}$$

$$n_{\mathrm{t}} \simeq n_{\mathrm{ex}} + \left(\frac{\phi}{1-\phi}\right) \frac{m_s}{M} \frac{\rho_b}{\rho_s} \quad [2.54]$$

where V_ϕ is the connected porous volume of the material, M is the molar mass of the adsorbed gas, m_s is the adsorbent sample mass, and ρ_s is the density of the material composing the solid matrix of the porous adsorbent. In the following sections, we use relation [2.54] to compute the total number of interstitial fluid moles from adsorption isotherms data.

Experimental data on the swelling of saturated cement paste are rather scarce in the literature. In order to provide the reader with some validation studies, we are going to focus on carbon dioxide and methane adsorption in coal. The fluids considered are simple fluids and a typical pore size distribution of coal is not that far from cement paste, with pore sizes in the nanometer range. This setting has the merit of providing a simple configuration on which future models should at least perform well.

2.4.1. *Comparison with data by Day et al.*

Day *et al.* [DAY 08a, DAY 08b] performed adsorption experiments and swelling measurements on several Australian bituminous coals. More specifically, they used digital cameras and a pressure cell equipped with sight windows to measure the swelling strain of a Bowen basin coal sample during sorption of carbon dioxide at $T = 55\,^\circ\mathrm{C}$ and up to $P_b = 15\,\mathrm{MPa}$ [DAY 08b]. In addition, they performed CO_2 adsorption isotherms measurements on other Bowen basin coal samples at $T = 53\,^\circ\mathrm{C}$ and up to $P_b = 16\,\mathrm{MPa}$ with a gravimetric technique [DAY 08a]. To compare the theoretical model predictions with the swelling data from [DAY 08b], we use the adsorption data from [DAY 08a] corresponding to the Bowen basin coal sample referred to as “Qld 5,” whose porosity $\phi = 0.148$ was measured by helium pycnometry. Figure 2.3a shows the measured excess adsorption isotherm n_{ex} of CO_2 on the Qld 5 sample as well as the quantity n_{t} deduced from n_{ex} and $\phi = 0.148$ using relation [2.54]. The volumetric strain is then computed using equation [2.38] and fitted to the swelling measurements from [DAY 08b], with K and K_s being the adjustable parameters. Table 2.1 summarizes the model parameters used in the calculations. Figure 2.3b superposes the experimental data with the fitting curve obtained for $K = 5.64\,\mathrm{GPa}$ and $K_s = 30.1\,\mathrm{GPa}$. For coal, the static Young's modulus and Poisson's ratio, respectively, range from 1 to 3 GPa and from 0.25 to 0.45 [ZHE 91, GEN 07]. Consecutively, the fitted incompressibility modulus of the porous skeleton, $K = 5.64\,\mathrm{GPa}$, falls in the range of the incompressibility modulus of coals. Furthermore, the incompressibility modulus of the solid matrix $K_s = 30.1\,\mathrm{GPa}$ is consistent with the typical value of 35 GPa found in the literature for graphite [KEL 81, BRI 45]. In addition, as Figure 2.3b demonstrates, the model predicts the evolution of the swelling strain with the bulk pressure in fair agreement with the experimental observations.

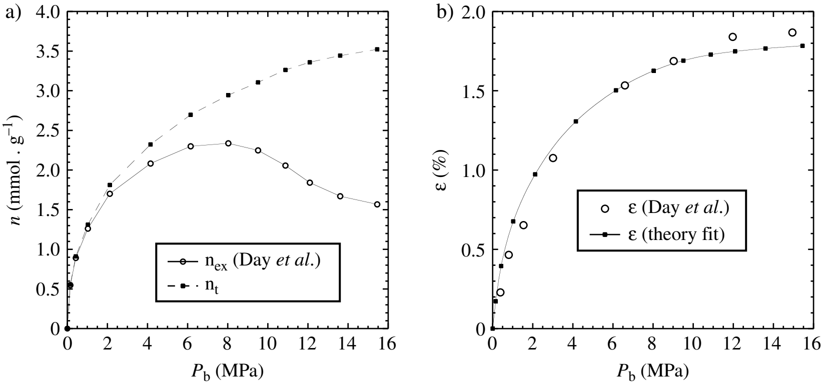

Figure 2.3. *(a) Adsorption isotherm of CO_2 on a Bowen basin coal. White circles stand for the excess adsorption isotherm measured by Day et al. [DAY 08a]. Black squares stand for the total number of moles of interstitial fluid, computed from n_{ex} data and the value of the coal sample porosity reported in [DAY 08a]. The lines are visual guides. (b) Evolution of the swelling strain with the bulk pressure. White circles stand for the swelling measured by Day et al. [DAY 08b]. The black squares represent the fit of the model prediction. The solid line is a visual guide*

Data source	Gas type	m_s (g)	ρ_s (kg.m^{-3})	ϕ	K (GPa)	K_s (GPa)
Day *et al.*	CO_2	4.1	1,358	0.148	5.64*	30.1*
Ottiger *et al.*	CH_4	40.81	1,265	0.1379*	3.0*	30.1[a]
Ottiger *et al.*	CO_2	40.81	1,265	0.1194*	3.0*	30.1[a]

* Adjusted.

[a] Assumed.

Table 2.1. *Summary of model parameters for coal swelling*

2.4.2. *Comparison with data by Ottiger et al.*

Ottiger *et al.* [OTT 08] performed adsorption isotherms measurements of pure CO_2, pure CH_4, and (CO_2, CH_4) mixtures on bituminous coal samples from the Sulcis Province (Italy) at $T = 45\,^{\circ}\mathrm{C}$ and up to $P_b = 19\,\mathrm{MPa}$, coupling manometric and gravimetric techniques. In addition, they used a pressure cell equipped with sight windows and a digital camera to measure the swelling strain during sorption. In their paper, Ottiger *et al.* do not report any measurement on the porosity of coal samples. As a consequence, we set the solid matrix incompressibility modulus to $K_s = 30.1\,\mathrm{GPa}$, as found in the fitting of the data by Day *et al.*, and we fit the model predictions to the swelling data with K and ϕ as adjustable parameters. Figure 2.4 shows the results for pure CH_4. The fitted parameters read $K = 3.0\,\mathrm{GPa}$, $\phi = 0.1379$. We observe a good understanding between the theoretical predictions and the experimental data.

2.4.3. *Variation of effective permeability*

According to equation [2.52], the knowledge of the excess number of adsorbed moles n_{ex} and the total number of interstitial fluid moles is necessary to compute the effective permeability. Hence, Figure 2.5 reports the predicted permeability ratio κ_f/κ, calculated from the adsorption data given in [DAY 08a] and [OTT 08]. Equation [2.54] provides an approximation of the total number of interstitial fluid moles. In this figure, we may observe that the effective permeability is always higher than the permeability in the absence of confinement. On the other hand, the mass density of the fluid increases with the pressure, which explains why the effective permeability is decreasing with an increase in the bulk pressure.

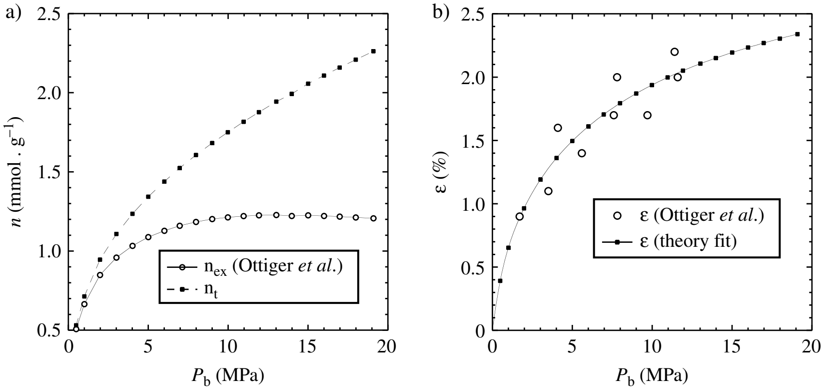

Figure 2.4. *(a) Adsorption isotherm of* CH_4 *on a Sulcis Province coal. White circles stand for the excess adsorption isotherm measured by Ottiger et al. [OTT 08]. Black squares stand for the total number of moles of interstitial fluid, computed from the* n_{ex} *data and the coal sample porosity* $\phi = 0.1379$*, obtained from the fit of the swelling data. The lines are visual guides. (b) Evolution of the swelling strain with the bulk pressure. White circles stand for the swelling measured by Ottiger et al. [OTT 08]. The black squares represent the fit of the model prediction. The solid line is a visual guide*

2.5. Discussion – interaction energy and entropy

According to equation [2.26], the specific interaction energy is defined as the difference between the specific Helmholtz energies of the interstitial and bulk fluids when the system reaches equilibrium. If we consider isothermal transformations, equations [2.27] and [2.31] show that the sign of the interaction energy is given by the following function F:

$$F(P_b) = f(P_b)P_b - \int_0^{P_b} dP_b f(P_b) \qquad [2.55]$$

in which f is the function defined as

$$f(P_b) = \frac{\phi^*}{\phi} = (1 - n_{\mathrm{ex}}/n_{\mathrm{t}})^{-1}. \qquad [2.56]$$

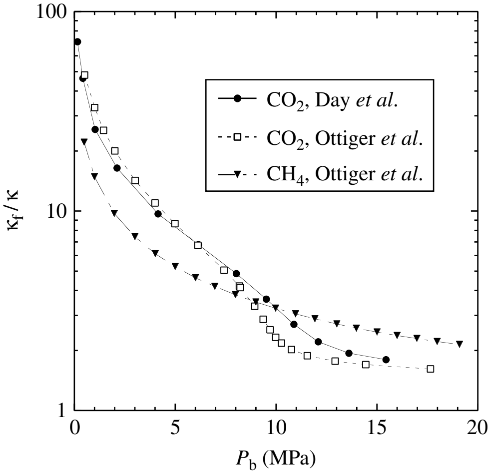

Figure 2.5. *Evolution of the permeability ratio κ_f/κ with the bulk pressure in semi-log scale. The permeability ratio is deduced from adsorption data found in the literature: black dots stand for the CO_2 adsorption data from [DAY 08a]; white squares stand for the CO_2 adsorption data from [OTT 08]; black triangles stand for the CH_4 adsorption data from [OTT 08]. Lines are visual guides*

Function F is always negative if function f monotonically decreases with P_b. The derivative of f with respect to P_b reads

$$\frac{df}{dP_b} = (1 - n_{\mathrm{ex}}/n_{\mathrm{t}})^{-2} \frac{d}{dP_b}\left(\frac{n_{\mathrm{ex}}}{n_{\mathrm{t}}}\right). \qquad [2.57]$$

Experimental data found in the literature and reported in Figures 2.3a and 2.4a clearly show that the ratio $n_{\mathrm{ex}}/n_{\mathrm{t}}$

decreases with P_b. Consequently, we deduce from equation [2.57] that f is a monotonic decreasing function of P_b, and thus, F is negative. As a result, the interaction energy is negative as well, and we find:

$$\psi_f - \psi_b = \psi_{\text{int}} \leq 0. \qquad [2.58]$$

Therefore, because of fluid–solid and fluid–fluid interactions in the nanopores, the interstitial fluid cedes free energy to the skeleton in the form of mechanical work, which provokes the swelling phenomenon. When adsorption and confinement effects become negligible, the ratio $n_{\text{ex}}/n_{\text{t}}$ tends to 0 and so does the interaction energy. In such conditions, the interstitial and bulk-fluid-specific Helmholtz energies are equal.

A simplified poromechanical model which addresses fluid adsorption and molecular packing effects in nanoporous materials has been proposed by Pijaudier-Cabot *et al.* [PIJ]. The interaction free energy was introduced directly in the formulation, accounting for the same thermodynamical equilibrium condition and an equivalent form of equation [2.29] was obtained:

$$d\Psi_s = \underline{\Sigma} : d\underline{\Delta} + P_b d\phi^* - d\Psi_{\text{int}} \qquad [2.59]$$

where Ψ_{int} is the interaction energy, which is related to the specific interaction energy ψ_{int} by $\Psi_{\text{int}} = m_f \psi_{\text{int}}$. While the approach was quite similar to the present study, the effective pore pressure was not introduced in this formulation. The interaction energy Ψ_{int} was directly related to the true pore pressure at the pore scale. More specifically, the interaction energy was set as a function of the corrected porosity ϕ^* only, and consecutively, an interaction pressure P_{int} was defined as:

$$P_{\text{int}} = \frac{\partial \Psi_{\text{int}}}{\partial \phi^*} \qquad [2.60]$$

This interaction pressure plays exactly the same role as that of the effective pore pressure. A prototype constitutive equation was also postulated:

$$P_{\text{int}} = -k\, n_{\text{ex}} \qquad [2.61]$$

where k is a proportionality constant. This empirical constitutive relation was based on the experimental observation of Levine, who pointed out the relation of proportionality between the Gibbs adsorption isotherm and the swelling strain of coal at low bulk pressures [LEV 96].

As observed in the comparisons with experimental results, this approximation breaks down at high bulk pressures, as the swelling strain is monotonic, whereas the Gibbs adsorption isotherm reaches a maximum and then decreases (see Figure 2.3). Therefore, the knowledge of the excess number of adsorbed moles n_{ex} is not sufficient to accurately predict the pressure inducing the swelling.

Let us now focus on the sign of the interaction entropy s_{int} in the general case of non-isothermal transformations. By rearranging equation [2.30], we obtain

$$s_{\text{int}} = \frac{1}{\rho_b}\left(\frac{\phi}{\phi^*}\frac{dP_f}{dT} - \frac{dP_b}{dT}\right). \qquad [2.62]$$

Several experimental studies point out that the swelling strain, as well as the adsorbed excess number of fluid molecules, decreases upon increasing the temperature [OTT 08, BAT 10]. If we consider the paradigm of section 2.3.3, these results suggest that the effective pore pressure P_f and the number of bulk fluid moles in the external bulk solution, n_b, respectively, decreases and increases with temperature ($dP_f/dT \leq 0$ and $dn_b/dT \geq 0$). Moreover, in the case of small swelling strain, the volume V_b occupied by the external bulk fluid (i.e. the volume of the fluid container minus the volume of the porous solid) does not significantly vary upon swelling

($dV_b \simeq 0$). Consecutively, assuming the bulk fluid behaves as an ideal gas, the derivative of the bulk fluid pressure with respect to temperature reads

$$\frac{dP_b}{dT} \simeq \frac{Rn_b}{V_b} + \frac{RT}{V_b}\frac{dn_b}{dT}. \qquad [2.63]$$

In such conditions, the bulk fluid pressure increases with temperature ($dP_b/dT \geq 0$). Therefore, considering the above remarks and the expression of the interaction entropy [2.62], we have:

$$s_{\text{int}} \leq 0. \qquad [2.64]$$

By using the definition of the interaction entropy [2.28], relation [2.64] leads to

$$s_f \leq s_b. \qquad [2.65]$$

This result makes sense as the order in the fluid continuum increases due to the confinement of the fluid molecules in the nanopores, and consecutively, the increase in the fluid density. Thus, the interaction entropy quantifies the loss of entropy of the interstitial fluid with respect to the bulk reference state. When adsorption and confinement effects become negligible, as the ratios ϕ/ϕ^* and P_f/P_b asymptotically tend to unity. In these conditions, equation [2.62] shows that the interaction entropy vanishes.

2.6. Conclusions

We have shown how the poromechanical theory should be refined in the context of saturated isotropic nanoporous solids.

– Because of fluid adsorption and confinement effects in the nanopores, the interstitial fluid pressure is greater than the bulk fluid pressure P_b, which eventually leads to the swelling of the porous solid. We have defined an effective pore pressure P_f in order to account for this effect of adsorption and molecular packing of fluid in small pores.

– When a nanoporous material is immersed in a container filled with a bulk fluid, at thermodynamical equilibrium the interstitial fluid is in chemical equilibrium with the external bulk solution. The chemical potentials throughout the fluid phase are equal.

– In the case of isothermal sorption-induced swelling of nanoporous materials, the effective pore pressure P_f has been related to the excess number of adsorbed moles n_{ex}, to the total number of moles of interstitial fluid n_{t}, and to the bulk pressure P_b.

– The sorption-induced volumetric strain is computed by inserting the effective pressure in the standard poromechanical constitutive equations for the solid phase. A fair agreement between the fit of the theroretical predictions and several sets of experimental data found in the literature is obtained.

Full experimental validation of the model is left for future work, before addressing more complex issues dealing with non-satuation of the pores and complex fluids such as water and electrical effects due to the presence of ions in the interstitial solution of cement paste.

2.7. Acknowledgments

This chapter summarizes several results obtained by the authors over the past four years and more extensively described in [MEN], [KNO 10], [PIJ], and [VER]. It has been partially supported by the Total SA under the Tight Gas Project and the European Research Council under Ad-G 27769 Failflow.

2.8. Bibliography

[BAN 28] BANGHAM D., FAKHROURY N., "The expansion of charcoal accompanying sorption of gases and vapours", *Nature*, vol. 122, pp. 681–682, 1928.

[BAT 10] BATTISTUTTA E., VAN HEMERT P., LUTYNSKI M., BRUINING H., WOLF K.-H., "Swelling and sorption experiments on methane, nitrogen and carbon dioxide on dry Selar Cornish coal", *International Journal of Coal Geology*, vol. 84, no. 1, pp. 39–48, 2010.

[BEL 05] BELTZUNG F., WITTMANN F.H., "Role of disjoining pressure in cement based materials", *Cement and Concrete Research*, vol. 35, no. 12, pp. 2364–2370, 2005.

[BRI 45] BRIDGMAN P.W., "The compression of sixty-one solid substances to $25{,}000\,\mathrm{kg/cm^2}$, determined by a new rapid method", *Proceedings of the American Academy of Arts and Sciences*, vol. 76, no. 1, pp. 9–24, 1945.

[COU 04] COUSSY O., *Poromechanics*, John Wiley, 2004.

[COU 10] COUSSY O., *Mechanics and Physics of Porous Solids*, John Wiley, 2010.

[DAY 08a] DAY S., DUFFY G., SAKUROVS R., WEIR S., "Effect of coal properties on CO_2 sorption capacity under supercritical conditions", *International Journal of Greenhouse Gas Control*, vol. 2, no. 3, pp. 342–352, 2008.

[DAY 08b] DAY S., FRY R., SAKUROVS R., "Swelling of Australian coals in supercritical CO2", *International Journal of Coal Geology*, vol. 74, no. 1, pp. 41–52, 2008.

[FRE 02] FRENKEL D., SMIT B., *Understanding Molecular Simulation*, Academic Press, 2002.

[GEN 07] GENTZIS T., DEISMAN N., CHALATURNYK R., "Geomechanical properties and permeability of coals from the Foothills and Mountain regions of western Canada", *International Journal of Coal Geology*, vol. 69, no. 3, pp. 153–164, 2007.

[GOG 03] GOGOTSI Y., NIKITIN A., YE H., ZHOU W., FISCHER J.E., YI B., FOLEY H.C., BARSOUM M.W., "Nanoporous carbide-derived carbon with tunable pore size", *Nature Materials*, vol. 2, no. 9, pp. 591–594, 2003.

[KEL 81] KELLY B.T., *Physics of Graphite*, Applied Science, 1981.

[KNO 10] KNORST-FOURAN A., Contribution à l'étude de propriétés interfaciales d'alcanes confinés par simulation moléculaire de type Monte Carlo, PhD Thesis, Université de Pau et des Pays de l'Adour, September 2010.

[LEV 96] LEVINE J.R., "Model study of the influence of matrix shrinkage on absolute permeability of coal bed reservoirs", *Geological Society*, vol. 109, pp. 197–212, 1996.

[MEE 27] MEEHAN F., "The expansion of charcoal on sorption of carbon dioxide", *Proceedings of the Royal Society A*, vol. 115, pp. 199–207, 1927.

[MEN] MENDIBOURE B., MIQUEU C., "Evaluation of the pressure tensor of fluids confined into slit micropores", forthcoming.

[OTT 08] OTTIGER S., PINI R., STORTI G., MAZZOTTI M., "Competitive adsorption equilibria of CO_2 and CH_4 on a dry coal", *Adsorption*, vol. 14, nos. 4–5, pp. 539–556, 2008.

[PEN 09] PENSÉE V., HE Q.-C., LE QUANG H., "Poroelasticity of fluid-infiltrated nanoporous media", *Materials Science Forum*, vol. 614, pp. 35–40, 2009.

[PIJ] PIJAUDIER-CABOT G., VERMOREL R., MIQUEU C., MENDIBOURE B., "Revisiting poromechanics in the context of microporous materials", *Comptes Rendus Mecanique*, forthcoming.

[ROU 99] ROUQUEROL F., ROUQUEROL J., SING K., *Adsorption by Powders and Porous Solids*, Academic Press, 1999.

[SAR 01] SARKISOV L., MONSON P.A., "Modeling of adsorption and desorption in pores of simple geometry using molecular dynamics", *Langmuir*, vol. 17, no. 24, pp. 7600–7604, 2001.

[VAR 00] VARNIK F., BASCHNAGEL J., BINDER K., "Molecular dynamics results on the pressure tensor of polymer films", *Journal of Chemical Physics*, vol. 113, no. 10, pp. 4444–4453, 2000.

[VER] VERMOREL R., PIJAUDIER-CABOT G., "Poromechanics of saturated isotropic nanoporous materials: a new analytical model for the adsorption induced swelling phenomenon", *Journal of the Mechanics and Physics of Solids*, forthcoming.

[YAN 10] YANG K., LU X., LIN Y., NEIMARK A.V., "Deformation of coal induced by methane adsorption at geological conditions", *Energy and Fuels*, vol. 24, no. 11, pp. 5955–5964, 2010.

[ZHE 91] ZHENG Z., KHODAVERDIAN M., MCLENNAN J.D., "Static and dynamic testing of coal specimens", in *1991 SCA Conference*, no. 9120, 1991.

Chapter 3

Stress-based Non-local Damage Model

Progressive microcracking in brittle or quasi-brittle materials described by damage models presents softening behavior that needs the use of regularization methods to keep the results' objectivity. These regularization methods, describing interaction between points, not only show important properties (objectivity, non-alteration of a uniform field, etc.), but also show problems (damage initiation, free boundary, etc.).

A modification of the non-local integral regularization method, taking into account the stress state, is proposed in this chapter. The orientation and the intensity of the non-local interactions depend on the stress state. The main framework of the original non-local method is kept, allowing us to maintain its advantages, and modification is introduced through the weighted function, which depends in this modified

---

Chapter written by Cédric GIRY and Frédéric DUFOUR.

version, not only on the distance between two points as originally, but also on the stress state at the distant point.

The efficiency of the new approach is illustrated with several examples. A one-dimensional test shows the evolution of the interaction between points from a low-damage state spread over a large area up to a strongly localized high-damage area corresponding to a crack. Besides, the proposed modification improves the numerical solution of problems observed in numerical simulations of damage initiation in mode I problem. Furthermore, behavior at complete failure is analyzed through crack opening.

3.1. Introduction

In quasi-brittle materials, non-locality can find its origins in the interactions between microcracks [BAŽ 91]. It leads to a stress magnification of the surrounding area of a microcrack, thereby allowing the creation or growth of new microcracks. Non-local damage models aim at describing the behavior of quasi-brittle materials for the microcracked area which does not degenerate into a significant opened crack. In addition to restoring the objectivity of the numerical modeling for strain-softening behavior, these models give physical reliability to results by explicitly introducing the non-local character of the microcracking.

Gradient-enhanced media [PEE 96] or non-local integral method [PIJ 87], as localization limiters, avoid ill-posedness of the governing equations of equilibrium, and thus, mesh dependencies. Both of the methods introduce an internal length in the constitutive law that may be related to the characteristic size of the material (aggregate size). However, on top of this length the non-local approach also introduces explicitly the shape of the interaction domain through the shape of the weighted function. Peerlings *et al.* [PEE 01] have demonstrated that both the methods are strictly equivalent when the Green's function is used as the weighted function in the integral approach. Although the shape of the weighted function plays only a minor role in a 1D setting, we will focus on the second approach since it gives more flexibility by expressing the interactions between points directly in the weighted function. In other words, the gradient-enhanced approach contains only one scalar parameter (i.e. the internal length) since the shape of the interaction domain is set in stone, while the integral approach gives the possibility to modify the interaction length and the shape of the interaction domain.

Non-local regularization methods aim at catching global behavior of the structure and macrocracking in a diffuse manner by means of the damage field. However, when high-damage states are reached, the method fails to represent open macrocracks with localized strains through the crack. The origin of the inaccurate resolution of local quantities is that the non-locality introduced in the calculation is fixed during the damage process and depends only on the distance between neighboring points. Moreover, Eringen *et al.* [ERI 77] have also pointed out crack tip problem in non-local elasticity. They have shown that the point encountering the maximum stress is not located at the crack tip. Simone *et al.* show that this problem leads to a wrong initiation of damage due to a wrong prediction of the maximum non-local equivalent strain [SIM 04] in the presence of a predefined notch.

Jirasek *et al.* have shown that different strategies can be adopted to model the notch [JIR 04] either explicitly by the mesh or by filling it with fully damaged material. They have shown that they can better fit the size effect on fracture energy in the case of a notch modeled as a layer of completely damaged material. However, we can expect to physically observe the initiation and evolution of damage from the crack tip and not along the notch as it can be obtained with a layer of fully damaged material.

More generally, the isotropic character of the interactions leads to a bad treatment of interactions in the vicinity of free boundaries [KRA 09, PIJ 10] or a cracked zone that is a damaged free boundary.

The interactions are expected to change according to the loading encountered by the media. We can observe, in the presence of a fracture process zone (FPZ), a development of numerous microcracks in front of the FPZ, whereas back at the front, no microcrack is expected to appear due to unloading. In the same way, a nearby boundary of a solid, as the loading conditions are modified, non-locality is expected to be different compared to this in the bulk of the material. To take into account these evolutions of non-localities, a modification of the interactions between points needs to be done.

To overcome the problems inherent to the non-local method, several propositions have been made in the past. Regarding gradient-enhanced media, Voyiadjis and Abu Al-Rub proposed for ductile materials, following experimental observations, a dependency of the internal length to several parameters such as dislocation density, and more particularly to the plastic strain [VOY 05]. This leads to a decrease of the length scale parameter with the increase of the plastic strain. This approach allows an evolution of the internal length linked to the evolution of the microstructure, but the interactions are still isotropic, and thus, does not allow us to improve the treatment of the free boundaries or cracks.

For damage models with non-local integral regularization technique, new propositions are expressed for an evolution of the interactions with damage [PIJ 10]; pointed out in [DES 10] and described in detail in [DES 07]. For the first two authors, the distance between points is replaced by a distance integrating the damage along the path to reflect the distance over which an elastic wave propagates. As damage increases, this distance increases as well, thereby leading to a progressive degradation of the interactions. On a simple case of a 1D bar under tension, it gives interesting results with a progressive reduction of the area with increasing damage. It leads to a localized area with damage equal to 1 that can be seen as a macrocrack. However, the implementation of this approach seems to be numerically costly for 2D and 3D calculations. Indeed, for each step, an integration along all possible paths between two Gauss points of the damage field needs to be performed.

In the second approach, the interactions depend on an internal time of propagation of elastic waves instead of the distance between points. As the material evolves, the time of propagation is modified, leading to a similar result of a progressive degradation of interactions between points around a damaged area. However, there are still some pending issues with this approach regarding the choice of the wave used or the interactions of the waves with the boundaries, and it is still computationally time-consuming.

Bažant *et al.* have recently proposed a modification of the description of the non-local field to overcome boundary condition problems [BAŽ 10]. They use a layer of local finite elements along boundaries that can be seen as the introduction of a zero internal length in the boundary layer. This approach considers such an attenuation of the non-localities close to a boundary; however, the behavior remains isotropic and does not take into account the creation of new boundaries as macrocracks that could modify the non-local interactions.

In further developments on the interactions of microcracks at the origin of non-locality, Bažant proposes a modification of the non-local method by adding a term to the original non-local method depending on the principal stress directions, based on interactions between penny-shaped cracks [BAŽ 94]. Depending on the principal stress directions, microcracks will be more or less activated and can develop magnification of the surrounding stress state by interactions with neighboring microcracks. The interactions are no longer isotropic and tend to enhance the description of the non-locality. However, this approach keeps a minimum interaction weight corresponding to the original non-local method that does not avoid remaining interactions between points on both sides of a crack at complete failure and the mistreatment of boundaries.

More recently, Krayani *et al.* proposed a modification of the domain of interactions in the vicinity of boundaries [KRA 09]. They show, by simple considerations on interactions between circular voids with the method of analysis developed by Kachanov [KAC 87], that stress redistribution due to interactions (non-local stress) should decrease in the vicinity of boundaries in the direction normal to these boundaries [PIJ 10]. At its limit, the non-locality is null in the normal direction of the boundary for a point located on the boundary.

This last proposition is at the bottom of the present work in the specific case of a free boundary. This method aims at properly describing non-local interactions in the vicinity of boundary leading to improvements in the description of the FPZ initiation, and thus, a better description of size effects [KRA 09]. However, the modifications consider only the geometry of the specimen and does not allow an evolution of the interactions during the damage process. Indeed, the non-local regularization domain is only modified in the neighborhood of explicitly defined cracks. New damaged areas do not affect the regularization as new boundaries are not created in the model.

We propose, in this chapter, to enhance the non-local method proposed in [KRA 09] by giving a more general framework. To take into account the evolution of non-locality in the media, we introduce a modification of the interactions depending on the principal stress directions, as proposed by Bažant [BAŽ 94], and furthermore, the intensity of the interactions is proportional to the stress magnitude. An area under low stress will not influence its neighborhood as is the case in the normal direction to a free boundary or to a fully damaged zone.

The non-local damage model used in our study is briefly recalled before introducing the modifications of the regularization method. Then, a test performed on notched plate under tension, compares the original and stress-based non-local methods regarding damage initiation. A second test on a 1D bar under tension allows us to illustrate the method in terms of improvements to describe mechanical quantities in the FPZ such as the strain field.

Finally, the description of the evolution of the strain localization is studied in terms of cracking analysis through a three-point bending test (3PBT) on a notched beam.

3.2. Non-local damage models

3.2.1. *Continuum damage theory*

A scalar isotropic damage model for describing the non-linear behavior of concrete under monotonic loading is used.

The general stress–strain relationship is:

$$\sigma_{ij} = (1 - D)C_{ijkl} : \varepsilon_{kl} \qquad [3.1]$$

where σ_{ij} and ε_{kl} are the components of the Cauchy stress tensor and the strain tensor, respectively (*i, j, k, l* $\in [1,3]$) and C_{ijkl} are the components of the fourth-order elastic stiffness tensor. D is a damage scalar variable quantifying material degradation that grows from 0 (virgin material) to 1 (completely degraded material).

The evolution of D is driven by an equivalent strain ε_{eq} that quantifies the local deformation state in the material. Among several definitions, we consider here the equivalent strain defined by Mazars for failure in mode I with its corresponding evolution law, and the equivalent strain defined by de Vree for failure in mode II with the evolution law proposed by Peerlings *et al.* [MAZ 86, VRE 95, PEE 98]. The damage scalar variable D is a function of the internal variable Y. This parameter equals the damage threshold ε_{D_0} initially, and is the largest ever reached value of ε_{eq} during the damage process. The evolution is governed by the Kuhn–Tucker conditions:

$$\varepsilon_{eq} - Y \leq 0 \ , \ \dot{Y} \geq 0 \ , \ \dot{Y}(\varepsilon_{eq} - Y) = 0 \qquad [3.2]$$

Mazars introduced a local measure ε_{eq} of the strain tensor defined by:

$$\varepsilon_{eq} = \sqrt{\sum_{i=1}^{3} \langle \varepsilon_i \rangle_+^2} \qquad [3.3]$$

where $\langle \varepsilon_i \rangle_+$ denotes the positive principal strains. This model considers that damage is driven by positive strains, i.e. extension. It makes it possible to accurately reproduce the behavior of quasi-brittle materials such as concrete under uniaxial loading. However, this model leads to a too brittle behavior under shear loading. This explains the reason why we use the de Vree model for mode II failure. In this model, damage is determined as a linear combination of two damage variables (see equation [3.4]): D_t and D_c, which are damage due to tension and compression, respectively [MAZ 86]:

$$D = \alpha_t D_t + \alpha_c D_c \qquad [3.4]$$

The parameters α_t and α_c depend on the stress state (e.g. $\alpha_t = 1$ in pure traction).

The damage evolution is characterized by the following exponential law:

$$D_{c,t} = 1 - \frac{\varepsilon_{D_0}(1 - A_{c,t})}{Y} - \frac{A_{c,t}}{\exp^{[B_{c,t}(Y - \varepsilon_{D_0})]}} \qquad [3.5]$$

where A_t, B_t, A_c, and B_c are the parameters governing the shape of the evolution law. ε_{D_0} is the strain threshold for damage initiation. Standard values can be found in [MAZ 86].

When shear failure is expected, we use another definition for the equivalent strain, introduced by de Vree, the von Mises strain [VRE 95]:

$$\varepsilon_{eq} = \frac{k-1}{2k(1-2\nu)} I_1 + \frac{1}{2k}\sqrt{\frac{(k-1)^2}{(1-2\nu)^2} I_1^2 + \frac{12k}{(1+\nu)^2} J_2'} \qquad [3.6]$$

with ν being the Poisson's ratio, and I_1 and J_2' being two invariants of the strain tensor $\boldsymbol{\varepsilon}$ defined as:

$$I_1 = tr(\boldsymbol{\varepsilon}) = \varepsilon_1 + \varepsilon_2 + \varepsilon_3 \qquad [3.7]$$

$$J_2' = \frac{1}{6}\left(3tr(\boldsymbol{\varepsilon}.\boldsymbol{\varepsilon}) - tr^2(\boldsymbol{\varepsilon})\right) \qquad [3.8]$$

Parameter k corresponds to the ratio of compressive strength to tensile strength.

The damage evolution law proposed by Peerlings *et al.* is slightly different [PEE 98] from the law used by Mazars:

$$D = 1 - \frac{\varepsilon_{D_0}}{Y}\left(1 - \alpha + \alpha \exp^{-\beta(Y - \varepsilon_{D_0})}\right) \qquad [3.9]$$

with α and β being the parameters governing the shape of the evolution law.

Both the constitutive relations exhibit strain softening and, as a consequence, need a regularization technique (for a complete review, see [BAŽ 02]).

3.2.2. *Original integral non-local approach*

In the non-local damage model, the equivalent strain given by equation [3.3] or equation [3.6] is replaced by an average equivalent strain $\overline{\varepsilon}_{eq}$ over a volume Ω in the equation governing the growth of damage as defined by Pijaudier-Cabot and Bažant [PIJ 87] and adapted to the Mazars' model by Saouridis and Mazars [SAO 92]

$$\overline{\varepsilon}_{eq}(\boldsymbol{x}) = \frac{\int_{\Omega} \phi(\boldsymbol{x}-\boldsymbol{s})\varepsilon_{eq}(\boldsymbol{s})d\boldsymbol{s}}{\int_{\Omega} \phi(\boldsymbol{x}-\boldsymbol{s})d\boldsymbol{s}} \qquad [3.10]$$

where $\phi(\boldsymbol{x}-\boldsymbol{s})$ is the weight function defining the interaction between the considered point located at x and the neighboring points located at s inside the volume of the structure Ω. This formulation fulfills the requirement of non-alteration of an uniform field.

The most used non-local weight function is taken as the Gauss distribution function:

$$\phi(\boldsymbol{x}-\boldsymbol{s}) = \exp\left(-\left(\frac{2\left\|\boldsymbol{x}-\boldsymbol{s}\right\|}{l_c}\right)^2\right) \qquad [3.11]$$

where l_c is the internal length of the model and $\|\boldsymbol{x}-\boldsymbol{s}\|$ is the distance between points located at x and $\boldsymbol{s}$. The characteristic size of the weighting domain depends directly on the internal length l_c.

The point located at s (distributing point) has an isotropic influence (Figure 3.1a), except close to boundaries where the interaction domain is chopped off. Considering a point at the level of the boundary, the number of distributing points with an influence non-negligible on it is divided by 2. The term in the numerator of equation [3.10] is also divided by 2, thus leading to a double amplitude of the interactions close to the boundary. As a consequence, an attraction of the damage by the boundaries due to the truncation of the volume of interaction, as illustrated by Krayani *et al.* [KRA 09], can be observed.

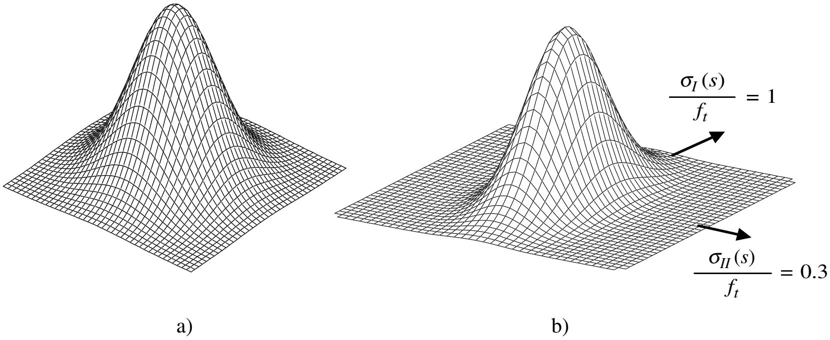

Figure 3.1. *Influence of a distributing point. Gaussian function. (a) Original non-local model, (b) stress-based non-local model*

Another issue that has been pointed out is the treatment of the FPZ at high-damage level. In Figure 3.2a, quarter of a plate with a central notch is represented. It is submitted to tension of equal magnitude in both directions. The circles given in the figure represent isovalues of the Gaussian function, similar for each point of the specimen and corresponding to the influence of the point located at the center of these circles. In the original non-local model, this point can influence a point on the other side of the crack as only the distance between them is considered in the model. Physically, this interaction should not exist.

Since the presence of an FPZ or a fully developed crack as well as a free boundary modifies the loading on an RVE (Representative Volume Element) considered in its neighborhood, the resulting redistribution of this RVE at the origins of non-locality had to be modified to reflect the evolution of the interactions.

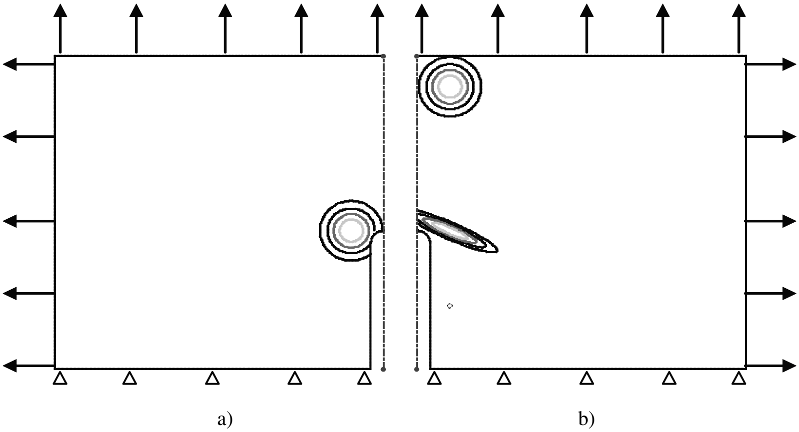

Figure 3.2. *Isovalues of the influence of different points in the specimen. (a) Original non-local model, (b) stress-based non-local model*

3.2.3. *Non-local integral method based on stress state*

As quoted previously, the truncation of the interaction volume in the vicinity of boundary leads to a double amplitude of the non-local terms compared to those in the bulk of the material. Based on micromechanic considerations, Pijaudier-Cabot and Dufour [PIJ 10] show that non-locality corresponds to a stress redistribution due to the presence of defects. In this framework, they show that non-localities should disappear in the vicinity of boundary in the normal direction. As a consequence, they proposed a modification of the interaction domain [KRA 09] whose shape is an ellipsoid with a radius equal to the minimum between the internal length and the distance between the considered point and the boundary. The domain of interaction is oriented (isotropy is lost) but does not evolve in time as only geometrical aspects are considered. However, we can see fully damaged area as a new boundary surrounded by a damaged zone. As a consequence, the non-local interactions should vanish in the direction perpendicular to this new boundary.

In our approach, the point of view of the calculation of non-local quantities is slightly different. *We do not consider what a point located at x can receive but what a point located at s can distribute*. The non-locality is defined as a quantity given by each point located at s along its principal stress direction with an intensity depending on the level of the principal stress. We introduce in the non-local regularization both the notion of directionality, as shown by Pijaudier and Dufour [PIJ 10] in the limited case of the vicinity of boundaries and the variation of the intensity depending on the state of loading in the structure. The stress field allows us to describe directly the presence of free boundary or the development of FPZ that are at the origins of the modification of the non-localities. During the calculation, the evolution of the interactions between points is considered through a single coefficient β that multiplies the internal length l_c. This coefficient depends on the stress state of the distributed points. Besides, it is important to note that no new parameter is introduced in the model.

Let us denote $\boldsymbol{\sigma}_{prin}(\boldsymbol{s})$ as the stress state of the point located at s, expressed in its principal frame. The vectors forming this frame are $\boldsymbol{u}_1(\boldsymbol{s})$, $\boldsymbol{u}_2(\boldsymbol{s})$, and $\boldsymbol{u}_3(\boldsymbol{s})$ with the associated principal stresses $\sigma_1(\boldsymbol{s})$, $\sigma_2(\boldsymbol{s})$, and $\sigma_3(\boldsymbol{s})$, respectively,

$$\boldsymbol{\sigma}_{prin}(\boldsymbol{s}) = \sum_{i=1}^{3} \sigma_i(\boldsymbol{s})(\boldsymbol{u}_i(\boldsymbol{s}) \otimes \boldsymbol{u}_i(\boldsymbol{s})) \qquad [3.12]$$

where $\otimes$ is the tensor product. We define an ellipsoid centered at point s, corresponding to a homothety of the original interaction domain, with a ratio $|\frac{\sigma_i(\boldsymbol{s})}{f_t}|$ along the principal stress direction $\boldsymbol{u}_i(\boldsymbol{s})$. f_t denotes the tensile strength of concrete.

The choice of f_t leads to no modification of the interactions at the tensile stress peak, in the direction associated with the maximum tensile stress, and corresponds to mode I cracking considerations. Furthermore, the ratio along the axes cannot exceed 1 in order to prevent high values for principal stress in compression and limit the size of the connectivity matrix that is computed only once at the beginning of the numerical simulation.

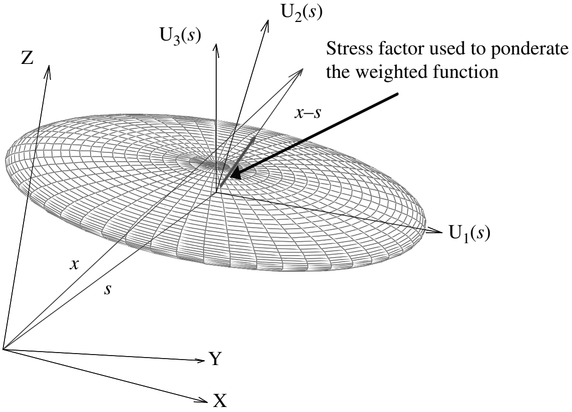

Figure 3.3. *Definition of the β coefficient giving the influence of s on x*

By using the spherical coordinates (ρ, θ, and ϕ), the following equation describes the ellipsoid associated with the stress state of the point located at s (Figure 3.3)

$$\rho(\boldsymbol{\sigma}_{prin}(\boldsymbol{s}))^2 = \frac{1}{f_t^2\left(\frac{\sin^2\varphi\cos^2\theta}{\sigma_1^2(\boldsymbol{s})} + \frac{\sin^2\varphi\sin^2\theta}{\sigma_2^2(\boldsymbol{s})} + \frac{\cos^2\varphi}{\sigma_3^2(\boldsymbol{s})}\right)} \qquad [3.13]$$

where θ is the angle between u_1 and the projection of $(\boldsymbol{x} - \boldsymbol{s})$ onto the plane defined by u_1 and u_2, and φ is the angle between u_3, and $(\boldsymbol{x} - \boldsymbol{s})$. Considering these angles, we obtain:

$$\begin{array}{ll} \cos\theta = \frac{\boldsymbol{u}_1.(\boldsymbol{u}_3\wedge((\boldsymbol{x}-\boldsymbol{s})\wedge\boldsymbol{u}_3))}{\|\boldsymbol{u}_3\wedge((\boldsymbol{x}-\boldsymbol{s})\wedge\boldsymbol{u}_3)\|} & \sin\theta = \frac{\boldsymbol{u}_2.(\boldsymbol{u}_3\wedge((\boldsymbol{x}-\boldsymbol{s})\wedge\boldsymbol{u}_3))}{\|\boldsymbol{u}_3\wedge((\boldsymbol{x}-\boldsymbol{s})\wedge\boldsymbol{u}_3)\|} \\ \cos\varphi = \frac{\boldsymbol{u}_3.(\boldsymbol{x}-\boldsymbol{s})}{\|\boldsymbol{x}-\boldsymbol{s}\|} & \sin\varphi = \frac{(\boldsymbol{x}-\boldsymbol{s}).(\boldsymbol{u}_3\wedge((\boldsymbol{x}-\boldsymbol{s})\wedge\boldsymbol{u}_3))}{\|(\boldsymbol{x}-\boldsymbol{s})\|.\|\boldsymbol{u}_3\wedge((\boldsymbol{x}-\boldsymbol{s})\wedge\boldsymbol{u}_3)\|} \end{array} \qquad [3.14]$$

where $\wedge$ is the vector product and "." is the scalar product.

The weight function now reads:

$$\phi(\boldsymbol{x}-\boldsymbol{s}) = \exp\left(-\left(\frac{2\,\|\boldsymbol{x}-\boldsymbol{s}\|}{l_c\;\beta(\boldsymbol{x},\boldsymbol{\sigma}_{prin}(\boldsymbol{s}))}\right)^2\right) \qquad [3.15]$$

with $\beta(\boldsymbol{x},\boldsymbol{\sigma}_{prin}(\boldsymbol{s}))$ equal to the "radius" of the ellipsoid defined previously in the direction $(\boldsymbol{x}-\boldsymbol{s})$.

The intensity of the influence of a point at s on its neighborhood depends on the magnitude and direction of the principal stresses at s.

Figure 3.1b shows the influence of the point located at s (distributing point) on its neighborhood.

With the stress-based non-local method proposed here, we retrieve the specific shape of a flat ellipsoid proposed by Krayani *et al.* [KRA 09] in the case of free boundary. Indeed, we have the following condition for the stress tensor: $\boldsymbol{\sigma}_{prin}(\boldsymbol{s}).\vec{n} = \vec{0}$, with $\vec{n}$ being the normal vector to the free boundary. As a consequence, points in this area are local in the normal direction.

For illustration, we study a plate with a central notch under isotropic biaxial traction. In Figure 3.2b, the upper point is not influenced by the notch; as a consequence, the isovalues are close to circles. For the middle point, in the vicinity of the crack tip, its stress state is highly disturbed and oriented, thus leading to ellipses for the isovalues. The lower point is shielded by the crack; as a consequence, it encounters very low stress state and has no influence on the surrounding points as expected from micromechanics.

3.2.4. *Numerical implementation*

The general algorithm of the original non-local method is described in detail by Pegon and Anthoine [PEG 97]. Initially, a fixed connectivity matrix is created defining a list of interacting neighboring elements j for each element i. The surrounding domain is limited in order to reduce the volume of integration during the calculation, and therefore, a geometrical criterion is considered by keeping only the elements j for which the distance between one of their nodes and one node of the element i is lower than $1.5 \times l_c$. It corresponds to a value of 1% for a Gaussian distribution as the weighted function. During the calculation, the non-local regularization is performed just after the evaluation of the equivalent strain ε_{eq}. The distance with each surrounding Gauss points is used to compute the weight function. The introduction of the non-local regularization leads to a non-symmetric matrix due to the treatment of the boundaries. It does not allow for the use of algorithms considering the symmetry of the tangent operator. The width of the band of the stiffness matrix is proportionnal to the internal length as the domain of interaction is directly linked to l_c. The original non-local approach yields a fixed computational cost at the beginning to compute the connectivity matrix, and then for each time step, the computational time is increased depending on the bandwidth of the stiffness matrix, i.e. the internal length.

The procedure introduced for the original non-local method is kept for the stress-based non-local method. It needs only the introduction of the stress state in the computation of the weight function. As the coefficient β (Figure 3.3) stays minor or equal to 1, the domain of interactions is always included in the one of the original non-local method. We consider the same surrounding domain to reduce the volume of integration during the calculation. As a consequence, the calculation of the connectivity matrix is not affected and is kept for the stress-based non-local approach. Only the calculation of the weight is changed with the introduction of the coefficient β (see equation [3.15]). Furthermore, under an uniaxial loading, the ellipsoid degenerates in a line. With no minimum size, we can have, in this specific case, no interaction, whereas a point can encounter a relatively high stress magnitude in one direction. Thus, a minimal value of β is prescribed to avoid problems with zero stress in some directions that could lead to a zero-volume ellipsoid. This value is fixed arbitrarily in an order of a thousandth of the tensile strength. Besides, we ensure a minimum size of the interaction domain lower than one element at zero stress in order to avoid interactions between points upon macrocrack. To keep an explicit resolution of the constitutive law, the interactions are computed with the stress state of the last converged step. Due to the non-reciprocity of the interactions as the stress state can be different for each Gauss point, the consistent stiffness matrix becomes non-symmetric even in the bulk of the material. In terms of computational cost, the stress-based non-local method follows the same algorithm as that of the original non-local method. Only the calculation of the coefficient β brings an additional step to the algorithm.

Furthermore, as illustrated in the following tests, when a FPZ is initiated, the stress-based non-local formulation can lead to a lower number of points with an evolving damage compared to the original non-local method. This last point can even bring a lower computational time. For example, with the test of a bar under tension, we get a reduction of 30% of the computational time with the stress-based non-local method.

All the calculations presented in this paper are made with the finite-element code Cast3M developed by the C.E.A. (French Nuclear Agency) [VER 88] in which the stress-based non-local method has been implemented.

3.3. Initiation of failure

Damage initiation in mode I is analyzed by means of the compact tension specimen with a pre-existing crack of length

h depicted in Figure 3.4. This test performed originally by Simone *et al.* [SIM 04] to study the location of the damage initiation for regularized damage model is reproduced with the stress-based non-local method. As we are interested in the description of the crack initiation and to be in agreement with the work done by Simone *et al.*, we describe the notch explicitly. Due to symmetry, only a half part of the specimen is studied.

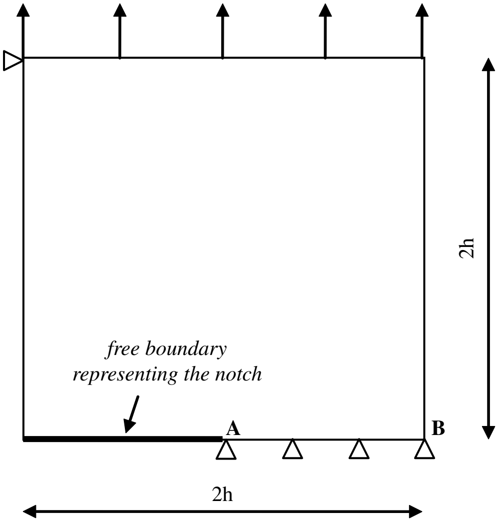

Figure 3.4. *Compact tension specimen (CTS)*

The following parameters are used for the analysis: $E = 1{,}000\,\text{MPa}$, $\nu = 0$, $l_c = 0.0005$, 0.001, or 0.002 mm. Various characteristic lengths for the non-local integral method are used for the calculation in order to analyse its effect on the position of the maximum equivalent strain. The equivalent strain, as defined by Mazars, is calculated from the strain field obtained under an imposed displacement. Then, the non-local equivalent strain is computed (see equation [3.10]). Figure 3.5b shows the shift of the maximum pointed out by Simone *et al.* [SIM 04], using gradient or non-local regularization methods. Furthermore, Figure 3.5a shows the value of the non-local equivalent strain projected along the line in front of the crack. We observe that the shift is proportional to the internal length of the non-local method as it has been pointed out also in the paper quoted previously. In contrast to the stress-based non-local, in the original version the interaction domain expands over the shadow zone of the notch where strains are close to 0. As the non-local equivalent strain is a weighted summation, it proportionally reduces the impact of the singular strain. Since the strain gradient is smaller in front of the notch than at the back, the non-local equivalent strain is shifted to the notch front.

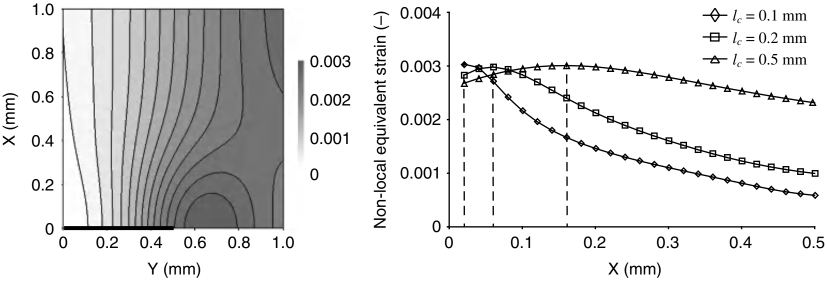

a) b)

Figure 3.5. *CTS (original non-local method): (a) contour plot of the non-local equivalent strain ($l_c = 0.5$ mm) and (b) influence of the internal length on the shift of the maximum non-local equivalent strain*

On the contrary, it is worth noting that for the same test with the stress-based non-local method, the shift is null whatever the internal length l_c (Figure 3.6). Indeed, the points in the shadow of the notch that encounter a small local equivalent strain have also a low stress state. As a consequence, their influence on the neighborhood is hardly null. We have also checked that the choice of the definition of the equivalent strain proposed in the first section does not affect the results. This important result shows, through this example, the capability of the stress-based non-local method to correctly locate the material nonlinearities in mode I problem with a preexisting crack.

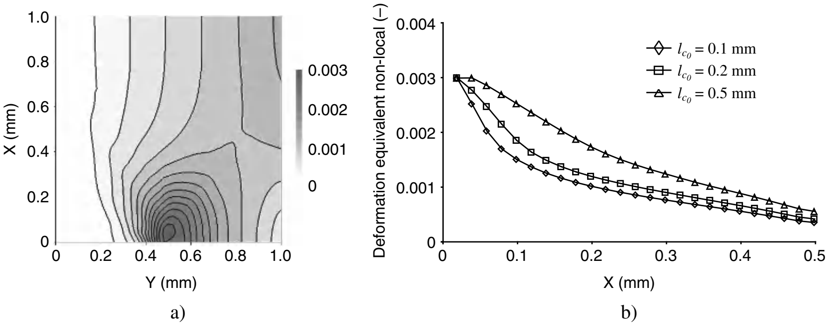

Figure 3.6. *CTS (stress-based non-local method): (a) contour plot of the non-local equivalent strain ($l_c = 0.5$ mm) and (b) influence of the internal length on the shift of the maximum non-local equivalent strain*

3.4. Bar under traction

The test used here to illustrate the functioning of the stress-based non-local formulation is a bar under tension with a 2D geometry and a 1D loading (no Poisson's effect). In spite of its simplicity, this test allows us to show the change in the behavior obtained with this improvement, more particularly when dealing with high-damage state.

The bar is 1 m long and 0.01 m high. It is fixed at one end and the load is applied via an imposed displacement up to $U_{max} = 0.0005$ m at the other end. We use, for this example, the evolution law proposed by Peerlings *et al.* (see equation [3.9]). Compared to the evolution law proposed by Mazars (see equation [3.5]), a relatively slower decrease of the strength can be fixed. As a consequence, "snap-back" phenomenon can be avoided. The following parameters are taken for the damage model describing concrete (see equation [3.9]): $E_b = 33.7$ GPa,

$\alpha = 0.99$, $\nu = 0$, and $\beta = 1{,}000$. The coefficient β introduced here is relative to the evolution law [3.9] and should not be confused with the coefficient of interaction used in the weight function (see equation [3.15]).

The bar is composed of isoparametric elements with linear interpolation. Only one element is put along the height. The central element is weakened with a lower Young's modulus ($E_{b_{weak}} = 31$ GPa) in order to initiate the damage in the bar.

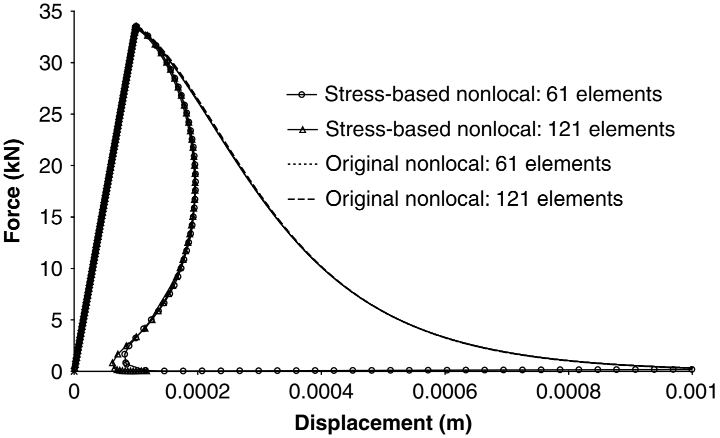

Figure 3.7. *Bar under tension: evolution of the force versus displacement for the stress-based and the original non-local models with two sizes of element*

3.4.1. *Global behavior*

The objectivity of both the non-local versions is analyzed using two different mesh sizes. A coarse mesh of 31 elements and a fine mesh of 61 elements are used. Figure 3.7 shows the evolution of the force versus the imposed displacement for both mesh sizes and non-local versions. Although no mesh dependency is observed on the global response for the same set of constitutive law parameters, the response given by the stress-based non-local model is more brittle. However, the peak force is identical as we recover the value of the internal length l_c for the stress-based non-local model. Indeed, the decrease in the internal length with the stress level yields an incremental decrease of the FPZ, and thus, a decrease in the dissipated energy.

3.4.2. *Mechanical quantities in the FPZ*

Figure 3.8 shows the evolution of the strain and damage profiles along the bar for both non-local approaches with the finest mesh. The quantities plotted are nodal fields. Therefore, although strain and damage are maximum in a single element, two peaks appear in the plots. The chosen state for the curves are for $0.1, 0.2, 0.3, 0.4, 0.5, 0.6, 0.7, 0.75, 0.8, 0.85, 0.9$, and $1.U_{max}$. The original integral non-local method leads to a completely damaged area ($D = 1$) spread over several elements when the force vanishes. The interactions between Gauss points do not evolve during the test and yields to the so-called spurious diffusion of damage. Physically, a single macrocrack is expected for such a test. Thus, in the numerical model damage should reach the value of 1 in a single finite element (smallest numerical entity), whereas the surrounding elements should be partially damaged only.

At the peak $\beta = 1$, the stress-based approach brings no modification, and the onset of damage is identical since the stress state is homogeneous. Just beyond the peak, modifications are minor as β is close to 1, and the damage profiles have the same width. Thus, the FPZ size is not altered. Finally, as we get closer to the rupture (β decreases up to 0), the damage increment occurs in a narrower band and the value $D = 1$ is reached only in one element. As the Gauss points along the bar we have encountered their peak stress, we observe a decrease in the interactions. Each point tends to be more local in the sense that interaction effects are decreasing.

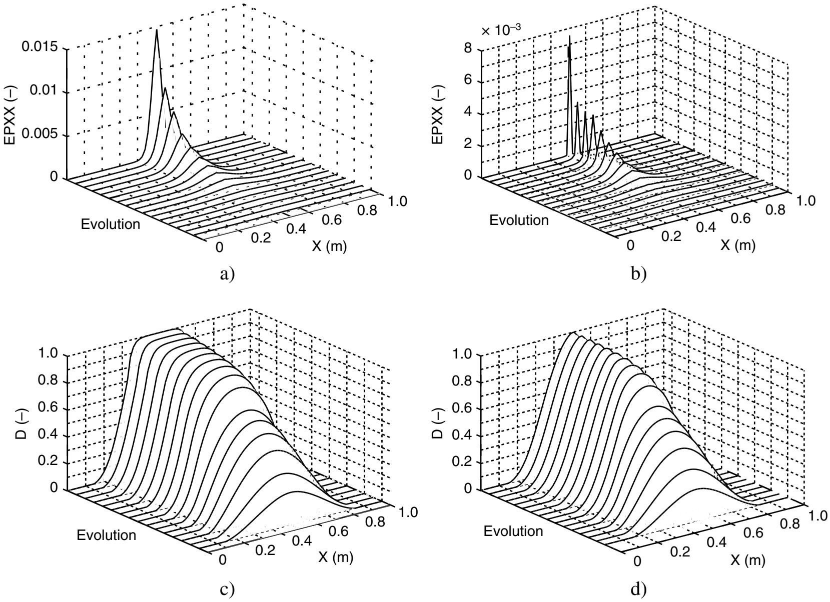

a) b)

c) d)

Figure 3.8. *Bar under tension: Evolution of strain. (a) Original non-local model and (b) stress-based non-local model. Evolution of damage. (c) Original non-local model and (d) stress-based non-local model*

Identically, for the original integral non-local method, the strain field is localized within a band proportional to the internal length of the model. On the contrary, the strain field along the bar is much sharper with the stress-based non-local model since only one element is deformed at failure. It sounds more physical since across a crack the strain profile is a Dirac function (i.e. the displacement field is discontinuous with a jump across the crack that is the crack opening). However, with a continuous modeling such as FEM, we can obviously never get a Dirac for the strain profile as performed analytically with a strong discontinuity approach or numerically with X-FEM [MOE 99]. Therefore, the best that can be done with classical FEM is to localize strain in one element (weak discontinuity) upon failure and this has been reached with the stress-based non-local approach.

As for the global behavior, the objectivity is obtained for damage profile upon failure (Figure 3.9). This result is also true for a strain profile up to failure. However, as soon as the most damaged element reaches a value of 1 for D, the stress intensity is null. With the stress-based non-local model, the non-local interactions no longer exist as the minimum size is lower than the size of an element and the imposed displacement is localized into the most damaged element.

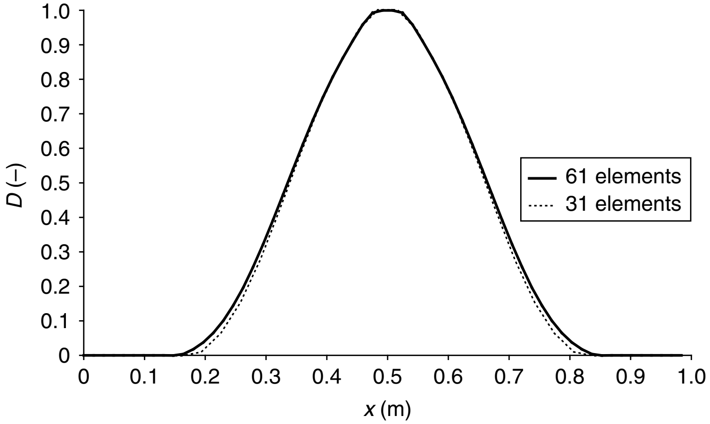

Figure 3.9. *Bar under tension: Damage profile with the stress-based non-local model for different mesh sizes*

By denoting l_e the length of the element and ε the strain level encounter by this element along the loading axis, we get:

$$[U] = \varepsilon . l_e \qquad [3.16]$$

We keep the objectivity for the displacement field after complete failure, but at this state, the strain magnitude depends on the size of the most damaged element as a function of l_e^{-1} (Figure 3.10). This result is also obtained by

Pijaudier-Cabot and Dufour with a modification of the non-local regularization method by considering an integration of damage along path between interacting points [PIJ 10]. As long as, in terms of kinematics only, the displacement fields are of importance, this is out of interest. However, if this model is used for the modeling of reinforced concrete structures, the peak strain depending on the mesh size could change the occurrence time of plasticity in rebars. This has to be checked for future work.

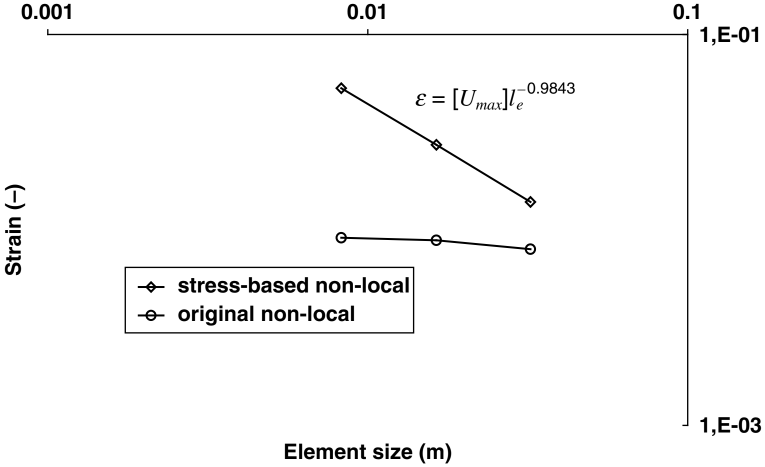

Figure 3.10. *Bar under tension: maximum strain after failure for different mesh size with both the non-local methods*

3.4.3. *Crack opening estimation*

Dufour *et al.* [DUF 08] have developed a method to obtain information on crack opening by post treatment of the continuous calculation. The main aspects of the method are detailed for the 1D case. The numerical strain profile is compared to an analytical strain profile obtained by a strong discontinuity approach of the crack. In the strong discontinuity approach, at the location of the crack ($x = x_0$), the displacement profile U_{sd} is discontinuous with a jump $[U]$, mathematically represented by the Heavyside function H_Γ (Figure 3.11) and the strain profile ε_{sd} is represented by a Dirac function δ (Figure 3.12).

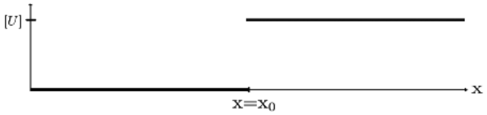

$$\mathrm{u}_{sd}(x, x_0) = [U]\, H_\Gamma(x - x_0)$$

Figure 3.11. *Displacement profile with the strong discontinuity approach*

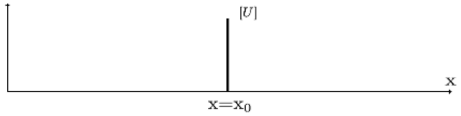

$$\varepsilon_{sd}(x, x_0) = \nabla^s u_{sd} = [U]\, \delta(x - x_0)$$

Figure 3.12. *Strain profile with the strong discontinuity approach*

As it is mathematically a nonsense to compare directly a Dirac with the numerical strain profile ε_{FE}, a convolution product is performed for both the profiles (analytical and numerical) with a Gaussian function ϕ and the resulting profiles are compared. Finally, hypothesis of equal magnitude of the convoluted strain at the crack location leads to an estimation of the crack opening:

$$[U] = \frac{(\varepsilon_{FE} * \phi)(x_0)}{\phi(0)} \qquad [3.17]$$

The specificity of this method over others [MAT 10] is to give an error indicator Δ^γ by computing the integrated distance between both the convoluted profiles [3.18]

$$\Delta^\gamma(x_0, [U]) = \frac{\int_\Gamma |(\varepsilon_{sd} * \phi)(s, x_0, [U]) - (\varepsilon_{FE} * \phi)(s)|\, ds}{\int_\Gamma (\varepsilon_{FE} * \phi)(s) ds} \qquad [3.18]$$

One of the aims of the modification made on the non-local regularization is to better treat the post-peak behavior of concrete structure in terms of the mechanical description of the FPZ. By reducing the highly damaged area, we get closer to a strong discontinuity response and the strain profile is similar to a Dirac function. As the mesh is refined, we can expect to reduce the error as defined previously.

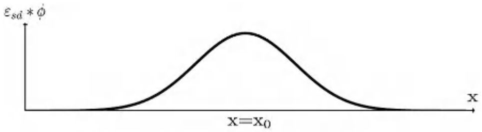

$$(\varepsilon_{sd} * \phi)(s, x_0, [U]) = [U]\,\phi(x - x_0)$$

Figure 3.13. *Resulting strain profile of the strong discontinuity after the convolution product with a Gaussian function*

Figure 3.14 shows the evolution of the crack opening as a function of the displacement. Figure 3.15 shows the evolution of the error between the regularized FE strain profile and the regularized strong discontinuity strain profile as a function of crack opening. Physically, except some permanent strains not taken into account in the modeling, we should retrieve after failure a crack opening equal to the imposed displacement. As a consequence, in Figure 3.14, the curves should join the bisector of the graph. This is the case for the stress-based non-local method. The first part of the curve corresponds to the error just after the peak at a state where both the numerical models give strain fields far from a Dirac, and therefore, it is still meaningless to talk about a single-crack approach. As a consequence, a relatively high error is observed. However, when the crack is gradually formed, the error, with respect to the strong discontinuity, decreases faster in the case of the stress-based non-local model validating the observations we could have made previously on the strain and damage profiles. It shows the capability of the stress-based non-local model to improve the modeling of cracking up to complete failure without losing the advantages of the original version.

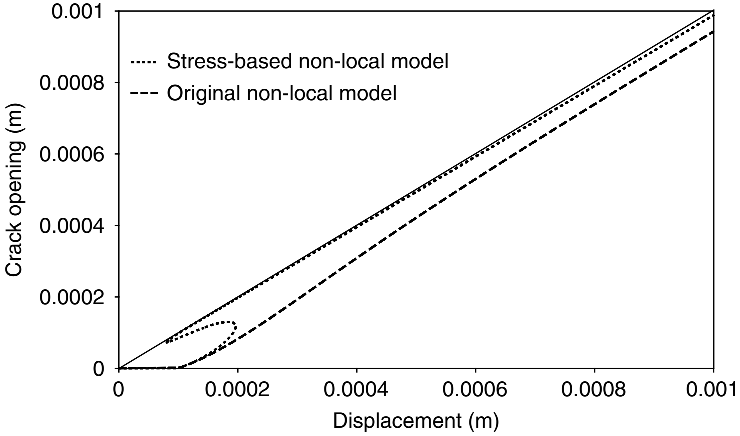

Figure 3.14. *Crack opening as a function of the imposed displacement*

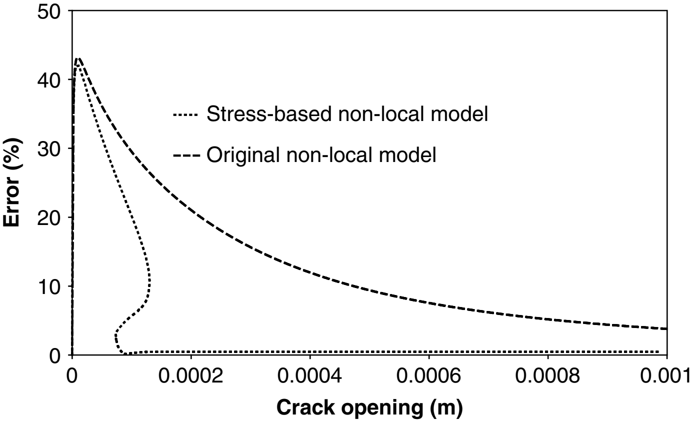

Figure 3.15. *Bar under tension: relative error as a function of the crack opening*

3.5. Description of the cracking evolution in a 3PBT of a concrete notched beam

The efficiency of the stress-based non-local method to describe the failure process of quasi-brittle material is explored through the comparison with experimental results on the evolution of crack opening along the height of a notched beam under 3PBT. This beam tested at the GEM Laboratory in Nantes by [DUF 11] is depicted in Figure 3.16 with the associated mesh used for the numerical investigation. This beam has been modeled in 2D with plane stress conditions. The loading has been applied via displacement control. We have used the evolution law proposed by Mazars (see equation [3.5]) to describe the non-linear behavior of concrete. Both original non-local method and stress-based non-local method have been used successively with the same set of parameters to be compared. The following parameters are taken for the damage model describing concrete (see equation [3.5]): $E = 30{,}000\,\text{MPa}$, $\nu = 0.24$, $\varepsilon_{D_0} = 0.00004$, $\beta = 1.06$, $A_t = 0.9$, $B_t = 4{,}000$, $A_c = 1.25$, $B_c = 1{,}000$, and $l_c = 0.008\,\text{m}$. The beam is composed of isoparametric elements with linear interpolation. A unusual attention was taken to finely describe the notch tip where stress concentration was supposed to appear.

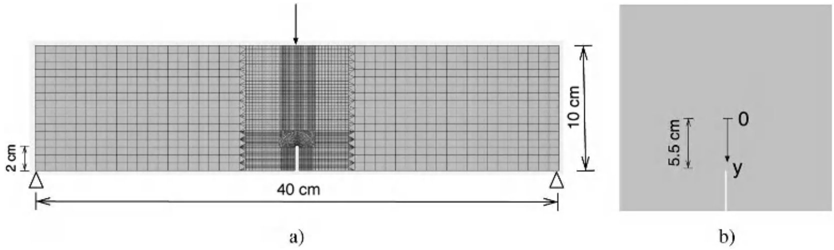

Figure 3.16. *3PBT: (a) mesh and loading conditions for the test. (b) Axis used for the digital image correlation to extract crack opening*

3.5.1. *Global behavior*

Figure 3.17 shows the global behavior of the beam under 3PBT for the original and the stress-based non-local regularization techniques and is compared with the experimental results. The stress-based non-local method better reproduces the peak with the same set of parameters than the original non-local method. We have seen that damage initiation at the notch tip is better described with the stress-based non-local method. Furthermore, it is coherent to retrieve a dissipation of energy lower than the stress-based non-local method as the domain of interactions is equal to lower than the domain with the original non-local method. It leads to a narrower damage profile close to complete failure (see Figure 3.18).

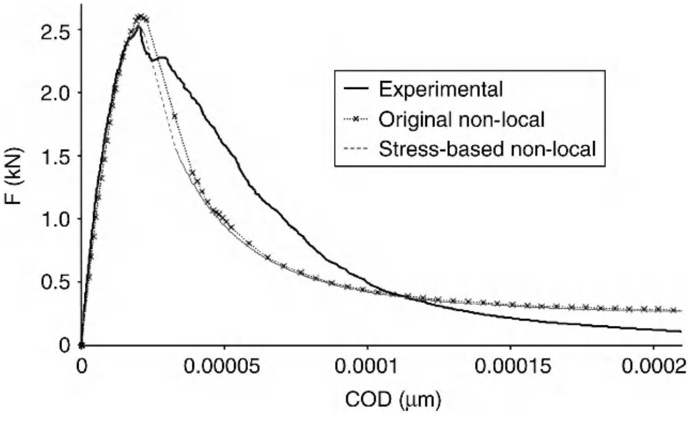

Figure 3.17. *3PBT: evolution of the force versus crack mouth opening displacement (CMOD) for the stress-based models, the original non-local models, and experimental results*

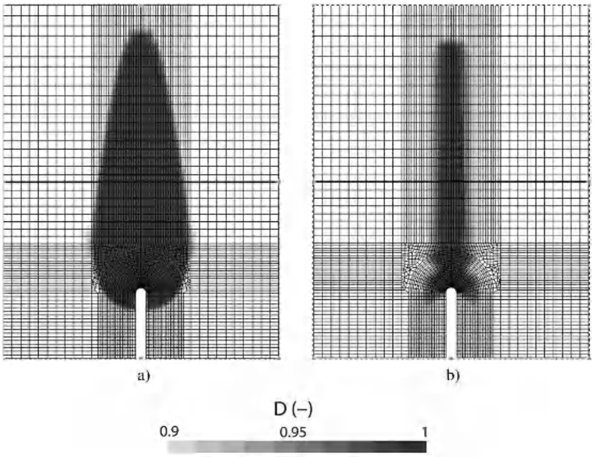

Figure 3.18. *3PBT: damage field (CMOD:* 71 μm*). Original non-local model (a) and stress-based non-local models (b)*

3.5.2. *Cracking analysis*

Image correlation procedure was used during the experiment to follow the cracking process. Figure 3.19a gives the orientation and the origin along the height of the beam of the measured cracking. Hereafter we compare these experimental results with the results obtained from numerical calculations using the post-treatment method given previously. Figure 3.19 shows the crack opening along the height at different CMOD level. One can observe that for the lowest CMOD considered, both cracking predictions by means of the stress-based and the original non-local models are close to each other. The microcracking is still diffused far from the crack tip, the interactions are not really modified. This yields a strain field similar with both methods. For higher CMOD, as soon as the macrocracking state is reached, we obtained a sharper strain profile in the case of the stress-based non-local model. Therefore, it leads to a better estimation of the crack opening as was also previously observed for the bar under tension. A reason for the shift between the experimental and the numerical results regarding the crack opening can be due to the 2D approximation used for the calculation. Indeed, experimentally, the crack opening was measured on surface, and we can expect to have different values along the depth. Numerically, by assuming 2D conditions, the crack opening is identical by nature along the depth.

3.6. Conclusions

We have proposed in this chapter a modification of the integral non-local model in order to adapt the regularization close to the free boundaries and during the cracking process. The stress state of each point is used during the calculation in order to create an evolution of the interaction between points. Each point interacts with its neighborhood as a function of the intensity and direction of its principal stress values. This modification has been presented in the 3D case. It has allowed us to retrieve results concerning boundary effects given in a previous article by the second author without specific treatments of boundaries.

The modification has been illustrated through the example of a bar under tension. Damage and strain profiles across a FPZ are more physically sounded. The result's objectivity is conserved and our proposal allows us to obtain a weak discontinuity that gets as close to a strong discontinuity upon mesh refinement. As a result, the estimation of crack opening is much improved. This is a key issue as information on crack opening is a hot topic in structural engineering for durability analysis or the leakage rate estimation for confining vessels. It has been shown that continuous modeling can provide this kind of information. By improving the FE calculation, and more particularly, by taking into account the effect of a damaged zone on its vicinity, crack opening estimation is greatly improved.

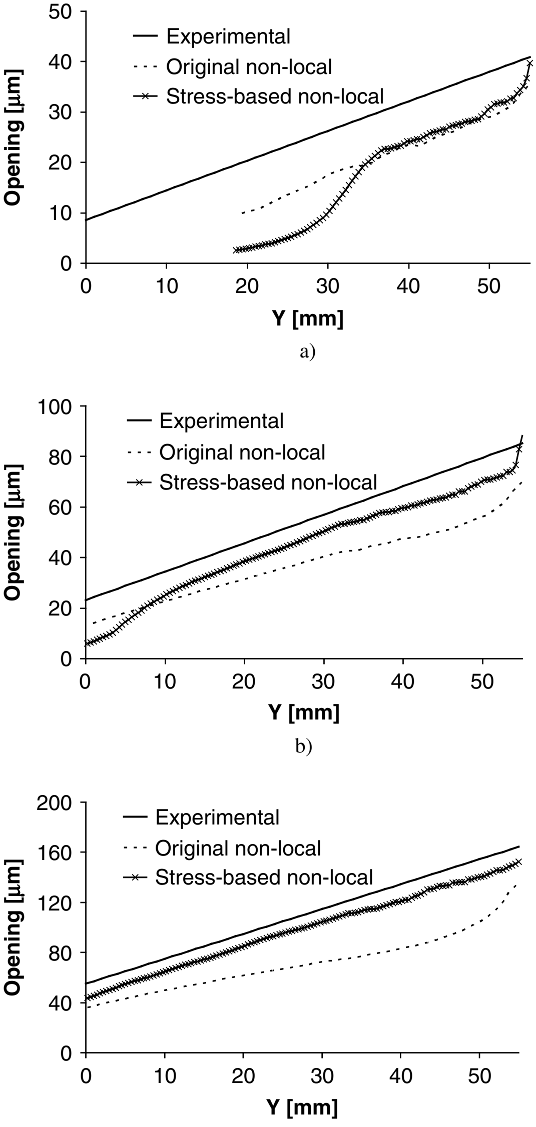

a)

b)

c)

Figure 3.19. *3PBT: crack opening along the height of the beam at different loading levels for the stress-based models, the original non-local models, and the experimental results (CMOD : (a)* 50 μm*, (b)* 100 μm*, and (c)* 200 μm*)*

Finally, the stress-based non-local approach provides a better solution to model damage initiation and localization band propagation as shown by Giry *et al*. We have shown on the crack tip problem that the proposed approach is capable of perfectly locating the damage initiation which is poorly estimated by any other regularization techniques. The stress-based non-local method is based on the reduction of the principal stress perpendicular to the crack.

All these improvements are made with no addition of parameter that would be difficult to calibrate and the computational cost is similar to the original non-local method. This can be easily implemented in any FE code that already includes the non-local approach.

In future works, loaded interface between two materials and loaded boundaries will be investigated. This will be of great interest for structural analysis with interaction between a crack in concrete and rebars.

3.7. Acknowledgments

Financial support from the Agence Nationale de la Recherche through the sustainable cities program (contract VD08_323065) is gratefully acknowledged.

3.8. Bibliography

[BAŽ 91] BAŽANT Z., "Why continuum damage is nonlocal: Micromechanics arguments", *Journal of Engineering Mechanics*, vol. ASCE 117, no. 5, pp. 1070–1087, 1991.

[BAŽ 94] BAŽANT Z.P., "Nonlocal damage theory based on micromechanics of crack interactions", *Journal of Engineering Mechanics*, vol. 120, pp. 593–617, 1994.

[BAŽ 02] BAŽANT Z.P., JIRASEK M., "Nonlocal integral formulations for plasticity and damage: Survey of progress", *Journal of Engineering Mechanics*, vol. 128, pp. 1119–1149, 2002.

[BAŽ 10] BAŽANT Z.P., LE J.-L., HOOVER C.G., "Nonlocal boundary layer (NBL) model: Overcoming boundary condition problems in strength statistics and fracture analysis of quasibrittle materials", *7th International Conference on Fracture Mechanics of Concrete and Concrete Structures (FraMCoS-7)*, 2010.

[DES 07] DESMORAT R., GATUINGT F., Introduction of an internal time in nonlocal integral theories, Internal report LMT-Cachan, number 268, year 2007, ENS Cachan/CNRS/ University of Paris 6/PRES Universud Paris, 2007.

[DES 10] DESMORAT R., GATUINGT F., RAGUENEAU F., "Nonstandard thermodynamics framework for robust computations with induced anisotropic damage", *International Journal of Damage Mechanics*, vol. 19, no. 1, pp. 53–73, 2010.

[DUF 08] DUFOUR F., PIJAUDIER-CABOT G., CHOINSKA M., HUERTA A., "Extraction of a crack opening from a continuous approach using regularized damage models", *Computers and Concrete*, vol. 5, no. 4, pp. 375–388, 2008.

[DUF 11] DUFOUR F., LEGRAIN G., PIJAUDIER-CABOT G., HUERTA A. "Estimate of crack opening from a 2D continuum-based FE computation", *International Journal for Numerical and Analytical Methods in Geomechanics*, 2011.

[ERI 77] ERINGEN A.C., SPEZIALE C.G., KIM B.S., "Crack-tip problem in non-local elasticity", *Journal of the Mechanics and Physics of Solids*, vol. 25, pp. 255–339, 1977.

[JIR 04] JIRASEK M., ROLSHOVEN S., GRASSL P., "Size effect on fracture energy induced by non-locality", *International Journal for Numerical and Analytical Methods in Geomechanics*, vol. 28, nos. 7–8, pp. 653–670, 2004.

[KAC 87] KACHANOV M., "Elastic solids with many cracks-a simple method of analysis", *International Journal of Solids and Structures*, vol. 23, pp. 23–43, 1987.

[KRA 09] KRAYANI A., PIJAUDIER-CABOT G., DUFOUR F., "Boundary effect on weight function in non-local damage model", *Engineering Fracture Mechanics*, vol. 76, pp. 2217–2231, 2009.

[MAT 10] MATALLAH M., LABORDERIE C., MAUREL O., "A practical method to estimate crack opening in concrete sructures", *International Journal for Numerical and Analytical Methods in Geomechanics*, vol. 34, no. 15, 2010.

[MAZ 86] MAZARS J., "A description of micro- and macroscale damage of concrete structures", *Engineering Fracture Mechanics*, vol. 25, nos. 5–6, pp. 729–737, 1986.

[MOE 99] MOES N., DOLBOW J., BELYTSCHKO T., "A finite element method for crack growth without remeshing", *International Journal for Numerical Methods in Engineering*, vol. 46, pp. 131–150, 1999.

[PEE 96] PEERLINGS R.H.J., DE BORST R., BREKELMANS W.A.M., DE VREE J.H.P., "Gradient enhanced damage for quasi-brittle materials", *International Journal for Numerical Methods in Engineering*, vol. 39, pp. 937–953, 1996.

[PEE 98] PEERLINGS R.H.J., DE BORST R., BREKELMANS W.A.M., GEERS M., "Gradient enhanced damage modelling of concrete fracture", *International Journal for Numerical and Analytical Methods in Geomechanics*, vol. 3, pp. 323–342, 1998.

[PEE 01] PEERLINGS R.H.J., GEERS M.G.D., DE BORST R., BREKELMANS W.A.M., "A critical comparison of nonlocal and gradient-enhanced softening continua", *International Journal of Solids and Structures*, vol. 38, pp. 7723–7746, 2001.

[PEG 97] PEGON P., ANTHOINE A., "Numerical strategies for solving continuum damage problems with softening: Application to the homogenization of Masonry", *Computers & Structures*, vol. 64, nos. 1–4, pp. 623–642, 1997.

[PIJ 87] PIJAUDIER-CABOT G., BAŽANT Z., "Nonlocal damage theory", *Journal of Engineering Mechanics*, vol. 113, pp. 1512–1533, 1987.

[PIJ 10] PIJAUDIER-CABOT G., DUFOUR F., "Nonlocal damage model: boundary and evolving boundary effects", *European Journal of Environmental and Civil Engineering*, vol. 14, nos. 6–7, pp. 729–749, 2010.

[RIZ 95] RIZZI E., CAROL I., WILLIAM K., "Localization analysis of elastic degradation with application to scalar damage", *Journal of Engineering Mechanics*, vol. 121, no. 4, pp. 541–554, 1995.

[SAO 92] SAOURIDIS C., MAZARS J., "Prediction of the failure and size effect in concrete via a bi-scale damage approach", *Engineering Computations*, vol. 9, pp. 329–344, 1992.

[SIM 04] SIMONE A., ASKES H., SLUYS L.J., "Incorrect initiation and propagation of failure in non-local and gradient-enhanced media", *International Journal of Solids and Structures*, vol. 41, pp. 351–363, 2004.

[VER 88] VERPEAUX P., CHARRAS T., MILLARD A., "CASTEM 2000 une approche moderne du calcul des structures", in FOUET J.M., LADEVÈZE P., OHAYON R., *Calcul des structures et intelligence artificielle*, Pluralis, pp. 261–271, 1988.

[VOY 05] VOYIADJIS G., ABU AL-RUB R., "Gradient plasticity theory with a variable length scale parameter", *International Journal of Solids and Structures*, Pergamon-Elsevier Science Ltd, vol. 42, no. 14, pp. 3998–4029, 2005.

[VRE 95] DE VREE J., BREKELMANS W., VAN GILS A., "Comparison of nonlocal approaches in continuum damage mechanics", *Computers and Structures*, vol. 55, pp. 581–588, 1995.

Chapter 4

Discretization of Higher Order Gradient Damage Models Using Isogeometric Finite Elements

4.1. Introduction

Continuum damage models [LEM 90] are widely used for the simulation of diffuse fracture processes. Several modifications of the original theory have been proposed to overcome the mesh dependency problems associated with the absence of an internal length scale (see, e.g. [VRE 95] and [BOR 04]). One way to avoid mesh dependencies is to relate the material parameters to the element size [WIL 84, BRE 95]. Alternatively, an internal length scale can be introduced by a spatial smoothing function in the continuum formulation [PIJ 87]. Gradient approximations of this smoothing function have led to the development of

---

Chapter written by Clemens V. VERHOOSEL, Michael A. SCOTT, Michael J. BORDEN, Thomas J.R. HUGHES, and René DE BORST.

damage models where an internal length scale is introduced through gradients of an equivalent strain field. Among the gradient damage formulations, the implicit gradient enhancement [PEE 96] is considered the most effective. In its original form, a second-order Taylor expansion is used to approximate a smoothing integral, which results in a system of two second-order partial differential equations. This formulation is attractive from a discretization point of view since it can be solved using C^0-continuous finite elements. It has, however, been demonstrated that the accuracy of the second-order approximation can be limited [HUE 94, ASK 00]. For that reason, it is important to study the effect of the higher order terms in the Taylor approximation of the non-local formulation, which result in higher order gradient damage formulations.

Mixed finite-element formulations can be used for the discretization of higher order gradient damage formulations. In these formulations, the introduction of higher order continuous basis functions is avoided by introducing auxiliary fields. This results in systems with many more degrees of freedom than required by the second-order gradient formulation, thus making the method computationally expensive. To avoid the introduction of auxiliary fields, meshless methods have been used [ASK 00]. The smoothness of meshless methods is inherently derived from the way in which the basis functions are constructed. Although meshless methods have been applied successfully for the discretization of the fourth-order gradient damage formulation, they have not been used widely. A reason for this is the inability of meshless methods to define geometry [SAK 06]. The incompatibility with traditional finite-element formulations, in the sense that the method is not element-based, may be another reason why meshless methods are not commonly applied to higher order gradient damage formulations.

In this chapter, we use isogeometric finite elements to overcome the problems associated with the use of mixed formulations and meshless methods for gradient damage formulations. The isogeometric analysis concept was introduced by Hughes *et al.* [HUG 05], and it has been applied successfully to a wide variety of problems in solids, fluids, and fluid–structure interactions (see [COT 09] for an overview). Use of higher order, smooth spline bases in isogeometric analysis has computational advantages over standard finite elements, especially when higher order differential equations are considered [GÓM 08]. In contrast to meshless methods, the geometry and solution space are one and the same. This makes it possible to construct bases for complex geometries, which can be obtained directly from a computer-aided design (CAD) tool [BEN 10]. From an analysis point of view, isogeometric analysis can be considered as an element-based discretization technique. This compatibility with traditional finite elements facilitates the application to industrial problems.

We first review the non-local continuum damage formulation and the gradient-based approximation in section 4.2. We then introduce in section 4.3 the isogeometric finite-element discretization. In section 4.4, we present numerical simulations utilizing isogeometric finite elements for the discretization of the second-order, fourth-order, and sixth-order gradient formulations.

4.2. Isotropic damage formulation

We consider a body $\Omega \subset \mathbb{R}^N$ with $N \in \{1,2,3\}$ and boundary $\partial\Omega$ (see Figure 4.1). The displacement of a material point $x \in \Omega$ is denoted by $u(x) \in \mathbb{R}^N$. The displacements satisfy Dirichlet boundary conditions, $u_i = \tilde{u}_i$, on $\partial\Omega_{u_i} \subseteq \partial\Omega$. Under the assumption of small displacement gradients, the infinitesimal strain tensor

$$\varepsilon_{ij} = u_{(i,j)} = \frac{1}{2}\left(\frac{\partial u_i}{\partial x_j} + \frac{\partial u_j}{\partial x_i}\right) \qquad [4.1]$$

is used as an appropriate measure for the deformation of the body. The Cauchy stress tensor, $\sigma(x) \in \mathbb{R}^{N\times N}$, is used as the corresponding stress measure. An external traction $\tilde{t}_i$ acts on the Neumann boundary $\partial\Omega_{t_i} \subseteq \partial\Omega$ and is equal to the projection of the stress tensor on the outward pointing normal vector $n(x) \in \mathbb{R}^N$, i.e. $\tilde{t}_i = \sigma_{ij}n_j$. The solid body is loaded by increasing the boundary tractions or boundary displacements.

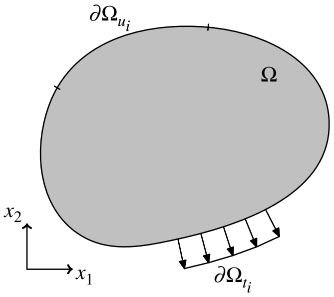

Figure 4.1. *Solid domain Ω with boundary $\partial\Omega$*

4.2.1. *Constitutive modeling*

In isotropic continuum damage models, the Cauchy stress is related to the infinitesimal strain tensor by

$$\sigma_{ij} = (1-\omega)H_{ijkl}\varepsilon_{kl}, \qquad [4.2]$$

where $\omega \in [0,1]$ is a scalar damage parameter and H is the Hookean elasticity tensor for undamage material (i.e. with $\omega = 0$). When damage has fully developed ($\omega = 1$), a material has lost all stiffness. Note that we adopt index notation with summation from 1 to N over repeated italic subscript indices, for example, $u_iv_i = \sum_{i=1}^{N} u_iv_i$.

The damage parameter is related to a history parameter κ by a monotonically increasing function $\omega = \omega(\kappa)$, which is referred to as the damage law. Various damage laws will be considered in section 4.4. The history parameter evolves according to the Kuhn–Tucker conditions

$$f \leq 0, \quad \dot{\kappa} \geq 0, \quad \dot{\kappa} f = 0 \tag{4.3}$$

for the loading function $f = \bar{\eta} - \kappa$, where $\bar{\eta}$ is a non-local strain measure, referred to as the non-local equivalent strain. The monotonicity of both κ and $\omega(\kappa)$ guarantees that the damage parameter is monotonically increasing at every material point, thereby introducing irreversibility in the constitutive model.

Non-locality is introduced into the model by means of the non-local equivalent strain which ensures a well-posed formulation at the onset of damage evolution. If instead the damage parameter was related to a local strain measure, η, the resulting medium would suffer from a local loss of ellipticity in the case of material softening [SLU 94]. The model is then unable to smear out the damage zone over a finite volume. In other words, a local continuum damage formulation fails to introduce a length scale for the damage zone, resulting in spurious mesh dependencies in numerical solutions.

A straightforward way of introducing non-locality in the formulation is by defining the non-local equivalent strain, $\bar{\eta}(x)$, as the volume average of a local equivalent strain, $\eta = \eta(\varepsilon)$,

$$\bar{\eta}(x) = \frac{\int\limits_{y \in \Omega} g(x,y)\eta(y)\,\mathrm{d}y}{\int\limits_{y \in \Omega} g(x,y)\,\mathrm{d}y}, \tag{4.4}$$

where $g(x,y)$ is the weighting function

$$g(x,y) = \exp\left(-\frac{\|x-y\|^2}{2l_c^2}\right). \tag{4.5}$$

We refer to this model as the non-local damage formulation [PIJ 87]. The local equivalent strain maps the strain tensor onto a scalar.

Although the non-local formulation is straightforward, it requires the computation of a volume integral for the evaluation of the constitutive behavior at every material point. This makes the numerical implementation both cumbersome and inefficient. In particular, the stiffness matrix is full. Even when truncated, the non-local operator has a negative impact on the sparsity of the matrix. This results in computationally expensive assembly and solution routines. To circumvent these deficiencies, approximations of the integral equation are commonly used.

The non-local equivalent strain [4.4] can be approximated by substitution of a Taylor expansion for the equivalent strain field around the point x

$$\begin{aligned}\eta(y) = \eta|_{y=x} + \left.\frac{\partial\eta}{\partial y_i}\right|_{y=x}(y_i - x_i) + \frac{1}{2}\left.\frac{\partial\eta}{\partial y_i \partial y_j}\right|_{y=x} \\ \times (y_i - x_i)(y_j - x_j) + \mathcal{O}((x_i - y_i)^3). \qquad [4.6]\end{aligned}$$

Assuming the solid volume stretches to infinity leads to the gradient approximation of equation [4.4]

$$\begin{aligned}\bar{\eta}(x) = \eta(x) + \frac{1}{2}l_c^2\frac{\partial^2\eta}{\partial x_i^2}(x) + \frac{1}{8}l_c^4\frac{\partial^4\eta}{\partial x_i^2 \partial x_j^2}(x) \\ + \frac{1}{48}l_c^6\frac{\partial^6\eta}{\partial x_i^2 \partial x_j^2 \partial x_k^2}(x) + \dots. \qquad [4.7]\end{aligned}$$

This gradient approximation is known as the explicit gradient formulation. As an alternative, the implicit gradient formulation (e.g. see [PEE 96]) is obtained by direct manipulation of equation [4.7]

$$\bar{\eta}(x) - \frac{1}{2} l_c^2 \frac{\partial^2 \bar{\eta}}{\partial x_i^2}(x) + \frac{1}{8} l_c^4 \frac{\partial^4 \bar{\eta}}{\partial x_i^2 \partial x_j^2}(x) - \frac{1}{48} l_c^6 \frac{\partial^6 \bar{\eta}}{\partial x_i^2 \partial x_j^2 \partial x_k^2}(x) + \ldots = \eta(x). \qquad [4.8]$$

Because only C^0-continuity is required for the second-order approximation, the corresponding implicit gradient formulation has enjoyed widespread use.

In the remainder of this chapter, we study the convergence of the implicit gradient formulation toward the non-local formulation upon increasing the number of gradient terms involved. If we truncate equation [4.8] after the d derivative, we can rewrite it using a linear operator $\mathcal{L}^d$ as

$$\mathcal{L}^d \bar{\eta}(x) = \eta(x). \qquad [4.9]$$

We restrict ourselves to the second-order ($d = 2$), fourth-order ($d = 4$), and sixth-order ($d = 6$) implicit gradient damage formulations.

4.2.2. *Implicit gradient damage formulation*

In contrast to the non-local and explicit gradient damage formulations, the implicit formulation requires the solution of a boundary-value problem for the non-local equivalent strain field, $\bar{\eta}(x)$, in addition to the usual problem for the displacement field, $u(x)$. In the absence of body forces, the resulting boundary-value problem for the d-order formulation is given by

$$\begin{cases} \left.\begin{array}{l} \frac{\partial \sigma_{ij}}{\partial x_j} = 0 \\ \mathcal{L}^d \bar{\eta} = \eta \end{array}\right. & \forall x \in \Omega \\ \sigma_{ij} n_j = \tilde{t}_i & \forall x \in \partial\Omega_{t_i} \\ \frac{\partial}{\partial x_n}\left(\frac{\partial^\alpha \bar{\eta}}{\partial x_{j\dots}}\right) = 0 & \forall x \in \partial\Omega,\ \alpha \in \{0, \dots, d-2\} \\ u_i = \tilde{u}_i & \forall x \in \partial\Omega_{u_i} \end{cases} \qquad [4.10]$$

where $\tilde{t}$ and $\tilde{u}$ are the prescribed boundary traction and displacements, respectively. Note that we assume that all directional derivatives, $\frac{\partial}{\partial x_n} = n_i \frac{\partial}{\partial x_i}$, of the non-local equivalent strain field are zero on the boundary. We verify this choice numerically by comparing the results with the non-local formulation based on the integral equation [4.4]. The kinematic and constitutive relations [4.1] and [4.2] are used to express the Cauchy stress in terms of the displacement field.

We solve the system [4.10] using the Galerkin method. The same solution spaces are used for the displacement field and non-local equivalent strain field, denoted by $\mathcal{S}_i^u \subset H^{\frac{d}{2}}(\Omega)$ and $\mathcal{S}^{\bar{\eta}} \subset H^{\frac{d}{2}}(\Omega)$, respectively. We denote our trial spaces as $\mathcal{V}_i^u$ and $\mathcal{V}^{\bar{\eta}}$ and assume that $\mathcal{V}^{\bar{\eta}} = \mathcal{S}^{\bar{\eta}}$ and $\mathcal{V}_i^u$ and $\mathcal{S}_i^u$ are the same modulo inhomogeneous boundary conditions. Then the weak form of equation [4.10] is as follows:

$$\begin{cases} \left(\sigma_{ij}, v^u_{(i,j)}\right)_\Omega = \left(\tilde{t}_i, v_i^u\right)_{\partial\Omega} & \forall v_i^u \in \mathcal{V}_i^u \\ \left(\bar{\eta} - \eta, v^{\bar{\eta}}\right)_\Omega + \sum\limits_{\beta=1}^{d/2} \left(\mathcal{H}^\beta \bar{\eta}, \mathcal{H}^\beta v^{\bar{\eta}}\right)_\Omega = 0 & \forall v^{\bar{\eta}} \in \mathcal{V}^{\bar{\eta}} \end{cases} \qquad [4.11]$$

where $v^u_{(i,j)} = \frac{1}{2}\left(\frac{\partial v_i^u}{\partial x_j} + \frac{\partial v_j^u}{\partial x_i}\right)$ and $(\cdot,\cdot)_\Omega$ is the L^2-inner product. No boundary terms appear in the equation for the equivalent strain field, since the derivatives of this field in the direction of the normal vector are assumed zero on the boundary of the domain. For the damage formulations considered in this chapter (i.e. with $d \in \{2, 4, 6\}$), the linear operator $\mathcal{H}^\beta$ is written as

$$\mathcal{H}^1 = \frac{l_c}{\sqrt{2}} \frac{\partial}{\partial x_i}, \quad \mathcal{H}^2 = \frac{l_c^2}{\sqrt{8}} \frac{\partial^2}{\partial x_i \partial x_j}, \quad \mathcal{H}^3 = \frac{l_c^3}{\sqrt{48}} \frac{\partial^3}{\partial x_i \partial x_j \partial x_k}. \tag{4.12}$$

4.3. Isogeometric finite elements

Discretization of the weak formulation [4.11] for the d-order damage formulation requires $(\frac{d}{2} - 1)$-times continuously differentiable basis functions. With isogeometric finite elements C^{p-1}-continuous basis functions can be constructed using splines of order p. We will consider B-splines and non-uniform rational B-splines (NURBS) [ROG 01]. Although T-splines [SED 03] are considered beyond the scope of this chapter, it is emphasized that a unified analysis approach for splines is provided by Bézier extraction [BOR 10].

4.3.1. *Univariate B-splines and NURBS*

The fundamental building block of isogeometric analysis is the univariate B-spline, e.g. [ROG 01] and [COT 09]. A univariate B-spline is a piecewise polynomial defined over a knot vector $\Xi = \{\xi_1, \xi_2, \ldots, \xi_{n+p+1}\}$, with n and p denoting the number and order of basis functions, respectively. The knot values ξ_i are non-decreasing with increasing knot index i, i.e. $\xi_1 \leq \xi_2 \leq \ldots \leq \xi_{n+p+1}$. A partition of the parameter space $[\xi_1, \xi_{n+p+1})$ is provided by the elements

$$\Xi_e = \left[\xi_{\imath(e)}, \xi_{\imath(e)+1}\right) \tag{4.13}$$

where $\imath(e)$ is a map from the element indices to the knot vector indices.

The B-spline basis is defined recursively, starting with the zeroth-order ($p = 0$) functions

$$N_{i,0}(\xi) = \begin{cases} 1, & \xi_i \leq \xi < \xi_{i+1} \\ 0, & \text{otherwise} \end{cases} \qquad [4.14]$$

from which the higher order ($p = 1, 2, \ldots$) basis functions can be constructed using the Cox-de Boor recursion formula [COX 72, BOO 72]

$$N_{i,p}(\xi) = \frac{\xi - \xi_i}{\xi_{i+p} - \xi_i} N_{i,p-1}(\xi) + \frac{\xi_{i+p+1} - \xi}{\xi_{i+p+1} - \xi_{i+1}} N_{i+1,p-1}(\xi). \qquad [4.15]$$

Efficient and robust algorithms exist for the evaluation of these non-negative basis functions and their derivatives, e.g. see [PIE 97]. B-spline basis functions satisfy the partition of unity property and B-spline parameterizations possess the variation diminishing property, e.g. see [FAR 93]. An example of a univariate B-spline basis is shown in Figure 4.2. For notational convenience, we will drop the subscript p of the basis functions.

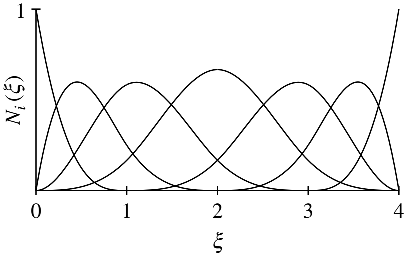

Figure 4.2. *Third-order B-spline basis for the global knot vector* $\Xi = \{0, 0, 0, 0, 1, 2, 3, 4, 4, 4, 4\}$

A B-spline is defined as a linear combination of B-spline basis functions

$$a(\xi) = \sum_{i=1}^{n} N_i(\xi) A_i, \qquad [4.16]$$

where A_i is called a control point or variable. Equation [4.16] is typically used for the parameterization of curves in two (with $X_i \in \mathbb{R}^2$) or three (with $X_i \in \mathbb{R}^3$) dimensions by

$$x(\xi) = \sum_{i=1}^{n} N_i(\xi) X_i. \qquad [4.17]$$

In combination with equation [4.13], this parametric map provides a definition of the elements in the physical space

$$\Omega_e = \{x(\xi),\ \xi \in \Xi_e\}. \qquad [4.18]$$

B-splines used for analysis purposes are generally open B-splines, i.e. the first and the last knot values have a multiplicity of $p + 1$. Dirichlet boundary conditions can be applied to the control points on the boundary of the domain in the same way as done for the nodal variables in traditional finite elements. B-splines can also be refined, which is important in the context of isogeometric analysis, e.g. see [COT 07].

A drawback of B-splines is their inability to exactly represent many objects of engineering interest, such as conic sections. For this reason, NURBS, which are a rational generalization of B-splines, are commonly used. An NURBS is defined as

$$a(\xi) = \sum_{i=1}^{n} R_i(\xi) A_i, \qquad [4.19]$$

with the NURBS basis functions defined as

$$R_\beta(\xi) = \frac{N_\beta(\xi) W_\beta}{w(\xi)}, \qquad [4.20]$$

where $w(\xi) = \sum_{i=1}^{n} N_i(\xi) W_i$ is called the weighting function. Note that in equation [4.20] no summation is performed over the repeated index β. In the special case that $W_i = c\ \forall i \in \{1, \ldots, n\}$, and c an arbitrary constant, the NURBS basis reduces to the B-spline basis.

4.3.2. *Multivariate B-splines and NURBS*

Computational domains in two and three dimensions can be parametrized by means of bivariate and trivariate splines, respectively. An N-variate B-spline is contructed over the tensor product of knot vectors

$$\Xi = \Xi^1 \otimes \ldots \otimes \Xi^N = \left\{\xi_1^1, \ldots, \xi_{n_1+p_1+1}^1\right\} \otimes \ldots \otimes \left\{\xi_1^N, \ldots, \xi_{n_N+p_N+1}^N\right\}. \qquad [4.21]$$

where n_α and p_α are the number of basis functions and the order of the basis functions in the direction α, respectively. The parameter space $[\xi_1^1, \xi_{n_1+p_1+1}^1) \otimes \ldots \otimes [\xi_1^N, \xi_{n_N+p_N+1}^N)$ is partitioned by the elements

$$\Xi_e = \left[\xi_{\imath_1(e)}^1, \xi_{\imath_1(e)+1}^1\right) \otimes \ldots \otimes \left[\xi_{\imath_N(e)}^N, \xi_{\imath_N(e)+1}^N\right), \qquad [4.22]$$

where $\imath_\alpha(e)$ is a map from the element indices to the indices of the knot vector Ξ^α for $\alpha = 1, \ldots, N$.

Multivariate B-spline basis functions $N_i(\xi)$, with parametric coordinate $\xi = (\xi^1, \ldots, \xi^N)$, are defined by the product

$$N_i(\xi) = \prod_{\alpha=1}^{N} N_{\jmath_\alpha(i)}^\alpha(\xi^\alpha), \qquad [4.23]$$

where $\jmath_\alpha(i)$ maps the global control point indices on the indices of the univariate basis functions in the direction α. Multivariate NURBS basis functions are defined by equation [4.20] using a weight vector $W \in \mathbb{R}^n$, where $n = \prod_{\alpha=1}^{N} n_\alpha$ is the number of multivariate basis functions.

Using the multivariate basis functions, an N-variate B-spline is defined by equation [4.19]. When, in addition to a weight vector W, a set of control points $X \in \mathbb{R}^{n\times N}$ is provided, a parameterization of an N-dimensional body Ω is obtained by

$$x(\xi) = \sum_{i=1}^{n} R_i(\xi) X_i. \qquad [4.24]$$

In combination with the partitioning of the multivariate parameter space by the elements Ξ_e in equation [4.22] this parametric map provides the definition of elements Ω_e in the physical space through equation [4.18].

4.3.3. *Isogeometric finite-element discretization*

Let $\mathcal{S}_i^{u,h} \subset \mathcal{S}_i^u$ and $\mathcal{S}^{\bar{\eta},h} \subset \mathcal{S}^{\bar{\eta}}$ be the discrete solution spaces for the displacement field, $u(x)$, and non-local equivalent strain field, $\bar{\eta}(x)$, respectively. In isogeometric analysis, these spaces are written in terms of the NURBS basis functions $R_i(\xi)$ defined in sections 4.3.1 and 4.3.2 for the univariate and multivariate cases, respectively. We can approximate the displacement field and non-local equivalent strain field as

$$\begin{aligned} u_i^h(x) &= \sum_{k=1}^{n} R_k(\xi(x)) U_{ki} \\ \bar{\eta}^h(x) &= \sum_{k=1}^{n} R_k(\xi(x)) H_k \end{aligned} \qquad [4.25]$$

where $U \in \mathbb{R}^{n\times N}$ are the control point displacements, and $H \in \mathbb{R}^n$ are the control point non-local equivalent strains. From the displacement field, the strain, $\varepsilon(x)$, and local equivalent strain, $\eta(x)$, can be computed. In combination with the non-local equivalent strain field, the damage parameter, $\omega(x)$, and Cauchy stress, $\sigma(x)$, can be obtained at every point using the constitutive relations provided in section 4.2.1.

We use the Galerkin method to discretize the weak formulation [4.11] as

$$\begin{cases} \left(\sigma_{ij}, v^{u,h}_{(i,j)}\right)_{\Omega} = \left(\tilde{t}_i, v^{u,h}_i\right)_{\partial\Omega} & \forall v^{u,h}_i \in \mathcal{V}^{u,h}_i \\ \left(\bar{\eta} - \eta, v^{\bar{\eta},h}\right)_{\Omega} + \sum\limits_{\beta=1}^{d/2} \left(\mathcal{H}^{\beta}\bar{\eta}, \mathcal{H}^{\beta} v^{\bar{\eta},h}\right)_{\Omega} = 0 & \forall v^{\bar{\eta},h} \in \mathcal{V}^{\bar{\eta},h} \end{cases} \qquad [4.26]$$

Using the NURBS basis functions, $R_i(\xi)$, as trial functions results in a system of $(N+1)n$ equations

$$\begin{cases} f^{u_m}_{\text{int},k} = f^{u_m}_{\text{ext},k} & \forall (k,m) \in \{1 \ldots n\} \otimes \{1 \ldots N\} \\ f^{\bar{\eta}}_{\text{int},k} = 0 & \forall k \in \{1 \ldots n\} \end{cases} \qquad [4.27]$$

which can be solved for every load step using Newton–Raphson iteration to determine the control point coefficients U_{ki} and H_k in equation [4.25]. The internal force vectors are assembled by looping over the elements

$$\begin{aligned} f^{u_m}_{\text{int},k} &= \mathop{\mathsf{A}}_{e=1}^{n_e} f^{e,u_m}_{\text{int},k} &&= \mathop{\mathsf{A}}_{e=1}^{n_e} \left(\sigma_{ij}, \frac{1}{2}\left(\frac{\partial R_k}{\partial x_j}\delta_{im} + \frac{\partial R_k}{\partial x_i}\delta_{jm}\right)\right)_{\Omega_e} \\ f^{\bar{\eta}}_{\text{int},k} &= \mathop{\mathsf{A}}_{e=1}^{n_e} f^{e,\bar{\eta}}_{\text{int},k} &&= \mathop{\mathsf{A}}_{e=1}^{n_e} \left(\bar{\eta} - \eta, R_k\right)_{\Omega_e} + \sum_{\beta=1}^{d/2} \left(\mathcal{H}^{\beta}\bar{\eta}, \mathcal{H}^{\beta} R_k\right)_{\Omega_e} \end{aligned} \qquad [4.28]$$

The integrals in these expressions are evaluated on the elements Ω_e defined through equation [4.18]. In this contribution, we use the Gaussian quadrature of order $p+1$ in each direction. Numerical integration of NURBS for analysis purposes was studied in [HUG 10] and remains an active topic of research. In order to evaluate the integrals, the Jacobian of the isogeometric map needs to be evaluated at every integration point. Since rational basis functions are used, this requires application of the quotient rule. Since higher order derivatives with respect to the physical coordinate x are used in this contribution, higher order derivatives of the parametric map are also required. These higher order derivatives are obtained by application of the chain rule to the differentiation of the NURBS basis functions with respect to the physical coordinates [COT 09].

The consistent tangent matrix, required by the Newton–Raphson procedure, can be obtained by differentiation of [4.28] with respect to the control point variables in equation [4.25]. Evaluation of the tangent requires the derivatives of the stress, σ, with respect to the strain, ε, and non-local equivalent strain, $\bar{\eta}$. These derivatives are provided through the constitutive behavior elaborated in section 4.2.1. The derivative of the local equivalent strain, η, with respect to the strain tensor follows from the equivalent strain law, $\eta = \eta(\varepsilon)$.

4.4. Numerical simulations

4.4.1. *One-dimensional rod loaded in tension*

We consider a one-dimensional rod loaded in tension, as shown in Figure 4.3. The 10 mm-wide central section of the rod has a reduced cross-sectional area in order to develop a centralized damage zone. The modulus of elasticity of the rod is $E = 20\,\text{GPa}$, and the Cauchy stress is written as $\sigma = (1-\omega)E\varepsilon$. As a damage law, we consider [PEE 96]

$$\omega(\kappa) = \begin{cases} 0, & \kappa \leq \kappa_0 \\ \frac{\kappa_u}{\kappa}\frac{\kappa-\kappa_0}{\kappa_u-\kappa_0}, & \kappa > \kappa_0 \end{cases} \qquad [4.29]$$

with $\kappa_0 = 1 \times 10^{-4}$ and $\kappa_u = 0.0125$. We define the local equivalent strain law as $\eta = \langle\varepsilon\rangle$, where $\langle\cdot\rangle$ is the Macaulay bracket and take the non-local length scale in [4.5] equal to $l_c = \sqrt{2}\,\text{mm}$.

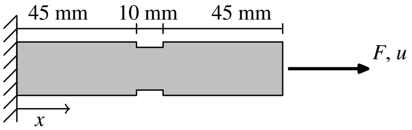

Figure 4.3. *Schematic representation of a one-dimensional rod loaded in tension. The cross-sectional area of the rod is 10* mm^2 *except for the central section where it is equal to 9* mm^2

Force–displacement curves have been determined for the second-, fourth-, and sixth-order implicit gradient models and for the non-local damage formulation. A dissipation-based path-following constraint [VER 09] is used to trace the equilibrium path beyond the snapback point. Mesh convergence studies have been performed using uniform meshes with 80, 160, 320, 640, and 1,280 elements of orders 1, 2, and 3. The control points are equidistantly spaced and all control weights are equal to 1, which leads to a linear parameterization of the domain. An overview of the meshes is given in Table 4.1. Note that in contrast to higher order finite elements, the number of degrees of freedom is practically independent of the order of the basis (since for practical meshes $p \ll n_e$).

Linear B-spline ($p = 1$)

Number of elements, n_e	80	160	320	640	1,280
Number of basis functions, n	81	161	321	641	1,281

Quadratic B-spline ($p = 2$)

Number of elements, n_e	80	160	320	640	1,280
Number of basis functions, n	82	162	322	642	1,282

Cubic B-spline ($p = 3$)

Number of elements, n_e	80	160	320	640	1,280
Number of basis functions, n	83	163	323	643	1,283

Table 4.1. *Meshes used for the uniaxial rod simulation. Note that for this case* $n = n_e + p$

The force–displacement results for the second-order gradient formulation obtained on all meshes are presented in Figure 4.4. Increasing the order of the basis from linear to quadratic significantly improves the rate of convergence. A further increase of the order of the basis to cubics has minor effects on the mesh-convergence behavior. This is explained by the fact that both quadratic and cubic basis functions are unable to accurately represent the solution in the region where loss of ellipticity has occurred. Accurate results for the second-order formulation are obtained using 1,280 elements of any order. Force–displacement results for the fourth-order gradient formulation are shown in Figure 4.5. The presence of fourth-order spatial derivatives in this formulation requires C^1-continuity. For that reason, meaningful results are only obtained on quadratic and cubic meshes. The response obtained on the 1,280-element meshes cannot be visually distinguished from that obtained on the 640-element meshes. A very accurate result is already obtained on the 320-element mesh. The improved convergence behavior of the fourth-order formulation compared to the second-order formulation is attributed to the fact that smoother results are obtained. The increased smoothness of the fourth-order formulations compared to the second-order formulation is closely related to the postponed loss of ellipticity for these formulations, as demonstrated by the dispersion analysis performed in [ASK 00]. Meaningful results for the sixth-order formulation are only obtained on cubic meshes and are shown in Figure 4.6. The convergence behavior of the sixth-order formulation closely resembles that of the fourth-order formulation. In Figure 4.7, we present the results obtained on all meshes for the non-local formulation. Compared to the results obtained using the second-order formulation, the non-local formulation shows superior convergence behavior for the linear, quadratic, and cubic meshes. As expected, the difference in convergence behavior diminishes as the order of the gradient formulation is increased. In fact, the results for the non-local formulation obtained using cubic basis functions can hardly be distinguised from those obtained using the sixth-order formulation (Figure 4.6). For the purpose of comparing the various formulations, the accuracy of the solutions obtained on the 1,280 cubic element meshes suffices. A detailed study of the convergence rates is a topic of future research.

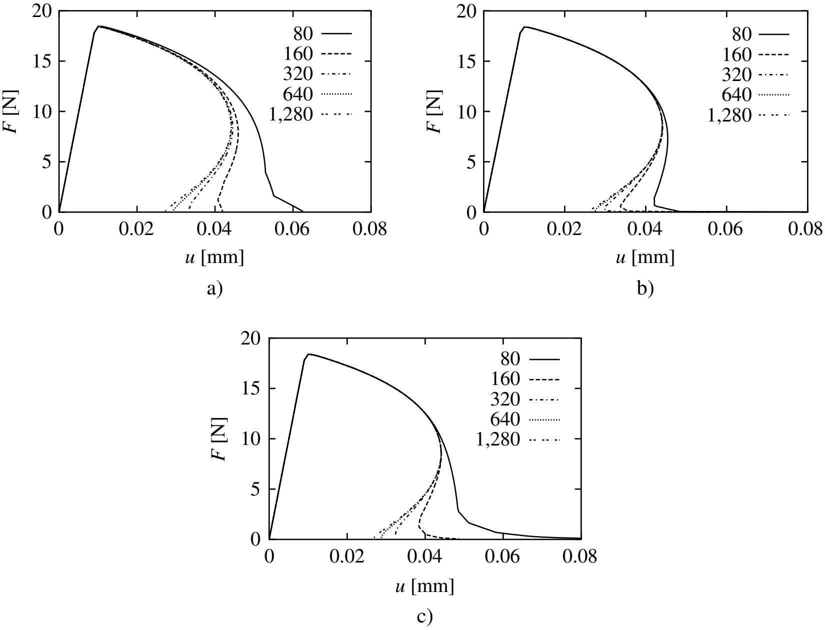

a)

b)

c)

Figure 4.4. *Mesh convergence studies for the rod using the second-order gradient formulation, discretized using linear B-splines (a), quadratic B-splines (b), and cubic B-splines (c). The key labels indicate the number of elements*

In Figure 4.8, we show a comparison of the various formulations. All results are obtained on a mesh with 1,280 cubic elements. The results are in excellent agreement with those reported, e.g. in [PEE 96] and [ASK 00]. As in [ASK 00], it is observed that the incorporation of fourth-order derivatives in the implicit scheme improves the results, in the sense that the obtained force–displacement curve is closer to that of the non-local formulation. Consistent with this observation we find that the sixth-order formulation gives an even better approximation of the non-local result. Similar trends are observed from the final damage profiles (see Figure 4.8). The sixth-order formulation is found to be very efficient since the results are in good agreement with the non-local formulation, while the involved computational effort is very small compared to the non-local formulation. Based on the resemblance of the sixth-order and non-local result it is concluded that, for the considered simulation, ignoring the non-local equivalent strain boundary terms appearing in the gradient formulation has a minor effect on the results.

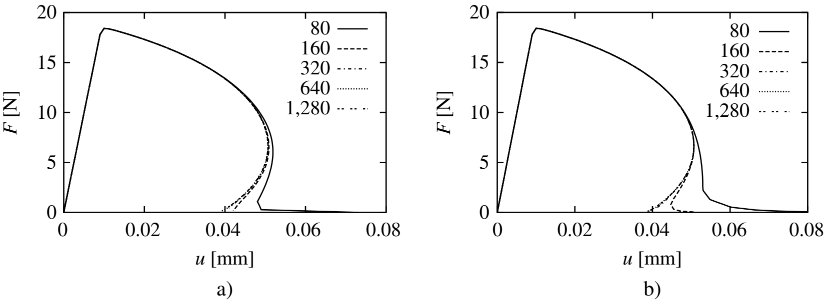

Figure 4.5. *Mesh convergence studies for the rod using the fourth-order gradient formulation, discretized using quadratic B-splines (a) and cubic B-splines (b). The key labels indicate the number of elements*

4.4.2. *Three-point bending beam*

As a second numerical experiment, we consider the three-point bending beam experiment considered in [ASK 00] and shown in Figure 4.10. The $1{,}000 \times 300\,\text{mm}^2$ beam is supported by hinges on the left and right bottom corners, and is loaded by a distributed load $\bar{t}$ over the central 100 mm section of the specimen.

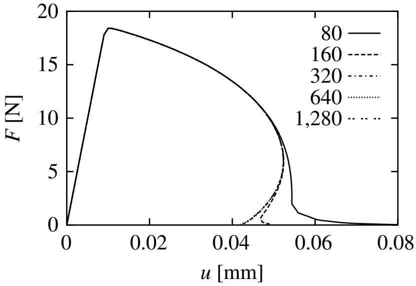

Figure 4.6. *Mesh convergence studies for the rod using the sixth-order gradient formulation, discretized using cubic B-splines. The key labels indicate the number of elements*

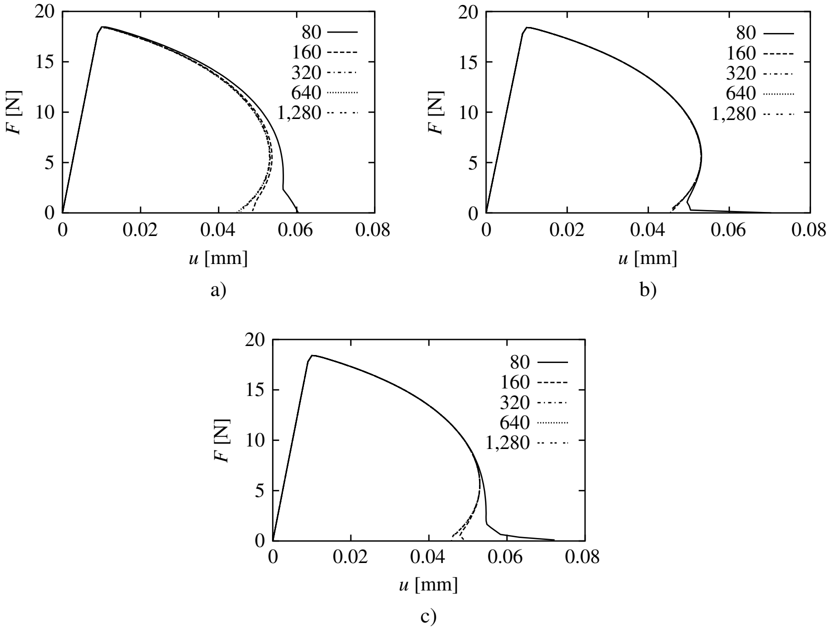

Figure 4.7. *Mesh convergence studies for the rod using the non-local formulation, discretized using linear B-splines (a), quadratic B-splines (b), and cubic B-splines (c). The key labels indicate the number of elements*

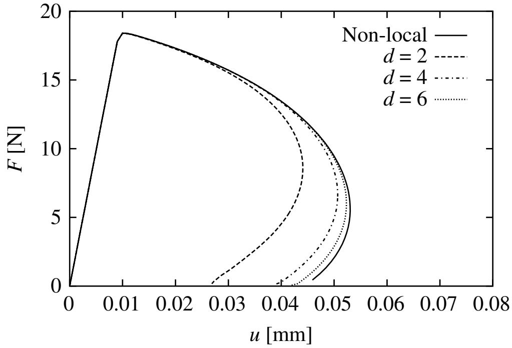

Figure 4.8. *Force–displacement diagrams for the rod loaded in tension using the non-local formulation and d-order gradient formulations. All results are obtained using 1,280 cubic elements*

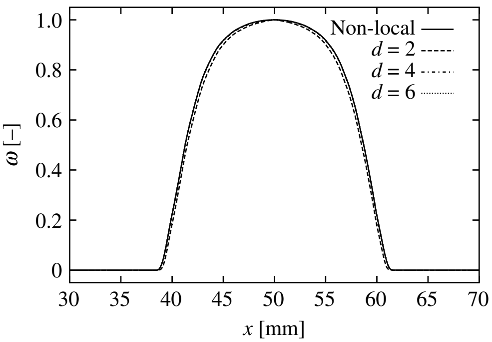

Figure 4.9. *Final damage profile for the rod loaded in tension using the non-local formulation and the d-order gradient formulations. All results are obtained using 1,280 cubic elements*

A linear isotropic material is considered with modulus of elasticity $E = 20\,\text{GPa}$ in the undamaged state and Poisson's ratio $\nu = 0.2$. Plane strain conditions are assumed, and the local equivalent strain is given by

$$\eta(\varepsilon) = \sqrt{\langle\varepsilon_i\rangle^2} = \sqrt{\langle\varepsilon_1\rangle^2 + \langle\varepsilon_2\rangle^2} \qquad [4.30]$$

where ε_1 and ε_2 are the principal strains of the two-dimensional strain tensor. The Macaulay bracket distinguishes the cases of tension and compression. The following damage law, as proposed in [GEE 98], is used:

$$\omega(\kappa) = \begin{cases} 0, & \kappa \leq \kappa_0 \\ 1 - \frac{\kappa_0}{\kappa} \left\{(1-\alpha) + \alpha \exp\left[\beta(\kappa_0 - \kappa)\right]\right\}, & \kappa > \kappa_0 \end{cases} \quad [4.31]$$

with parameters $\kappa_0 = 1 \times 10^{-4}$, $\alpha = 0.99$, and $\beta = 500$. The non-local length scale is taken as $l_c = 20\,\text{mm}$.

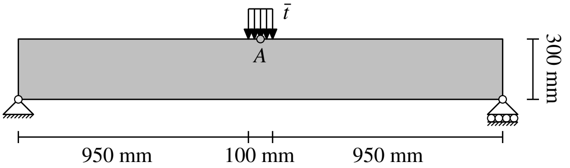

Figure 4.10. *Three-point bending specimen. The thickness of the specimen is 50 mm*

Force–displacement curves are obtained using the meshes shown in Figure 4.11 with linear, quadratic, and cubic basis functions. A summary of the mesh parameters is given in Table 4.2. Note that in two dimensions the number of basis functions is also practically independent of the order of the formulation, in contrast to traditional cubic finite elements. The control point weights are all taken equal to 1, and control points are placed such that a bilinear parameterization of the beam is obtained. The force F is defined as the distributed load $\bar{t}$ times the width to which it is applied. The displacement u is measured by the downward displacement of point A, as indicated in Figure 4.10. This displacement is used as a path-following constraint to trace the equilibrium path.

In Figure 4.12, we show the response curves for the second-order gradient formulation obtained on all meshes. As in the one-dimensional study in section 4.4.1, we see a significant improvement in the convergence rate when using quadratic basis functions instead of linear basis functions. Accurate results are obtained using Mesh 4 with quadratic or cubic basis functions. The results obtained on the quadratic and cubic meshes for the fourth-order formulation are shown in Figure 4.13. For both the quadratic and cubic basis functions, the results obtained on Mesh 4 cannot be visually distinguished from those obtained on Mesh 3. The same holds for the results obtained for the sixth-order formulation, as shown in Figure 4.14. Due to the considerable computational effort required, the mesh-convergence behavior of the non-local formulation is only studied using Meshes 1, 2, and 3. As seen from Figure 4.15, a significant change in the force–displacement curves is observed when comparing the Mesh 2 and Mesh 3 results with linear basis functions. When using quadratic basis function, the response curves cannot be visually distinguished. For the purpose of comparing the various formulations, the result of the non-local formulation obtained on the quadratic Mesh 3 is sufficiently accurate.

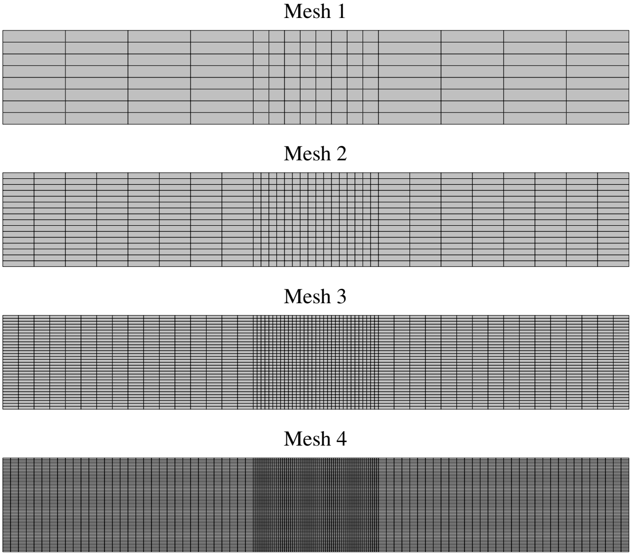

Figure 4.11. *Meshes for the three-point bending specimen*

Linear B-spline ($p = 1$)

	Mesh 1	Mesh 2	Mesh 3	Mesh 4
Number of elements, n_e	128	512	2,048	8,192
Number of basis functions, n	153	561	2,145	8,385

Quadratic B-spline ($p = 2$)

	Mesh 1	Mesh 2	Mesh 3	Mesh 4
Number of elements, n_e	128	512	2,048	8,192
Number of basis functions, n	180	612	2,244	8,580

Cubic B-spline ($p = 3$)

	Mesh 1	Mesh 2	Mesh 3	Mesh 4
Number of elements, n_e	128	512	2,048	8,192
Number of basis functions, n	209	665	2,345	8,777

Table 4.2. *Meshes used for the three-point bending beam. Note that for these meshes* $n = (\sqrt{2n_e} + p)(\sqrt{n_e/2} + p)$

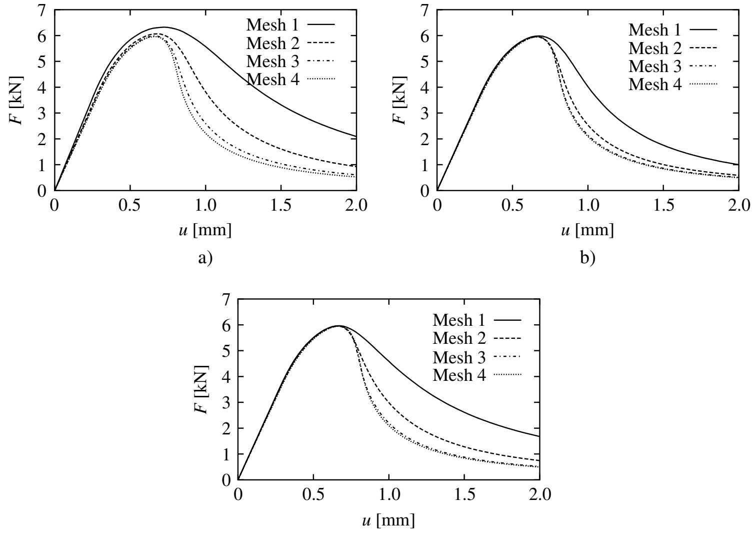

a)

b)

c)

Figure 4.12. *Mesh-convergence studies for the three-point bending beam using the second-order gradient formulation, discretized using linear B-splines (a), quadratic B-splines (b), and cubic B-splines (c)*

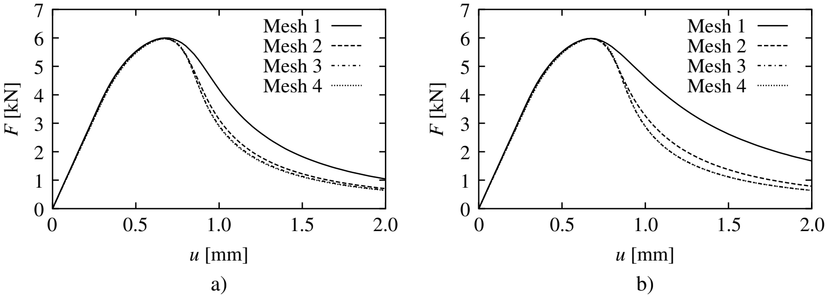

Figure 4.13. *Mesh convergence studies for the three-point bending beam using the fourth-order gradient formulation, discretized using quadratic B-splines (a) and cubic B-splines (b)*

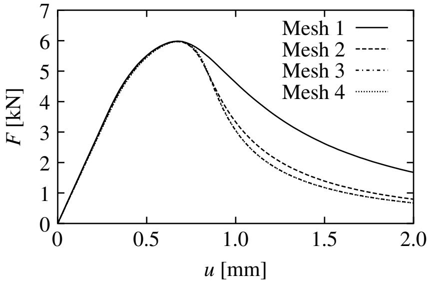

Figure 4.14. *Mesh convergence studies for the three-point bending beam using the sixth-order gradient formulation, discretized using cubic B-splines*

In Figure 4.16 the results of the various formulations are compared. Typical damage profiles are shown in Figure 4.17. Upon increasing the order of the formulation, the approximation of the non-local result is improved. Increasing the order of the formulation increases the total amount of dissipated energy. This is caused by the additional smoothing effect of the higher order derivatives. For the considered problem, the sixth-order formulation is observed to be very efficient, since it accurately approximates the non-local result, whereas the involved computational effort is negligible compared to the non-local formulation. As in the case of the rod simulation, setting all the Neumann boundary conditions [4.10] for the equivalent strain field to zero does not have a significant effect on the results.

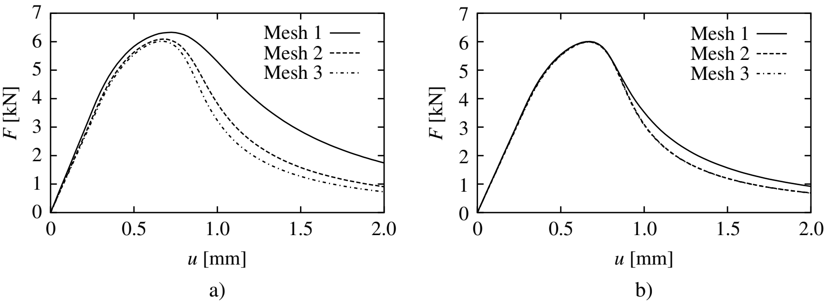

Figure 4.15. *Mesh-convergence studies for the three-point bending beam using the non-local formulation, discretized using linear B-splines (a) and quadratic B-splines (b)*

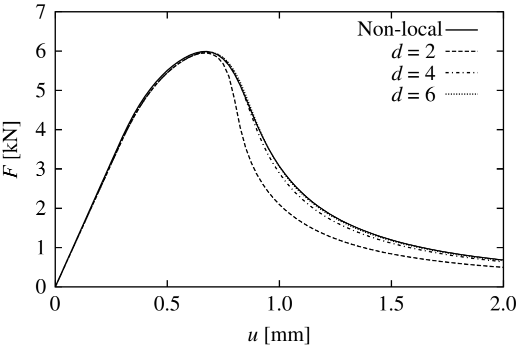

Figure 4.16. *Force–displacement results for the three-point bending beam specimen using the non-local formulation and* d*-order gradient formulations. All results for the gradient formulation are obtained using Mesh 4 with cubic basis functions. The result for the non-local formulation is obtained on Mesh 3 with quadratic basis functions*

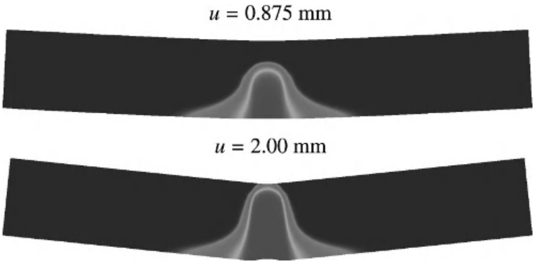

Figure 4.17. *Damage profiles for the three-point bending experiment obtained using the fourth-order gradient formulation. Undamaged material is indicated in dark gray and fully damaged material in medium gray. Deformations are 50 times amplified*

4.5. Conclusions

Isogeometric analysis allows for the construction of smooth basis functions on complex domains, providing an appropriate solution space for higher order differential equations. Dirichlet boundary conditions can be applied by specifying control variables along the boundary, in the same way as nodal variables are specified for traditional finite elements.

Isogeometric analysis is shown to be a very good candidate for the discretization of higher order gradient-damage formulations. Using cubic basis functions allow's us the discretization of the sixth-order gradient damage formulation. Since, from a practical point of view, the number of degrees of freedom is independent of the polynomial order of the basis functions, the fourth- and sixth-order formulations, require only slightly more computational effort than the second-order formulation. This makes it practical to study the convergence of the implicit gradient damage formulation toward the non-local formulation upon increasing its order.

Numerical simulations have been performed for a one-dimensional rod loaded in tension, for which a univariate

B-spline basis is constructed. A two-dimensional three-point bending beam specimen is discretized using a bivariate NURBS patch. For both simulations, it is observed that the result of the non-local formulation is approached upon increasing the order of the gradient damage formulation. Since the computational effort involved in the non-local formulation is much larger than that for the gradient approximations, increasing the order of the gradient formulation yields efficient approximations of the non-local result. For the two simulations considered, the sixth-order formulation gave an accurate approximation.

4.6. Acknowledgments

T. J. R. Hughes and M. A. Scott were partially supported by the ONR Contract N00014-08-0992, T. J. R. Hughes was also partially supported by the National Science Foundation (NSF) Grant 0700204, and M. A. Scott was also partially supported by an ICES CAM Graduate Fellowship. M. J. Borden was supported by Sandia National Laboratories. Sandia is a multiprogram laboratory operated by Sandia Corporation, a Lockheed Martin Company, for the United States Department of Energy's National Nuclear Security Administration under Contract No. DE-AC04-94AL85000.

4.7. Bibliography

[ASK 00] ASKES H., PAMIN J., DE BORST R., "Dispersion analysis and element-free Galerkin solutions of second- and fourth-order gradient-enhanced damage models", *International Journal for Numerical Methods in Engineering*, vol. 49, no. 6, pp. 811–832, 2000.

[BEN 10] BENSON D.J., BAZILEVS Y., DE LUYCKER E., HSU M.C., SCOTT M.A., HUGHES T.J.R., BELYTSCHKO T., “A generalized finite element formulation for arbitrary basis functions: from isogeometric analysis to XFEM”, *International Journal for Numerical Methods in Engineering*, vol. 83, no. 6, pp. 765–785, 2010.

[BOO 72] DE BOOR C., “On calculating with B-splines”, *Journal of Approximation Theory*, vol. 6, no. 1, pp. 50–62, 1972.

[BOR 04] DE BORST R., “Damage, material instabilities, and failure, in chapter 10, *Solids and structures*, vol. 2, *Encyclopedia of Computational Mechanics*”, Wiley, Chichester, pp. 335–373, 2004.

[BOR 10] BORDEN M.J., SCOTT M.A., EVANS J.A., HUGHES T.J.R., “Isogeometric finite element data structures based on Bézier extraction”, *International Journal for Numerical Methods in Engineering*, vol. 87, nos. 1–5, pp. 15–47, 2011.

[BRE 95] BREKELMANS W.A.M., DE VREE J.H.P., “Reduction of mesh sensitivity in continuum damage mechanics”, *Acta Mechanica*, vol. 110, no. 1, pp. 49–56, 1995.

[COT 07] COTTRELL J.A., HUGHES T.J.R., REALI A., “Studies of refinement and continuity in isogeometric structural analysis”, *Computer Methods in Applied Mechanics and Engineering*, vol. 196, nos. 41–44, pp. 4160–4183, 2007.

[COT 09] COTTRELL J.A., HUGHES T.J.R., BAZILEVS Y., *Isogeometric Analysis: Toward Integration of CAD and FEA*, Wiley, Chichester, 2009.

[COX 72] COX M.G., “The numerical evaluation of B-splines”, *IMA Journal of Applied Mathematics*, vol. 10, no. 2, pp. 134–149, 1972.

[FAR 93] FARIN G., *Curves and Surfaces for CAGD*, Academic Press, Inc., 1993.

[GEE 98] GEERS M.G.D., DE BORST R., BREKELMANS W.A.M., PEERLINGS R.H.J., “Strain-based transient-gradient damage model for failure analyses”, *Computer Methods in Applied Mechanics and Engineering*, vol. 160, nos. 1–2, pp. 133–153, 1998.

[GÓM 08] GÓMEZ H., CALO V.M., BAZILEVS Y., HUGHES T.J.R., "Isogeometric analysis of the Cahn-Hilliard phase-field model", *Computer Methods in Applied Mechanics and Engineering*, vol. 197, nos. 49–50, pp. 4333–4352, 2008.

[HUE 94] HUERTA A., PIJAUDIER-CABOT G., "Discretization influence on regularization by two localization limiters", *Journal of Engineering Mechanics*, vol. 120, no. 6, pp. 1198–1218, 1994.

[HUG 05] HUGHES T.J.R., COTTRELL J.A., BAZILEVS Y., "Isogeometric analysis: CAD, finite elements, NURBS, exact geometry and mesh refinement", *Computer Methods in Applied Mechanics and Engineering*, vol. 194, nos. 39–41, pp. 4135–4195, 2005.

[HUG 10] HUGHES T.J.R., REALI A., SANGALLI G., "Efficient quadrature for NURBS-based isogeometric analysis", *Computer Methods in Applied Mechanics and Engineering*, vol. 199, nos. 5–8, pp. 301–313, 2010.

[LEM 90] LEMAITRE J., CHABOCHE J.L., *Mechanics of Solid Materials*, Cambridge University Press, Cambridge, 1990.

[PEE 96] PEERLINGS R.H.J., DE BORST R., BREKELMANS W.A.M., DE VREE J.H.P., "Gradient enhanced damage for quasi-brittle materials", *International Journal for Numerical Methods in Engineering*, vol. 39, no. 19, pp. 3391–3403, 1996.

[PIE 97] PIEGL L., TILLER W., *The NURBS Book*, second edition, Springer-Verlag, Berlin, 1997.

[PIJ 87] PIJAUDIER-CABOT G., BAŽANT Z.P., "Non-local damage theory", *Journal of Engineering Mechanics*, vol. 113, no. 10, pp. 1512–1533, 1987.

[ROG 01] ROGERS D.F., *An Introduction to NURBS*, Academic Press, San Diego, 2001.

[SAK 06] SAKURAI H., "Element-free methods vs. mesh-less CAE", *International Journal of Computational Methods*, vol. 3, no. 4, pp. 445–464, 2006.

[SED 03] SEDERBERG T.W., ZHENG J., BAKENOV A., NASRI A., "T-splines and T-NURCCs", *ACM Transactions on Graphics*, vol. 22, no. 3, pp. 477–484, 2003.

[SLU 94] SLUYS L.J., DE BORST R., "Dispersive properties of gradient-dependent and rate-dependent media", *Mechanics of Materials*, vol. 18, no. 2, pp. 131–149, 1994.

[VER 09] VERHOOSEL C.V., REMMERS J.J.C., GUTIÉRREZ M.A., "A dissipation-based arc-length method for robust simulation of brittle and ductile failure", *International Journal for Numerical Methods in Engineering*, vol. 77, no. 9, pp. 1290–1321, 2009.

[VRE 95] DE VREE J.H.P., BREKELMANS W.A.M., VAN GILS M.A.J., "Comparison of non-local approaches in continuum damage mechanics", *Computers & Structures*, vol. 55, no. 4, pp. 581–588, 1995.

[WIL 84] WILLAM K.J., BICANIC N., STURA S., "Constitutive and computational aspects of strain-softening and localization in solids", *Constitutive Equations: Macro and Computational Aspects*, ASME, p. 233, 1984.

Chapter 5

Macro and Mesoscale Models to Predict Concrete Failure and Size Effects

The prediction of failure in quasi-brittle materials needs enhancement of existing damage models. Existing non-local models are capable of capturing the inception of cracking and sometimes crack propagation in well-defined cases, close to the conditions of their calibration. Changing geometry, e.g. from tensile to bending loads or from unnotched to notched specimens, generally results in the loss of predictive capabilities of the models. The internal length in the non-local model is the parameter that has to be changed from one case to another and there is a consensus that this quantity may not be constant, but should depend on the geometry of the specimen. By geometry, we mean to account for boundary effects, free boundaries existing initially, or evolving boundaries in the course of crack propagation in the

---

Chapter written by David GRÉGOIRE, Peter GRASSL, Laura B. ROJAS-SOLANO and Gilles PIJAUDIER-CABOT.

structure. A general issue is that non-locality ought to evolve in the course of failure in order to achieve a proper description of the continuous–discontinuous transition involved during the crack propagation. In order to investigate such boundary effects, size effect test data have been obtained on three-point bending specimens with different notch lengths. The purpose of this chapter is to examine the capabilities of both continuum-based and discrete models to capture the size effects, and at the same time its evolution for different specimen geometries. Such a comparison has never been performed mainly because the test data did not exist.

5.1. Introduction

Modeling failure in geomaterials, concrete, or other quasi-brittle materials and properly accounting for size, geometry, and boundary effect is still a pending issue. These quasi-brittle materials have the particularity to exhibit a fracture process zone (FPZ) surrounding the crack tip whose size is not negligible (e.g. in concrete the FPZ size is approximately equal to 3–6 times the maximum aggregate size). This is the main reason why linear elastic fracture mechanics does not apply to fracture modeling of such quasi-brittle materials. For geometrically similar structures, the ratio of the size of the FPZ to the size of the structure is not constant and a decrease of the nominal stress with an increase of the structure size is observed. This is commonly called “size effect”, and it is a purely deterministic effect which depends on the geometry of the specimen. Moreover, the FPZ shape and the FPZ size are different if the fracture initiates from a flat boundary (unnotched specimen) or from a notch. On top, the FPZ expansion may be constrained close to a boundary. These two phenomena are usually merged and called “boundary effect”. Size effect and boundary effect are an important engineering issue since (i) most of actual large-scale structural design is based on the identification of material properties at a smaller scale, and (ii) in most instances, cracks initiate from the surface of the specimens where boundary effect exists.

Size effects have been investigated by scientists for years in different contexts and for different materials. The pioneers were Leonardo da Vinci (1452–1519) (tension tests on iron wire), Galileo Galilei (1564–1642) (tension tests on marble columns), and Georges-Louis Leclerc de Buffon (1707–1788) (three-point bending tests on wood), but intensive studies of size effect in quasi-brittle materials started from the middle of the 20th Century. Even recently, experimental tests involving size effect have been carried out on many materials such as concrete [GET 98, KAR 03], mortar [LEB 00], marble [WAN 10], sandstone [VLI 00], brittle ceramic [FIS 02], wood [MOR 11], or polymers [LUN 03], under pure tension, bending, or shear. At the same time, different theories for describing the size effect in quasi-brittle materials have been promoted in the literature, such as the energetic-statistical theory [BAŽ 84, BAŽ 98, MOR 11], the fractal theory [CAR 94], or the Weibull-statistical theory [VLI 00]. There are still active discussions about the domains of validity of these different theories. One of the issues is that most theories provide almost similar results for laboratory tests and very small scale and very large scale experimental results on the same material are quite scarce in the literature.

Numerical modeling of failure of structures made of these quasi-brittle materials is of great interest because it may replace classical large-scale experiments by proper accounting for size and boundary effects. Classical failure constitutive models involve strain softening due to progressive cracking and a regularization technique aimed at avoiding spurious strain and damage localization. Different regularization techniques have been promoted in the literature such as integral-type non-local models [PIJ 87] or gradient damage formulations [PEE 96]. Recently, mesoscale models [VAN 03, GRA 10] have also provided promising results. Macroscale non-local models have been applied on a wide range of problems, including the description of damage and failure in strain-softening quasi-brittle materials [PIJ 87], softening plasticity [TVE 95, BAŽ 02], creep [SAA 89], or composite degradation [GER 07]. Nowadays, most failure models for strain-softening materials involve non-locality, but different authors pointed out that these models still present some inconsistencies when size effects or boundary effects are involved [JIR 04, SIM 04, KRA 09, GRÉ b].

A fundamental element of validation of numerical models is that they should be able to capture size, geometry, and boundary effects. Size effect on a specific geometry, typically on a three-point bending test on geometrically similar notched beams with a fixed notch-to-beam-depth ratio [BAŽ 84, LEB 00, CED 08] usually serves as a basis for the calibration of failure models [LEB 03, CAR 99]. Once the material parameters have been calibrated, validation studies such as the description of size effect on different geometries or the description of boundary effect are quite rare in the literature. One of the reasons is that a well-documented experimental database presenting, for the same material, size effect for different specimen geometries, and thus, different boundary effects at the same time, is missing. Indeed, if experiments involving size effect are abundant in the literature, they are restricted to one specific geometry and barely consider structures made of the same material, with different geometries. Most of the time, the notch-to-depth ratio tends to zero without reaching zero [TAN 96, DUA 06] and unnotched specimens are studied in separate experimental campaigns [BAŽ 96], with different materials compared to size effect tests on notched specimens. Some authors present studies involving both notched and unnotched specimens [KAR 03, BIO 10]. Because such experiments are performed with a view toward the calibration of a specific size effect theory, and not at providing a rather general database, they are not complete in the sense that not all notched configurations are studied with regard to all beam depth configurations.

Section 5.2 is dedicated to the presentation of experiments performed on geometrically similar notched and unnotched specimens made of the same concrete material. Three different geometries have been considered in order to obtain results involving size and boundary effects at the same time. Section 5.2 provides a summary of the experimental procedure and the results, and complete details can be found in [GRÉ a].

Section 5.3 is dedicated to the numerical simulations of these tests by both continuum-based and discrete models. First, the shortcomings of the classical–integral type–non-local damage model, with respect to the description of size and boundary effects are briefly outlined. Then, it is shown how a simple, but well-chosen mesoscale model is able to reproduce both size and boundary effects for experimentally tested configuration, and thus, can be used to further propose new relevant macroscale models.

5.2. Experimental procedure

5.2.1. *Material, specimens and test rig descriptions*

The concrete formulation is based on a ready-mix concrete mixture obtained from Unibéton (www.unibeton.fr) for paving slab applications. The mixture formulation, the gradings of the sand, the aggregates, and the mix are presented in [GRÉ a].

The experiments deal mainly with bending beams of different sizes. All tested beams were made of the same formulation. However, eight batches were needed to manufacture the specimens with a 150-L concrete mixer. After production, the different specimens were stored immersed under water at 20 °C. In order to characterize the material properties of each batch of concrete and to check the global reproducibility, standard compressive tests and splitting (Brazilian) tests were performed following the European standards (EN 12390-1-3-6[1]). For each batch of concrete, 51 standard cylinders (with height to diameter ratio of two) were manufactured in addition to the beams in order to quantify the mechanical properties. Compressive strength, splitting tensile strength, Young's modulus, and Poisson's ratio were thus characterized, and Table 5.1 presents the results in term of mean values, standard deviations, and coefficients of variation (see [GRÉ a] for more details). Material characterization and structural testing were performed at the same age for each batch plus or minus two days and no aging influence was observed.

Compressive strength			Young's modulus			Poisson's ratio			Tensile strength		
μ (MPa)	σ (MPa)	c_v (%)	μ (GPa)	σ (GPa)	c_v (%)	μ	σ	c_v (%)	μ (MPa)	σ (MPa)	c_v (%)
42.3	2.8	6.6	37.0	0.9	2.4	0.21	0.02	8.7	3.9	0.2	6

μ: mean value; σ: standard deviation; $c_v = \mu/\sigma$: coefficient of variation.

Table 5.1. *Concrete mean mechanical properties*

Geometrically similar beams were tested in three-point bending. Four different size configurations were designed with span-to-depth ratio of 2.5, a depth varying between 50 and 400 mm and a constant thickness of 50 mm. In order to capture some boundary effects, three different central edge molded notch configurations[2] were designed. They are labeled:

---

[1] Testing hardened concrete —Part 1, Part 3, and Part 6.

[2] Note that the notch thickness is kept constant (2 mm) irrespective of the specimen depth.

unnotched (notch-to-depth ratio 0), *fifth-notched* (notch-to-depth ratio 0.2), and *half-notched* (notch-to-depth ratio 0.5). For each size and each notched configuration, three concrete beams were manufactured based on the same formulation. Overall, 34 three-point bending tests have been carried out. The different beam specimen geometries are presented in Figure 5.1.

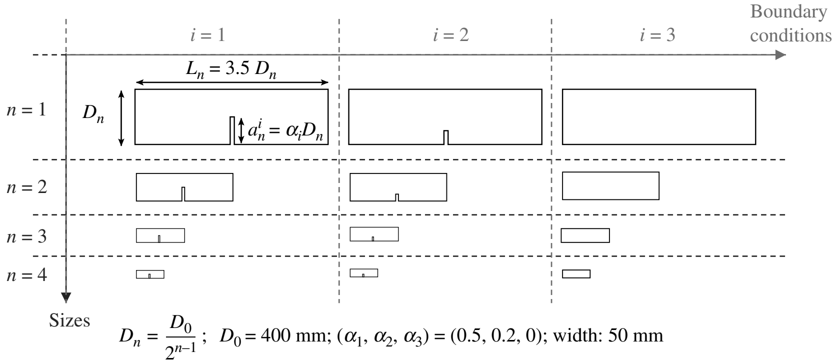

Figure 5.1. *Beam specimen geometries (reproduced from [GRÉ a])*

The testing rig consists of a three-point bending setup mounted on a servo-hydraulic testing machine (HB250, Zwick/Roell). In order to avoid post-peak unstable crack propagation, the three-point bending tests are crack mouth opening displacement (CMOD) controlled. The CMOD measurement consists of recording the distance between two alumina plates stuck on the bottom beam surface on each side of the initial notch. When the beam is unnotched, the alumina plates are stuck at a distance from the middle of the beam equal to half the depth to ensure that the crack initiates between the two plates (see Figure 5.2). Hence, the measurement of the relative distance between the alumina plates is not exactly a CMOD. Still, we will denote in the case of unnotched structures this relative displacement as a CMOD for the sake of simplicity of the presentation. The resulting force is measured by a 50 kN load cell, in addition to the 250 kN load cell available with the machine. The deflection of the neutral axis is measured using a laser sensor with a setup which avoids accounting for the deformation at the supports (similar to that in e.g. [LEB 00]). Additional details (e.g. raw data measurements, sensors uncertainties, etc.) can be found in [GRÉ a].

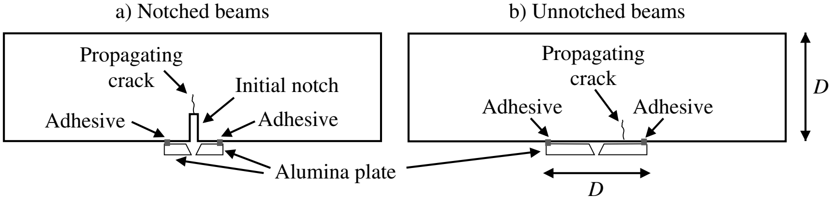

Figure 5.2. *CMOD measurement for (a) notched and (b) unnotched beams (reproduced from [GRÉ a])*

5.2.2. *Experimental results*

5.2.2.1. *Half-notched specimens*

A total of 13 half-notched specimens have been tested (notch-to-depth ratio 0.5 and span-to-depth ratio of 2.5, with depth varying between 50 and 400 mm). A first analysis of size effect consists of estimating the ligament strength for each beam specimen and comparing its value at the peak load. The ligament strength is defined here as the maximum stress in the ligament (beam unnotched part) and is denoted σ_{HN} (see equation [5.1]).

$$\sigma_{HN} = \frac{3}{2}\frac{FS}{bh^2} = \frac{15F}{bD} \qquad [5.1]$$

where F is the load, and $S, b, h,$ and D are, respectively, the span, the width, the ligament height, and the depth of the beam.

Figure 5.3 presents load and maximum stress in the ligament versus the CMOD averaged on all specimens of the same geometry. Figure 5.3a shows that the peak load of geometrically similar specimens is not geometrically similar and Figure 5.3b shows that the ligament strength is dependent of the structure size. Smaller structures are stronger.

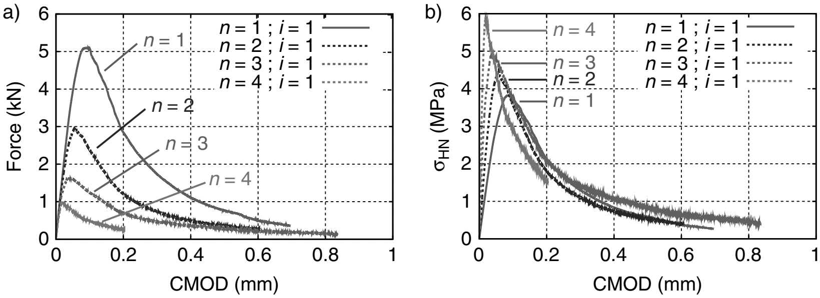

Figure 5.3. *Averaged load (a) and maximum stress in the ligament (b) vs. CMOD (half-notched specimens – reproduced from [GRÉ a])*

5.2.2.2. *Fifth-notched specimens*

A total of 11 fifth-notched specimens have been tested (notch-to-depth ratio 0.2 and span-to-depth ratio of 2.5, with depth varying between 50 and 400 mm). The ligament strength is now denoted σ_{FN} and is given by:

$$\sigma_{FN} = \frac{3}{2}\frac{FS}{bh^2} = \frac{375}{64}\frac{F}{bD} \qquad [5.2]$$

where F is the load, and $S, b, h,$ and D are, respectively, the span, the width, the ligament height, and the depth of the beam.

Figure 5.4 presents load and maximum stress in the ligament versus the CMOD (averaged on all specimens of the same geometry). Figure 5.4a shows that the response of geometrically similar specimen is not geometrically similar and Figure 5.4b shows that the ligament strength is dependent of the structure size.

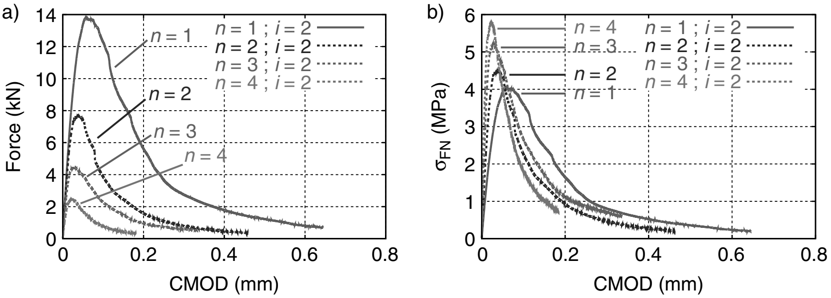

Figure 5.4. *Averaged load (a) and maximum stress in the ligament (b) vs. CMOD (fifth-notched specimens – reproduced from [GRÉ a])*

5.2.2.3. *Unnotched specimens*

A total of 10 unnotched specimens have been tested (span-to-depth ratio of 2.5, depth varying between 50 and 400 mm).

The ligament strength is denoted σ_{UN} and is given by:

$$\sigma_{UN} = \frac{3}{2}\frac{FS}{bh^2} = \frac{15}{4}\frac{F}{bD} \qquad [5.3]$$

where F is the load, and $S, b, h,$ and D are, respectively, the span, the width, the ligament height, and the depth of the beam.

Figure 5.5 presents load and maximum stress in the ligament versus the CMOD averaged on all specimens of the same geometry. Again, size effect is observed. The ligament strength decreases with the structure size.

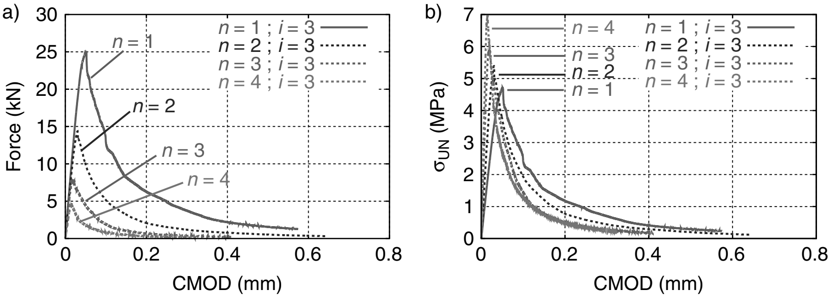

Figure 5.5. *Averaged load (a) and maximum stress in the ligament (b) vs. CMOD (unnotched specimens – reproduced from [GRÉ a])*

5.2.3. *Size effect analysis*

5.2.3.1. *First outcomes*

At first, a simple size effect analysis consists of collecting the ligament strength for each beam specimen. Upon averaging for each geometry and for each size of specimen, the size effect plot in Figure 5.6 is obtained. The abscissa on the figure is the index representing the size of the structure (the larger the index, the smaller the structure) and $i \in \{1, 2, 3\}$ denotes the geometry (see Figure 5.1). As previously noted, the ligament strength decreases as the size of the structure increases. What is more interesting also is that the trends depend on the geometry of the structure and this is due to the boundary effect. Even though the beams are made of the same material, those with deep notches exhibit a slope on the size effect plot in Figure 5.6 which is slightly larger than those with a small notch. Unnotched beam also exhibits a strength which is consistently higher than that of notched beams.

5.2.3.2. *Universal size effect law*

A more detailed analysis using the multifractal scaling law proposed in [CAR 95] and different Bažant's size effect laws (classical, intrinsic, and universal) for notched and unnotched specimens is presented in [GRÉ a].

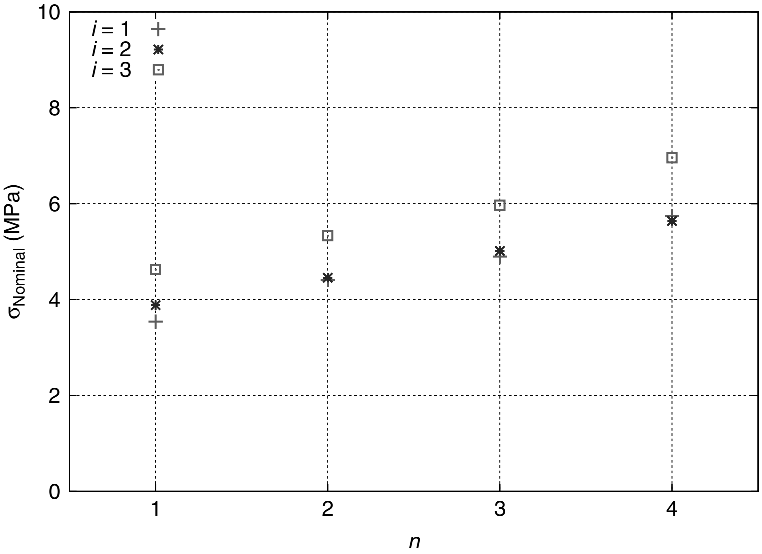

Figure 5.6. *Primary size effect analysis*

A general asymptotic matching formula that satisfies all the asymptotic properties (large size, small size) for both notched and unnotched specimens has been proposed in [BAŽ 97]. This formula is called universal size effect law, and it reads:

$$\sigma_N(D, \alpha_0) = B(\alpha_0) f_t \left[1 + \left(\frac{D}{D_0(\alpha_0)}\right)^r\right]^{-\frac{1}{2r}} \times \left[1 + s\frac{2l_f(\alpha_0)D_0(\alpha_0)}{(2\gamma l_f(\alpha_0) + D)(D_0(\alpha_0) + D)}\right]^{\frac{1}{s}} \quad [5.4]$$

where (r, s) are free parameters (which will be set equal to 1 thereafter), σ_N is the nominal stress, f_t is the tensile strength of the material, D is depth of the beam, B is a dimensionless constant, D_0 is a constant with the dimension of length, and γ is a small positive constant that must be calibrated experimentally (γ is introduced in such a way that the nominal stress is finite for $D \to 0$). Both B and D_0 depend on the fracture properties of the material and on the geometry of the structure (through the shape but not directly the size of the structure). l_f is a length parameter related to the size of the FPZ which is not a constant but generalized as a variable given by:

$$l_f(\alpha_0) = \frac{\langle -g''(\alpha_0)\rangle_+}{4g'(0)}\kappa c_f \qquad [5.5]$$

where $\langle \bullet \rangle_+$ represents the positive part of $\bullet$, c_f is the effective FPZ length, defined in [BAŽ 98] as the distance from the notch tip to the tip of the equivalent crack in a linear elastic fracture mechanics model in an infinitely large specimen, g is a geometric shape function depending on the notch-to-depth ratio α_0, and κ is a parameter which must be calibrated empirically. The details of the analysis presenting all the equations are available in [GRÉ a].

Figure 5.7 presents the comparison between the experimental results presented in section 5.2, and the universal size effect law given in equation [5.4] where (r, s) have been set equal to 1, (f_t, c_f) are equal to the values calibrated from the intrinsic size effect law on notched specimens ($f_t = 3.73$ MPa and $c_f = 36.4$ mm), and γ is chosen equal to the value calibrated from the size effect law on unnotched specimens ($\gamma = 0.74$). Moreover, we choose here to calibrate κ by enforcing the value of l_f corresponding to $\alpha_0 = 0$ for notched specimens to coincide with the one identified from unnotched specimens ($l_{f_0} = 47.8$ mm). Therefore, $\kappa = 4g'(0)l_{f_0}/\langle -g''(0)\rangle_+ c_f$ and

$l_f(\alpha_0) = \langle -g''(\alpha_0)\rangle_+ / \langle -g''(0)\rangle_+ l_{f0}$. The details of the calibrations are available in [GRÉ a].

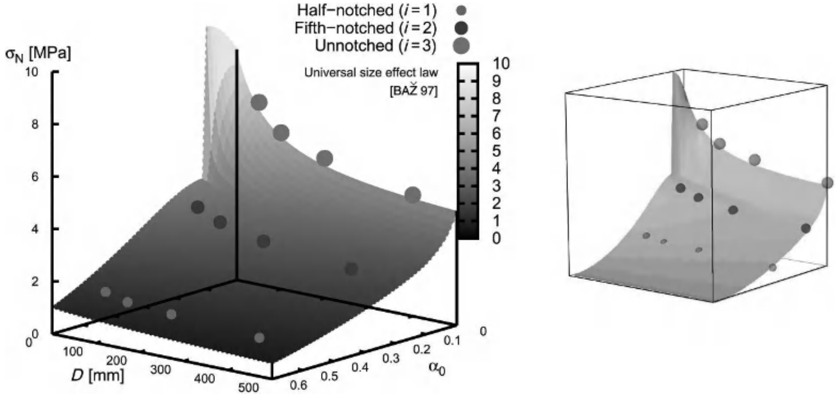

Figure 5.7. *Comparison between experimental results and the Bažant's universal size effect law*

Figure 5.7 shows that the universal size effect law, calibrated from separate intrinsic laws for notched and unnotched specimens (see [GRÉ a] for details), provides a very good fit of the experimental results obtained on the three different geometries at the same time. Formally, a single-notched geometry and an unnotched geometry are sufficient for the calibration of the universal size effect law. Here, we have a redundancy with a second-notched geometry. However, a more challenging issue is to be able to fit the entire load–displacement responses obtained, and possibly to fit continuum models on one geometry and being able to check simulations with experimental data on other geometries. In the following, we illustrate the methodology using a classical non-local macroscopic model and a new mesoscale model.

5.3. Numerical simulations

In this last section, we are going to illustrate how the above experimental results may be useful for assessing constitutive models for failure of concrete. As we will see, shortcomings of the existing macroscale formulation and the efficiency of new mesoscale modeling will be emphasized.

5.3.1. *Macroscale modeling*

5.3.1.1. *Constitutive model*

We are going to consider the classical isotropic scalar damage model. The non-local version of this constitutive relations has been used on many occasions for the numerical simulation of size effect [LEB 03, KRA 09, MAZ 91]. The stress–strain relation is classically given by

$$\sigma = (1 - D)\mathrm{C} : \varepsilon \tag{5.6}$$

where $(\sigma, \varepsilon, \mathrm{C})$ are the stress, strain, and stiffness tensors, respectively, and D is a scalar damage variable which represents the material degradation ($D \in [0, 1]$, $D = 0$ for a virgin material, and $D = 1$ for a completely damage material).

The formulation used in this paper is the integral-type non-local damage models proposed in [PIJ 87]. Damage is a function of the amount of extension in the material, defined locally by the equivalent strain (see equation [5.7]) which is a scalar measure introduced in [MAZ 86]

$$\varepsilon_{eq} = \sqrt{\sum_{i \in [\![1,3]\!]} \langle \varepsilon_k \rangle_+^2} \tag{5.7}$$

where ε_k are the principal strains ($k = 1, 2, 3$) and $\langle \varepsilon_k \rangle_+$ their positive part. The non-local equivalent strain is defined as:

$$\begin{gathered} \bar{\varepsilon}_{eq} = \frac{1}{\Omega_r(x)} \int_\Omega \psi_0(x, \xi) \varepsilon_{eq}(\xi) \mathrm{d}\xi, \quad \Omega_r(x) = \int_\Omega \psi_0(x, \xi) \mathrm{d}\xi \\ \psi_0(x, \xi) = \exp\left(- \left(\frac{2\|x - \xi\|}{l_{c_0}} \right)^2 \right) \end{gathered} \tag{5.8}$$

where Ω is the volume of the structure, Ω_r is a characteristic volume introduced in such a way that the non-local operator does not affect the uniform field, $\bar{\varepsilon}_{eq}$ is the non-local strain, ψ_0 is a Gaussian weight function, and l_{c_0} is the internal length of the non-local continuum which is related to the size of the FPZ.

The evolution of damage (see equation [5.9b]) is a function of the non-local equivalent strain (see equation [5.8]), and it is governed by the Kuhn-Tucker loading–unloading condition (see equation [5.9a]).

$$\Gamma(\varepsilon, h) = \varepsilon_{eq}(\varepsilon) - h, \quad \Gamma(\varepsilon, h) \leq 0, \quad \dot{h} \geq 0, \quad \dot{h}\Gamma(\varepsilon, h) = 0$$
$$h = \max(\varepsilon_{D_0}, \max(\varepsilon_{eq}))$$
[5.9a]

$$D(\varepsilon_{eq}, x) = \sum_{i \in \{t,c\}} \alpha_i \left[1 - (1 - A_i)\frac{\varepsilon_{D0}}{\varepsilon_{eq}(x)} - A_i \exp(-B_i(\varepsilon_{eq} - \varepsilon_{D_0}))\right]$$
$$\alpha_i = \sum_{k \in [\![1,3]\!]} \left(\frac{\varepsilon_k^i \langle \varepsilon_k \rangle_+}{\varepsilon_{eq}^2}\right)^\beta$$
[5.9b]

In equation [5.9a], Γ is the loading function which defines the limit of the elastic (reversible) domain, ε_{D_0} the damage threshold, h is the history variable, the largest ever reached value of the equivalent strain; in equation [5.9b], which defines the kinetics of damage growth, the damage variable is split into two parts to capture the differences of mechanical responses in tension ($i = t$) and in compression ($i = c$), as proposed in [MAZ 86]. (α_t, α_c) are coefficients defined as functions of the principal values of the strain tensors $(\varepsilon^t, \varepsilon^c)$ due to positive and negative stresses, i.e. the strain tensors obtained according to equation [5.6] in which the positive (resp. negative) principal stresses are retained only. Note that in uniaxial tension $(\alpha_t = 1, \alpha_c = 0)$ and $(\alpha_t = 0, \alpha_c = 1)$ in uniaxial compression. $(A_t, B_t, A_c, B_c, \beta)$ are model parameters representing the exponential softening of the material.

5.3.1.2. *Finite-element model and calibration of material properties*

The numerical simulations are performed using the finite element code *Cast3M*. Two-dimensional geometrically similar meshes have been designed for each configuration presented in Figure 5.1. The elements consist of four-node elements with four integration points. Figure 5.8 shows a typical mesh (514 elements) corresponding to the smallest half-notched configuration ($n = 4$, $i = 1$). In order to avoid mesh bias, the element size is kept constant for all specimens in the vicinity of the notch and the future FPZ, with a typical element size of (1×1.25) mm^2. Half of the specimen is meshed, with a symmetry condition. The loads at the three-point bending clamps are distributed along a finite line (5 mm). The numerical tests are CMOD controlled (same as in the experiments) and the notch is 2 mm width which corresponds to one element in each half-specimen meshes.

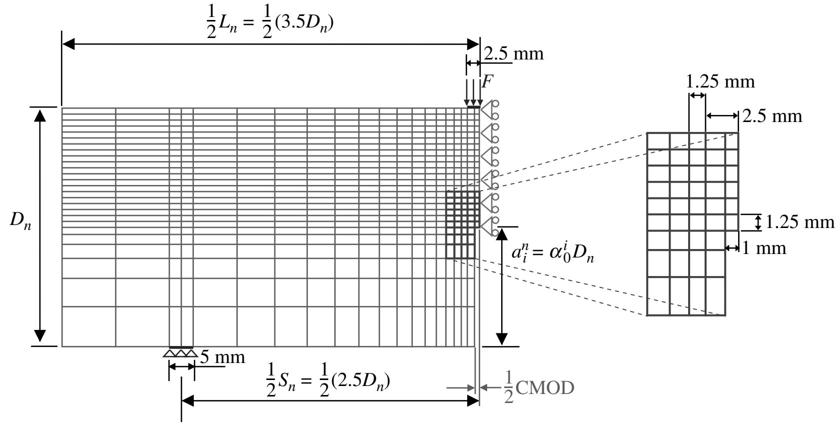

Figure 5.8. *Mesh and boundary conditions ($n = 4$, $i = 1$)*

The Young's modulus and the Poisson's ratio used for the computations are the mean values provided in Table 5.1: $E = 37$ GPa and $\nu = 0.21$. Damage in compression (in the upper part of the bending beams) is not expected; therefore, typical values of the model parameters in compression have been used, making sure that in uniaxial compression, the average compressive strength observed in the experiments is recovered. We obtain, $(\varepsilon_{D_0}, A_c, B_c)$=$(10^{-5}, 1.15, 370)$. Note that the threshold of damage, which is the same in tension and in compression has been obtained from the calibration of the material parameters in tension.

In order to calibrate the model parameters in tension, the procedure outlined in [LEB 03] has been followed. An initial fit of the bending test on a notched specimen ($n = i = 2$) is achieved following a trial-and-error process. The model parameters are adjusted so that a good description of the force versus CMOD curve is achieved, with an emphasis on the peak load since we deal here with size effect. At this step, the internal length in the model is constant, equal to three times the maximum aggregate size [BAŽ 89]. Then, the internal length has been varied until a reasonable fit would be obtained. Note that the sensitivity analysis proposed in [LEB 03] is a guide in this iterative process. We obtain, $(\varepsilon_{D_0}, A_t, B_t, l_{c_0}) = (10^{-5}, 0.75, 7,000, 40\,\mathrm{mm})$.

Figure 5.9 shows the result of the fit on the size effect tests from the fifth-notched specimens.

Obviously, the fit is not perfect. It provides a good description of the peak loads for the middle-size specimens, but the description of the smallest or the largest specimens looses accuracy. It underlines the difficulty of the classical non-local model to capture size effect over a wide range of sizes. Usually, only three different sizes are considered for the calibration. An automatic algorithm as proposed in [LEB 03] and [IAC 06] could have been implemented in order to arrive to a calibration of better quality, but for the purpose of the present illustration, the present fit may be sufficiently accurate.

5.3.1.3. *Capabilities of the identified model to reproduce size effect on other geometries and boundary effect*

Given the model parameters calibrated on one type of geometry, the issue is now to be able to describe size effect for other geometries. Figure 5.10 shows the comparison between the computations and the experiments for all beams depths and geometries in term of nominal strength errors (the experimental data taken as reference come from Figure 5.6). Mean error is also represented by lines. It is clear that the non-local model does not provide a good description of size effect for all geometries. Note that the reverse analysis, i.e. the calibration of model parameters from data on half-notched specimens and then the simulation of tests on fifth notched specimen would exhibit the same deficiency. The worse deviation ($\approx 40\%$) is obtained in the case of simulations on unnotched specimens.

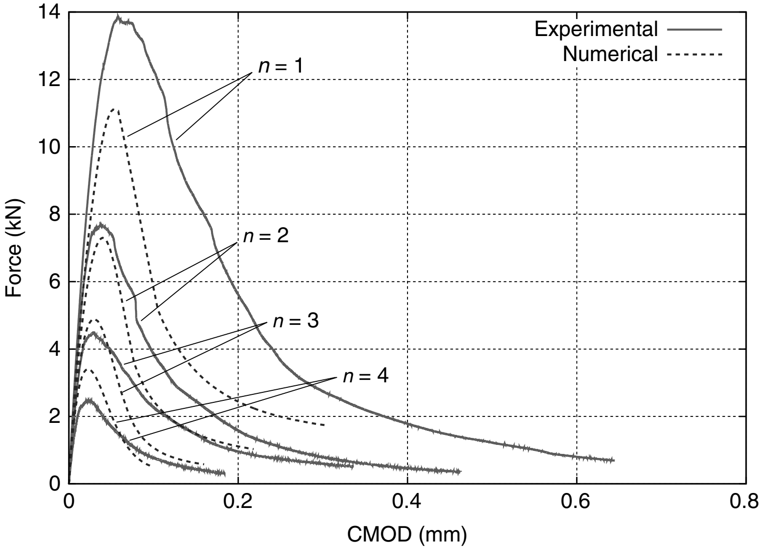

Figure 5.9. *Capabilities of the identified model to reproduce size effect (experimental data are reproduced from Figures 5.3 to 5.5)*

The present computations suggest that the capabilities of the non-local model to describe size effect accurately are limited to data sets from which the model parameters are fitted. This result agrees with the calculation performed in [KRA 09] and calls for a revision of the constitutive model. One way of progress might be a better approval of boundary effect in non-local averaging [GRÉ b].

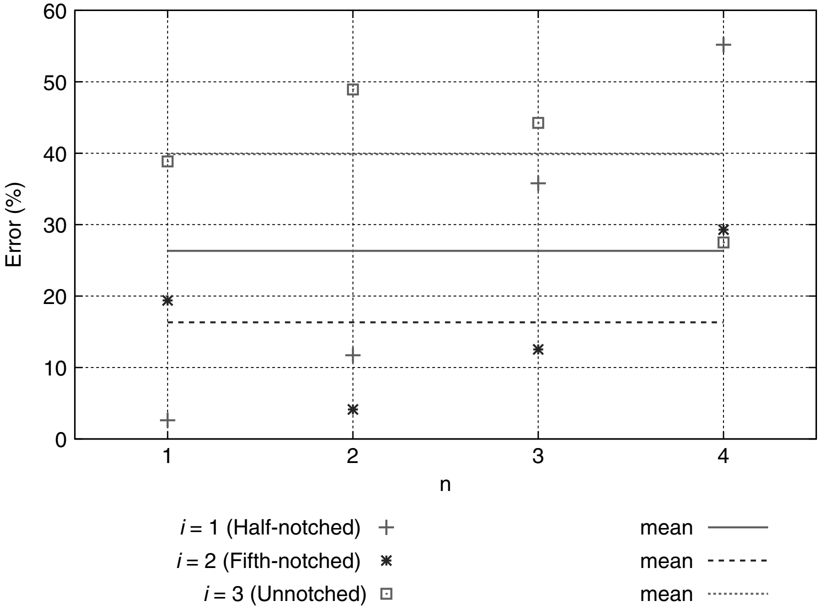

Figure 5.10. *Comparisons between experimental and numerical results in term of nominal strength errors (the experimental data taken as reference come from Figure 5.6)*

5.3.2. *Mesoscale modeling approach*

In recent years, one discrete approach based on a lattice determined by Voronoi tessellation has been shown to be suitable for fracture simulations [BOL 98]. This lattice approach is robust, computationally efficient, and allows for fracture description by a stress–inelastic displacement relationship, similar to continuum models with discontinuities. Therefore, this approach is suitable for modeling interfaces on the mesoscale of concrete. Furthermore, with a specially designed constitutive model, the crack openings obtained with this approach were shown to be independent of the size of the elements [BOL 05]. This type of model is used in the present study. In the lattice framework, the mesostructure of concrete is either idealized by modeling the interaction of two aggregates by a single element [ZUB 87] or by mapping the mesostructure of concrete on the lattice by employing a field of spatially varying material properties [SCH 92]. The latter approach is chosen in the present study, since the finer resolution allows for a detailed description of the tortuosity of crack patterns, which is important for the modeling of the FPZ [GRA 10]. Only a summary of the mesoscale modeling approach is presented here, but more details can be found in [GRA].

The structural response is modeled by a discrete system of structural elements forming a lattice. The nodes of the lattice are randomly located in the domain, subject to the constraint of a minimum distance. The lattice elements are obtained from the edges of the triangles of the Delaunay triangulation of the domain (solid lines in Figure 5.11a), whereby the middle cross-sections of the lattice elements are the edges of the polygons of the dual Voronoi tessellations (dashed lines in Figure 5.11a). For the discretely modeled aggregates, the lattice nodes are placed at special locations, such that the middle cross-sections of the lattice elements form the boundaries between aggregates and mortar [BOL 04] (Figure 5.11b). Each lattice node possesses three degrees of freedom, namely two translations and one rotation. Heterogeneous materials are characterized by spatially varying material properties. In the present work, this is reflected at two levels. Aggregates with diameters greater than $\phi_{\min}$ are modeled directly. The aggregates are placed randomly within the domain to be analyzed, avoiding overlap of aggregates. The heterogeneity represented by finer particles is described by autocorrelated random fields of tensile strength and fracture energy, which are assumed to be fully correlated. The random fields are characterized by an autocorrelation length that is independent of the spacing of lattice nodes [GRA 09].

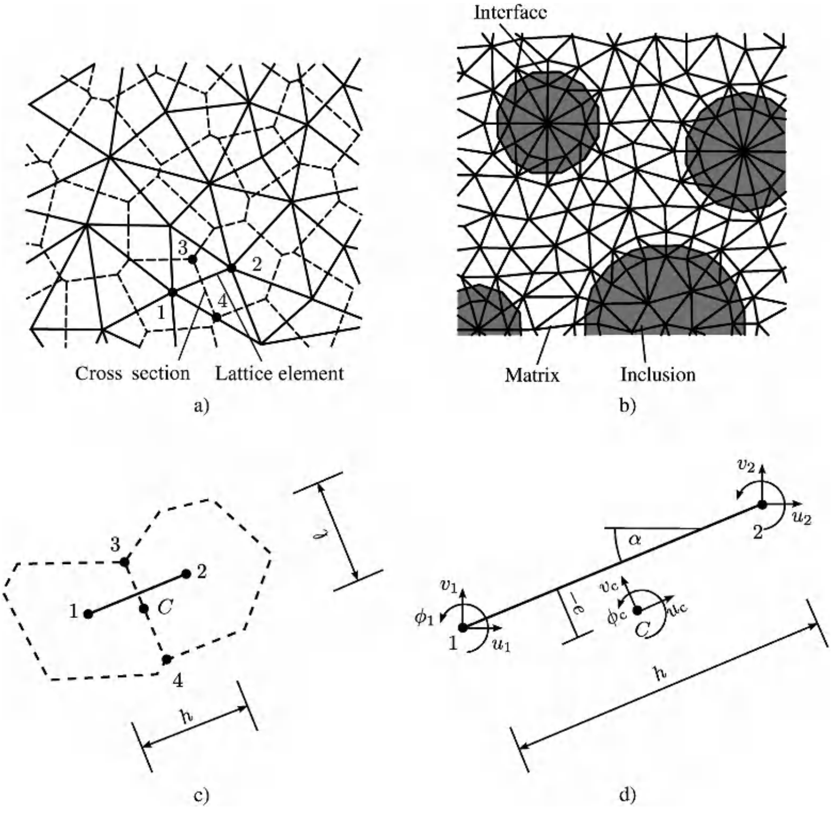

Figure 5.11. *(a) Set of lattice elements (solid lines) with middle cross-sections (dashed lines) obtained from the Voronoi tessellation of the domain, (b) arrangement of lattice elements around inclusions. (c) and (d) Lattice element in the global coordinate system*

The constitutive response for the individual phases can either be described by micromechanics or phenomenological constitutive models, commonly based on the theory of plasticity, damage mechanics, or a combination of the two. For predominantly tensile loading, an isotropic damage model has been shown to provide satisfactory results [GRA 10]. Such a model is used in the present study. The crack openings obtained with this constitutive model are independent of the length of the element, which has been shown for a very similar constitutive model in [GRA 10].

5.3.3. *Analysis of three-point bending tests*

In this section, the geometry, loading setup, and results of mesoscale analyses of notched and unnotched three-point bending tests are described. The numerical geometries are not exactly the same as the ones used during the experiments reported in section 5.2 (the spans are different). However, the numerical analyses remain valid and these first results are shown here to highlight how mesoscale analyses may help to propose a better macroscale modeling of the failure and the damage evolution in quasi-brittle materials. A complete comparison between experimental and mesoscale results with the exact same geometries is reported in [GRA].

5.3.3.1. *Load–CMOD curves*

A schematic drawing of the geometries of notched and unnotched beams is shown in Figures 5.12a and 5.12b. Four beam depths $d = 50$, 100, 200, and 400 m, and three notch lengths $a = 0$, $0.2 \times d$, and $0.5 \times d$ were considered. For the different sizes, all dimensions were scaled proportionally to the beam depth, except the out-of-plane thickness, which was kept constant for all sizes at $t = 0.05$ m, see section 5.2 and [GRÉ a] for more details. In the analyses, a zero notch thickness was assumed, which idealizes the experimental procedure in which a thin metal plate of constant thickness was used to cast the notch. The load and support reactions were applied by support plates with a width of 50 mm. The width of the plates was kept constant for all the sizes. Only the middle parts of the beams were modeled using the mesoscale approach (Figures 5.12a and 5.12b). The remaining parts of the beam were modeled by elastic properties describing the average of the elastic response of matrix, aggregate and interfacial transition zone of composite in the mesoscale region. The aggregate volume fraction was chosen as $\rho = 0.3$ with a maximum and minimum aggregate diameter of $\phi_{\mathrm{max}} = 10$ mm and $\phi_{\mathrm{min}} = 5$ mm, respectively. The approach to generate the distribution of aggregate diameters is described in [GRA 08]. Furthermore, the random field was characterized by the autocorrelation length $l_{\mathrm{a}} = 1$ mm and the coefficient of variation $c_{\mathrm{v}} = 0.2$. For more information on the generation of random fields and the definition of l_{a}, see [GRA 09]. For the random placement of the aggregates, a trial-and-error approach is chosen so that overlap of aggregates is avoided. Overlap with specimen boundaries and the notch are allowed. These values were determined by inverse analysis using a constant ratio of the stiffnesses for matrix and aggregate and strengths for matrix and interfacial transition zones of two, which are in the range of experimental results reported in [HSU 63] and [MIE 97].

The analyses were controlled by the CMOD, which is the relative horizontal displacement of the points A and B shown in Figure 5.12. For the notched specimens ($a = 0.2$ and 0.5), the points were located at the end of the notch. For the unnotched specimen ($a = 0$), the two points were apart a distance d, since the location of the FPZ initiating from the surface was indeterminate. The CMOD was increased incrementally up to complete failure of the specimen, which, in the present analyses, was defined as a residual load of less than 1/100 of the peak value. For the unnotched specimen, for which the region in which the mesoscale model is applied is smaller than the depth of the beam ($d = 200$ and 400 mm) the analyses were stopped shortly after the peak.

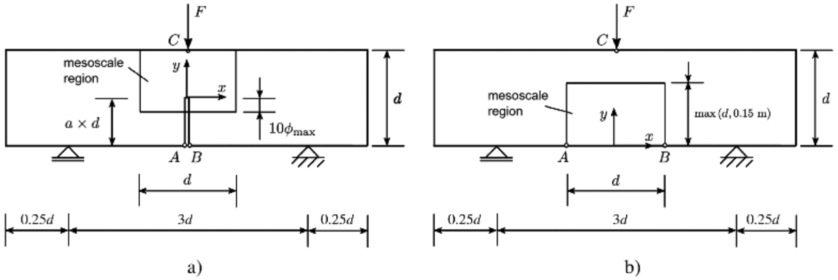

Figure 5.12. *Geometries of three-point bending tests for (a) notched case and (b) unnotched case*

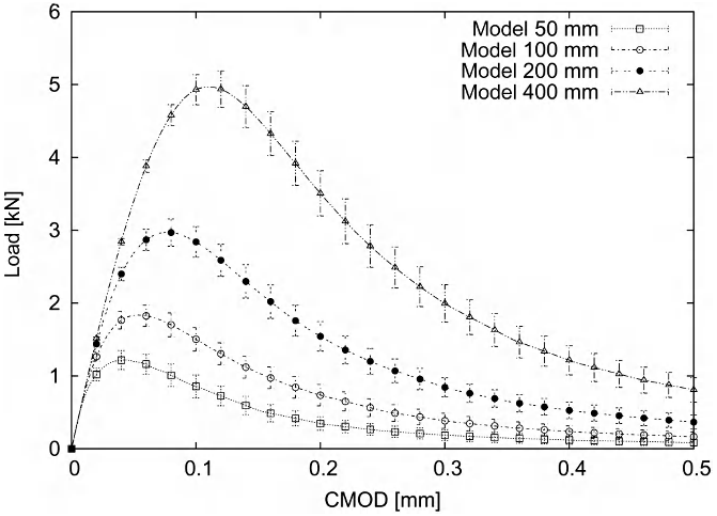

Figure 5.13. *Load versus CMOD for the beams with the long notch ($a = 0.5$) and four sizes $d = 50$, 100, 200, and 400 mm. Error bars of the numerical results show the mean plus and minus one standard deviation*

The load–CMOD curves obtained in the analyses for long-notched, short-notched, and unnotched beams for the four sizes are presented in Figures 5.13–5.15, respectively. The load–CMOD curves presented are averages of 100 analyses with random mesostructures and autocorrelated fields. The error bars indicate the +/− standard deviation obtained in the mesoscale analyses.

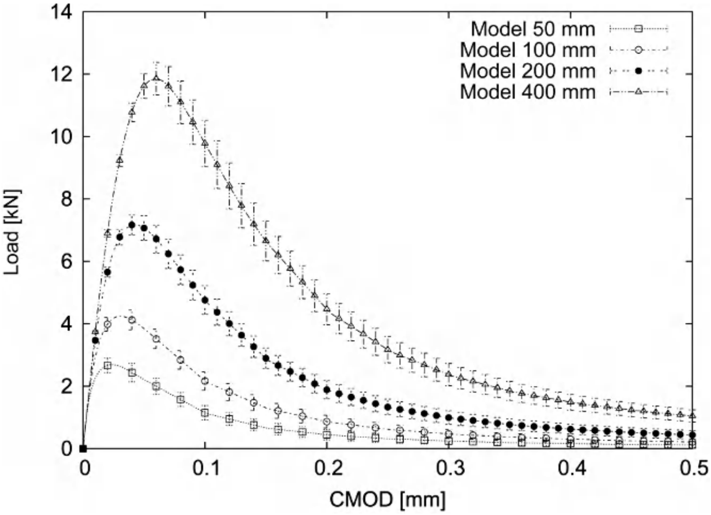

Figure 5.14. *Load vs. CMOD for the beams with the short notch ($a = 0.2$) and four sizes $d = 50$, 100, 200, and 400 mm. Error bars of the numerical results show the mean plus and minus one standard deviation*

5.3.3.2. *Size effect analysis*

The same size effect analysis presented in section 5.2.3.2 for the experimental results is presented here for the numerical results at the mesoscale.

Figure 5.16 presents the comparison between the mesoscale results presented in section 5.3.3.1 and the universal size effect law given in equation [5.4]. A similar calibration of the one presented in section 5.2.3.2 for the experimental results is performed even if the calibrated parameters cannot be directly compared with the experimental ones since the beam span is not the same. The following calibrated parameters are obtained for the mesoscale results: $(r, s, f_t, c_f, \gamma, l_{f0}) = (1, 1, 6.38\ \text{MPa}, 11.1\ \text{mm}, 0.95, 28.3\ \text{mm})$.

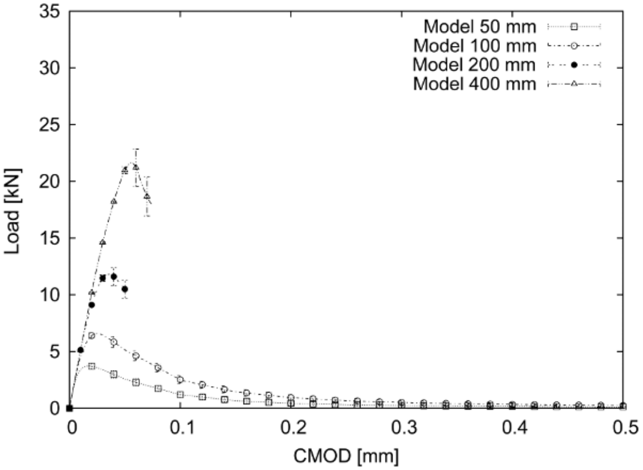

Figure 5.15. *Load versus CMOD for the beams without notch ($a = 0$) and four sizes $d = 50$, 100, 200, and 400 mm. Error bars of the numerical results show the mean plus and minus one standard deviation*

Figure 5.16 shows that the mesoscale model is able to properly represent size effect for different notched specimens with different notch-to-depth ratios, but it provides limited results concerning unnotched specimens. It means that we are still not able to fit parameters on one notched geometry and then predict relevant results on unnotched geometries. Even if these mesoscale results are still preliminary results and if we can expect a better predictability with a model calibrated on the exact experimental geometry (same span-to-depth ratio), modeling properly boundary effects with relevant predictability is still a outstanding issue. However, a huge advantage of such mesoscale modeling is the information it can provide concerning the damage patterns and the spatial distributions of dissipated energy densities. This information is very useful in order to imagine new macroscale models able to properly represent both size effect and boundary effect during quasi-brittle failure.

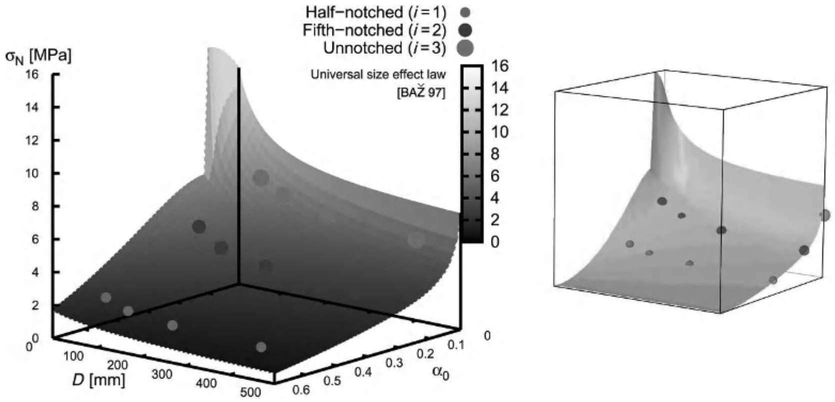

Figure 5.16. *Comparison between mesoscale results and the Bažant's universal size effect law*

5.3.3.3. *Damage patterns and spatial distributions of dissipated energy densities*

In addition to the global results in the form of load–CMOD curves, local results such as damage patterns and spatial distributions of dissipated energy densities were studied. First, the procedure to determine these results are illustrated for the largest specimen with the long notch ($a = 0.5$, $d = 400$ mm). Then selected distributions of dissipated energy densities are compared for different beam sizes and boundary conditions.

In the nonlinear analyses, the fracture process is modeled by damage in the lattice elements. The evolution of the resulting damage patterns was studied for the long notch beam at peak. The resulting damage patterns are shown in Figure 5.17, for three random analyses at peak.

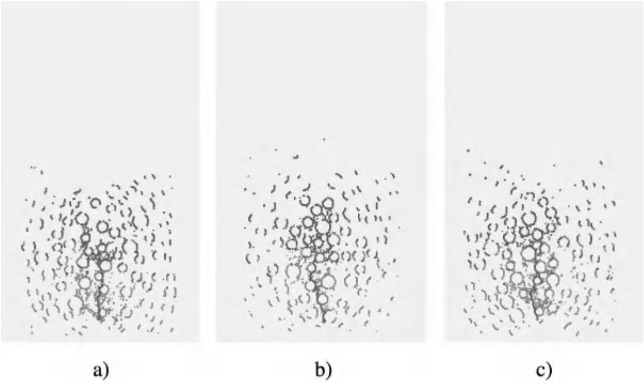

Figure 5.17. *Damage patterns for the largest beam* $d = 400$ *mm with the long notch (*$a = 0.5$*) at peak for three random analyses. Dark gray lines indicate middle cross-sections with increasing damage at this stage. Light gray lines indicate middle cross-sections of damaged elements, in which damage does not increase at this stage*

Dark gray lines mark the middle cross-sections of elements in which damage increases at this step of the analysis. On the other hand, gray lines indicate middle cross-sections of elements in which damage increased at an earlier stage of analyses, but did not increase at this stage. From the damage patterns, it can be seen that the FPZ obtained from the analyses consists of a localized tortuous row of cross-sections of elements, in which damage increases. The location of this row of damaged elements differs considerably for the three random analyses. To be able to compare the local results of beams of different sizes and geometries, it is required to average the response of the random analyses. On the other hand, dissipated energy, which can be integrated and averaged, is a physical quantity that is independent of the choice of model. Therefore, this quantity is used to analyze the results further. The increment of dissipated energy in a lattice element of length h was calculated as

$$\Delta D_{\mathrm{d}} = \Delta\omega A h \frac{1}{2} \boldsymbol{\varepsilon} \mathbf{D} \boldsymbol{\varepsilon} \qquad [5.10]$$

where $\Delta\omega$ is the increment of the damage parameter. This expression is a good approximation of the rate of dissipated energy, if the increment of damage is very small. Therefore, subincrementation was applied for the evaluation of the dissipated energy, so that the accuracy of the computed value is independent of the CMOD increments used to control the analysis. For the averaging of dissipated energy, the domain to be analyzed was discretized by a square grid, with a cell size of 3.125 mm, which is greater than $d_{\mathrm{min}} = 1$ mm used to determine the length of lattice elements. For this grid, the locations of the mid cross-section of lattice elements determine the amount of energy that is dissipated in the cells. If a mid cross-section of an element is located in multiple cells, the energy is allocated in proportion to the section of the mid cross-section that is located in each cell. In the next step, the energy density of a cell is determined as the sum of energy divided by the cell area. The spatial distributions of dissipated energy densities for the increment of CMOD can be estimated for each interesting step (peak or post-peak) and for all the random analysis. This spatial distribution of dissipated energy density represents the FPZ at this stage of analysis. Such spatial distributions, detailed in [GRA], show that the majority of energy is dissipated in a localized region, which is tortuous. This has already been observed by studying the damage patterns in Figure 5.17. Similar results have been reported in [CED 87, PLA 93, NIR 92], and [BOL 93].

To be able to compare the distribution of dissipated energy densities for different sizes and geometries, the results of 100 random analyses were averaged for the same increment of CMOD at peak (Figure 5.18). The CMOD increment was chosen so that the mean dissipated energy increment is equal to 0.23 J/m. This average dissipated energy density is distributed over a wider zone compared to the densities of the individual random zones, whereby the width of the average distribution is mainly determined by the tortuosity of the FPZ of individual analyses.

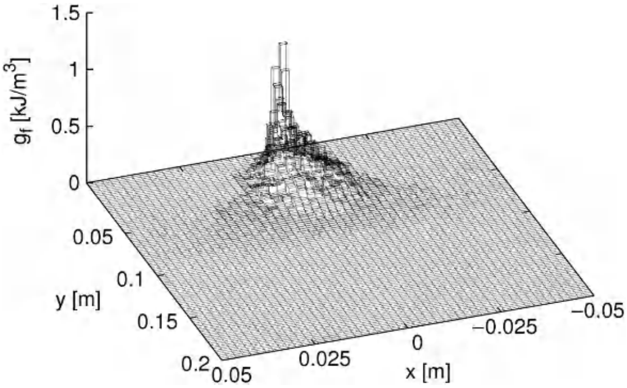

Figure 5.18. *Mean of dissipated energy densities of 100 random analyses for the largest beam $d = 400$ mm with the long notch ($a = 0.5$) at peak*

This strategy for determining the FPZ by averaging the spatially distributed rate of dissipation has been developed recently in [JIR 07] and [GRA 10]. In Figure 5.18, the average density distributions for CMOD increments at peak is shown. These plots of the spatial distributed energy are suitable to illustrate the FPZ for one specimen and stage at a time. However, for comparing quantitatively the results for different steps and geometries, it is suitable to reduce the dimensions of the plots. Therefore, the FPZs were also presented by the distribution of dissipated energy in the x- and y-direction only. These one-dimensional distributions are obtained by integrating the dissipated energy density in the opposite direction and can be found in [GRA].

5.4. Conclusions

An experimental campaign of three-point bending fracture tests exhibiting size effect and boundary effect for geometrically similar half-notched, fifth-notched, and unnotched specimens made of the same concrete material has been presented. The classical results of structural size effect theory are highlighted, smaller structures are stronger. The response of geometrically similar specimens is not geometrically similar and the nominal stress depends on the structure size. Moreover, it has been noted that the response of notched and unnotched specimens is quite different.

This database composed of three-point bending tests provides force versus CMOD results for different initial notch lengths, and thus, different geometries and boundary conditions at the onset of cracking. Such comparisons involving different initial lengths are precious in order to validate the relevance of size effect theories as well as to test the capabilities of constitutive models for quasi-brittle fracture on different geometries.

These experimental results have been compared with numerical simulations performed using integral-type non-local models. Results illustrate the shortcomings of the classical non-local integral formulation. The model fails to describe size effect over the investigated range of geometries and sizes. This analysis, which ought to be extended to other existing (and probably more advanced) constitutive models indicates that there is a definite need for further investigations and enhancements of constitutive models in order to achieve a better description of geometry and size effect on structural failure.

Mesoscale analyses have also been performed on similar geometries in order to better understand how damage evolves during quasi-brittle failure. The width of the FPZ does not depend on the size of the specimen for the specimen with a notch. For the unnotched specimens, the greater the specimen size, the wider the FPZ. The length of dissipated energy along the ligament length depends on the size of the specimens. The greater the specimen size, the longer the region of dissipated energy is. There is no influence of the boundary type on the distribution of the dissipated energy along the ligament length for beams with the same ligament length. However, the width of the FPZ differs for notched and unnotched beams of the same ligament length.

The observations made in the present study will be used to develop non-local models which describe the FPZ. However, the modeling techniques used in the present study are based on many simplifications. Therefore, additional experiments should be carried out to verify, at least qualitatively, the results presented here.

5.5. Acknowledgments

This work was sponsored by the *ERC advanced grant Failflow (27769)*. This financial support is gratefully acknowledged. The macroscale analyses were performed with the finite-element code *Cast3M* (www-cast3m.cea.fr). The mesoscale analyses were performed with the finite element package OOFEM [PAT 99, PAT 01].

5.6. Bibliography

[BAŽ 84] BAŽANT Z., “Size effect in blunt fracture: concrete, rock, metal”, *Journal of Engineering Mechanics*, vol. 110, no. 4, pp. 518–535, 1984.

[BAŽ 89] BAŽANT Z., PIJAUDIER-CABOT G., “Measurement of characteristic length of nonlocal continuum”, *Journal of Engineering Mechanics*, vol. 115, no. 4, pp. 755–767, 1989.

[BAŽ 96] BAŽANT Z.P., LI Z., "Zero-brittleness size-effect method for one-size fracture test of concrete_JEngMech_1996.pdf", *Journal of Engineering Mechanics*, vol. 122, no. 5, pp. 458–468, 1996.

[BAŽ 97] BAŽANT Z., "Scaling of quasibrittle fracture: asymptotic analysis", *International Journal of Fracture*, Springer, vol. 83, no. 1, pp. 19–40, 1997.

[BAŽ 98] BAŽANT Z., PLANAS J., *Fracture and Size Effect in Concrete and Other Quasibrittle Materials*, CRC, 1998.

[BAŽ 02] BAŽANT Z., JIRÁSEK M., "Nonlocal integral formulations of plasticity and damage: survey of progress", *Journal of Engineering Mechanics*, ASCE, vol. 128, p. 1119, 2002.

[BIO 10] BIOLZI L., LABUZ J., MUCIACCIA G., "A problem of scaling in fracture of damaged rock", *International Journal of Rock Mechanics and Mining Sciences*, Elsevier, vol. 48, no. 3, pp. 451–457, 2010.

[BOL 93] BOLANDER J., HIKOSAKA H., SHIRAISHI T., "The effects of strain gradient on concrete tensile fracture", *Memoirs of the Faculty of Engineering, Kyushu University*, vol. 53, pp. 103–119, 1993.

[BOL 98] BOLANDER J.E., SAITO S., "Fracture analysis using spring networks with random geometry", *Engineering Fracture Mechanics*, vol. 61, pp. 569–591, 1998.

[BOL 04] BOLANDER J.E., BERTON S., "Simulation of shrinkage induced cracking in cement composite overlays", *Cement and Concrete Composites*, vol. 26, pp. 861–871, 2004.

[BOL 05] BOLANDER J.E., SUKUMAR N., "Irregular lattice model for quasistatic crack propagation", *Physical Review B*, vol. 71, 2005.

[CAR 94] CARPINTERI A., "Fractal nature of material microstructure and size effects on apparent mechanical properties", *Mechanics of Materials*, Elsevier, vol. 18, no. 2, pp. 89–101, 1994.

[CAR 95] CARPINTERI A., CHIAIA B., FERRO G., “Size effects on nominal tensile strength of concrete structures: multifractality of material ligaments and dimensional transition from order to disorder”, *Materials and Structures*, Springer, vol. 28, no. 6, pp. 311–317, 1995.

[CAR 99] CARMELIET J., “Optimal estimation of gradient damage parameters from localization phenomena in quasi-brittle materials”, *Mechanics of Cohesive-frictional Materials*, Wiley Online Library, vol. 4, no. 1, pp. 1–16, 1999.

[CED 87] CEDOLIN L., POLI S.D., IORI I., “Tensile behavior of concrete”, *Journal of Engineering Mechanics*, vol. 113, no. 3, pp. 431–449, 1987.

[CED 08] CEDOLIN L., “Identification of concrete fracture parameters through size effect experiments”, *Cement and Concrete Composites*, vol. 30, no. 9, pp. 788–797, October 2008.

[DUA 06] DUAN K., HU X., WITTMANN F., “Scaling of quasi-brittle fracture: boundary and size effect”, *Mechanics of Materials*, vol. 38, no. 1–2, pp. 128–141, January 2006.

[FIS 02] FISCHER H., RENTZSCH W., MARX R., “A modified size effect model for brittle nonmetallic materials”, *Engineering Fracture Mechanics*, Elsevier, vol. 69, no. 7, pp. 781–791, 2002.

[GER 07] GERMAIN N., BESSON J., FEYEL F., “Composite layered materials: anisotropic nonlocal damage models”, *Computer Methods in Applied Mechanics and Engineering*, Elsevier, vol. 196, no. 41–44, pp. 4272–4282, 2007.

[GET 98] GETTU R., SALDÍVAR H., KAZEMI M., “Implications of the size effect method for analyzing the fracture of concrete”, *International Journal of Solids and Structures*, Elsevier, vol. 35, no. 31–32, pp. 4121–4132, 1998.

[GRA 08] GRASSL P., REMPLING R., “A damage-plasticity interface approach to the meso-scale modelling of concrete subjected to cyclic compressive loading”, *Engineering Fracture Mechanics*, vol. 75, pp. 4804–4818, 2008.

[GRA 09] GRASSL P., BAŽANT Z.P., “Random lattice-particle simulation of statistical size effect in quasi-brittle structures failing at crack initiation”, *Journal of Engineering Mechanics*, vol. 135, pp. 85–92, 2009.

[GRA 10] GRASSL P., JIRÁSEK M., "Meso-scale approach to modelling the fracture process zone of concrete subjected to uniaxial tension", *International Journal of Solids and Structures*, Elsevier, vol. 47, no. 7–8, pp. 957–968, 2010.

[GRA] GRASSL P., GRÉGOIRE D., ROJAS-SOLANO L., PIJAUDIER-CABOT G., "Meso-scale modelling of the size effect on the fracture process zone of concretes", *International Journal of Solids and Structures*, forthcoming.

[GRÉ a] GRÉGOIRE D., ROJAS-SOLANO L., PIJAUDIER-CABOT G., "Continuum to discontinuum transition during failure in non-local damage models", *International Journal of Multiscale Computational Engineering*, forthcoming.

[GRÉ b] GRÉGOIRE D., ROJAS-SOLANO L., PIJAUDIER-CABOT G., "Failure and size effect for notched and unnotched concrete beams", *International Journal of Solids and Structures*, forthcoming.

[HSU 63] HSU T.T.C., SLATE F.O., "Tensile bond strength between aggregate and cement paste or mortar", *ACI Journal Proceedings*, ACI, vol. 60, no. 4, pp. 465–486, 1963.

[IAC 06] IACONO C., SLUYS L., VAN MIER J., "Estimation of model parameters in nonlocal damage theories by inverse analysis techniques", *Computer Methods in Applied Mechanics and Engineering*, Elsevier, vol. 195, no. 52, pp. 7211–7222, 2006.

[JIR 04] JIRASEK M., ROLSHOVEN S., GRASSL P., "Size effect on fracture energy induced by non-locality", *International Journal for Numerical and Analytical Methods in Geomechanics*, Wiley Online Library, vol. 28, no. 7–8, pp. 653–670, 2004.

[JIR 07] JIRÁSEK M., GRASSL P., "Boundary effect induced by nonlocal damage formulations", *Proceedings of CFRAC 2007*,CD-ROM, Nantes, France, 2007.

[KAR 03] KARIHALOO B., ABDALLA H., XIAO Q., "Size effect in concrete beams", *Engineering Fracture Mechanics*, Elsevier, vol. 70, no. 7–8, pp. 979–993, 2003.

[KRA 09] KRAYANI A., PIJAUDIER-CABOT G., DUFOUR F., "Boundary effect on weight function in nonlocal damage model", *Engineering Fracture Mechanics*, Elsevier, vol. 76, no. 14, pp. 2217–2231, 2009.

[LEB 00] LE BELLEGO C., GÉRARD B., PIJAUDIER-CABOT G., "Chemo-mechanical effects in mortar beams subjected to water hydrolysis", *Journal of Engineering Mechanics*, ASCE American Society of Civil Engineers, vol. 126, no. 3, pp. 266–272, 2000.

[LEB 03] LE BELLÉGO C., FRANÇOIS DUBÉ J., PIJAUDIER-CABOT G., GÉRARD B., "Calibration of nonlocal damage model from size effect tests", *European Journal of Mechanics-A/Solids*, Elsevier, vol. 22, no. 1, pp. 33–46, 2003.

[LUN 03] LUNA P., BERNAL C., CISILINO A., FRONTINI P., COTTERELL B., MAI Y., "The application of the essential work of fracture methodology to the plane strain fracture of ABS 3-point bend specimens", *Polymer*, Elsevier, vol. 44, no. 4, pp. 1145–1150, 2003.

[MAZ 86] MAZARS J., "A description of micro-and macroscale damage of concrete structures", *Engineering Fracture Mechanics*, Elsevier, vol. 25, no. 5–6, pp. 729–737, 1986.

[MAZ 91] MAZARS J., PIJAUDIER-CABOT G., SAOURIDIS C., "Size effect and continuous damage in cementitious materials", *International Journal of Fracture*, Springer, vol. 51, no. 2, pp. 159–173, 1991.

[MIE 97] VAN MIER J.G.M., *Fracture Processes of Concrete*, CRC Press, Boca Raton, 1997.

[MOR 11] MOREL S., DOURADO N., "Size effect in quasibrittle failure: analytical model and numerical simulations using cohesive zone model", *International Journal of Solids and Structures*, Elsevier, vol. 48, no. 10, pp. 1403–1412, 2011.

[NIR 92] NIRMALENDRAN S., HORII H., "Analytical modelling of microcracking and bridging in fracture of quasi-brittle materials", *Journal of the Mechanics and Physics Solids*, vol. 40, no. 2, pp. 863–86, 1992.

[PAT 99] PATZÁK B., "Object oriented finite element modeling", *Acta Polytechnica*, vol. 39, pp. 99–113, 1999.

[PAT 01] PATZÁK B., BITTNAR Z., "Design of object oriented finite element code", *Advances in Engineering Software*, vol. 32, pp. 759–767, 2001.

[PEE 96] PEERLINGS R., DE BORST R., BREKELMANS W., DE VREE J., "Gradient enhanced damage for quasi-brittle materials", *International Journal for Numerical Methods in Engineering*, John Wiley & Sons, vol. 39, no. 19, pp. 3391–3403, 1996.

[PIJ 87] PIJAUDIER-CABOT G., BAŽANT Z., "Nonlocal damage theory", *Journal of Engineering Mechanics*, vol. 113, no. 10, pp. 1512–1533, 1987.

[PLA 93] PLANAS J., ELICES M., "Asymptotic analysis of a cohesive crack: 2. Influence of the softening curve", *International Journal of Fracture*, vol. 64, pp. 221–237, 1993.

[SAA 89] SAANOUNI K., CHABOCHE J., LESNE P., "On the creep crack-growth prediction by a non local damage formulation", *European Journal of Mechanics. A. Solids*, Elsevier, vol. 8, no. 6, pp. 437–459, 1989.

[SCH 92] SCHLANGEN E., VAN MIER J.G.M., "Simple lattice model for numerical simulation of fracture of concrete materials and structures", *Materials and Structures*, vol. 25, pp. 534–542, 1992.

[SIM 04] SIMONE A., ASKES H., SLUYS L., "Incorrect initiation and propagation of failure in non-local and gradient-enhanced media", *International Journal of Solids and Structures*, Elsevier, vol. 41, no. 2, pp. 351–363, 2004.

[TAN 96] TANG T., BAŽANT Z., YANG S., ZOLLINGER D., "Variable-notch one-size test method for fracture energy and process zone length", *Engineering Fracture Mechanics*, Elsevier, vol. 55, no. 3, pp. 383–404, 1996.

[TVE 95] TVERGAARD V., NEEDLEMAN A., "Effects of nonlocal damage in porous plastic solids", *International Journal of Solids and Structures*, Elsevier, vol. 32, no. 8–9, pp. 1063–1077, 1995.

[VAN 03] VAN MIER J., VAN VLIET M., "Influence of microstructure of concrete on size/scale effects in tensile fracture", *Engineering Fracture Mechanics*, Elsevier, vol. 70, no. 16, pp. 2281–2306, 2003.

[VLI 00] VAN VLIET M., VAN MIER J., "Experimental investigation of size effect in concrete and sandstone under uniaxial tension", *Engineering Fracture Mechanics*, Elsevier, vol. 65, no. 2–3, pp. 165–188, 2000.

[WAN 10] WANG Q., ZHANG S., XIE H., “Rock dynamic fracture toughness tested with holed-cracked flattened Brazilian discs diametrically impacted by SHPB and its size effect”, *Experimental Mechanics*, Springer, vol. 50, no. 7, pp. 877–885, 2010.

[ZUB 87] ZUBELEWICZ A., BAŽANT Z.P., “Interface modeling of fracture in aggregate composites”, *Journal of Engineering Mechanics, ASCE*, vol. 113, pp. 1619–1630, 1987.

Chapter 6

Statistical Aspects of Quasi-Brittle Size Effect and Lifetime, with Consequences for Safety and Durability of Large Structures

6.1. Introduction

The understanding of strength distributions, which is essential for a rational determination of safety factors guarding against the uncertainties of structural strength, is of paramount importance for safe and economic design of engineering structures. For perfectly ductile or perfectly brittle materials, the proper cumulative distribution functions (cdf's) of the nominal strength of structure are known to be either Gaussian or Weibullian, respectively. The type of cdf does not change with structure size and geometry, although the coefficient of variation decreases with size for the former and the mean decreases for the latter.

Chapter written by Zdeněk P. BAŽANT, Jia-Liang LE and Qiang YU.

This chapter focuses on positive geometry structures consisting of quasi-brittle materials, which include, at normal scale, concrete, fiber–polymer composites, tough ceramics, rocks, sea ice, wood, bone, etc., and many more at the scale of microelectromechanical systems (MEMS) and thin films. Quasi-brittle materials are materials that are: 1) incapable of purely plastic deformations, and 2) in normal use, have a fracture process zone (FPZ) which is not negligible compared to the structure size. A salient property of quasi-brittle materials is that they obey, on a small scale, the theory of plasticity characterized by material strength, and on a large scale the linear elastic fracture mechanics (LEFM) characterized by fracture energy. Over the past three decades, extensive studies have shown that the quasi-brittle structures exhibit a strong size effect on their nominal strength [BAŽ 76, BAŽ 84, BAŽ 04, BAŽ 05]. Two types of simple size effect laws have been distinguished: Type-1 SEL, occurring in structures that fail at crack initiation from a smooth surface, and Type-2 SEL, which occurs in structures with a deep notch or stress-free (e.g. fatigued) crack formed stably before failure. The Type-2 SEL is also called the size–shape effect law (SEL), since its fracture mechanics-based extension [BAŽ 90] captures the effect of structure geometry through the LEFM energy release function.

The Type-1 SEL applies to quasi-brittle structures failing at crack initiation from a smooth surface. Because of material heterogeneity, a finite cracking zone representing the FPZ must develop before the cracking can coalesce into an initial macrocrack of finite depth attached to the surface. Formation of the initial FPZ causes stress redistribution and energy release necessary to drive the macrocrack. Except for the large size limit, the Type-1 SEL can be derived by considering the limiting case of energy release where the energy release approaches zero with a vanishing crack length. For the large size limit, the Type-1 size effect must converge to the classical Weibull theory.

Bažant and Pang [BAŽ 06, BAŽ 07a] and Bažant *et al.* [BAŽ 09c] presented a probabilistic theory for the size effect on strength distribution, by which the Type-1 size effect can be explained alternatively and more fundamentally. For failures at crack initiation, the structure can be statistically modeled as a chain of representative volume elements (RVEs). It is important that the chain is finite, which rules out Weibull distribution. The strength distribution of one RVE was derived by relating the free energy loss at each single-atom crack jump to the energy release from an atomic lattice block, and introducing a multiscale transition based on a hierarchy of series and parallel coupling, with the former accounting for compatibility conditions and the latter for strain localizations. It is found that the strength distribution of one RVE must be Gaussian with a remote power-law (or Weibull) tail grafted to the probability of about 0.001.

The strength distribution of quasi-brittle structures modeled as a finite chain depends on the structure size and geometry, and varies gradually from a Gaussian cdf with a remote Weibull tail to a fully Weibull cdf at large sizes. The same theoretical framework also provides a plausible physical explanation for the crack growth rate law. The theory can further be extended to the distribution of lifetime under sustained load [BAŽ 09a, BAŽ 09c, LE 09].

The Type-2 SEL applies to the case where the structure has a deep notch or stress-free (e.g. fatigued) crack formed before the peak load is reached. Due to the stress concentration, there is no chance for the dominant crack to initiate elsewhere in the structure volume, which means that material randomness cannot cause any size effect in the mean. Thus, the size effect on the mean nominal strength of structure is essentially energetic, while material randomness can affect only the standard deviation of structure strength [BAŽ 91b]. The Type-2 size effect law can be derived by using asymptotic approximation of the energy release function for the propagating crack based on the equivalent LEFM, or the J-integral [BAŽ 05]. Investigation of a large database collected from various laboratories shows that if Type-2 size effect is ignored, the safety margin for large structures is substantially compromised.

6.2. Type-I size effect derived from atomistic fracture mechanics

6.2.1. *Strength distribution of one RVE*

The fracture at macro-RVE scale originates from the breakage of interatomic bonds at the nanoscale [HEN 70, ZHU 65, ZHU 74]. Consequently, the statistics of structural failure of an RVE must be related to the statistics of interatomic bond breakage. Consider a nanostructure, either an atomic lattice block or a disordered nanostructure, with some intrinsic defects such as nanocracks. The stress applied at macroscale causes nanostress concentrations under which the nanocrack begins to propagate (Figure 6.1). When it advances by one atomic spacing in the atomic lattice (or, in a disordered nanostructure, by one nanobond spacing), the energy release increment must equal the change of activation energy barrier. With the equivalent LEFM, the energy release increment can be expressed as a function of the remote stress applied on the nanostructure [BAŽ 09a, BAŽ 09b].

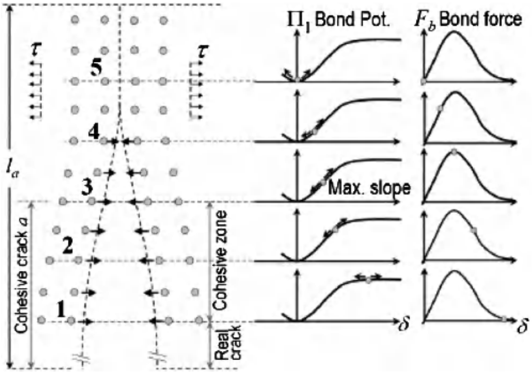

Figure 6.1. *Propagation of nanocrack*

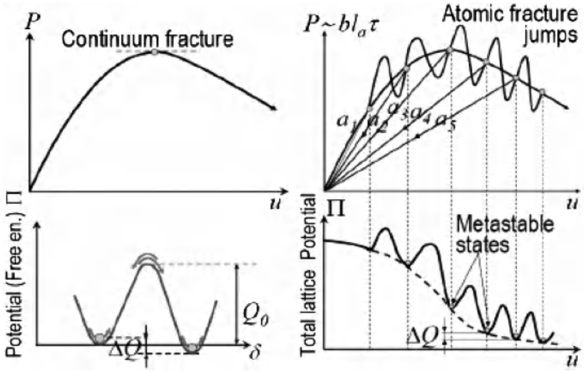

Figure 6.2. *Mechanism of nanocrack jumps*

Since the crack jumps by one atomic spacing or one nanoinhomogeneity are numerous and thus very small, the activation energy barrier for a forward jump differs very little from the activation energy barrier for a backward jump. Therefore, the jumps of the state of the nanostructure, characterized by its free energy potential, must be happening in both directions, albeit with different frequencies (Figure 6.2). After a certain number of jumps of the nanocrack tip, the length of the nanocrack reaches a critical value at which the crack loses its stability and propagates dynamically, thereby causing a break of the nanostructure. Since, at nanoscale, it may generally be assumed that each jump is statistically independent, the failure probability of the nanostructure is proportional to the sum of the frequencies of all the jumps that cause its failure. The failure probability of the nanostructure has been shown to follow a power-law function of the remote stress with a zero threshold [BAŽ 09a], i.e.

$$P_f \propto \tau^2 = (c\sigma)^2 \qquad [6.1]$$

where τ is the microstress, σ is the macrostress, and c is the nano-macrostress concentration factor.

To relate the strength distributions of a nanostructure and a macroscale RVE, certain statistical multiscale transition framework is needed. Though various stochastic multiscale numerical approaches have been proposed to capture the statistics of structural response [GRA 06, WIL 06, XU 07], the capability of these approaches is always limited due to the incomplete knowledge of the uncertainties in the information across all the scales. In this study, the multiscale bridging between the strength cdf at the nanoscale and at the RVE scale is statistically represented by a hierarchical model consisting of parallel and series couplings (Figure 6.3). The parallel couplings statistically reflect the load redistribution mechanisms at various scales subject to compatibility conditions. The series couplings, represented by the weakest-link chain model, reflect the localization of subscale cracking and slippage (or damage) into larger scale cracks or slips.

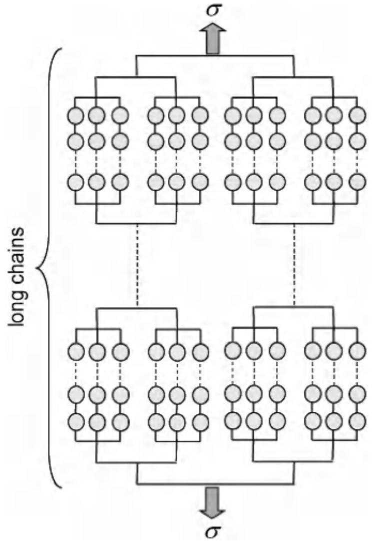

Figure 6.3. *Hierarchical model for statistical multiscale transition*

For a chain of n elements, where all the elements have a strength cdf with a power-law tail of exponent p, the strength cdf of the entire chain has also a power-law tail, and its exponent is also p. If the tail exponents for different elements in the chain are different, then the smallest one is the tail exponent of the cdf of strength of the entire chain.

For parallel coupling of elements of random strength (fiber bundle), the strength distribution of the bundle depends on the mechanical behavior of each element. However, two asymptotic properties of the strength distribution of the bundle are independent of the behavior of each element: 1) If the cdf of strength of each element has a power-law tail of exponent *p*, then the cdf of strength of a bundle of *n* elements also has a power-law tail, and its exponent is *np* [BAŽ 06, BAŽ 07a, BAŽ 09b], while the reach of the power-law tail is drastically shortened as the number of elements *n* increases. 2) The strength cdf of bundle converges to Gaussian distribution for an increasing number of elements [BAŽ 06, BAŽ 07a, BAŽ 09b, DAN 45, HAR 83, PHO 97]. The reach of the power-law tail and the rate of convergence to Gaussian distribution depend on the deformation behavior of the element [BAŽ 06, BAŽ 07a].

Numerical simulation shows that the strength distribution of one RVE, which is statistically modeled by the hierarchical model (Figure 6.3), can be approximately described as Gaussian, with a Weibull tail grafted on the left at the probability of about 10^{-4} to 10^{-3} [BAŽ 09b]. Mathematically, we may approximate the strength distribution of one RVE as [BAŽ 06, BAŽ 07a]:

$$P_1 = 1 - \exp\left[-(\sigma_N / s_0)^m\right] \quad (\sigma \le \sigma_{gr}) \qquad [6.2]$$

$$P_1 = P_{gr} + \frac{r_f}{\delta_G \sqrt{2\pi}} \int_{\sigma_{gr}}^{\sigma_N} e^{-(\sigma' - \mu_G)^2 / 2\delta_G^2} \mathrm{d}\sigma' \quad (\sigma > \sigma_{gr}) \qquad [6.3]$$

where σ_N is the nominal strength, which is a maximum load parameter of the dimension of stress. In general, $\sigma_N = P/bD$ or P/D^2 for two- or three-dimensional scaling (*P* is the maximum load of the structure or parameter of load system, b is the structure thickness in the third dimension, and D is the characteristic structure dimension or size). Furthermore, m (Weibull modulus) and s_0 are the shape and scale parameters of the Weibull tail, and μ_G and δ_G are the mean and standard deviation of the Gaussian core if considered extended to $-\infty$, r_f is a scaling parameter required to normalize the grafted cdf such that $P_1(\infty) = 1$, and P_{gr} = grafting probability = $1-\exp[-(\sigma_{gr}/s_0)^m]$. Finally, continuity of the probability density function (pdf) at the grafting point requires that $(\mathrm{d}P_1/\mathrm{d}\sigma_N)|_{\sigma gr+} = (\mathrm{d}P_1/\mathrm{d}\sigma_N)|_{\sigma gr-}$.

6.2.2. *Size effect on mean structural strength*

In the context of softening damage and failure of a structure, the RVE cannot be defined by homogenization theory. Rather, it must be defined as the smallest material volume whose failure triggers the failure of a structure. The structure can thus be statistically represented by a chain of RVEs. By virtue of the joint probability theorem, and under the assumption of independence of random strengths of links in a finite weakest-link model, the strength distribution of a structure can be calculated as:

$$P_f(\sigma_N) = 1 - \prod_{i=1}^{n} [1 - P_1(\langle \sigma(x_i) \rangle)] \qquad [6.4]$$

where σ_N is the nominal strength of the structure, $\sigma(x_i) = \sigma_N\, s(x_i)$ is the maximum principal stress at the center of ith RVE with the coordinate x_i, $s(x_i)$ is the dimensionless stress describing the stress distribution in the structure, n is the number of RVEs in the structure, and $P_1(\sigma)$ is the strength cdf of one RVE. Equation [6.4] directly indicates the size effect on the type of strength cdf. For small-size structures (small n), the strength cdf is predominantly Gaussian, which corresponds to the case of quasi-plastic behavior. For large-size structures, what matters for P_f is only the tail of the strength cdf of one RVE, and it means that the entire cdf of strength of very large structures follows the Weibull distribution.

Based on the finite weakest link model (equation [6.4]) and the grafted cdf of strength for one RVE (equations [6.2] and [6.3]), the strength cdf of a structure must depend on its size and geometry. The mean strength for a structure with any number of RVEs can be calculated as:

$$\bar{\sigma}_N = \int_0^{\infty} [1 - P_f(\sigma_N)] \mathrm{d}\sigma_N \qquad [6.5]$$

Clearly, it is impossible to express $\bar{\sigma}_N$ analytically. However, its approximate form can be obtained through asymptotic matching. It has been proposed that the size effect on mean strength can be approximated by [BAŽ 04, BAŽ 05]:

$$\bar{\sigma}_N = \left[\frac{N_a}{D} + \left(\frac{N_b}{D} \right)^{r/m} \right]^{1/r} \qquad [6.6]$$

where parameters N_a, N_b, r, and m are to be determined by asymptotic properties of the size effect curve. It has been shown that such a size-effect curve agrees well with the predictions by other mechanics models such as the non-local Weibull theory [BAŽ 00] and with the experimental observations on concrete [BAŽ 07b]. As the large size asymptote, equation [6.6] converges to $(N_b/D)^{1/m}$. Calculation of the mean strength from the Weibull distribution shows that m must be equal to the Weibull modulus of strength distribution, which can be determined by the slope of the left tail of strength histogram plotted on the Weibull scale. The other three parameters, N_a, N_b, and r, can be determined by solving three simultaneous equations based on three asymptotic conditions, $\left[\bar{\sigma}_N\right]_{D\to l_0}$, $\left[\mathrm{d}\bar{\sigma}_N/\mathrm{d}D\right]_{D\to l_0}$, and $\left[\bar{\sigma}_N D^{1/m}\right]_{D\to\infty}$.

6.3. Size effect on structural lifetime

The probability of not achieving the design lifetime of a structure must be tolerable, i.e. sufficiently small. Although the theory just outlined has not yet been extended to fatigue under cyclic loads, the lifetime problem has already been solved for a constant load or stress. The creep crack growth law is needed as a link between the strength and lifetime statistics [BAŽ 09a, BAŽ 09c]. For decades, extensive experimental evidences showed that the crack growth rate law has a power-law form [EVA 72, EVA 84, THO 83, MUN 99]:

$$\dot{a} = Ae^{-Q_0/kT}K^n \qquad [6.7]$$

where K is the stress intensity factor, Q_0 is the activation energy barrier at absence of stress, k is the Boltzmann constant, T is the absolute temperature, A, and n is the empirical constants. A recent study showed that the power-law form of the crack growth rate can be physically justified by considering the fracture mechanics of random crack front jumps through the atomic lattice and the condition of equality of the energy dissipation rates calculated on the nanoscale and the macroscale [BAŽ 09b, BAŽ 09c, LE 09].

Now consider both the strength and the lifetime tests for an RVE. 1) In the strength test, the load is rapidly increased till the RVE fails. The maximum load registered corresponds to the strength of the RVE, which may be chosen to be equal to σ_N. 2) In the lifetime test, the load is rapidly increased to a certain level σ_0 and is then kept constant till the RVE fails. The load duration up to failure represents the lifetime λ of the RVE at stress σ_0. By applying equation [6.7] to both of these tests, we find that the structural strength and the lifetime are related through the following simple equation:

$$\sigma_N = \beta \sigma_0^{n/(n+1)} \lambda^{1/(n+1)} \qquad [6.8]$$

where κ is the loading rate for the strength test and $\beta = [\kappa (n+1)]^{1/(n+1)}$ is a constant. Christensen [CHR 08] used the same approach to study the damage accumulation rules and showed that equation [6.8] represents a nonlinear damage accumulation rule, which is more physical compared to the widely adopted linear damage accumulation rule such as the Palmgren–Miner rule [PAL 24, MIN 45]. By substituting equation [6.8] into equations [6.2] and [6.3], we obtain the lifetime distribution of one RVE. Similar to strength statistics, we can calculate the lifetime distribution of a structure of any size (equation [6.4]) and the mean structural lifetime. A simple asymptotic matching formula for the size effect on the mean structural lifetime is given by:

$$\bar{\lambda} = \left[\frac{C_a}{D} + \left(\frac{C_b}{D} \right)^{r/m} \right]^{(n+1)/r} \qquad [6.9]$$

where m is the Weibull modulus of strength distribution, n is the exponent of the power-law crack growth rate, and $m/(n+1)$ is the Weibull modulus of lifetime distribution. Parameters C_a, C_b, and r can be determined from three known asymptotic conditions for $\left[\bar{\lambda}\right]_{D \to l_0}$, $\left[\mathrm{d}\bar{\lambda} / \mathrm{d}D\right]_{D \to l_0}$, and $\left[\bar{\lambda} D^{(n+1)/m}\right]_{D \to \infty}$.

Figure 6.4 shows the calculated size effect on the mean structural strength and lifetime of 99.9% Al_2O_3, based on the strength and lifetime cdf's calibrated by Fett and Munz's histogram testing [FET 91]. It can be seen that the size effect on mean structural lifetime is much stronger than that on mean structure strength.

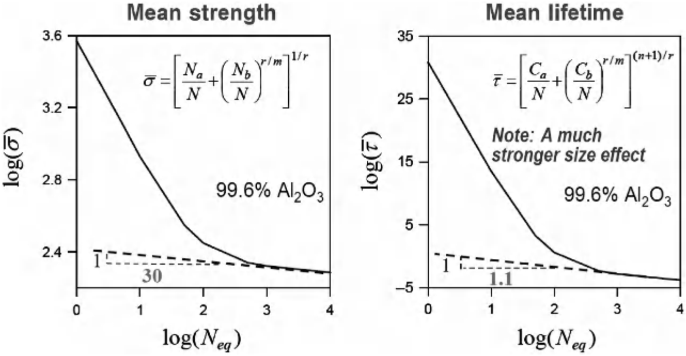

Figure 6.4. *Size effects on structural strength and lifetime*

This is physically plausible. Consider two geometrically similar beams, with size ratio, say, 1:8. Let the nominal strength of the small beam be μ. Due to the size effect on the mean strength, the nominal strength of the large beam is about $\mu/2$. If a nominal load of $\mu/2$ were applied on both beams, the large beam will fail within the standard laboratory testing period (i.e. about 5 minutes), while the small beam is expected to survive at that load for years if not forever. An important consequence is that, for a given tolerable probability, a slightly larger structure would have a much shorter lifespan.

6.4. Consequences of ignoring Type-2 size effect

In many common failure types, such as shear, torsion, and compression crushing, reinforced concrete structures exhibit a strong deterministic size effect of Type 2. Due to its energetic nature, the randomness of material properties affects only the standard deviation of strength, but not its mean. Nevertheless, statistical analysis of a large database presents other statistical problems. Using a large database, we should note that: 1) the major source of scatter in the database is the differences among different concretes tested in different laboratories and among the subjective selections of different experimenters according to their research interests; 2) the entire database cannot be treated as one statistical population; rather, because of the size effect, it should be separated into size intervals and the statistics should be treated as a statistical regression based on the Type-2 size effect.

Figure 6.5 shows a database of 398 data points collected from various research groups to investigate the conservativeness of the current (American Concrete Institute) ACI shear design formula for concrete beams, which assumes a size-independent shear strength $v_c = 2\sqrt{f_c'}$ (f_c' is the specific compressive strength of concrete, which typically equals about 70% of the average compressive strength f_{cr}'). Although obscured by enormous scatter, it can still be noted that the data cloud of shear strength values in the database displays a downward trend with respect to the beam depth *d*, which rules out applying population statistics to the database as a whole.

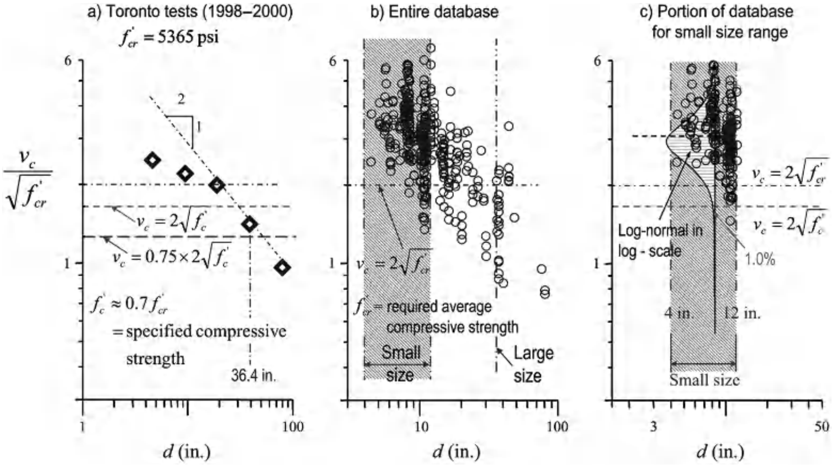

Figure 6.5. *(a) Toronto size effect tests; (b) shear database of 398 data points; (c) isolated data points in the small size range*

However, if data points in small size range (100–300 mm) are isolated from the database, the size effect is weak enough for treating the data as a population with no statistical trend. The mean and coefficient of variation (CoV) are found to be $\overline{y} = v_c / \sqrt{f'_{cr}} = 3.2$ and ω = 27% (see Figure 6.5). The relatively high value of ω indicates that the scatter band of the isolated points is wider than what is observed in individual test series.

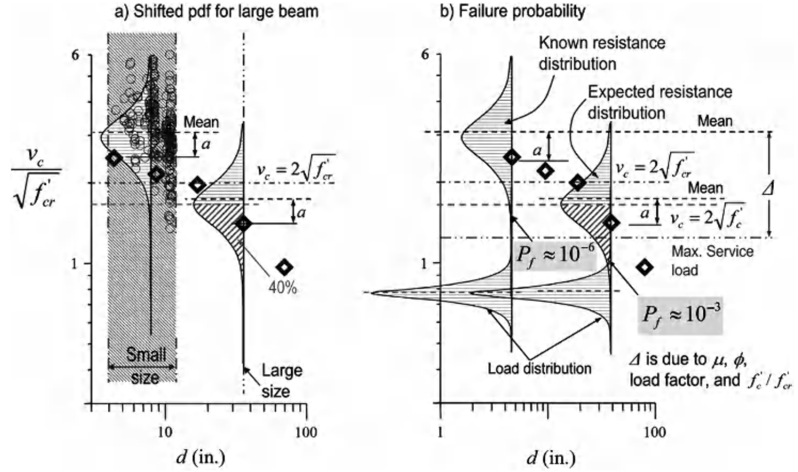

Figure 6.6. *(a) Log-normal pdf of shear strength in small size range and its shift to d = 1 m; (b) failure probability of beams in different size ranges according to the corresponding pdf*

For example, the size effect tests of shear beam at the University of Toronto [LUB 04, POD 98L] showed ω = 6.9%, and those at Northwestern University showed ω = 12% [BAŽ 91a]. The reason is that the database covers a wide range of secondary characteristics such as the steel ratio, shear–span ratio, and concrete type, which all vary throughout the database and have a significant effect on the shear strength of beam. The non-uniform distribution of these secondary characteristics is the result of the subjective selection in different laboratories, and its contribution to the scatter of shear strength dominates. Therefore, the choice of the pdf to be calibrated by the test data in each interval must be empirical. Among the normal distribution, log-normal distribution, and Weibull distribution, the log-normal distribution is found to give the best fit for the first size interval, in which many data exist [BAŽ 09d]. It should be noted that a log-normal distribution would be physically inadmissible for the scatter due purely to material randomness; but this randomness plays a negligible role in the database scatter.

For large-size beams, the type of pdf of shear strength cannot be obtained by the same process because of the scarcity of data points in this size range. However, in view of the origin of scatter, it would be surprising that the type of pdf changed with the structure size. Therefore, it is logical to assume the log-normal pdf will apply for each size interval.

In Figure 6.5c, the log-normal pdf obtained from small size range is plotted in the double-logarithmic scale. Figure 6.6a shows the same pdf superposed on size effect tests made at the University of Toronto. The strength value for the test of the single beam 0.925 m deep was just at the limit of the ACI shear design formula $v_c = 2\sqrt{f_c'}$ (Figure 6.6), and the test of the single beam 1.89 m deep was below this limit, but nevertheless exceeded the value $\phi 2\sqrt{f_c'}$, where ϕ = 0.75 is the required capacity reduction factor (understrength factor). Some engineers deemed it to be acceptable, and thus, to justify the disregard of size effect. However, a probabilistic analysis demonstrates the opposite.

To explain, note that, for the particular secondary characteristics (such as the shear span, steel ratio, or concrete type) used in the Toronto tests, the shear strength value (the first bold diamond point) of the Toronto test lies (in the logarithmic scale) at certain distance *a* below the mean of the pdf of the database interval [Figure 6.6a]. Since the width of the scatter band in the logarithmic scale does not vary appreciably with the beam size, the same pdf and the same distance a between the pdf mean and the Toronto test result must be expected for every beam size d, including the sizes of d = 0.925 and 1.89 m. In other words, if the Toronto test for d = 925 mm were repeated for the same secondary characteristics as displayed in the small size range, we would have to expect the same pdf but shifted downwards in the logarithmic scale by distance a, as shown in Figure 6.6a. By assuming the value of a to be the same for the small and large size ranges, we simply imply that the probability, or frequency, of beams having shear strength below the value characterized by a will be the same for these size ranges.

Now note that the pdf of shear strength in the small size range lies almost entirely above the ACI shear design formula $v_c = 2\sqrt{f_c'}$, but extends well below it for size range centered at $d \approx 1$ m. This means that if the Toronto large size test could be repeated for many different concretes, shear spans, steel ratios, etc. a large portion of the test results would likely fall below the ACI shear strength limit. According to the log-normal pdf obtained here, the percentage of the unsafe large beams would be 40%. This is unacceptable.

Consider now the consequences for the failure probability, P_f, of a structure exposed to the actual service loads. To this end, we must consider the randomness of these loads, reflected in design in the load factor μ. Let $p(y)$ be the pdf of the extreme service loads y. Determining the type of pdf is a demanding task, but for the purpose of comparing small and large structures it will suffice to assume that $p(y)$ is log-normal and that its coefficient of variation is 10%.

Evaluating the classical Freudenthal's reliability integral [ANG 84, MAD 86, HAL 99] $P_f = \int_0^\infty f(y)R(y)dy$ (where $R(y)$ is the cdf of structure resistance, Figure 6.5), we obtain $P_f \approx 10^{-6}$ for beams of $d \approx 200$ mm (centroid of the chosen small size interval in Figure 6.6). This is safe since, compared to the inevitable risks that people face, 10^{-6} is generally considered the maximum tolerable. However, for beams of $d = 1$ m, the failure probability increases to $P_f = 10^{-3}$, which is far beyond what the risk analysis experts generally accept as safe. For $d = 1.89$ m, the P_f value is still higher. Therefore, Type-2 size effect must be incorporated in the design code. Otherwise, a uniform safety margin is unachievable.

6.5. Conclusion

The gradual transition of the type of distribution of structural strength and lifetime from Gaussian to Weibullian has serious implications for the safety factors and minimum lifetime guarantees of quasi-brittle structures. This needs to be taken into account in the design and safety assessments of large concrete structures, as well as large composite aircraft frames and ship hulls, microelectronic devices, bone implants, etc. By contrast with perfectly ductile and perfectly brittle structures, their safety factors cannot be decided empirically, but must be calculated.

6.6. Acknowledgments

The probabilistic and atomistic analysis was supported under the U.S. National Science Foundation Grant CMS-0556323 and Grant N997613 from Boeing, Inc., both to Northwestern University. The application to the size effect on safety of shear-sensitive concrete beams was supported by the U.S. Department of Transportation through Grant 23120 from the Infrastructure Technology Institute of

Northwestern University. This is a republication of a plenary leture from FraMCoS-7, authorized by proceedings editor and conference chairman Byun-Hwang Oh.

6.7. Bibliography

[ANG 84] ANG A.H.-S., TANG W.H., *Probability concepts in engineering planning and design – decision, Risk and Reliability*, J. Wiley, New York, Vol. II, 1984.

[BAŽ 76] BAŽANT Z.P., “Instability, ductility, and size effect in strain-softening concrete”, *Journal of Engineering Mechanics Division, ASCE*, vol. 102, EM2, pp. 331–344, 1976.

[BAŽ 84] BAŽANT Z.P., “Size effect in blunt fracture: Concrete, rock, metal”, *Journal of Engineering Mechanics, ASCE*, vol. 110, no. 4, pp. 518–535, 1984.

[BAŽ 90] BAŽANT Z.P., KAZEMI, M.T., “Determination of fracture energy, process zone length and brittleness number from size effect, with application to rock and concrete”, *International Journal of Fracture*, vol. 44, pp. 111–131, 1990.

[BAŽ 91a] BAŽANT Z.P., KAZEMI M.T., “Size effect on diagonal shear failure of beams without stirrups”, *ACI Structural Journal*, vol. 88, no. 3, pp. 268–276, 1991.

[BAŽ 91b] BAŽANT Z.P., XI Y., “Statistical size effect in quasi-brittle structures: II. Nonlocal theory”, *Journal of Engineering Mechanics, ASCE*, vol. 117, no. 7, pp. 2623–2640, 1991.

[BAŽ 91c] BAŽANT Z.P., XU K., “Size effect in fatigue fracture of concrete”, *ACI Materials Journal* vol. 88, no. 4, pp. 390–399, 1991.

[BAŽ 00] BAŽANT Z.P., NOVÁK D., “Energetic-statistical size effect in quasibrittle failure at crack initiation”, *ACI Materials Journal*, vol. 97, no. 3, pp. 381–392, 2000.

[BAŽ 04] BAŽANT Z.P., “Scaling of scaling theory for quasibrittle structural failure”, *Proceedings of the National Academy of the United States of America*, vol. 101, no. 37, pp. 14000–14007, 2004.

[BAŽ 05] BAŽANT Z.P., *Scaling of Structural Strength*, 2nd edition, London, Elsevier , 2005.

[BAŽ 06] BAŽANT Z.P. PANG S.-D., "Mechanics based statistics of failure risk of quasibrittle structures and size effect on safety factors", *Proceedings of the National Academy of Sciences of the United States of America*, vol. 103, no. 25, pp. 9434–9439, 2006.

[BAŽ 07a] BAŽANT Z.P., PANG S.-D., "Activation energy based extreme value statistics and size effect in brittle and quasibrittle fracture", *Journal of the Mechanics and Physics of Solids,* vol. 55, pp. 91–134, 2007.

[BAŽ 07b] BAŽANT Z.P., VOŘECHOVSKÝ M., NOVÁK D., "Asymptotic prediction of energetic-statistical size effect from deterministic finite element solutions", *Journal of Engineering Mechanics, ASCE*, vol. 128, pp. 153–162, 2007.

[BAŽ 09a] BAŽANT Z.P., LE J.-L., "Nano-mechanics based modeling of lifetime distribution of quasibrittle structures", *Journal of Engineering Failure Analysis*, vol. 16, pp. 2521–2529, 2009.

[BAŽ 09b] BAŽANT Z.P., LE J.-L., "Size effect on strength and lifetime distributions of quasibrittle structures", *Proceedings of the ASME 2009 International Mechanical Engineering Congress & Exposition*, (IMECE2009), Lake Buena Vista, Florida, pp. 1-9.

[BAŽ 09c] BAŽANT Z.P., LE J.-L., BAZANT M.Z., "Scaling of strength and lifetime distributions of quasibrittle structures based on atomistic fracture mechanics", *Proceedings of the National Academy of the United States of America*, vol. 106, no. 28, pp. 11484–11489, 2009.

[BAŽ 09d] BAŽANT Z.P., YU Q., "Does strength test satisfying code requirement for nominal strength justify ignoring size effect in shear", *ACI Structural Journal*, vol. 106, no. 1, pp. 14–19, 2009.

[BAŽ 10] BAŽANT Z.P., LE J.-L., "Statistical aspects of quasibrittle size effect and lifetime, with consequences for safety and durability of large structures", in B.-H. OH *et al.*, *Fracture Mechanics of Concrete and Concrete Structures – Recent Advances in Fracture Mechanics of Concrete* (*CD Proc., FraMCoS-7, 7th Int. Conf.*, Jeju, Korea, Plenary Lecture), Korea Concrete Institute, Seoul, pp. 1–8.

[CHR 08] CHRISTENSON R.M., "A physically based cumulative damage formalism", *International Journal of Fatigue*, vol. 30, pp. 595–602, 2008.

[DAN 45] DANIELS H.E., "The statistical theory of the strength of bundles and threads", *Proceedings of the Royal Society of London A*, vol. 183, pp. 405–435, 1945.

[EVA 72] EVANS A.G., "A method for evaluating the time-dependent failure characteristics of brittle materials and its application to polycrystalline alumina", *Journal of Matererials Science*, vol. 7, pp. 1173–1146, 1972.

[EVA 84] EVANS A.G., FU Y., "The mechanical behavior of alumina", *Fracture in Ceramic Materials*, Noyes Publications, Park Ridge, NJ, pp. 56–88, 1984.

[FET 91] FETT T., MUNZ D., "Static and cyclic fatigue of ceramic materials", in P. VINCENZINI, *Ceramics Today – Tomorrow's Ceramics*, Elsevier Science Publisher B.V., pp. 1827–1835, 1991.

[GRA 06] GRAHAM-BRADY L.L., ARWADEA S.R., CORRB D.J., GUTIÉRREZC M.A., BREYSSED D., GRIGORIUE M., ZABARAS N., "Probability and materials: From nano- to macro-scale: A summary", *Probabilistic Engineering Mechanics*, vol. 21, no. 3, pp. 193–199, 2006.

[HAR 83] HARLOW D.G., SMITH R.L., TAYLOR H.M., "Lower tail analysis of the distribution of the strength of load-sharing systems", *Journal of Applied Probability*, vol. 20, pp. 358–367, 1983.

[HAL 99] HALDAR A., MAHADEVAN S., *Probability, Reliability and Statistical Methods in Engineering Design*, J. Wiley & Sons, New York, 1999.

[HEN 70] HENDERSON C.B., GRAHAM P.H., ROBINSON C.N., "A comparison of reaction rate models for the fracture of solids", *International Journal of Fracture*, vol. 6, no. 1, pp. 33–40, 1970.

[LE 09] LE J.-L., BAŽANT Z.P., BAZANT M.Z., "Subcritical crack growth rate law and its consequence for lifetime statistics and size effect of quasibrittle structures", *Journal of Physics D: Applied Physics*, vol. 42, 214008, 2009.

[LUB 04] LUBELL A., SHERWOOD T., BENTZ E., COLLINS M.P., "Safe shear design of large, wide beams", *Concrete International*, vol. 26, no. 1, pp. 67–78, 2004.

[MAD 86] MADSEN H.O., KRENK S., LIND N.C., *Methods of Structural Safety*, Prentice Hall, Englewood Cliffs, NJ, 1986.

[MIN 45] MINER M.A., "Cumulative damage in fatigue", *Journal of Applied Mechanics*, vol. 12, pp. 159–164, 1945.

[MUN 99] MUNZ D., FETT T., *Ceramics: Mechanical Properties, Failure Behavior, Materials Selection*, Springer-Verlag, Berlin, 1999.

[PAL 24] PALMGREN A., "Die Lebensdauer von Kugellagren", *Zeitscrift des Vereins Deutscher Ingenieure*, vol. 68, pp. 339–341, 1924.

[PHO 97] PHOENIX S.L., IBNABDELJALIL M., HUI C.-Y., "Size effects in the distribution for strength of brittle matrix fibrous composites", *International Journal Solids and Structures*, vol. 34, no. 5, pp. 545–568, 1997.

[POD 98] PODGORNIAK-STANIK B.A., The Influence of Concrete Strength, Distribution of Longitudinal Reinforcement, Amount of Transverse Reinforcement and Member size on shear Strength of Reinforced Concrete Members, MASc Thesis, Department of Civil Engineering, University of Toronto, ON, Canada, 1998.

[THO 83] THOULESS M.D., HSUEH C.H., EVANS A.G., "A damage model of creep crack growth in polycrystals", *Acta Metallurgica*, vol. 31, no. 10, pp. 1675–1687, 1983.

[WIL 06] WILLIAMS T., BAXER S.C., "A framework for stochastic mechanics", *Probabilistic Engineering Mechanics*, vol. 21, no. 3, pp. 247–255, 2006.

[ZHU 65] ZHURKOV S.N., "Kinetic concept of the strength of solids", *International Journal of Fracture*, vol. 1, no. 4, pp. 311–323, 1965.

[ZHU 74] ZHURKOV S.N., KORSUKOV, V.E., "Atomic mechanism of fracture of solid polymer", *Journal of Polymer Science*, vol. 12, no. 2, pp. 385–398, 1974.

Chapter 7

Tertiary Creep: A Coupling Between Creep and Damage – Application to the Case of Radioactive Waste Disposal

Creep and damage are coupled phenomena that lead to tertiary creep and then failure in cases of a high level of loading compared to the strength of concrete. First, we will show how this coupling could be taken into account by means of a creep model (based on aging rheological elements) coupled to a mechanical damage model. Then the coupled tertiary creep is compared with experimental results. In the case of a radioactive waste disposal, concrete containment structures must be studied over extended periods during which it is necessary to account for a possible degradation by calcium leaching due to on-site water. Owing to this leaching process tertiary creep will eventually occur in the sound zone. Finally, a probabilistic approach is used with the leaching and the tertiary creep models to evaluate the lifetime of a concrete structure subjected to chemical and mechanical loading.

Chapter written by J.M. TORRENTI, T. DE LARRARD and F. BENBOUDJEMA.

7.1. Introduction to tertiary creep

Since Rüsch experiments [RÜS 60] (Figure 7.1), we know that when concrete is subjected to a high sustained compressive load (stress higher than 80% of the compressive strength) nonlinear creep is observed and failure occurs after a while. This phenomenon is called tertiary creep. Several experimental results confirm this behavior [ROL 64, SMA 87, LI 94]. In tension some experimental evidences also exist using a notched sample loaded in tension [REV 09], a notched bending beam [CAR 97], or a wedge splitting test [DEN 06]. And, at early age, tertiary creep could also be involved when shrinkage is restrained [BRI 11].

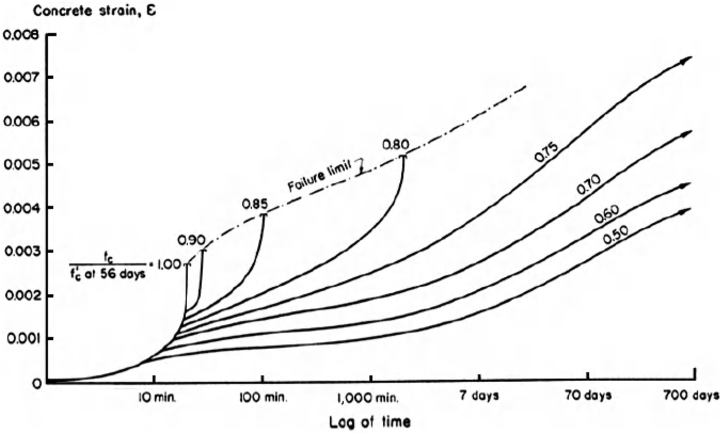

Figure 7.1. *Delayed strains of concrete under high sustained loads [RÜS 60]*

There is clearly a coupling between the high sustained load and the evolution of microcracking. Smadi and Slate [SMA 89] have shown that the length of the microcracks evolves rapidly when the stress level is higher than 80% of the compressive strength. Using acoustic emission, it is also possible to highlight microcracking during creep [ROS 94] or relaxation [DEN 06].

In this chapter, a model of coupling creep and damage is presented. This model is compared to experimental results and then applied to the case of nuclear waste disposal. The case of creep coupled to leaching of concrete is developed using a probabilistic approach.

7.2. Modeling of tertiary creep using a damage model coupled to creep

Many modeling approaches have been proposed for tertiary creep of concrete. Bazant and Xiang, assuming tertiary creep is only due to the growing of cracks with time, use a fracture mechanics approach coupled to creep to model this behavior [BAZ 97]. Coupling between creep and cracking can be modeled by combining a viscoelastic and a viscoplastic model [BER 04]. This model is built on the Duvault–Lion approach in which a generalized Maxwell model is integrated. It reproduces with a satisfactory accordance linear viscoelastic creep, creep failure, and rate effect on strength. Several damage models were also used. Li [LI 94] proposed that the temporal variable can be explicitly introduced in the mechanical damage evolution law (in terms of damage rate). In this case, the approach is that it is dissociated with linear viscoelastic creep strain. Challamel *et al.* have developed a softening viscodamage model that could be viewed as a generalization of a time-independent damage model and describes phenomena such as relaxation, creep, and rate-dependent loading [CHA 05]. Recently, Sellier *et al.* [SEL 11b] have proposed a creep-model taking into account a material consolidation and a creep-induced damage that affects the creep potential. Mazzotti and Savoia [MAZ 03] proposed to model nonlinear creep strain by introducing a stress rate reduction factor as a function of the damage variable in the solidification model [BAZ 89]. Moreover, an effective strain is then defined for creep damage, replacing the equivalent strain (as defined by [MAZ 86]) in damage evaluation for instantaneous loading case. The effective strain is defined as the sum of instantaneous damaged elastic strain with a fraction of creep strain. Omar *et al.* [OMA 04] and Reviron [REV 09] also used a similar approach.

Among these approaches, our model is based on the model proposed by Mazzotti and Savoia [MAZ 03], since the use of damage allows a simple and natural coupling with creep and, for the specific application of waste disposal, leaching through the use of the effective stress concept.

7.2.1. *Creep model*

The model used for creep strain evolution is based on the microprestress theory proposed by Bazant and Xiang [BAZ 97]. This model turns out to be particularly accurate when considering a very long time creep, and is in good accordance with experimental results (see the experimental campaign by Brooks [BRO 05] for 30 years creep). The microprestress solidification theory leads to introduce a dashpot whose viscosity depends on the microprestress so as to represent the microprestress relaxation mechanism. Therefore, this model is able to reproduce accurately aging, even after hydration is completed. Microprestress is a stress level induced in the material by capillary pressure, evolving with time during the hydration process and with pore humidity. The strain evolution $\hat{\varepsilon}$ for the dashpot is given by equation [7.1], where $\tilde{\sigma}$ is the effective stress (assuming that only the uncracked part of the material undergoes creep, see section 1.2.2 for the definition of the effective stress), η is the viscosity of the dashpot, and S is the microprestress

$$\frac{d\hat{\varepsilon}}{dt} = \frac{\tilde{\sigma}}{\eta(S)} \qquad [7.1]$$

The difficult part with this approach is to determine the viscosity evolution with microprestress as well as microprestress evolution with time. In the case of a saturated (meaning that there are neither drying nor wetting phenomena during the degradation and creep processes) and already aged structure (i.e. no hydration process is ongoing during the load application), microprestress and viscosity evolutions are quite simple [BAZ 97] and lead to equation [7.2], where α is a creep parameter that remains constant and depends only on the material

$$\frac{d\hat{\varepsilon}}{dt} = \tilde{\sigma}\frac{\alpha}{t} \tag{7.2}$$

The main disadvantage of the flow element is that it does not allow us to represent the creep recovery: when the load is removed, no recovery can be modeled by the flow element (σ = 0 in equation [7.2]). To represent recovery, a Kelvin–Voigt chain is added to the flow element in parallel. Figure 7.1 represents, for a unidirectional problem, the model. The Kelvin–Voigt element is composed of a dashpot (viscosity η_{KV}) and an elastic spring (stiffness k) connected in parallel. Illston [ILL 65] has shown that the creep recovery lasts for about one week, and this is why we consider a value of 7 days for the characteristic time $\tau_{KV} = \eta_{KV}/k$ of the Kelvin–Voigt chain. The strain evolution for the Kelvin–Voigt element is given by equation [7.3], where $\tilde{\varepsilon}$ is the creep strain for the element under a stress σ

$$\frac{\tilde{\sigma}}{k} = \tilde{\varepsilon} + \tau_{KV}\frac{d\tilde{\varepsilon}}{dt} \tag{7.3}$$

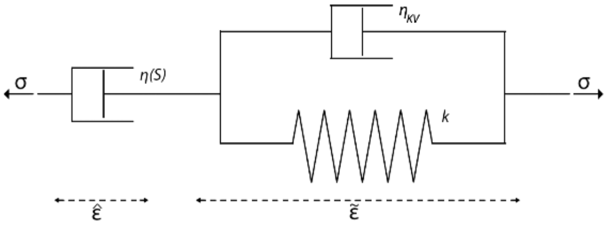

Figure 7.2. *Principle of the creep model*

7.2.2. *Damage model*

The damage model proposed by Mazars [MAZ 86] is used. In this model, a scalar mechanical damage variable D_c is associated with the mechanical degradation process of concrete induced by the development of microcracks. It is defined as the ratio between the microcracks area to the whole material area. An effective stress $\tilde{\sigma}$ is then defined from the apparent stress σ applied on the whole material section. The relationship between apparent stress σ, effective stress $\tilde{\sigma}$, damage D_c, elastic stiffness tensor ***E***, elastic strain ε_e, creep strain ε_c, and total strain ε reads:

$$\sigma = (1 - Dc)\ \tilde{\sigma} \text{ and } \frac{d\tilde{\sigma}}{dt} = E\frac{d\varepsilon_e}{dt} = E\left(\frac{d\varepsilon}{dt} - \frac{d\varepsilon_c}{dt}\right) \qquad [7.4]$$

The Poisson ratio is assumed to be constant. The mechanical damage evolution is deduced from the Mazars equivalent tensile strain ε_{eq} defined in equation [7.5], where $\langle\varepsilon\rangle_+$ is the positive part of the strain tensor. The evolution law for the mechanical damage variable is given in equation [7.6], where ε_D is the damage tensile strain threshold, *A* and *B* are constant material parameters which control the hardening/softening branch in the stress-strain curve

$$\varepsilon_{eq} = \sqrt{\langle\varepsilon\rangle_+ : \langle\varepsilon\rangle_+} \qquad [7.5]$$

$$D_c = 1 - \frac{\varepsilon_D(1-A)}{\varepsilon_{eq}} - \frac{A}{\exp\left(B\left(\varepsilon_{eq} - \varepsilon_D\right)\right)} \text{ if } \varepsilon_{eq} \geq \varepsilon_D \qquad [7.6]$$

7.2.3. *Coupling between damage and creep*

The coupling between creep and damage is taken into account twice. On the one hand, creep strains are considered to be driven by effective stresses (only the uncracked material creeps as shown in [BEN 05] and [BEN 08], see section 1.2.1). It slightly increases creep strains after damage occurs in compression, but it is not sufficient for correctly retrieving nonlinear creep. On the other hand, the calculation of the equivalent strain (equation [7.5]) is modified as proposed by Mazzotti and Savoia [MAZ 03] and includes a part of creep strains through a material parameter β, which can be identified from nonlinear basic creep data. Therefore, damage is also affected by basic creep strain. This allows us to accurately retrieve nonlinear basic creep evolution for high stress levels (see equation [7.7]). Note that with this coupling, due to the choice of a non-asymptotic damage, failure will finally occur due to tertiary creep (but in a very long time – several thousands of years – if the loading is lower than 40% of the compressive strength)

$$\varepsilon_{eq} = \sqrt{\left\langle \varepsilon + \beta \varepsilon_c \right\rangle_+ : \left\langle \varepsilon + \beta \varepsilon_c \right\rangle_+} \qquad [7.7]$$

7.3. Comparison with experimental results

Experimental results of Roll [ROL 64] are used. The specimens have been loaded at an age of 28 days when the compressive strength was equal to 42 MPa. The levels of loading were equal, respectively, to 20%, 35%, 50%, and 65% of the compressive strength. The lower level is used to calibrate the parameters of the creep model (for this level of loading, there is no cracking, only primary creep occurs). Figure 7.3 shows that, only taking into account creep and without coupling with damage, delayed strains are underestimated. Introducing a coupling with β = 0.31, the coupling between damage and creep allows us to fit the experimental results (Figure 7.4).

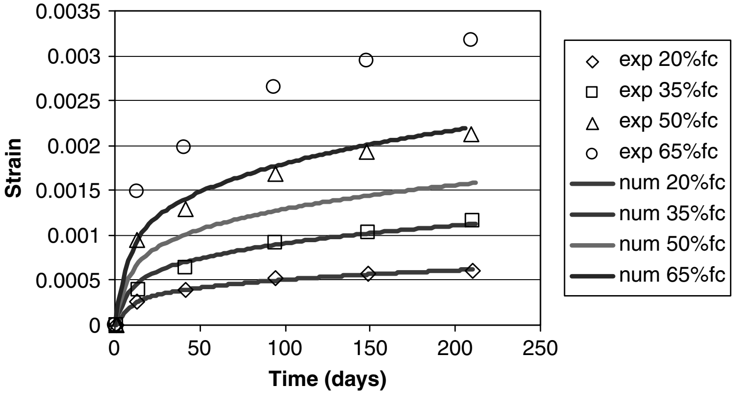

Figure 7.3. *Delayed strains for different stress to strength ratio (without coupling $\beta = 0$, equation [7.7]) – (experimental results from Roll [ROL 64])*

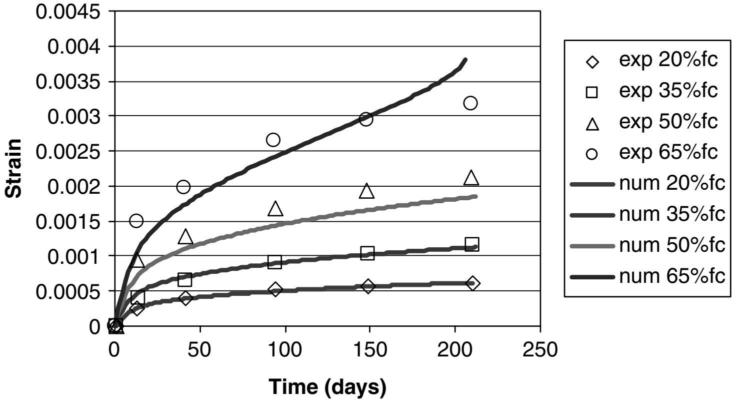

Figure 7.4. *Delayed strains for different stress to strength ratio (with coupling $\beta = 0.31$, equation [7.7]) – (experimental results from Roll [ROL 64])*

7.4. Application to the case of nuclear waste disposal

Deep nuclear waste disposal facilities need to be studied over periods of one or more orders of magnitude greater than those of classical civil engineering. This leads us to consider some degradation phenomena that are most of the time not taken into account because of their slow kinetics. This is the case with calcium leaching for concrete structures exposed to water from the host rock in a deep underground storage. Calcium leaching leads to important changes in the concrete microstructure, and especially a large increase of porosity [ADE 92, GER 96]. Therefore, the mechanical properties of the leached material are much below those of the sound properties [CAR 96, NGU 07].

7.4.1. *Leaching of concrete*

The phenomenon of leaching consists of the dissolution of solid calcium in cement hydrates when concrete is exposed to an aggressive solution (most of the time pure water or at least water with low calcium concentration). Indeed, the fluid component (solution) in concrete is very basic (pH around 13) and several ionic species are highly concentrated [TOR 99]. Therefore, water with low mineral concentration is an aggressive environment for concrete.

Considering that the dissolution is instantaneous (local equilibrium) and that only calcium species are to be taken into account, the leaching of a cement paste can be described by the mass balance equation of calcium (equation [7.8]), as was proposed by Buil *et al.* [BUI 92], where S_{Ca} is the concentration of solid calcium, C_{Ca} is the concentration of liquid calcium, D is the effective diffusivity of calcium in porous material, and ϕ is the porosity. We can recognize the two main phenomena involved in the leaching process: on the one hand, the solid and liquid phases of calcium in the cement paste and in the porous solution are in chemical equilibrium; on the other hand, the ionic calcium species diffuse through the material porosity. The nonlinearity of this equation is mainly due to the diffusivity which depends on the porosity, itself depending on the solid calcium concentration

$$\frac{\partial\left(C_{Ca}\phi\right)}{\partial t} = -div\left(-D\left(\phi\right)grad\left(C_{Ca}\right)\right) - \frac{\partial S_{Ca}}{\partial t} \qquad [7.8]$$

In a semi-infinite medium, because leaching is driven by diffusion, the degraded depth x_d, corresponding to the dissolution front of portlandite, is a function of the square root of time:

$$x_d = k\sqrt{t} \qquad [7.9]$$

7.4.2. *Coupled mechanical and chemical damage*

The coupling between mechanical behavior and chemical degradation of concrete has been studied in details, for example, by Carde *et al.* [CAR 96], Saetta *et al.* [SAE 98], Torrenti *et al.* [TOR 08], Bangert *et al.* [BAN 01], and Nguyen *et al.* [NGU 07]. Gérard *et al.* [GÉR 98] proposed a simplified modeling for chemical alteration and a coupling with the mechanical damage proposed by Mazars [MAZ 86]. The coupling appeared through the evolution of the coefficient of diffusion depending on the damage variable. The model proposed by Ulm *et al.* [ULM 99] is based on the theory of porous media and couples the hydrates dissolution with the evolution of porosity and strain. The model by Kuhl *et al.* [KUH 03a, KUH 03b] proposes to consider three components of porosity (initial porosity, porosity due to chemical degradation, and porosity due to mechanical damage). Recently, Sellier *et al.* [SEL 11a] have proposed a nonlinear viscoelastic model in which the nonlinearities are due to damage or creep. In this model, the mechanical properties are functions of the calcium concentration in the solid phase.

Studies conducted on degraded materials [NGU 07] have quantified the loss of residual mechanical properties for leached concrete. This decrease mainly depends on the mineral admixtures in the concrete mix design and on the degraded area, which are considered (dissolution of portlandite only does not lead to very significant decrease of the compressive strength, whereas dissolution of calcium-silicate-hydrate (C-S-H) does). Here, for the sake of simplicity, it will be considered that the leached area does not sustain any load. Indeed, considering more important residual mechanical properties for the degraded areas would lead us to introduce more input parameters in our model, and therefore, more variability. Such a strong hypothesis on the mechanical behavior of the degraded area has already been used by Torrenti *et al.* [TOR 08] and leads to an underestimation of the lifetime of the considered structure (which is acceptable in accordance with a view of preserving the safety of concrete structures).

7.4.3. *Chemical damage*

A chemical damage variable D_χ is associated with the leaching degradation process of concrete and is defined as the ratio of the degraded area over the whole material section. Figure 7.5 shows how the effective stress $\tilde{\sigma}$ is defined from the apparent stress σ applied on the whole material section (included the degraded area): the stress that is actually applied on the chemically sound area is increased according to the same ratio that the section is reduced. When a mechanical loading exists, the effective stress $\hat{\sigma}$ applied on the uncracked and chemically sound material is thus deduced from the apparent stress σ, and the chemical and mechanical damage variables D_χ and D_c (equation [7.10]):

$$\hat{\sigma} = \frac{\sigma}{(1-D_\chi)(1-D_c)} \qquad [7.10]$$

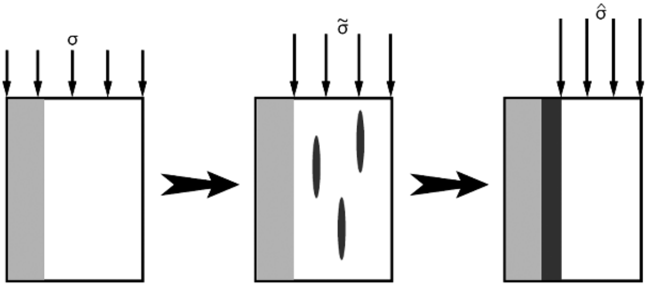

Figure 7.5. *Definition of effective stress on damaged material: no stress is sustained by the chemically damaged section (light gray), so the real stress* σ *becomes* $\tilde{\sigma}$ *on the sound material (white). Due to mechanical damage, cracks in the sound material (deep gray) reduce the material section to sustain the load, and thus, introduce an effective stress* $\hat{\sigma}$ *on the uncracked sound material*

7.4.4. *Example of application: creep coupled to leaching*

When a loaded cylindrical sample (radius R) is submitted to leaching (here accelerated leaching using an ammonium nitrate solution), the stress σ in the sound zone increases during the test [TOR 08]:

$$\sigma(t) = \sigma(t_0)\frac{\pi R^2}{\pi(R - k\sqrt{t})^2} \qquad [7.11]$$

and finally tertiary creep occurs (Figure 7.6). Using the coupling between chemical and mechanical damage, the experimental behavior could be modeled.

7.4.5. *Probabilistic effects*

We consider here a column made of concrete (reinforcement is not considered) in pure compression subjected to leaching due to pure water [LAR 10b]. The radius of the column is equal to 20 cm. With the values of the parameters that are given in Table 7.1, tertiary creep is obtained (Figure 7.7). The evolution of damage is also analyzed: in the first instance, only chemical damage occurs; then the coupling between chemical and mechanical damage appears; and finally, failure occurs due to mechanical damage (Figure 7.8).

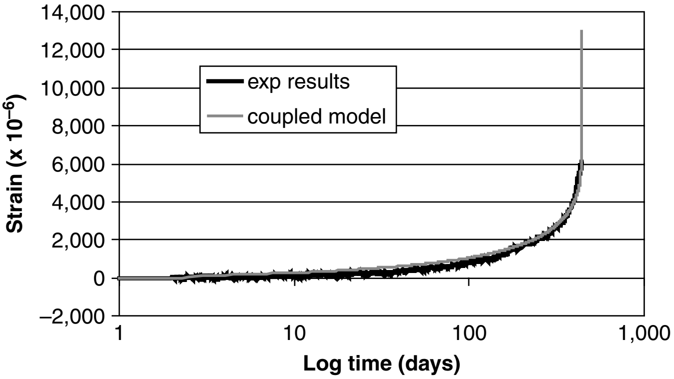

Figure 7.6. *Comparison between experimental strains in a leaching and creep test and the coupled chemical-mechanical model*

	Expected values	Standard deviation
ϕ [–]	0.129	0.010
τ [–]	0.134	0.020
E [GPa]	45.0	4.5
υ [–]	0.178	0.044
β [–]	0.15	0.03
ε_D [µm/m]	109	16
A [–]	0.95	0.10

Table 7.1. *Expected value and standard deviation for the nine variable input parameters of the model*

Considering Beta(2,2) distributions for each of the nine parameters of the model, 1,000 corresponding sets of input parameters were randomly generated according to the Latin Hypercube Sampling principle [KAY 79], optimized thanks to a simulated annealing algorithm [KIR 83]. The expected value and standard deviation for each variable parameter of the model are presented in Table 7.1.

The expected value for the lifetime of the concrete structure, evaluated over the 1,000 realizations, is 980 years. The observed standard deviation is 393 years, which correspond to a coefficient of variation of 40%. Of course, this important value for the coefficient of variation must be compared to the variability of the nine input parameters, whose coefficient of variation ranges between 10% and 25%. Thus, the coupled problem we are dealing with leads to an increasing uncertainty. It is interesting to note that lifetime follows a log-normal distribution, whereas all input parameters are distributed according to a Beta law. Figure 7.9 shows the lifetime distribution that has been calculated on the 1,000 realizations, which can be compared to a log-normal distribution.

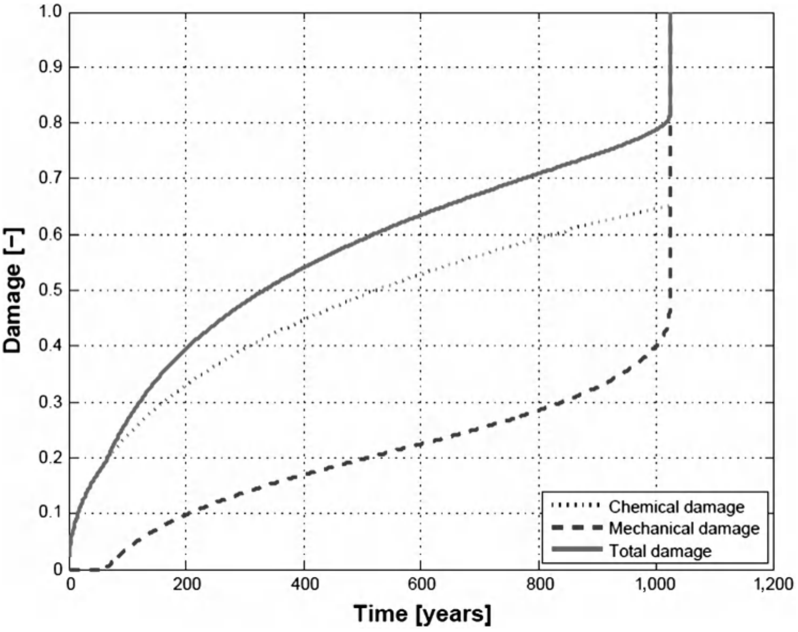

Figure 7.7. *Total, mechanical, and chemical damage time evolutions obtained in pure water*

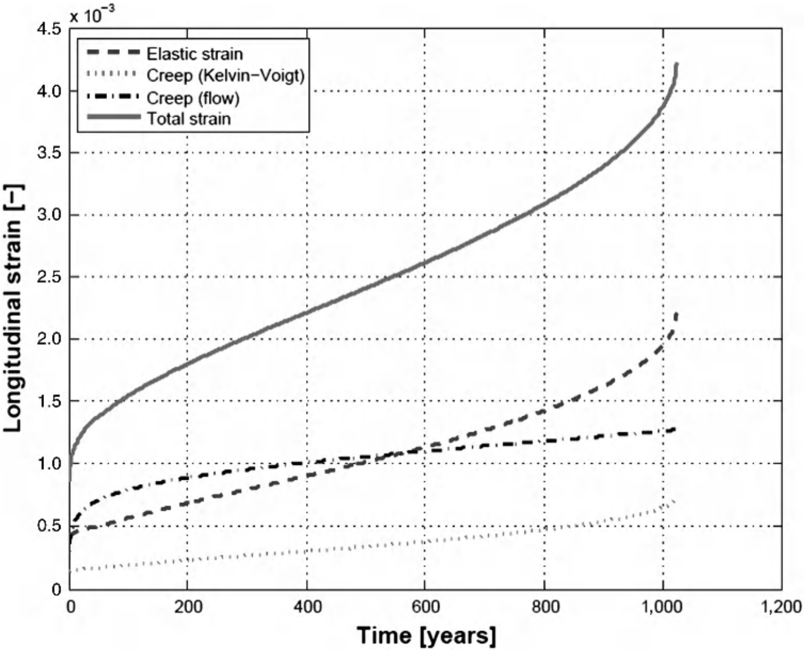

Figure 7.8. *Elastic strain* ε_e, *flow creep strain* $\hat{\varepsilon}$, *Kelvin–Voigt creep strain* $\tilde{\varepsilon}$, *and total strain* ε *time evolutions*

7.5. Conclusions

Creep and damage are coupled phenomena that lead to tertiary creep and then failure in case of a high level of loading compared to the strength of concrete. This coupling could be taken into account by means of a creep model coupled to a mechanical damage model. Creep strain evolution is modeled here with the microprestress solidification theory. The mechanical damage evolution is proposed by Mazars and the coupling between creep and damage is obtained by introducing a part of the creep strain through a coupling coefficient in the evolution of damage. This coupling allows modeling the experimental behavior.

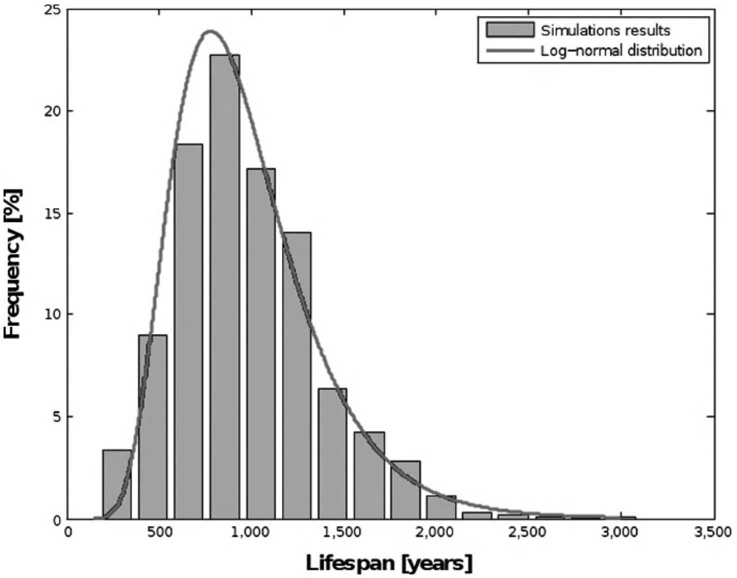

Figure 7.9. *Lifetime distribution for the 1,000 concrete structures simulated: accordance between the simulations results and a log-normal distribution*

When concrete is also submitted to leaching, a chemical coupling has to be taken into account. A model for calcium leaching based on the calcium mass balance equation is used. Assuming that only the sound zone of concrete is able to sustain stresses, the damage evolution with time of a concrete column under pure compression and exposed to leaching and creep, at the same time, could be forecast. Assuming a Beta distribution of all the parameters of the model, a probabilistic study shows that the lifetime of this simple structure is distributed according to a log-normal law.

7.6. Bibliography

[ADE 92] ADENOT F., Durabilité du béton: caractérisation et modélisation des processus physiques et chimiques de dégradation du ciment, PhD Thesis, University of Orléans, 1992 (in French).

[BAN 01] BANGERT F., KUHL D., MESCHKE G., "Finite element simulation of chemo-mechanical damage under cyclic loading conditions", in DE BORST J., MAZARS R., PIJAUDIER-CABOT G., VAN MIER J. (eds), *Proceedings of the International Conference FRAMCOS-4, Balkema Rotterdam, Fracture Mechanics of Concrete Structures*, vol. 1, p. 145–152, 2001

[BAŽ 89] BAŽANT Z.P., PRASANNAN S., "Solidification theory for concrete creep. Part I: formulation", *Journal of Engineering Mechanics*, vol. 115, no. 8, pp. 1691–1703, 1989.

[BAŽ 97] BAŽANT Z.P., XIANG Y., "Crack growth and life time of concrete under long time loading", *Journal of Engineering Mechanics*, vol. 123, no. 4, pp. 350–358, 1997.

[BEN 05] BENBOUDJEMA F., MEFTAH F., TORRENTI J.M., "Interaction between drying, shrinkage, creep and cracking phenomena in concrete", *Engineering Structures*, vol. 27, pp. 239–250, 2005.

[BEN 08] BENBOUDJEMA F., TORRENTI J.M., "Early age behaviour of concrete nuclear containments", *Nuclear Engineering and Design*, vol. 238, no. 10, pp. 2495–2506, October 2008.

[BER 04] BERTHOLLET A., GEORGIN J.F., REYNOUARD J.M., "Fluage tertiaire du béton en traction", *Revue européenne de Génie Civil*, vol. 8, nos. 2–3, pp. 235–260, 2004.

[BRI 11] BRIFFAUT M., BENBOUDJEMA F., NAHAS G., TORRENTI J.M., "Numerical analysis of the thermal active restrained shrinkage ring test to study the early age behavior of massive concrete structures", *Engineering Structures*, vol. 33, no. 4, pp. 1390–1401, 2011.

[BRO 05] BROOKS J.J., "30-year creep and shrinkage of concrete", *Magazine of Concrete Research*, vol. 57, no. 9, pp. 545–556, 2005.

[BUI 92] BUIL M., REVERTÉGAT E., OLIVER J., "A model of the attack of pure water or undersaturated lime solutions on cement", *American Society for Testing and Materials*, Philadelphia, vol. 2, pp. 227–241, 1992.

[CAR 96] CARDE C., FRANCOIS R., TORRENTI J.M., "Leaching of both calcium hydroxide and CSH from cement paste: modeling the mechanical behavior", *Cement and Concrete Research*, vol. 26, no. 8, pp. 1257–1268, 1996.

[CAR 97] CARPINTERI A., VALENTE S., ZHOU F.P., FERRARA G., MELCHIORRI G., "Tensile and flexural creep rupture tests on partiallydamaged concrete specimens", *Materials and Structures*, vol. 30, pp. 269–276, June 1997.

[CHA 05] CHALLAMEL N., LANOS C., CASANDJIAN C., "Creep damage modelling for quasi-brittle materials", *European Journal of Mechanics A / Solids*, vol. 24, pp. 593–613, 2005.

[DEN 06] DENARIÉ E., CÉCOT C., HUET C., "Characterization of creep and crack growth interactions in the fracture behavior of concrete", *Cement and Concrete Research*, vol. 36, pp. 571–575, 2006.

[LAR 10a] DE LARRARD T., BENBOUDJEMA F., COLLIAT J.B., TORRENTI J.M., DELERUYELLE F., "Concrete calcium leaching at variable temperature: experimental data and numerical model inverse identification", *Computational Materials Science*, 2010, doi:10.1016/j.commatsci.2010.04.017.

[LAR 10b] DE LARRARD T., BENBOUDJEMA F., COLLIAT J.B., TORRENTI J.M., DELERUYELLE F., "Uncertainty propagation on damage evolution of a concrete structure submitted to coupled leaching and creep", *EJECE*, vol. 14, nos. 6–7, pp. 891–921, 2010.

[GER 96] GÉRARD B., Contribution des couplages mécaniques-chimie-transfert dans la tenue à long terme des ouvrages de stockage de déchets radioactifs, PhD Thesis, ENS Cachan, 1996.

[GÉR 98] GÉRARD B., PIJAUDIER-CABOT G., LABORDERIE C., "Coupled diffusion-damage modelling and the implications on failure due to strain localization", *International Journal of Solids and Structures*, vol. 35, nos. 31–32, pp. 4107–4120, 1998.

[ILL 65] ILLSTON J.M., "The components of strains in concrete under sustained compressive stress", *Magazine of Concrete Research*, vol. 17, no. 50, pp. 21–28, 1965.

[KAY 79] MCKAY M.D., CONOVER W.J., BECKMAN R.J., "A comparison of three methods for selecting values of input variables in the analysis of output from a computer code", *Technometrics*, vol. 21, pp. 239–245, 1979.

[KIR 83] KIRKPATRIC S., GELATT C.D., VECCHI M.P., "Optimization by simulated annealing", *Science*, vol. 220, no. 4598, pp. 671–680, 1983.

[KUH 03a] KUHL D., BANGERT F., MESCHKE G., "Coupled chemo-mechanical deterioration of cementitious materials. Part 1: modeling", *International Journal of Solids and Structures*, vol. 41, pp. 15–40, 2003.

[KUH 03b] KUHL D., BANGERT F., MESCHKE G., "Coupled chemo-mechanical deterioration of cementitious materials. Part 2: numerical method and simulation", *International Journal of Solids and Structures*, vol. 41, pp. 41–67, 2003.

[LI 94] LI Z., "Effective creep Poisson's ratio for damages concrete", *International Journal of Fracture*, vol. 66, pp. 189–196, 1994

[MAZ 86] MAZARS J., "A description of micro and macroscale damage of concrete", *Engineering Fracture Mechanics*, vol. 25, pp. 729–737, 1986.

[MAZ 03] MAZOTTI C., SAVOIA M., "Non linear creep damage model for concrete under uniaxial compression", *Journal of Engineering Mechanics*, vol. 129, no. 9, 2003, doi:10.1061/(ASCE)0733-9399.

[NGU 07] NGUYEN V.H., COLINA H., TORRENTI J.M., BOULAY C., NEDJAR B., "Chemomechanical coupling behaviour of leached concrete. Part 1: experimental results", *Nuclear Engineering and Design*, vol. 237, pp. 2083–2089, 2007.

[OMA 04] OMAR M., PIJAUDIER-CABOT G., LOUKILI A., "Etude comparative du couplage endommagement – fluage", *Revue Française de Génie Civil*, vol. 8, pp. 457–482, 2004.

[REV 09] REVIRON N., Etude du fluage des bétons en traction. Application aux enceintes de confinement des centrales nucléaires à eau sous pression, thèse de doctorat de l'ENS de Cachan, 2009.

[ROL 64] ROLL R., "Long time creep-recovery of highly stressed concrete cylinders", *ACI SP-9, Symposium on Creep*, Portland Cement Association, Detroit, pp. 115–128, 1964.

[ROS 94] ROSSI P., GODART N., ROBERT J.L., GERVAIS J.P., BRUHAT D., "Investigation of the basic creep of concrete by acoustic emission", *Materials and Structures*, vol. 27, no. 9, pp. 510–514, 1994.

[RÜS 60] RÜSCH H, "Researches toward a general flexural theory for structural concrete", *ACI Journal*, vol. 32, no. 1, pp.1–28, 1960.

[SAE 98] SAETTA A., SCOTTA R., VITALIANI R., "Mechanical behavior of concrete under physical-chemical attacks", *Journal of Engineering Mechanics (ASCE)*, vol. 124, pp. 1100–1109, 1998.

[SEL 11a] SELLIER, A., BUFFO-LACARRIÈRE L., EL GONNOUNI M., BOURBON X., "Behavior of HPC nuclear waste disposal structures in leaching environment", *Nuclear Engineering and Design*, vol. 241, no. 1, pp. 402–414, 2011.

[SEL 11b] SELLIER A., MULTON S., BUFFO-LACARRIÈRE L., Non linear Creep Modelling, LMDC Report no. 03-201, 2011.

[SMA 87] SMADI M.M., SLATE F.O., NILSSON A.H., "Shrinkage and creep of high, medium and low strength concrete, including overloads", *ACI Materials Journal*, vol. 84, no. 3, pp. 224–234, 1987.

[SMA 89] SMADI M.M., SLATE F.O., "Microcracking of high and normal strength concretes under short and long term loadings", *ACI Materials Journal*, vol. 86, no. 2, pp. 117–127, 1989.

[TOR 08] TORRENTI J.M., NGUYEN V.H., COLINA H., LE MAOU F., BENBOUDJEMA F., DELERUYELLE F., "Coupling between leaching and creep of concrete", *Cement and Concrete Research*, vol. 38, no. 6, pp. 816–821, 2008.

[ULM 99] ULM F.J., TORRENTI J.M., ADENOT F., "Chemoporoplasticity of calcium leaching in concrete", *Journal of Engineering Mechanics*, vol. 125, no. 10, pp. 1200–1211, 1999.

Chapter 8

Study of Damages and Risks Related to Complex Industrial Facilities

8.1. Context

The design or the life extension of complex industrial structures involves different processes. One of them is the technical evaluation of the performance of the systems according to predefined requirements.

Several techniques can be used to assess the technical performance of civil engineering structures. The process to analyze the results requires computation simulators. These simulators allow formalizing a global vision of the performance of a complex structure and can help designers or project managers to extrapolate the results in time, to do impact analysis, identify main factors for risk management, and so on.

During the past 20 years, the scientific community has successfully developed a very high level of understanding in various disciplines of civil engineering. It has provided incredible new tools, models, and powerful simulators to the

---

Chapter written by Bruno GERARD, Bruno CAPRA, Gaël THILLARD and Christophe BAILLIS.

industry. Nevertheless, there remain three fundamental issues to be correctly applied from universities to industry: i) a methodology to define the technical requirements and how to use the results in the global process of decision-making, ii) a rigorous process to conduct such simulations in a quality insurance perspective, and iii) to have well-educated engineers able to make a jump between theory and industrial reality where only a small portion of required inputs are available.

The aim of this chapter is to contribute to formalize this industrial vision of risk and performance assessment of complex structures. The authors have chosen to illustrate the proposed methodology with a specific application combining several difficulties to be solved from the industrial point of view: the performance assessment of a high-stake prestressed structure with respect to an airplane crash.

8.2. Introduction to risk management

Risk management is a process that is used in industry to make decisions. This process involves several steps, as illustrated in Figure 8.1.

The risk estimation uses the simple formula that combines the probability of an event appearing multiple times by its impact on the different issues (availability of the service, safety, financial, environment, etc.). When studying a complex structure with respect to the numerous threats likely to affect it, it is possible to generate different risk profiles as a function of different parameters like materials aging, the local level of the regulations (standards, requirements, etc.), the environment of the structure (surrounding people, severity of climate, etc.). Figure 8.2 shows an example of the risk profile for a structure or a portfolio of structures. This kind of methodology offers a visualization of the priorities (dark gray risks must be treated as a priority compared to light gray risks) to the decision maker.

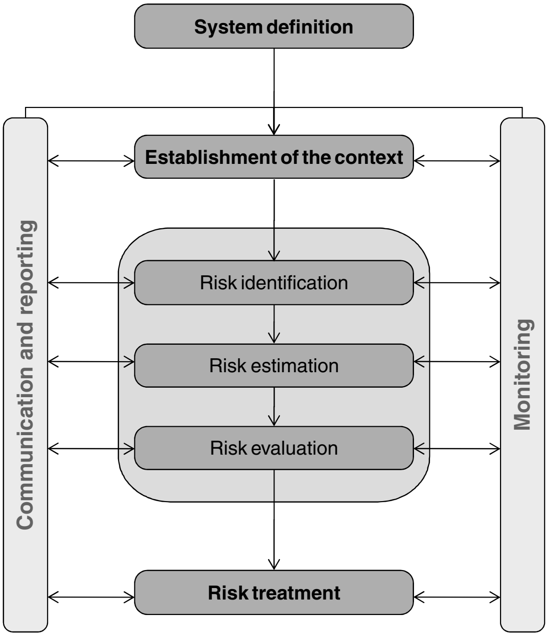

Figure 8.1. *Risk management process (adapted from ISO 31000)*

To be able to quantify the risks, several techniques are used: i) databases for the probability of events, ii) expert advice for impact assessment and probability estimations, and iii) numerical simulations.

For civil engineering structures, it is difficult to use the database to evaluate the probability. Indeed, there are rarely identical structures; the comparison of each past event is difficult as many reasons can create a difference between two apparently identical structures: construction process, season of construction, concrete materials, etc. This is the main reason why civil engineers have started using risk management methodologies recently compared to other industries where available feedback is more important. With the development of numerical simulations, it has been possible to quantify inputs in terms of probability and also the impacts of a failure due to a specific event.

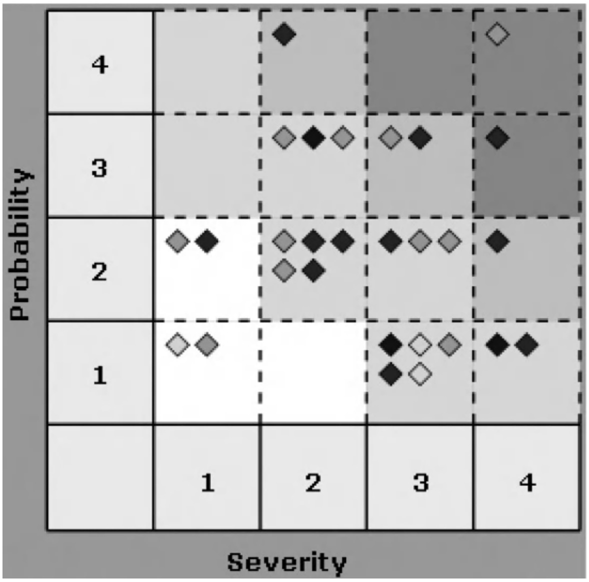

Figure 8.2. *Example of a risk profile for a system of structures*

8.3. Case study: computation process

Generally, an industrial project is subject to different types of external constraints: costs, delays, quality assurance of results, authority requirements, etc. (see Figure 8.3). Consulting firms advise/assist clients to answer questions on the subject to be analyzed ensuring quality of response, in alignment with the restrictions. This allows the client to make decisions or to implement relevant actions. For numerical calculations, the notion is not to seek a more realistic modeling, but to use a fairer modeling in terms of complexity, which would be more suitable to the constraints of the problem.

The flow diagram shown in Figure 8.4 presents the methodology which is supported by the questions/difficulties underlined and overcome in a particular study: mechanical behavior study of a prestressed concrete structure such as liquid natural gas (LNG) tanks or nuclear power containment (that is, structures presenting similar prestressed biaxial thick-walled cylinders). The steps mentioned in this flow diagram are detailed in the following sections.

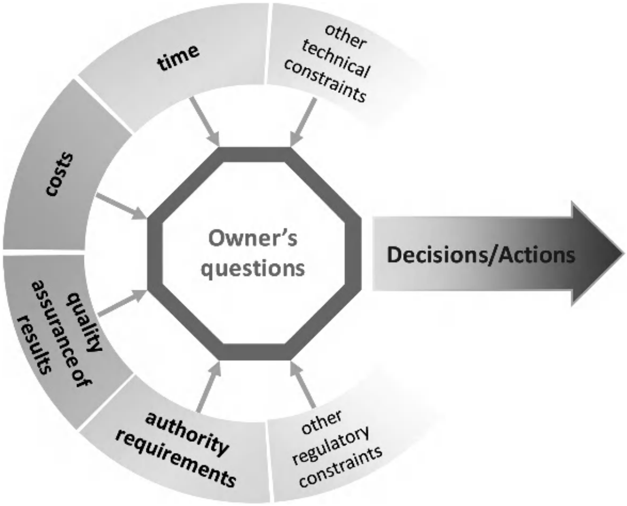

Figure 8.3. *Constraints of an industrial project*

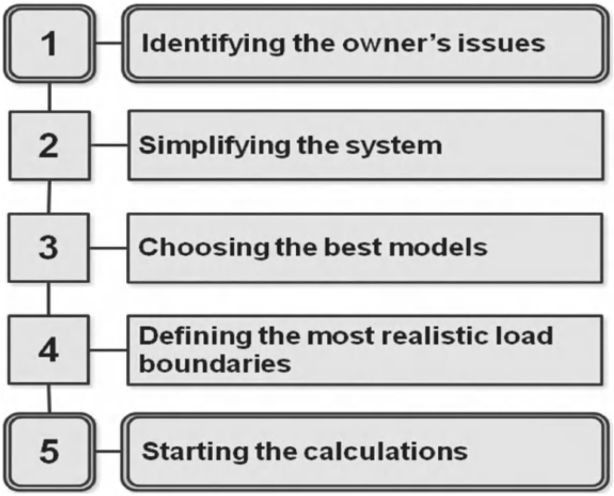

Figure 8.4. *Flow diagram*

8.3.1. *Identifying the owner's issues*

The owner's main issues concerning, for example, mechanical behavior of a structure following an aircraft crash involve investigating both concrete containment integrity and confinement functions. These issues involve knowing whether impacted structures will still be able to hold overall and local mechanical functions and have a total or partial confinement performance. This study considers only direct plane crash impact on the prestressed concrete wall by numerical computations.

8.3.2. *Simplifying the system*

The first step is to create a mesh of the existing structure from available data in the owner's archives: geometric data of concrete, densities of reinforcement rebars and tendons, etc. obtained from design engineering notes and drawings.

To optimize the computation time, the symmetries of i) geometry and ii) loading are used leading to the modeling of half a structure:

1) The overall geometry of the structure is considered perfectly axisymmetric. The study focuses on the mechanical response of the structure to the crash impact. The local singularities such as overflow, temporary construction openings, crossing pipes, and horizontal tendons anchorage system are neglected on the mesh (see Figure 8.5).

2) The impact is applied to an area at the plane of symmetry.

In order to optimize the mesh size of the structure without degrading the quality of the results, the numerous foundation piles are not modeled individually but represented by rings to take into account the boundary conditions.

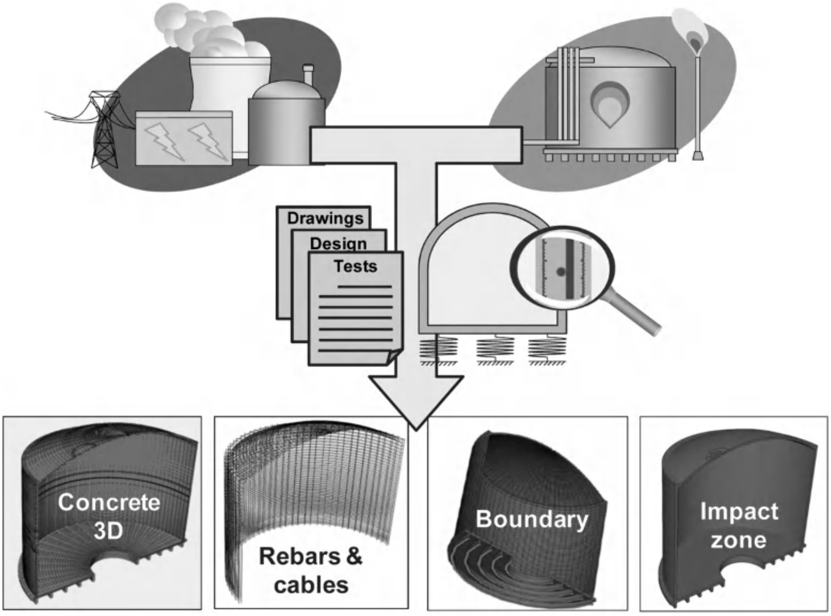

Figure 8.5. *Simplifications of the computed structures*

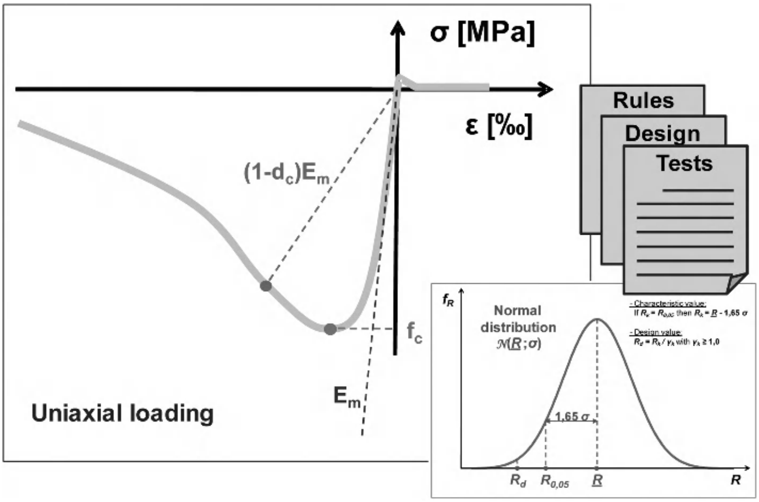

Figure 8.6. *Definition of a model for concrete*

8.3.3. *Choosing the best models*

To represent a modeling concept closer to reality, material behavior models used are nonlinear and consist of parameter values determined from values obtained by measurements made on site and completed by design concepts and data obtained from literature to control incertitude and randomness (see Figure 8.6). Nonlinear models represent the actual behavior patterns of aging damage model of concrete in the reservoirs and the elastic–plastic model of steel components.

8.3.4. *Defining the most realistic load boundaries*

In order to determine the thermomechanical initial state of the concrete structure (stress and strain fields), through specific finite-element analysis before dynamic effect computations due to crash impact, it is necessary to know the type of operating loads applied to the model.

8.3.4.1. *Operating loads*

The concrete structure is supposed to be subject to mean (or quasi-permanent) values of each operating load. These loads are particularly defined from the operator feedback and may be supplemented by aging-specific studies. They include non-exhaustively:

– dead loads (weight of materials);

– biaxial prestressing force on the concrete structure: the prestressing level may take into account some potential delayed losses caused by concrete shrinkage and creep or relaxation cables, but can also be considered as constant along the prestressing components (to produce a mean and homogeneous prestressed field);

– usual internal hydrostatic pressure;

– steady thermal gradient: when a thermal insulation system is present in the structure, the system aging may be taken into account (reduction of thermal capacities).

8.3.4.2. *How can we assess extreme load during the crash?*

The aircraft's technical characteristics are available from the manufacturer's website:

– the aircraft mass is assumed to be to its full capacity (fuel and payload);

– the impact surface is defined from the dimensions of the cabin; it is assumed constant during the impact (not time dependent);

– by default, for a civil aircraft, the impact velocity is assumed equal to 100 m/s (value usually described in [EDF 88] and [IAE 03]); this value may be adjusted on the basis of available data from air traffic control authorities.

The aircraft impact is modeled from [RIE 68] and [ABB 95]. These studies are based on experimental results obtained for three kinds of aircraft: Phantom F4, F111, and Boeing 707-320 (the first two are military aircraft, while the third is a civil transport aircraft). Modeling requires some data that are extremely difficult to get for a specific aircraft (for example, the crushing resistance and the distribution of mass along the axis of the plane). In the absence of specific information, extrapolations are made here from the experimental curves available for the Boeing 707-320. The other main assumptions of modeling, illustrated in Figure 8.7, are:

– the projectile (the aircraft) is a one-dimensional object and causes a total stress that is distributed uniformly over the surface of impact;

– the trajectory of the aircraft coincides with the axis of the projectile and the impact is assumed normal to the target (the LNG tank or the containment);

– the projectile is considered highly deformable compared to the target (soft impact conditions);

– the whole aircraft is crushed during the impact.

Two, *a priori* disadvantageous, areas are chosen for the application of impact loading:

– at the mid-height of the cylinder;

– at the mid-radius of the dome.

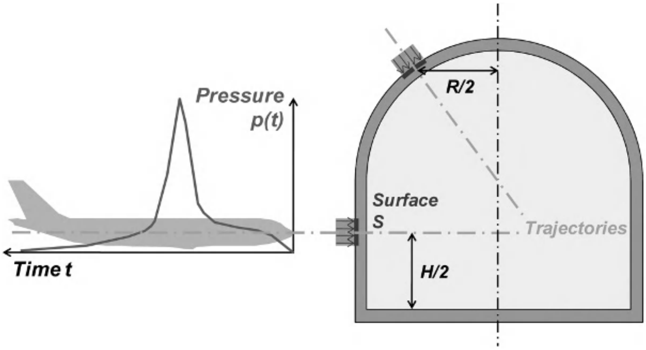

Figure 8.7. *Illustration of impact load cases on structure*

8.4. Application

Now it is possible to create different scenarios of crash impact from modeling assumptions pointed out in steps mentioned in Figure 8.3 (sections 8.3.1–8.3.4) with the help of a software for finite-element analysis. Abaqus software is chosen because of its wide material modeling capability, and its ability to be customized.

The main contribution of numerical simulations is to evaluate the mechanical behavior deviations related to differences between the event "impact of dynamic loading design" and the event "impact of the aircraft crash in real conditions" and the assumptions regarding each of these events.

8.4.1. *Deformed structure after impact*

8.4.1.1. *Impact at the mid-height of the cylinder*

The maximum displacement of the cylinder, at the peak of the impact pressure, is presented at the center of the impact surface (see Figure 8.8). Once equilibrium is re-established, i.e. after the duration of the impact, the structure retains a residual deformation whose amplitude is approximately three times lower than the maximum value. The amplitude of displacement decreases concentrically outwards from the center of the impact surface.

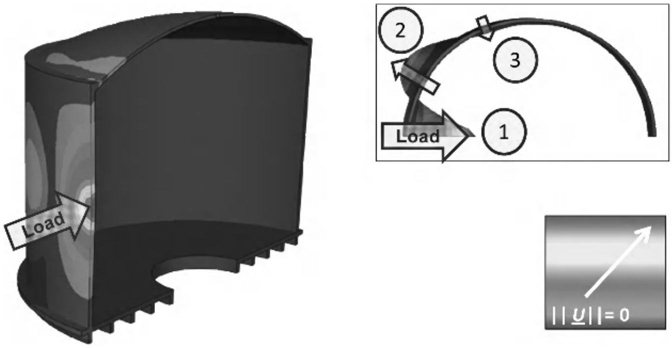

Figure 8.8. *Deformed structure after impact on the cylinder*

Figure 8.8 illustrates the effects of impact on the cylinder causing attenuated waves around the circular geometry of the impact zone. Three main areas, showing that the impact zone produces a significant impact on about half of the cylinder structure, are distinguished:

– in zone 1, corresponding to the impact zone, the cylinder structure penetrates into the reservoir and the double bending created by the shock exerts a tensile force on the inner surface of the cylinder;

– in zone 2, the impact creates a reaction causing the cylinder structure to push outward the reservoir (first wave), this time creating a tensile force in the outer surface of the cylinder;

– in zone 3, the wave produced by the impact tends to end and the structure deformation is similar to zone 1 with a lower amplitude leading to the apparition of tensile forces on the inner surface of the cylinder.

8.4.1.2. *Impact at the mid-radius of the dome*

Figure 8.9 illustrates the displacement in the central area of impact on the mid-radius of the dome. At the end of impact a residual deformation is retained by the structure whose amplitude is approximately four times lower than the maximum value.

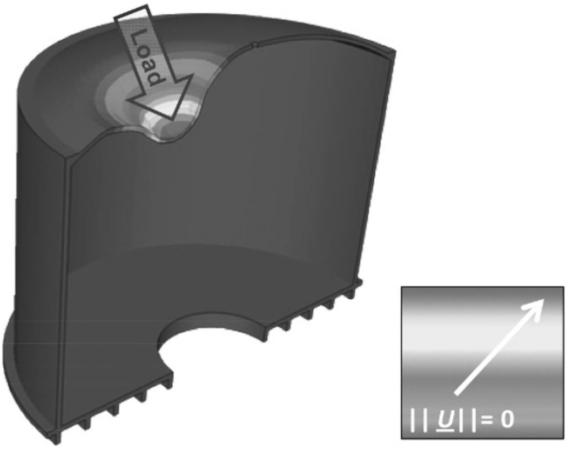

Figure 8.9. *Deformed structure after impact at the mid-radius of the dome (with amplification factor)*

8.4.2. *Damage variables of concrete*

8.4.2.1. *Damages to cylinder*

Figure 8.10 illustrates the tensile damage zones (light to dark colors shown the increased damage, i.e. the degree of damage parameter d_t). Three regions, coinciding with the oscillations consequences of impact, are identified in the structure:

– zone 1, which corresponds to the region where the concrete damage is more severe, has also two subareas with different levels of damage: subarea at the level of impact (area indicated in Figure 8.10 with dashed lines, where the total damage of concrete is present on about two-thirds of the wall) and subarea of partial damage on the rest of the height of the inner surface;

– zone 2, where a partial damage to the entire thickness of the concrete and a high risk of cracking due to transverse singularities of the structure (e.g. local concrete of poor quality) is appreciated;

– zone 3, where the beginning of damages is also present on the inner side of the reservoir.

Apparently, there is no significant damage to the concrete dome as a result of the impact on the cylinder.

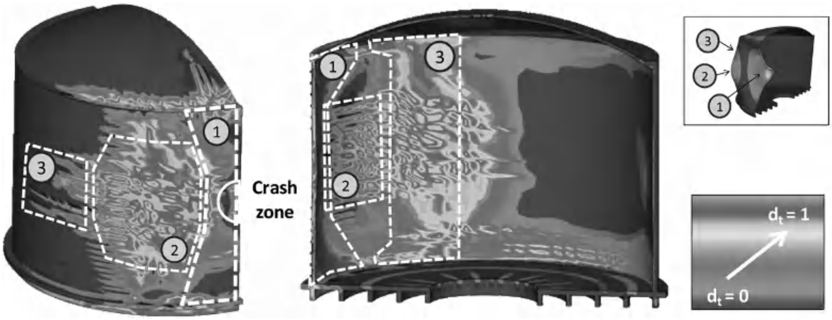

Figure 8.10. *Damages to concrete cylinder structure after an airplane impact*

Figure 8.11 shows concrete damages due to compressive force (crushing) near the impact area.

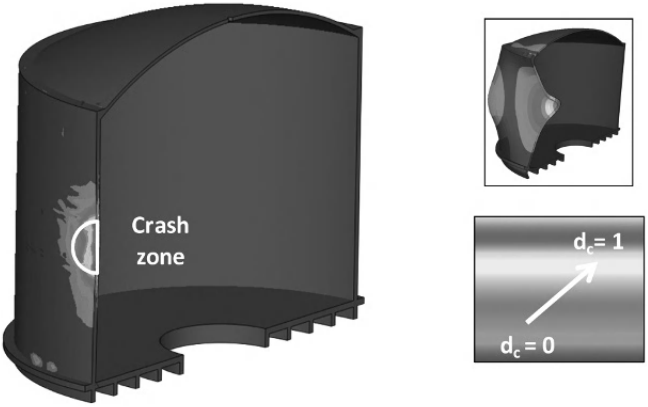

Figure 8.11. *Damages to concrete cylinder structure after an airplane impact*

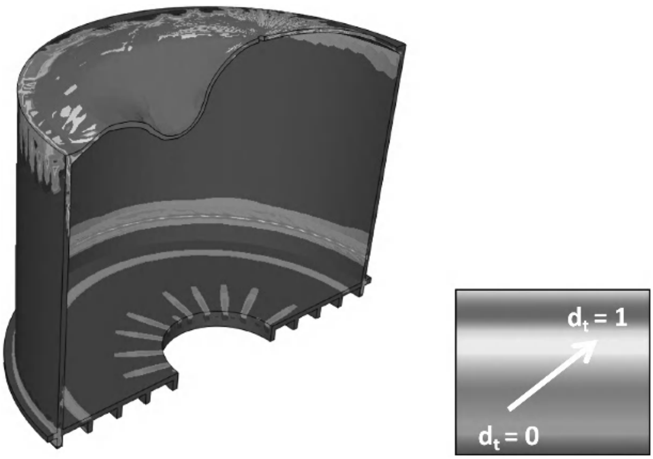

Figure 8.12. *Damages to concrete dome structure after an airplane impact*

8.4.2.2. *Damages to dome*

The damage to the concrete dome is severe at more than half of the surface (see Figure 8.12) and full thickness. The shock to the dome does not seem to affect the concrete cylinder structure; however, a significant damage at the junction of the cylinder and the dome near the impact is appreciated and could weaken the support of the cover.

Observed local plasticity in the impact zone does not reach the limit state of rupture.

8.4.3. *Analysis of results*

After completing the numerical calculations, the results should be analyzed to answer the owner's initial question: "*What are the impact consequences on the confinement functions of the tank?*"

The simulations have shown local material damages that should not affect the global mechanical stability of the reservoir. Therefore, the effects on the sealing capacity of concrete structure remain to be assessed.

8.4.3.1. *Impact analysis of aircraft crash at the mid-height of the cylinder*

The levels of concrete damages and plasticity of the concrete cylinder structure indicate that the structure resists direct mechanical effects of impact relatively well. Cracking occurs in areas where deformations are more important. As a direct consequence of impact, the overall mechanical stability of the reservoir is not questioned, neither the direct loss of capacity of the containment (although it should be checked whether the local behavior of the membrane is directly impacted). However, there is a decrease in the capacity of gas containment in the direct impact zone

(zone of transverse cracks, which is shown in dark gray in Figures 8.13 and 8.14) and a decreased ability of gas containment due to internal non-transverse cracks.

8.4.3.2. *Impact analysis of aircraft crash at the mid-radius of the dome*

The impact of the crash on the concrete dome shows severe damage in more than half of the total area. Particularly, severe local damage is observed at the junction of the dome and the cylinder near the impact. Moreover, the impact on the dome induces weak effects on its components (concrete, steel bars, and prestressed cables), and the passive steel bars, although slightly plasticized, do not reach the threshold of rupture. Likewise, the impact does not lead to a direct loss of capacity of the containment. The holding capacity of the dome could be questioned as to whether the spreading of concrete damage, in the real structure, could cause falls of large concrete blocks or whether there was a detachment of many steel bars of the dome or at the union cylinder/dome.

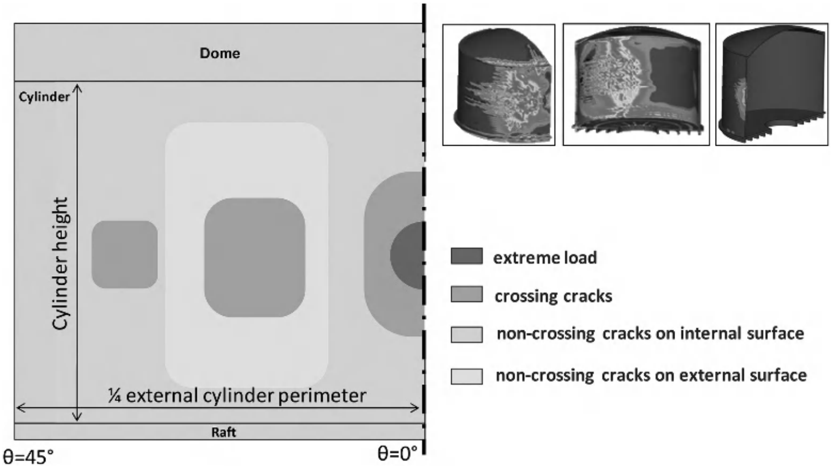

Figure 8.13. *Extreme load on cylinder (damage zones)*

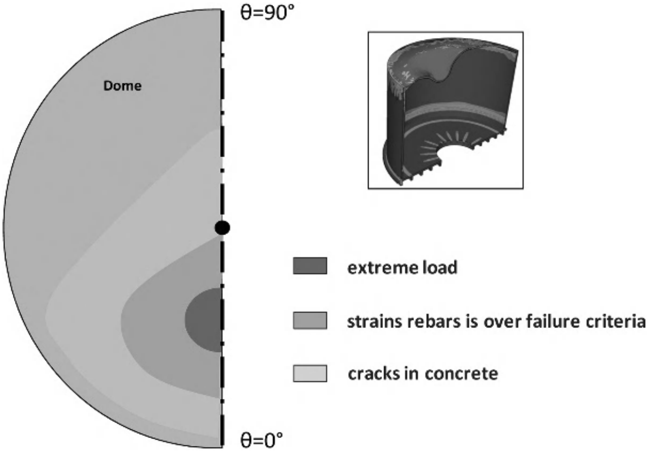

Figure 8.14. *Extreme load on dome (damage zones)*

8.5. Conclusion

This chapter has developed a process to apply most recent computational developments to industrial applications. The authors have considered that such a process requires defining the right level of accuracy needed for answering the industrial requirements. Moreover, it is important to never forget the decisions involved in the end (which issues are concerned). Then, the choice for the code, the models, and the level of simplifications must follow a rigorous process.

In our experimental work, a large part of the work is spent on defining a data set for the inputs in the models. This could be reduced if monitoring of these structures was generalized.

Regarding the previous application, modeling the energy of dissipation of the plane is an important issue. The impact of a fire due to kerosene remains a subject of discussion in the industry. For probability assessment, knowledge of uncertainties is required, and it is necessary to be performed with:

– on-site data (quality of monitoring and inspections);

– quality of material models.

8.6. Acknowledgment

The authors thank Dr. H. Yanez-Godoy from OXAND, France, for advice and support in writing this chapter.

8.7. Bibliography

[ABB 95] ABBAS H., PAUL D.K., GODBOLE P.N., NAYAK G.C., "Reaction-time response of aircraft crash", *Computers and Structures*, vol. 55, no. 5, pp. 809–817, 1995.

[AFN 03] NF EN 1990, Eurocodes structuraux – Bases de calculs des structures, AFNOR, 2003.

[AFN 05] NF EN 1992-1-1, Eurocode 2 – Calcul des structures en béton – Partie 1-1: règles générales et règles pour les bâtiments, AFNOR, 2005.

[CRE 03] CREMONA C., Applications des notions de fiabilité à la gestion des ouvrages existants, Presses des Ponts et Chaussées, 2003.

[EDF 88] EDF, Règles de conception et de construction du génie civil des îlots nucléaires REP, RCC-G, Tome I – Conception, AFCEN, 1988.

[IAE 03] IAEA, External Events Excluding Earthquakes in the Design of Nuclear Power Plants, Annexe I Aircraft Crash, Safety Guide, NS-G-1.5, IAEA, 2003.

[RIE 68] RIERA J.D. "On the stress analysis of structures subjected to aircraft impact forces", *Nuclear Engineering and Design*, North Holland Publishing Co., vol. 8, 1968.

Chapter 9

Measuring Earthquake Damages to a High-Strength Concrete Structure

9.1. Introduction

A large-scale dynamic testing project was recently completed on a full-scale, two-storey, reinforced high-performance-concrete (HPC) building. The building, shown in Figure 9.1 in front of a 7 m high reaction wall, was subjected to repeated pseudo-dynamic (PSD) and forced vibration tests as part of a research project on the seismic behavior of HPC structures and on damage detection. The main objectives of the tests were 1) to determine the damage and performance under increasing seismic loads applied with PSD testing techniques; 2) to provide experimental evidence for predicting damage under increasing seismic loads, using forced-vibration tests (FVTs); 3) to investigate whether the 55 MPa compressive strength limit in the Canadian standard CSA-A23.3 [CSA 94] is too conservative; 4) to investigate

---

Chapter written by Patrick PAULTRE, Benedikt WEBER, Sébastien MOUSSEAU and Jean PROULX.

the adequacy of the design and detailing requirements for moderate ductility as defined in the Canadian Standard; and 5) to investigate the force modification factor suitable for this structure designed and detailed to exhibit moderate ductility. This chapter will address the first two objectives listed above with an emphasis on i) the design of the test structure; ii) the forced vibration tests; iii) the PSD tests; and iv) damage detection. More details on the other objectives of this research project can be found in [MOU 08a] and [MOU 08b].

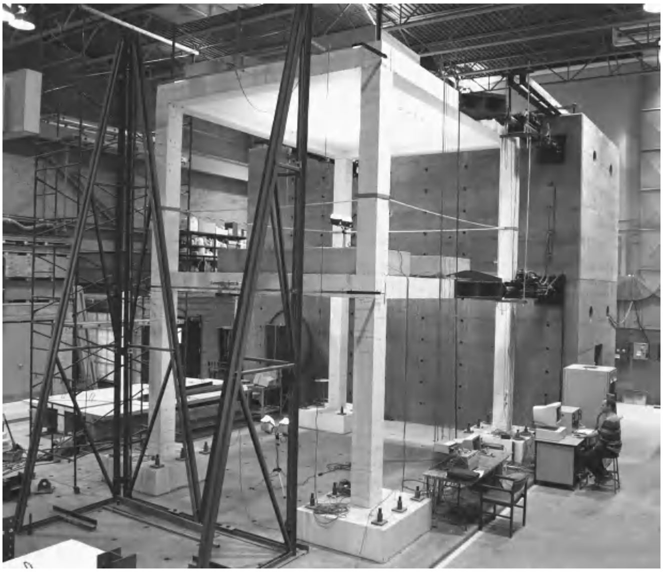

Figure 9.1. *Two-storey reinforced HPC building with reaction wall*

9.2. Overview of the selected testing methods

The PSD technique was used to simulate increasing earthquake loading on the structure with four hydraulic actuators. The input ground motion recording was scaled to five different intensities and successively applied to the building. Since one of the goals was the detection and identification of damage to the structure, FVTs were carried out between each application of the simulated earthquake loadings. Using a shaker mounted on top of the building, the key dynamic properties (vibration frequencies and mode shapes, as well as modal damping ratios) were obtained for each step. As the PSD method requires the development of a precise numerical model for the structure, the FVT results were used to calibrate this model and evaluate its performance. Finally, parameterized models were updated with the dynamic properties at each step to detect stiffness reduction in members and identify damage to the structure.

9.3. Two-storey HPC building

The two-storey reinforced concrete building has a 5 m bay in the E–W direction and a 4 m bay in the N–S direction. The storey height measured from top of slab to bottom of slab is 3 m. The building was designed in accordance with the *National Building Code of Canada* (NBCC) for a moment resisting frame with moderate ductility, located in Montreal (Canada). Typical office building live loads of 2.40 kN/m^2 were used and the snow load was estimated at 2.32 kN/m^2. A superimposed dead load of 1.70 kN/m^2 – corresponding to mechanical services, floor finishing, and partition loading – was used for the first floor, while a superimposed dead load of 2.10 kN/m^2 was used for the roof to account for mechanical services and insulation weight. Plan and elevation views of the building are shown in Figure 9.2.

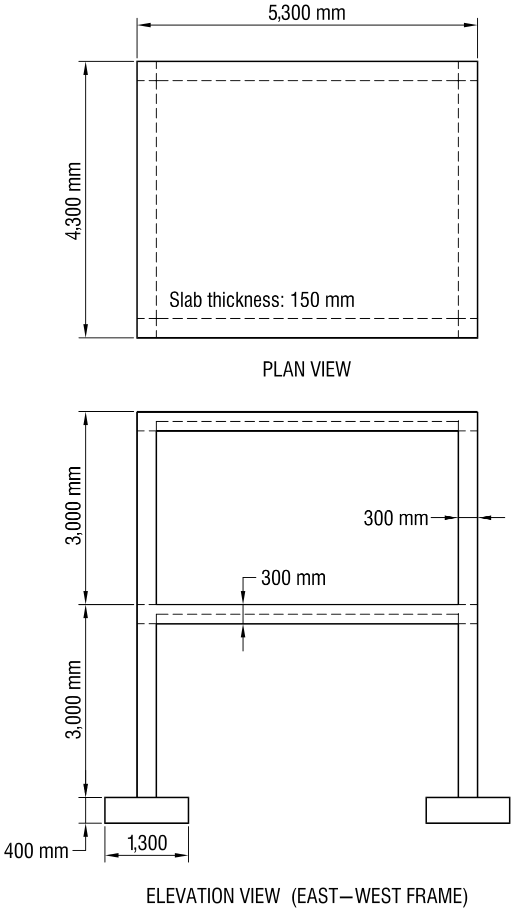

Figure 9.2. *Plan and elevation views of the building*

Figure 9.3 shows the seismic loads of moment-resisting frames with moderate ductility built in Montreal according to 2005 NBCC provisions [NRCC 05]. The graph illustrates base shear coefficient, expressed as the ratio of the base shear over the weight of the building (V/W), as a function of the fundamental lateral period of vibration. Using the specified equation for estimating the fundamental period of the two-storey, 6 m high moment resisting frame, and a finite-element model, values of 0.2875 and 0.4313 s were obtained and are shown in Figure 9.3.

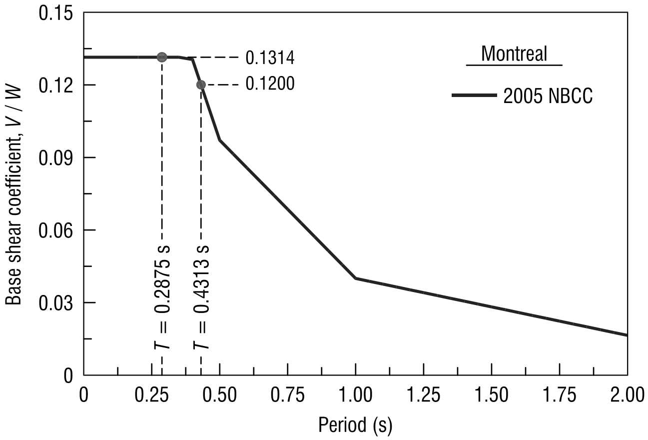

Figure 9.3. *Base shear coefficient* (V/W) *for reinforced concrete moderately ductile moment-resisting frames in Montreal*

Design and detailing of the structural members were in agreement with the special provisions for seismic design of CSA A23.3-94 *Design of Concrete Structures* [CSA 94], but accounted for new requirements of the 2004 edition [CSA 04]. The columns are all 300 mm × 300 mm. The two-way slab floor system consists of a 150-mm-thick slab supported by beams 300 mm × 300 mm on all four sides. The specified concrete strength was 70 MPa and the specified steel yield strength was 400 MPa. Some reinforcement details of the building are illustrated in Figure 9.4.

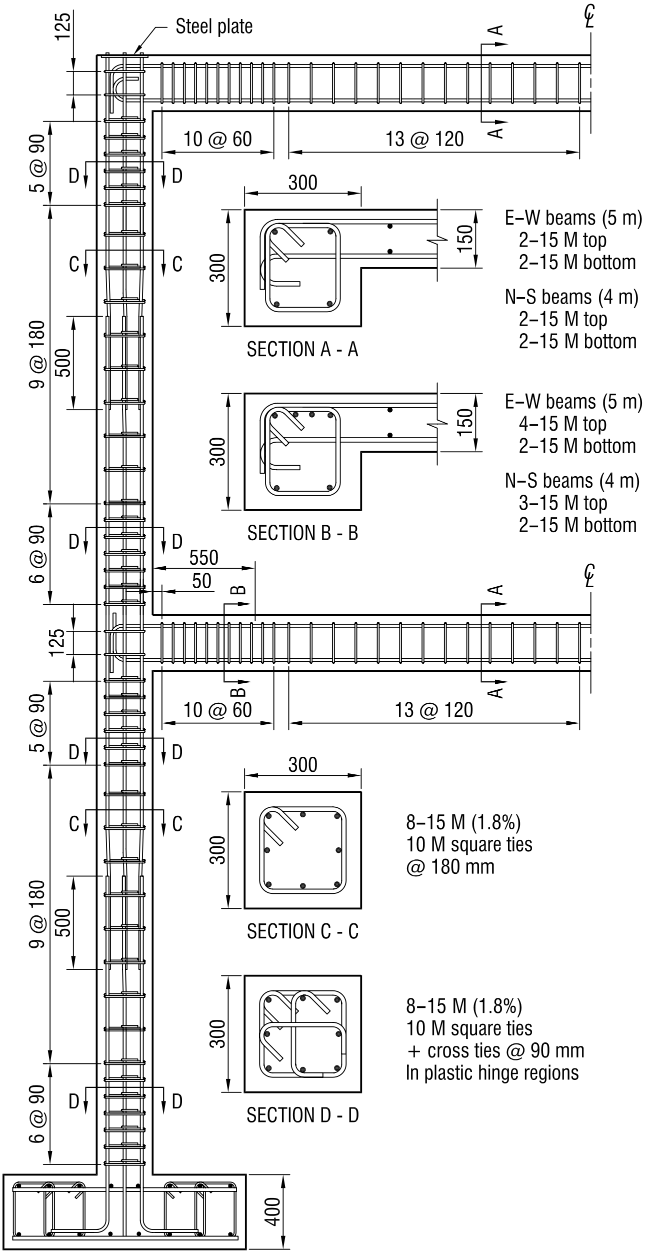

Figure 9.4. *Reinforcement details of beams and columns*

9.4. Inducing damage – pseudo-dynamic testing procedures

Damage was induced by repeated simulated earthquake loading using the PSD testing method. This technique involves an interactive closed-loop testing procedure where a computer program is used to predict the incremental displacements to be imposed on the structure for each time step. After receiving nonlinear force response feedback from the actual specimen subjected to the tests, the program predicts the next displacement step. This process is carried out for the duration of a particular input accelerogram. Therefore, measurements of the actual stiffness properties of the structure provide a realistic simulation of the dynamic response histories. The computer program solves the equations of motion for a discrete parameter model of the test structure using a step-by-step numerical time-integration method. While inertial and viscous damping forces are modeled analytically with known and measured quantities, respectively, the nonlinear structural restoring forces are measured experimentally because of the difficulty in modeling them accurately. In this way, the process automatically accounts for the hysteretic damping due to inelastic deformation and damage of the structural materials, which are the two major sources of energy dissipation.

PSD tests essentially require the same equipment as conventional quasi-static tests, in which prescribed histories of load or displacement are imposed on specimen structures by means of displacement-controlled hydraulic actuators. In this project, the lateral seismic loads were applied to the building by four 500 kN dynamic-rated servo-hydraulic actuators (as seen in Figure 9.1) reacting on the reaction wall. Two actuators were placed on each floor level and were attached at mid-span of the slabs and spandrel beams running in the E–W direction. The imposed displacements were measured with respect to two independent steel frames (as seen in Figure 9.1 in the foreground) using displacement transducers. The two-storey building was fully instrumented with strain gauges to measure the deformations in the longitudinal reinforcement in the beams, columns, and slabs, and in the transverse reinforcement in the columns and beams.

The stiffness matrix used for the PSD test is a 2×2 full matrix corresponding to a system with two degrees of freedom, one at each floor level. The initial-state stiffness matrix for the structure was determined by carrying out a preliminary static displacement test on the building. The mass matrix is a 2×2 diagonal matrix with the masses concentrated at the floor level. The damping matrix was obtained from the FVT results (described below), with modal damping information retrieved directly from the complete frequency response curves. The time-integration scheme adopted is based on the α-method [HIL 77], which is an unconditionally stable implicit algorithm. A time step of 0.02 s was used with the algorithm. The total duration of the PSD test for one ground motion record was approximately 1 h.

9.4.1. *Input ground motion*

The building was designed for a peak ground acceleration (PGA) of 0.180 g, which corresponds to a probability of exceedance of 10% in 50 years for Montreal (Canada). Two different accelerograms were used for the PSD test. The first ground motion was the S00E component of the accelerogram recorded in El Centro, California, during the May 18, 1940, Imperial Valley earthquake. The first 30 s time history for the input motion is shown in Figures 9.5b and 9.6e. This ground motion was scaled to different intensity levels of 0.078, 0.129, 0.180, 0.270, and 0.430 g to investigate the seismic behavior of the structure under increasing damage.

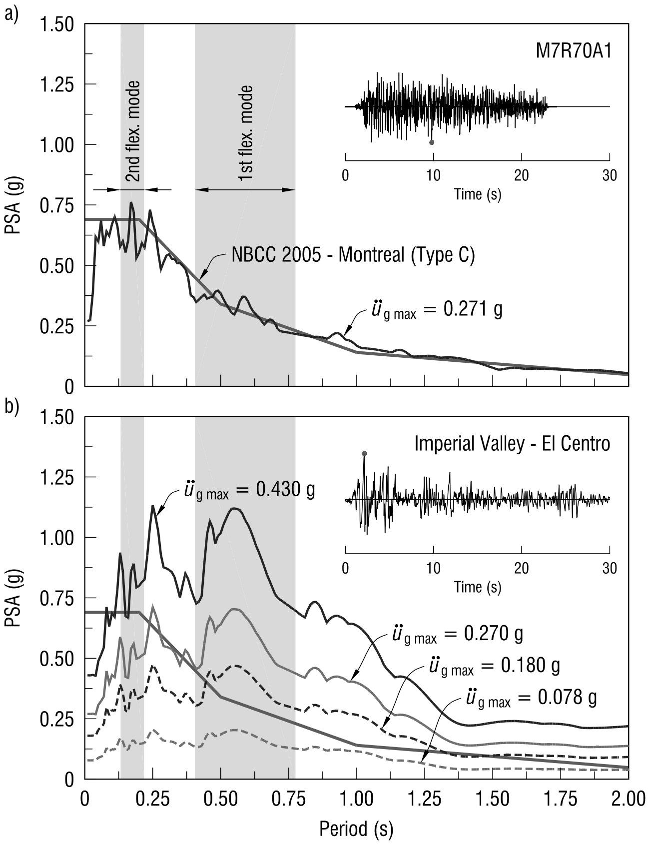

Figure 9.5. *Spectral accelerations of (a) M7R70A1 and (b) El Centro Earthquake N–S component scaled at different levels*

The second time history used to carry out the PSD tests was the M7R70A1 accelerogram generated for Montreal and having a probability of exceedance of 2% in 50 years [ATK 98]. This ground motion is compatible with the uniform hazard spectra (UHS) used in the 2005 NBCC [NRCC 05, ADA 03]. This time history (Figure 9.5a) was generated for a moment magnitude 7.0 earthquake at a hypocentral distance of 70 km. The PGA is 0.271 g. The 2005 NBCC UHS for a very dense soil and soft rock (Class C) site located in Montreal is shown on both graphs in Figure 9.5, along with the period ranges for the first and second flexural modes, obtained from the FVT after each PSD test. The 5% damped PSA response spectra are shown for each ground motion used during the tests. A list of each test carried out on the building is presented in Table 9.1.

9.4.2. *Earthquake responses*

The earthquake responses of the structure, in terms of storey displacements and base shear forces are presented in Figures 9.6 and 9.7, respectively, for different seismic excitation levels of the Imperial Valley earthquake (El Centro accelerogram).

Moderate seismic excitation was achieved by scaling the El Centro ground motion to 0.180 g PGA (Level 3 in Table 9.1) which corresponds to the design level of the building. The structure's earthquake responses are shown in Figures 9.6b and 9.7b. Some period elongation can be observed from the response history. All floor-displacement time histories are in phase, pointing to a dominant first-mode participation. Under this seismic input, the structure exhibited significant cracking in the beams, columns, and slabs, but performed with no yielding of the reinforcement and no spalling of the concrete covers. The building displayed a maximum first-storey displacement of 24.5 mm and a maximum top-storey displacement of 52.4 mm. Maximum storey drifts were 24.5 and 28.3 mm for the first and second stories, which are about 82% and 94% of the maximum 1% interstorey drift of 30 mm allowed by the Canadian code for post-disaster buildings. The maximum base shear measured just reached the design base shear (99.8 kN) in the 2005 NBCC. The test indicates that HPC performs well up to this level of excitation with little damage.

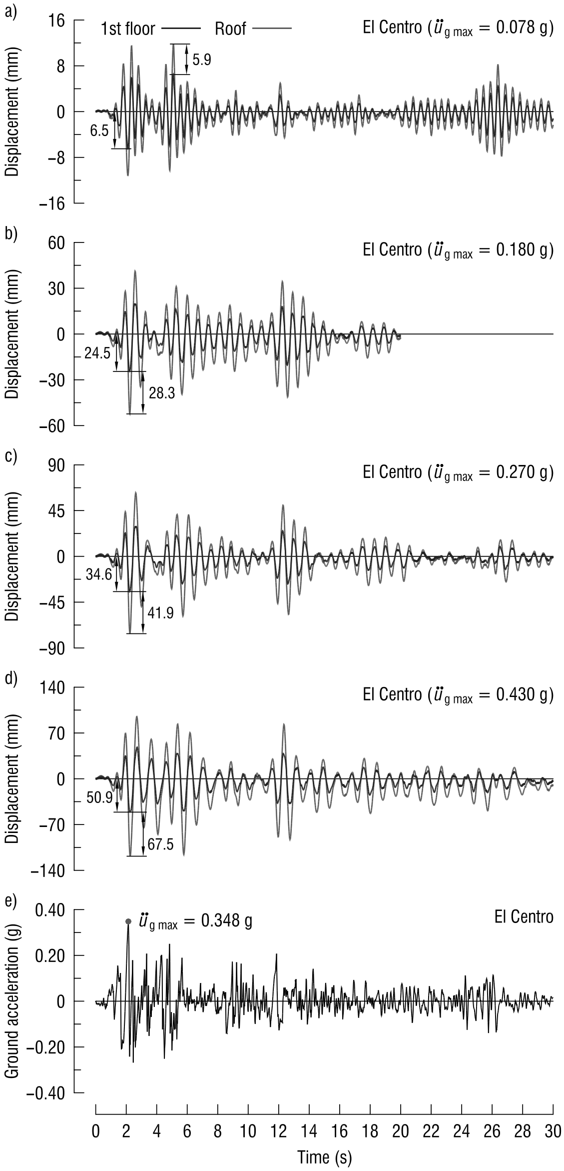

Figure 9.6. *Time histories of 1st floor and roof displacements for El Centro earthquake N–S component scaled to (a) 0.078 g PGA, (b) 0.180 g PGA, (c) 0.270 g PGA, (d) 0.430 g PGA, and (e) N–S component of horizontal ground acceleration of El Centro earthquake*

Phase	Type of tests	Description of the test
Preliminary	Forced-vibration	Preliminary dynamic characterization of the building
	Forced-vibration	Dynamic characterization without the actuators attaches
	Forced-vibration	Dynamic characterization with the actuators attaches
Level 1	Pseudo-dynamic	Test with the El Centro recording ($\ddot{u}_{g\,\max} = 0.078\,$g)
Level 2	Pseudo-dynamic	Test with the El Centro recording ($\ddot{u}_{g\,\max} = 0.129\,$g)
	Forced-vibration	Dynamic characterization after PSD ($\ddot{u}_{g\,\max} = 0.129\,$g)
Level 3	Pseudo-dynamic	Test with the El Centro recording ($\ddot{u}_{g\,\max} = 0.180\,$g)
	Forced-vibration	Dynamic characterization after PSD ($\ddot{u}_{g\,\max} = 0.180\,$g)
Level 4	Pseudo-dynamic	Test with the El Centro recording ($\ddot{u}_{g\,\max} = 0.270\,$g)
	Forced-vibration	Dynamic characterization after PSD ($\ddot{u}_{g\,\max} = 0.270\,$g)
Level 5	Pseudo-dynamic	Test with the M7R70A1 accelerogram ($\ddot{u}_{g\,\max} = 0.271\,$g)
Level 6	Pseudo-dynamic	Test with the El Centro recording ($\ddot{u}_{g\,\max} = 0.430\,$g)
	Forced-vibration	Dynamic characterization after PSD ($\ddot{u}_{g\,\max} = 0.430\,$g)
Final test	Push-over	Push over test until $\mu_\Delta = 3.62$
	Forced-vibration	Dynamic characterization after push over test

Table 9.1. *Chronology of the tests carried out on the building*

The first measured yielding occurred during the PSD test with the El Centro ground motion scaled to 0.27 g PGA (Level 4 in Table 9.1). The responses of the structure for this test are shown in Figures 9.6c and 9.7c. At the time of the first yielding, the base shear was 144.4 kN. As can be seen in Figure 9.5b, the PSA response spectra for this level of excitation at the measured periods of vibration of the building is clearly higher than the design spectrum for Montreal. Maximum interstorey drifts were 34.6 and 41.9 mm for the first and second stories, which correspond to drift ratios of 1.15% and 1.40%, respectively. The structure performed very well during the test. Few new cracks developed, but existing cracks widened. Neither spalling of the cover, nor local instabilities of reinforcement were observed.

The last PSD test was performed with the El Centro ground motion scaled to 0.43 g PGA (Level 6 in Table 9.1). The PGA level corresponds to a 2% in 50 years probability level for Montreal [ADA 03]. The earthquake responses of the structure are shown in Figures 9.6d and 9.7d. An important period elongation can be observed from the response history. The maximum interstorey drifts were 50.9 and 67.5 mm for the first and second stories, respectively. Maximum base shear was 204.3 kN during the test, which is more than twice the design base shear. Analysis of the results reveals the structure has significant inelastic behavior. The longitudinal reinforcement in the beams, near the column faces, and at the base of the first-storey columns suffered inelastic tensile strains. The column longitudinal bars, below the first-floor beam-column joints and all the longitudinal bars in the second-storey columns, remained in the elastic range of the steel reinforcement.

This high-intensity level caused some damages to the structure. Several new cracks in the beams, columns, slabs, and joints appeared, and most of the existing cracks widened significantly. On the other hand, no spalling of the cover was observed, which implies that no local instabilities of reinforcement took place. Despite the very high level of excitation, the building preserved its structural integrity and its capacity to sustain gravity loads.

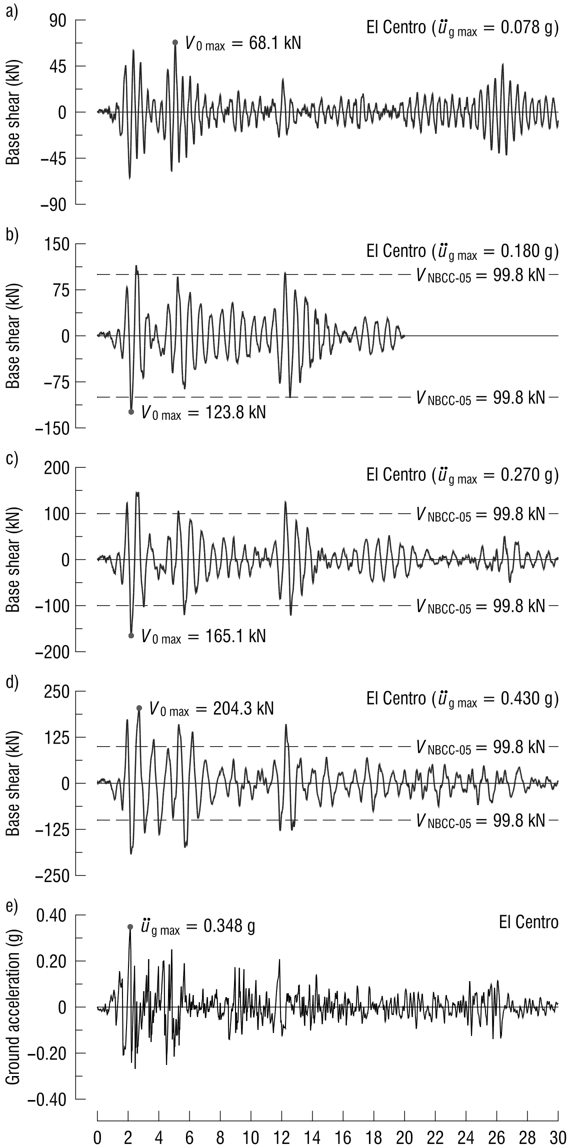

Figure 9.7. *Time histories of base shear for El Centro earthquake N–S component scaled to (a) 0.078g PGA, (b) 0.180g PGA, (c) 0.270g PGA, (d) 0.430g PGA, and (e) N–S component of horizontal ground acceleration of El Centro earthquake*

After the last very severe seismic excitation PSD test, a push-over test was carried out on the building. The test's objective was to verify the structure's ultimate capacity, thereby measuring its overstrength and ductility levels. The structure's was tested for incrementally increasing lateral loads. The shape of the lateral load distribution applied to the structure was calculated as combinations (square root of sum of squares) of the lateral load distributions obtained from modal analyses of the structure with the 2005 NBCC design spectra.

Figure 9.8 illustrates the building's response during the push-over test. It shows the overall hysteretic behavior of the building in terms of lateral load versus roof displacement. The maximum positive displacement of the roof was 183.1 mm, with a corresponding base shear of 237.6 kN. In contrast, the maximum negative roof displacement was 203.3 mm, with a corresponding base shear of 233.7 kN. Obviously, these displacements exceeded the drift ratio allowed by the NBCC 2005 for all buildings. The recorded base shear was 2.38 times greater than the design base shear and surpassed the base shear recorded during the PSD test with the El Centro ground motion scaled to 0.430 g PGA.

Spalling of the cover was observed at the base of the first-floor column during the push-over test. Furthermore, severe spalling of the concrete cover occurred in the spandrel beams of the first floor perpendicular to the loading (North–South) under important diagonal torsional compression stresses. Even at this level of loading and after several PSD tests, the building maintained its structural integrity and gravity load carrying capacity. In addition, according to the shape of the hysteretic curve, the structure had reserve strength and ductility at the end of the push-over test.

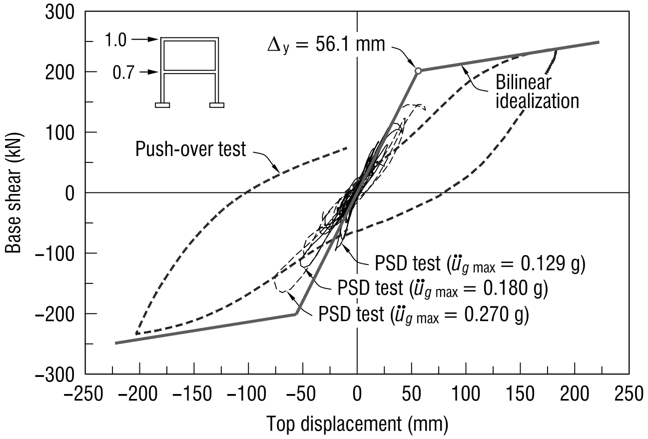

Figure 9.8. *Base shear–roof displacement response for push-over test*

9.5. Evaluating damage – forced vibration testing procedures

The dynamic characteristics (resonant frequencies, modes shapes, and modal damping) of the building were obtained by FVTs after each level of earthquake was applied to the structure. Table 9.1 presents test chronology, with a dynamic investigation following each PSD test to evaluate the damage sustained by the building.

The forced vibration tests consisted of subjecting the structure to a sinusoidal horizontal harmonic load generated by an eccentric-mass shaker. The recorded acceleration responses were then used to extract various vibration properties. Figure 9.9 shows the experimental setup for the FVT on the building. Plan views of the top slab (roof) and bottom slab (first floor) are illustrated. Concrete blocks, used on each floor to simulate the added mass resulting from superimposed dead and live loads, are shown on both floors, and the building orientation is indicated. The East–West axis was chosen for the PSD earthquake loading as well as the FVT.

The eccentric-mass shaker with variable-frequency motor was placed on the roof in a position selected to put the excitation force off-center by 430 mm. This position was chosen to excite both flexural and torsional modes of vibration. Low-frequency forced-balanced accelerometers were used on each floor to record horizontal accelerations in two orthogonal directions (parallel and perpendicular to the simulated earthquake loads).

The shaker generates a sinusoidal load with two equal weights counter-rotating about parallel vertical shafts. The amplitude of the resulting force, which is proportional to the square of the rotation frequency, can be adjusted by varying the weight eccentricities. The tests on the building were carried out with a frequency range of 1–16 Hz, with loads varying from 0.04 to 11.4 kN. The operation frequencies were computer controlled remotely. An optical pulse is emitted on each rotation of the masses to compute the exact rotating frequency for data processing. Several low-frequency servo-accelerometers were used; each measurement station is indicated in Figure 9.9.

Rapid frequency sweeps were first carried out to obtain a preliminary estimate of the resonant frequencies, to select the mass eccentricities, and to select the operation range in order to identify the first eight resonances of the building. Complete frequency sweeps were carried out for each measurement configuration, with a frequency increment of 0.01 Hz. Up to 1,500 frequency increments were necessary to cover the full range; samples were recorded during 4–8 s at 1,000 Hz. This is a very high sampling frequency, considering the fact that the data were filtered at 20 Hz, but it was necessary to record the optical pulse, using an unfiltered channel.

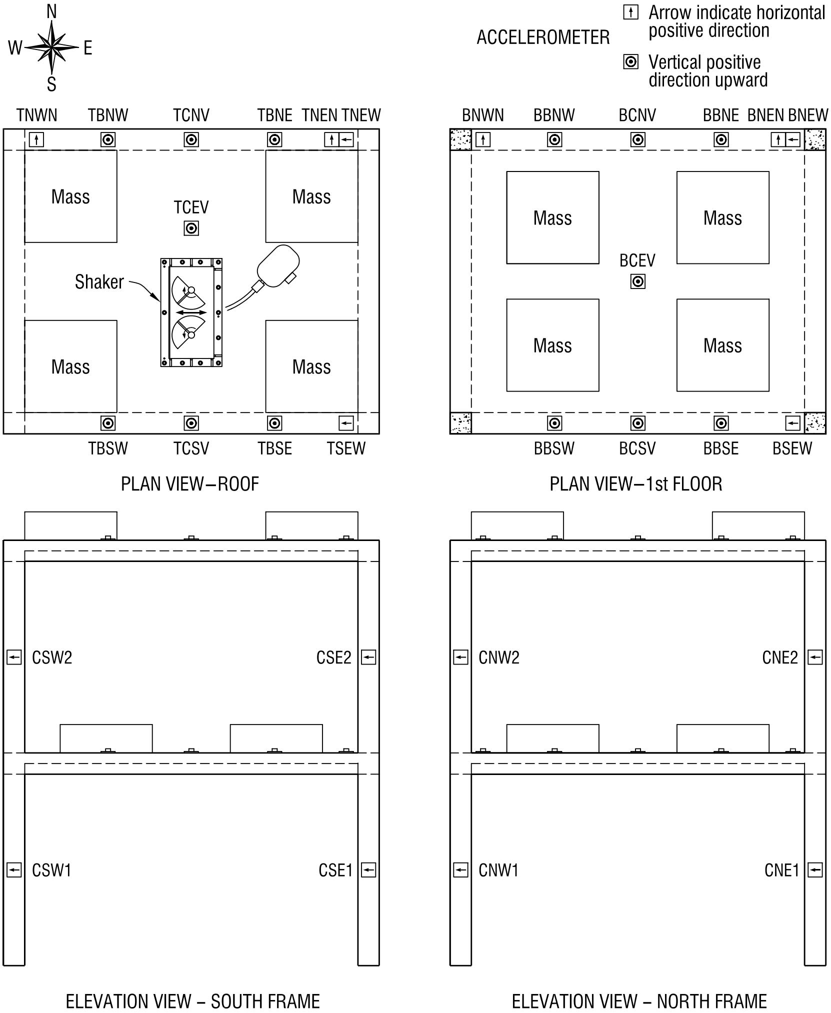

Figure 9.9. *Experimental setup*

9.5.1. *Frequency responses*

Figure 9.10 illustrates typical frequency responses obtained after each step. The responses were computed from the recorded time histories, extracting amplitude and phase information for each measurement position and for each frequency increment of the excitation force. Both acceleration and phase are plotted against frequency. Peaks in the amplitude response indicate resonances and, together with the corresponding phase, these values are used to plot the various mode shapes.

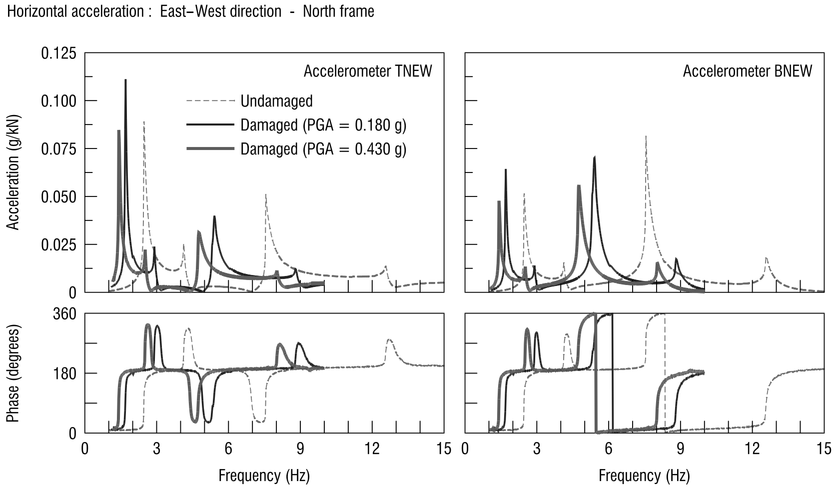

Figure 9.10. *Measured frequency responses (North frame)*

The undamaged frequency responses, obtained during the preliminary phase of the tests (see Table 9.1) are compared to the responses obtained after the 0.180 g PSD tests (the design level) and the 0.430 g PSD tests. The frequency shift and damping modification are clearly visible. Tracking the variation of the key modal parameters is the basis of the damage identification process, described in the following section.

9.6. Damage detection – analytical evaluation

The frequency–response curves from the FVT are used to identify the structure's dynamic properties and predict damage at each level. In this paper, eigenfrequencies and mode shapes are determined and used to update a parameterized finite element model. Changes in measured quantities are caused by stiffness reductions in members, which can be interpreted as damage. The method's theoretical and numerical aspects have been presented previously [WEB 07, WEB 08]. Since the earthquake excitation is in the East–West direction, the North and the South frames are affected most. In the following, only the North frame is analyzed.

9.6.1. *Modal analysis*

The changes in frequencies and mode shapes seen in Figure 9.10 indicate that considerable damage has occurred. The measured frequency response curves are used to extract eigenfrequencies, damping values, and mode shapes by the peak-amplitude method [EWI 01]. In this method, modal parameters are extracted considering one mode at a time and determining frequencies and damping values with the half-power bandwidth method. The amplitudes and phase angles of the mode shapes can then be determined easily. The method is rather simple but works adequately if the modes are well-separated and damping is not very high. Frequencies and damping values for those modes that lead to displacements in the East–West direction are given in Table 9.2. The two lateral and the two torsional modes for each damage level correspond to the peaks shown in Figure 9.10. For the analysis presented in this chapter, only the lateral modes were used and damping was ignored. Only real mode shapes were considered and the phase information was used only for determining the sign. The mode shapes were orthonormalized with respect to the mass.

9.6.2. *Finite-element model*

For updating, the frame was modeled by finite elements. The mass is concentrated on the two floors and the model has therefore only two degrees of freedom. However, displacements of the two floors only give information about overall damage: whether damage occurred in the columns or the floors cannot be distinguished. Rotations would also have to be measured to get that information. Since that is not practical, additional sensors were mounted at column mid-height and at the beam quarter points, as shown in Figure 9.11a. Consistently with the sensor positions, each column and each floor were modeled by four massless beam elements.

Mode	Damage level	Lateral E–W		Torsional	
		Frequency (Hz)	Damping (%)	Frequency (Hz)	Damping (%)
First	Initial	2.47	1.57	4.14	1.21
	0.129 g	2.09	2.63	3.61	1.73
	0.180 g	1.70	1.43	2.91	1.24
	0.270 g	1.65	2.42	2.91	1.40
	0.430 g	1.43	2.38	2.52	1.45
	Push-over	1.29	1.75	2.36	1.25
Second	Initial	7.56	0.76	12.59	1.14
	0.129 g	6.28	1.81	10.40	1.34
	0.180 g	5.41	1.54	8.84	1.40
	0.270 g	5.27	2.11	8.82	1.14
	0.430 g	4.76	1.80	8.06	1.21
	Push-over	4.59	1.29	7.85	1.26

Table 9.2. *Dynamic properties of building at different damage levels*

When updating a model, it should be recognized that stiffness changes in some elements hardly affect eigenfrequencies and mode shapes. These elements should not be included in the update because damage in them is undetectable. For the frame, these are the central elements of the columns and the floors, where the bending moments are close to zero. Fortunately, this is also where little earthquake-loading damage is expected. Figure 9.11b indicates the detectable elements used in the update.

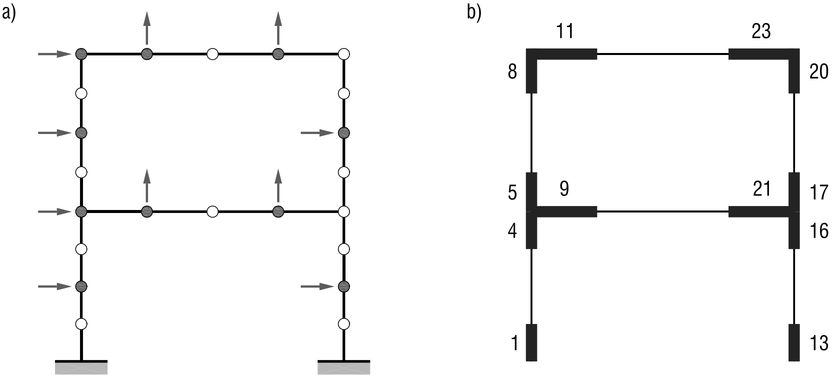

Figure 9.11. *Finite-element model of frame: (a) model with sensors and (b) detectable elements*

The global stiffness matrix is parameterized as follows:

$$\mathbf{K} = \mathbf{K}^{(0)} + \Delta\mathbf{K} = \mathbf{K}^{(0)} + \sum_{j=1}^{p} \alpha_j \mathbf{K}^{(j)} \qquad [9.1]$$

The first matrix, $\mathbf{K}^{(0)}$, is the stiffness matrix of the reference model. The corresponding beam properties were determined from uncracked concrete sections and a measured modulus of elasticity. The matrices $\mathbf{K}^{(j)}$ are stiffness matrices of the updated elements. The factors α_j are the update parameters and are collected in vector $\mathbf{a} = [\alpha_1, \ldots, \alpha_p]$.

9.6.3. *Model updating*

Model updating is performed by adjusting the parameters α_j of the finite-element model until eigenvalues and mode shapes are close to measured values, that is, by minimizing the weighted residual:

$$\mathbf{r}(\mathbf{a}) = \mathbf{W} \begin{bmatrix} \lambda_1^{\text{meas}} - \lambda_1 \\ \vdots \\ \lambda_m^{\text{meas}} - \lambda_m \\ \phi_1^{\text{meas}} - \phi_1 \\ \vdots \\ \phi_m^{\text{meas}} - \phi_m \end{bmatrix} \qquad [9.2]$$

For m modes and s sensors, the residual vector $\mathbf{r}(\mathbf{a})$ contains $n = m(s+1)$ data values. The weighting matrix is normally chosen as a diagonal matrix, that is, each component of the residual is weighted individually. Weighting is important because different components have different magnitudes and different accuracies. To get similar magnitudes, frequencies are normalized by measured frequencies and mode shapes are normalized to a maximum value of 1. There should also be a relative weight between frequencies and mode shapes. In this investigation, the relative weight was chosen such that eigenfrequencies and mode shapes converged at a similar rate during the update. This was the case when normalized eigenfrequencies were weighted by a factor of 2.0 relative to the normalized mode shapes.

The updating problem is nonlinear because the residual depends nonlinearly on the parameters α_j. The Gauss–Newton method is the conventional method to solve this nonlinear least-squares problem. In this method, the nonlinear problem is solved by a series of linear least-squares problems. In each iteration k, the problem is linearized as:

$$\mathbf{r}(\mathbf{a}_k + \Delta\mathbf{a}_k) = \mathbf{r}_k - \mathbf{S}_k \Delta\mathbf{a}_k \qquad [9.3]$$

where $\mathbf{S}_k$ is the sensitivity matrix

$$\mathbf{S}_k = -\left.\frac{\partial \mathbf{r}(\mathbf{a})}{\partial \mathbf{a}}\right|_{\mathbf{a}=\mathbf{a}_k} = -\begin{bmatrix} \dfrac{\partial r_1}{\partial \alpha_1} & \cdots & \dfrac{\partial r_1}{\partial \alpha_p} \\ \vdots & & \vdots \\ \dfrac{\partial r_n}{\partial \alpha_1} & \cdots & \dfrac{\partial r_n}{\partial \alpha_p} \end{bmatrix} \qquad [9.4]$$

and $\mathbf{r}_k = \mathbf{r}(\mathbf{a}_k)$. The negative sign is due to the definition of the residual, where the model dynamic properties have a minus sign.

9.6.4. *Regularization*

The updating procedure is challenging, in that it is an inverse, ill-posed problem. The associated forward problem of determining changes in the dynamic properties due to changes in the stiffness is well-posed, that is small variations in stiffness lead to small variations in the dynamic properties. The inverse problem of back-calculating the stiffness from the dynamic properties, however, is ill-posed. Small variations in the dynamic properties may lead to large changes in the identified stiffness. This happens if the measured dynamic properties are inconsistent with the model. For a reasonable model, the main source of inconsistent input are measurement errors. In order to fit inconsistent dynamic properties, the model typically has to undergo large stiffness changes of the opposite sign in neighboring elements.

In an analysis, the influence of input errors cannot be separated from the true results. This is acceptable in a well-posed problem, since its influence is known to be small. In an ill-posed problem, however, the influence of input errors can make the result unusable. To avoid this problem, we use Tikhonov regularization which is well-known in the mathematical literature [HAN 98, VOG 02]. Tikhonov regularization avoids overly large changes in the update parameters by introducing penalty functional that is added to the residual functional. The total functional is given as:

$$J(\mathbf{a}_{k+1}) = \|\mathbf{r}_{k+1}\|_2^2 + \gamma\|\mathbf{a}_{k+1}\|_2^2 \tag{9.5}$$

The first part, the residual functional, minimizes the difference between measured and calculated quantities. The second part, the penalty functional, restricts the size of the update parameters. Minimizing equation [9.5] leads to a compromise between an accurate update and small update parameters. The functional can be linearized as:

$$J(\mathbf{a}_{k+1}) = \|\mathbf{r}_k - \mathbf{S}_k(\mathbf{a}_{k+1} - \mathbf{a}_k)\|_2^2 + \gamma\|\mathbf{a}_{k+1}\|_2^2 \tag{9.6}$$

Minimizing equation [9.5] leads to the update equation

$$\mathbf{a}_{k+1} = \mathbf{a}_k + \left(\mathbf{S}_k^{\mathrm{T}}\mathbf{S}_k + \gamma\mathbf{I}\right)^{-1}\left(\mathbf{S}_k^{\mathrm{T}}\mathbf{r}_k - \gamma\mathbf{a}_k\right). \tag{9.7}$$

Note the extra term $\gamma\mathbf{a}_k$, which appears only if the linearization is performed after regularization. The extra term ensures that the regularization is still effective after many iterations [VOG 87]. We include line search in our algorithm to make the update procedure more robust.

The regularized solution is less accurate in matching measurements but it avoids overly large changes in model parameters that are due to inconsistent input data (due to measurement errors). The optimal trade-off, that is the optimal regularization parameter γ, can be found by minimizing the generalized cross-validation function [OSU 85]

$$GCV(\gamma) = \frac{\frac{1}{n}\|\mathbf{r}_\gamma\|_2^2}{\left[\frac{1}{n}\,\mathrm{trace}(\mathbf{I}_n - \mathbf{A}_\gamma)\right]^2} \tag{9.8}$$

where $\mathbf{r}_\gamma$ is the converged regularized residual and $\mathbf{A}_\gamma$ is the matrix

$$\mathbf{A}_\gamma = \mathbf{S}_\gamma\left(\mathbf{S}_\gamma^{\mathrm{T}}\mathbf{S}_\gamma + \gamma\mathbf{I}\right)^{-1}\mathbf{S}_\gamma^{\mathrm{T}} \tag{9.9}$$

with the sensitivity matrix $\mathbf{S}_\gamma$ at the regularized solution. For a decreasing regularization parameter γ, the converged regularized residual decreases, but the denominator also decreases at the same time, and somewhere is a minimal value of the quotient, giving the optimal regularization parameter. In the nonlinear scenario, the update procedure starts with a high value of γ and evaluates the update parameters $\mathbf{a}_{k+1}$ iteratively [VOG 87]. After convergence, the generalized cross-validation function is calculated. Then the value of γ is decreased and the update is repeated using the result from the previous calculation as starting values. In this way, the generalized cross-validation function is calculated for a whole range of regularization parameters and the optimal value can be determined. Starting with a large regularization parameter rather than a small one makes the procedure more stable.

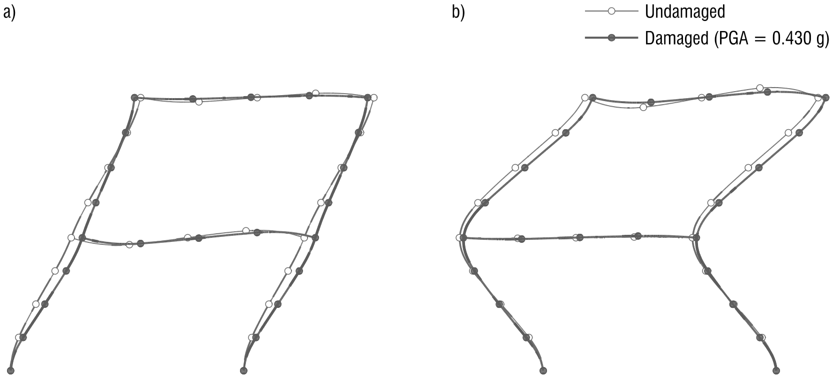

Figure 9.12. *Update of the two modes from undamaged level to damaged level (0.430 g PGA)*

9.6.5. *Results*

The damage detection procedure described above was applied to the building's North frame. Figure 9.12 shows the updated mode shapes for the undamaged state and for damage level 0.430 g. Other mode shapes are very close to those shown. For instance, those for damage level 0.180 g are not distinguishable by eye from those at level 0.430 g. Clearly, changes of mode shapes are rather small and only a sophisticated algorithm can give meaningful results.

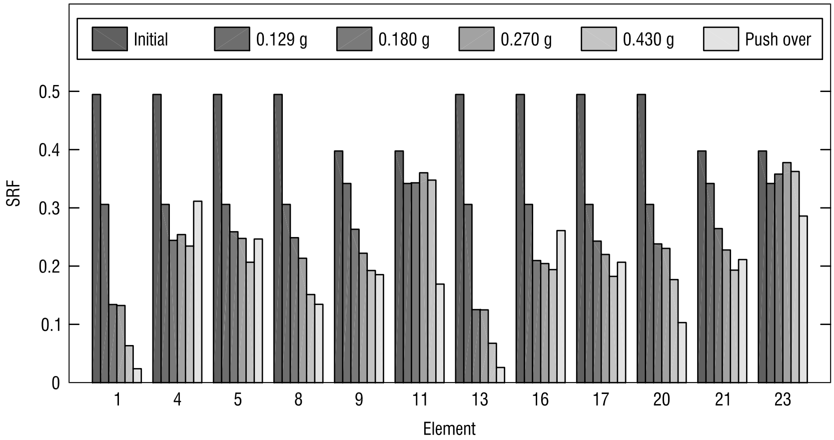

Figure 9.13. *Stiffness reduction factors for 6 damage levels (North frame)*

Figure 9.13 shows the stiffness reduction factors for each damage level. All factors are given relative to the nominal uncracked stiffness of the frame. Since all elements were cracked initially due to shrinkage and service loads, the initial stiffness is already reduced by about 50%. For the first two damage levels, only the two horizontal degrees of freedom were measured, which does not allow to update each element separately. Therefore, elements were updated in groups for these two levels, resulting in identical stiffness reduction factors in each group (elements 1–8, 9–11, 13–20, 21–23). Nevertheless, the results for the first two damage levels should be considered with caution since they depend somewhat on the element grouping and the weighting in the residual [WEB 07, WEB 08]. The problem is that the two sensors provide only $n = 6$ equations for $p = 4$ parameters, which are not sufficient for the generalized cross-validation to work reliably. For subsequent damage levels, 10 sensors are used leading to $n = 22$ equations for $p = 12$ parameters, which gives much more reliable results.

Damage is almost symmetric (compare elements 1–11 with 13–23), except for the roof (elements 11 and 23) at push-over level. The most severe damage is encountered at the base of the columns (elements 1 and 13). Column ends at the first floor (elements 4, 5, 16, 17) are cracked by the first earthquake level, but stay more or less constant thereafter. Beams (elements 9, 11, 21, 23) are less damaged than columns. The calculated stiffness reduction factors compare well with the observed cracks in the lab.

9.7. Summary and conclusions

An extensive dynamic and pseudo-dynamic testing program was presented. A two-storey, reinforced HPC building was subjected to several levels of earthquake excitation by PSD tests. Dynamic properties at each level were evaluated from FVT. These properties were used for model-based damage detection. Damage detection is based on a sensitivity-based update with some important modifications: only detectable elements were updated, Tikhonov regularization was employed to improve results in the presence of measurement noise; generalized cross-validation was used to determine the optimal regularization parameter. Stiffness reduction factors are presented for a frame of the structure for all damage levels. These values compare well with the observed crack patterns.

9.8. Bibliography

[ADA 03] Adams J., Halchuk S., *Fourth-Generation Seismic Hazard Maps of Canada: Values for Over 650 Canadian Localities Intended for the 2005 National Building Code of Canada*, Earthquakes Canada, Geological Survey of Canada Open File 4459, Structural Engineering Series, Ottawa, ON, 2003.

[ATK 98] Atkinson G.M., Beresnev I.A., "Compatible ground-motion time histories for new national seismic hazard maps", *Canadian Journal of Civil Engineering*, vol. 25, no. 2, pp. 305–Ü318, 1998.

[CSA 94] CSA, *Design of Concrete Structures*, Standard CSA-A23.3-94, Canadian Standards Association, Rexdale, ON, 1994.

[CSA 04] CSA, *Design of Concrete Structures*, Standard CSA-A23.3-04, Canadian Standards Association, Mississauga, ON, 2004.

[EWI 01] Ewins D.J., *Modal Testing: Theory, Practice and Application*, 2nd edition, Mechanical Engineering Research Studies Engineering Design Series, Taylor & Francis Group, 2001.

[HAN 98] Hansen P.C., "Rank-deficient and discrete ill-posed problems", *SIAM Monographs on Mathematical Modeling and Computation*, 1998.

[HIL 77] Hilber H.M., Hughes T.J.R., Taylor R.L., "Improved numerical dissipation for time integration algorithms in structural dynamics", *Earthquake Engineering and Structural Dynamics*, vol. 5, pp. 283–292, 1977.

[MOU 08a] Mousseau S., Paultre P., "Seismic performance of a full-scale reinforced high-performance-concrete building: Part I. Experimental study", *Canadian Journal of Civil Engineering*, vol. 37, no. 1, pp. 832–848, 2008.

[MOU 08b] Mousseau S., Paultre P., Mazars J., "Seismic performance of a full-scale reinforced high-performance-concrete building: Part II. Analytical study", *Canadian Journal of Civil Engineering*, vol. 37, no. 1, pp. 849–862, 2008.

[NRCC 05] NRCC, *National Building Code of Canada 2005*, National Research Council of Canada, Ottawa, ON, 2005.

[OSU 85] O'SULLIVAN F., WAHBA G., "A cross validated Bayesian retrieval algorithm for nonlinear remote sensing experiments", *Journal of Computational Physics*, vol. 59, pp. 441–455, 1985.

[WEB 07] WEBER B., PAULTRE P., PROULX J., "Structural damage detection using nonlinear parameter identification with Tikhonov regularization", *Structural Control and Health Monitoring*, vol. 14, no. 3, pp. 406–427, 2007.

[WEB 08] WEBER B., PAULTRE P., PROULX J., "Consistent regularization of nonlinear model updating for damage identification", *Mechanical Systems and Signal Processing*, vol. 23, no. 6, pp. 1965–1985, 2008.

[VOG 87] VOGEL C.R., "An overview of numerical methods for nonlinear ill-posed problems", in ENGL H.W., GROETSCH C.W., *Inverse and Ill-Posed Problems,* Academic Press, pp. 231–245, 1987.

[VOG 02] VOGEL C.R., "Computational methods for inverse Problems", *SIAM Frontiers in Applied Mathematics*, Philadelphia, PA, 2002.

List of Authors

Christophe BAILLIS
OXAND SA
Avon/Fontainebleau
France

Zdeněk P. BAŽANT
Northwestern University
Evanston
USA

Farid BENBOUDJEMA
IFSTTAR
France

Michael J. BORDEN
University of Texas
Austin
USA

René DE BORST
University of Technology
Eindhoven
Netherlands

Bruno CAPRA
OXAND SA
Avon/Fontainebleau
France

Frédéric DUFOUR
INP Grenoble
France

Bruno GÉRARD
OXAND SA
Avon/Fontainebleau
France

Cédric GIRY
INP Grenoble
France

Peter GRASSL
University of Pau and
Pays de l'Adour
France

David GRÉGOIRE
University of Pau and
Pays de l'Adour
France

Thomas J.R. HUGHES
University of Texas
Austin
USA

Thomas de LARRARD
IFSTTAR
France

Jia-Liang LE
University of Minnesota
Minneapolis
USA

Bruno MENDIBOURE
University of Pau and
Pays de l'Adour
France

Christelle MIQUEU
University of Pau and
Pays de l'Adour
France

Sébastian MOUSSEAU
University of Sherbrooke
Canada

Patrick PAULTRE
University of Sherbrooke
Canada

Roland J.M. PELLENQ
MIT
Cambridge
USA

Gilles PIJAUDIER-CABOT
University of Pau and
Pays de l'Adour
France

Jean PROULX
University of Sherbrooke
Canada

Laura B. ROJAS-SOLANO
University of Pau and
Pays de l'Adour
France

Michael A. SCOTT
University of Texas
Austin
USA

Gaël THILLARD
OXAND SA
Avon/Fontainebleau
France

Jean-Michel TORRENTI
IFSTTAR
Paris
France

Franz J. ULM
MIT
Cambridge
USA

Clemens V. VERHOOSEL
University of Technology
Eindhoven
Netherlands

Romain VERMOREL
University of Pau and
Pays de l'Adour
France

Benedikt WEBER
University of Sherbrooke
Canada

Qiang YU
Northwestern University
Evanston
USA

Index